



UNIVERSITÀ
DEGLI STUDI
DI PADOVA



Mittuniversitetet
MID SWEDEN UNIVERSITY

DIPARTIMENTO DI INGEGNERIA INDUSTRIALE (DII)
Sports Tech Research Centre, Department of Quality Technology and Management,
Mechanical Engineering and Mathematics, Mid Sweden University (SWE)

MASTER OF SCIENCE IN MECHANICAL ENGINEERING

**Development and validation of an
Instrumented Monoski
for kinematic and kinetic data collection**

Student:

Giovanni Colla

Home University Supervisor:

Prof. Nicola Petrone

Host University Supervisor:

Prof. Andrey Koptug

Academic year 2021-2022

ABSTRACT

OBJECTIVES: The main purpose of this thesis is to provide mechanical and electronic tools to study the monoski complex system in both indoor and outdoor environment. In order to collect kinematic and kinetic data, an Instrumented Monoski needs to be developed, which can be used in indoor and outdoor environment. In particular, ground reaction forces, the variation of damper stroke and speed, the seat and body vibrations and inclination are to be measured. To acquire the kinematics of the frame of the monoski and of the skier it is necessary to identify the best sensors. Moreover other objectives of the current research are: the improvement to the Multicomponent Load Cell by integrating the amplification stage, its calibration using an innovative method called Neural Networks.

MATERIALS AND METHODS: An extensive literature review was conducted to identify articles focusing on monoskis and dissertations with the same research objective. The research then focused on different methods for the calibration of load cells. The Neural Networks, which is part of the Deep Learning Toolbox of MATLAB, was used for the purpose of the research. To acquire the kinematics of the frame of the monoski and of the skier it is necessary to identify the best sensors. The ground reaction forces are measured using the Multicomponent load cell that was developed, the damper stroke and speed has been measured using a linear potentiometer placed in parallel to the shock absorber, the seat and body vibrations and inclination were acquired using triaxial accelerometers and a gyroscope. Moreover an investigation on the dynamic behaviour and vibrations of the monoski was performed. This research work was carried out mainly in the Sports Tech Research Centre in Östersund at the Mid Sweden University (SWE) from 22th of February to 13th of June. Further validation tests were performed in the final phase of investigation at the Department of Industrial Engineering at the University of Padua (ITA) from the end of August to the beginning of October 2022.

RESULTS: The outcomes of indoor tests show that the foot load cell is able to correctly measure static and dynamic loads with high accuracy. The whole measurement systems perfectly provide reliable data, which confirms the validity of the methods and instruments used.

CONCLUSIONS: The aim of this thesis to collect data for the design and development of monoskis was achieved, and reliable data are now available for further investigations. A limitation of this study is that data were collected indoor therefore outdoor testing would be necessary to further confirm the results achieved. It is hoped that this work will serve as reference for many future developments: the Instrumented Monoski can soon be used for tests on ski slopes, opening the way for the design of an innovative, cost-effective and high-performance monoski. This interesting work will lead to the development of a user friendly and safe monoski to make this sport more accessible to individuals with disabilities.

ACKNOWLEDGEMENTS

First of all, I would like to thank my professor Andrey Koptug for supporting me in developing this project and in my every day life during my staying in Östersund. A special thanks to his wife who provided me with a lot of tasteful food.

Equally I would like to thank professor Jonas Danvind for giving me the opportunity to experience the Swedish way of life with his dogs. He contributed to the drafting of my thesis and he also introduced me to the Swedish Para-Alpine Ski Team, which was a unique chance for me to talk with these amazing people and get insights on Para Alpine sports.

I am particularly grateful to my professor Nicola Petrone for his support all throughout the entire research work. He has contributed with his precious advice to my thesis and provided valuable guidance both on professional and personal level. Thanks to his initiative I had the opportunity to spend time abroad in a very stimulating and multicultural environment. It has been an amazing experience that I will never forget.

One person I cannot leave out is my mother, who has been always supporting me during my studies and my exams. Thank you so much. I share with you this important achievement. My whole family was always present and ready to adjust to my ups and downs during stressful times.

Finally, a special mention to Alessandro, Alice, Chiara, Giulia, Marta, Matteo, Mattia, Maverick for being source of distraction during this adventure. Please continue to make fun of me. There is no other way to cheer me up!

Huge thanks to Anton, Charlotte, Csaba and all the friends that I made in Sweden, thank you, you made this experience unforgettable. I hope to see you all one day. Maybe in Italy so we can enjoy some real Italian food together.

My last thoughts go to the PhD students and researchers in the Sports Tech Research Centre in Östersund and in Padua for helping me during my research. Thank you very much.

INTRODUCTION

Alpine sit skis enable wheelchair users and other disabled people to fly down mountains at speed. In the last decades, there has been a lot of progress to allow anyone to enjoy winter sports; this sport is an adaptation of alpine skiing designed for people who are wheelchair users or who have other mobility difficulties or paraplegia.

After the Second World War, Paralympic alpine skiing was born with the initial purpose of assisting the veterans and civilians who had been injured during the war.

At the first Paralympic Winter Games in Örnsköldsvik, Sweden, in 1976, athletes competed in Slalom and Giant Slalom and three distances in Nordic Skiing. Downhill was added to Paralympic program in 1984 in Innsbruck, Austria, and Super-G was added in 1994 in Lillehammer, Norway. Sit-skiing, or mono-skiing, was introduced as a demonstration sport at the Innsbruck 1984 Paralympic Games and became a medal event in Nagano 1998 Paralympic Games.

According to “IPC (International Paralympic Committee) Classification Rules and Regulations”, Paralympic Alpine Skiing is subdivided into three competition classes: Standing class (e.g. upper or lower body limb loss, skiing with or without prosthetic or cerebral palsy), Visually Impaired class, and Sitting class (IPC, 2015).

The present work is focused on the last class, sitting athletes having acquired or congenital paralysis or lower limb loss, because of the interesting (from a mechanical point of view) equipment used.

The hope of the author is that this work of acquisition and analysis of kinematic and kinetic data could be useful for future improvements of monoskis in order to make it a cheaper product, which utilization could be extended to a wider number of users attracting more people into the sport improving the life quality of many.

Ethic value

In the last decades, the evolution and application of assistive technologies have greatly aided individuals with disabilities. Advances in the technical sophistication of these assistive technologies parallel the progress made in information and computer technologies. However, it is very expensive to produce and develop adaptive devices, and rarely do companies have the money and resources to spend to develop these. Universities in this regard can be very helpful in stimulating the development and improvement of devices inclusive towards people with disabilities.

In parasport, equipment design also has a substantial impact on performance [1]. It can be strongly argued that in competitive sports, equipment should not be the limiting factor. In particular, the cost should not limit participation in the top categories. If athletes' individual performance parameters are identified, and equipment is customised accordingly, competition will be fairer and more focused on the athletes.

Due to the limited amount of research papers, design optimization is a challenging task depending on the type of sports. Therefore, the personal opinion of the users of the devices is a crucial element in engineering design to understand the design challenge, identify performance parameters, and implement results in engineering design for a particular case.

The aim of the project is to get data that can be very useful in two ways:

- for the design or development of monoskis and improve the performances
- safety and usability possibly making this sport more accessible
- to improve the performance and the skiing technique of the pro-athletes

Aim of the study

Thanks to the long-term collaboration between the University of Padua, Italy, and Mid Sweden University, Sweden, the first part of the thesis took place in the Sports Tech Research Centre in Östersund and the second in the Dipartimento di Ingegneria Industriale at University of Padua. The goal of this thesis is to provide mechanical and electronic tools to study the monoski complex system in both indoor and outdoor environment. The Instrumented Monoski delivered is a valid platform for the acquisition and analysis of kinetics and kinematics data: are measured the ground reaction forces, the variation of damper stroke and speed, the seat and body vibrations and inclination.

The instrumentation used for this work has been: a dynamometric load cell, linear motion position sensor, two triaxial accelerometers and a biaxial gyroscope.

In particular, the following tasks are individuated:

- Improvement on the load cell by integrating the amplification stage
- Development of an innovative calibration method for multicomponent load cells
- Individuate the best sensor to acquire the kinematics of the frame of the monoski and of the skier

CONTENTS

ABSTRACT.....	ii
ACKNOWLEDGEMENTS	iv
INTRODUCTION	vi
Ethic value	vii
Aim of the study.....	viii
CONTENTS.....	1
LIST OF FIGURES	5
1 MONOSKI: MAIN FEATURES.....	10
1.1 Survey	12
1.2 Interesting features	16
2 MONOSKI PROJECT	17
2.1 Matteo Ferrari.....	17
2.2 Davide Piccinin	19
2.3 Dario Vanzetto	24
3 INSTRUMENTATION	27
4 SCARVER BY TESSIER.....	28
4.1 Components and main features	29
5 DYNAMOMETRIC LOAD CELL	32
5.1 Strain gauges	32
5.2 Design of the load cell	34
5.3 Amplifiers	36
5.4 Calibration of load cell	40
5.4.1 Calibration instrumentation.....	40
5.4.2 Calibration procedure.....	43
5.5 Data analysis	46
5.6 Calibration using calibration matrix.....	46
5.6.1 Results of the calibration.....	48
5.6.2 Virtual channels.....	54

5.7	Calibration using neural networks	61
5.7.1	Neural Net Theory.....	62
5.7.2	Implementation of the NN.....	65
5.8	Comparison between the calibration methods	70
5.9	Limits of the load cell	73
6	ACQUISITION OF DAMPER STROKE AND SPEED	75
6.1	Resistive potentiometer.....	75
6.2	Magnetostrictive potentiometer.....	75
6.3	Model used	77
6.3.1	Calibration of linear potentiometer	78
7	GYROSCOPE	80
8	ACCELEROMETERS	83
9	DATA ACQUISITION HARDWARE	84
10	DATA ACQUISITION SOFTWARE	85
11	TEST AT SPORTS TECH RESEARCH CENTRE, ÖSTERSUND	92
11.1	Drop 15 kg on the knees of the skier	93
11.2	Jumps on the seat.....	95
11.3	Leaning left and right.....	99
11.4	Leaning forward and backwards	100
11.5	Study of vibrations.....	101
11.6	Tests with acc. and gyro attached to the chest of the skier.....	103
12	VALIDATION TEST AT PADOVA UNIVERSITY	105
12.1	Materials.....	105
12.1.1	MTS test bench	106
12.1.2	Load cells.....	110
12.1.3	Linear potentiometer	111
12.1.4	Accelerometers.....	112
12.1.5	DAQ	114
12.1.6	DAQ software and data processing.....	115
12.2	Reference system	116
12.3	Aims of the tests	117

12.4	Static location of the Centre of Pressure.....	118
12.4.1	COP by Quantitative Anthropometry	118
12.4.2	Skier leaning forward.....	120
12.4.3	Skier leaning backwards	122
12.4.4	COP by the load cells.....	124
12.5	Dynamic location of the Centre of Pressure	128
12.6	Forced excitations.....	131
12.6.1	Sinusoidal forced vibrations.....	133
12.6.2	Step forced vibrations	135
12.7	Compression of the shock absorber.....	137
12.7.1	Loads on the shock absorber	139
12.8	Dynamic behaviour of the shock absorber	142
12.9	Transfer function	143
12.9.1	Sinusoidal forced vibrations.....	144
12.9.2	Step forced vibrations	146
13	CONCLUSION AND FURTHER DEVELOPMENTS	148
13.1	Future developments.....	149
APPENDIX.....	152
	Load cell amplifiers boards design	152
	Technical drawings of the new foot.....	156
	Calibration of the load cell	162
	LabVIEW programs	163
	FEM analysis of the load cell	167
BIBLIOGRAPHY	171

LIST OF FIGURES

Figure 1.1: Monoski main parts.....	10
Figure 1.2: Change of direction.....	10
Figure 1.3: In blue the results from online form, in orange the answers of Lasse Ericsson	13
Figure 1.4: Importance – satisfaction results.....	15
Figure 1.5: DynAccess monoskis	16
Figure 1.6: Is highlighted in red the triangular arm of the suspension	16
Figure 2.1: Dynafoot.....	17
Figure 2.2: Result of Ferrari’s test.....	18
Figure 2.3: Dynaplate.....	19
Figure 2.4: Mean values of force peaks	20
Figure 2.5: Stella’s 3 rd wide run	21
Figure 2.6: Varotto’s 2 nd wide run.....	21
Figure 2.7: Mean values of X_{COP}	22
Figure 2.8: GRF (left/right) – position of COP	24
Figure 2.9: Results from run 302.....	25
Figure 4.1: Monoski Scarver.....	29
Figure 4.2: Suspension kinematics settings.....	30
Figure 4.3: COP setting.....	31
Figure 4.4: Aluminium foot for Dual-ski.....	31
Figure 5.1: Dynafoot by Matteo Ferrari.....	32
Figure 5.2: Wheatstone full bridge	32
Figure 5.3: Comparison between foot and load cell	34
Figure 5.4: Placement of the strain gauges	34
Figure 5.5: Multicomponent indirect load cell	35
Figure 5.6: Example of signal from not amplified vertical channels first when load cell unloaded, second when a vertical load of 65 kg is applied. Amplitude is in mV.	36
Figure 5.7: Amplifier with low pass filter.....	37
Figure 5.8: Example of signal from the channels with the amplifiers when the load cell is unloaded	38
Figure 5.9: Construction stages of the load cell	39
Figure 5.10: Kistler force plate connections with Built-In Amplifier	41

Figure 5.11: (a) New foot CAD drawing (b) The plates manufactured for the calibration	42
Figure 5.12: Material used in the calibration	42
Figure 5.13: (a) Calibration of Fy (b) Calibration of Mx	44
Figure 5.14: Load - Channel output for Fz Calibration	45
Figure 5.15: Load – Channel output for Fz calibration	49
Figure 5.16: Load – Channel output for Fy calibration	50
Figure 5.17: Load – Channel output for Mx calibration	51
Figure 5.18: Load – Channel output for My calibration	52
Figure 5.19: bx and by of the load cell	54
Figure 5.20: Virtual channels for Fz calibration	55
Figure 5.21: Virtual channels for Fy calibration	56
Figure 5.22: Virtual channels for Mx calibration	57
Figure 5.23: Virtual channels for My calibration	58
Figure 5.24: Calibration loads rebuilt using the Calibration Matrix	60
Figure 5.25: Example of NN	62
Figure 5.26: Scheme of NN with 4 inputs, 2 neurons in the hidden layer and an output layer of 1 neuron so one output only	62
Figure 5.27: Training process	64
Figure 5.28: Loads used for the calibration with the NN approach	66
Figure 5.29: Code for the creation of a NN part 1	67
Figure 5.30: Code for the creation of a NN part 2	68
Figure 5.31: Code for the creation of a NN part 3	69
Figure 5.32: NN structure. (a) One NN for all the loads (b) Four NN: one for each load	69
Figure 5.33: Loads to test the calibration methods	70
Figure 5.34: Results filtered using function ‘movmean’ value 5;	71
Figure 5.35: Results of FEM simulation	74
Figure 6.1: LVDT construction	76
Figure 6.2: Signal processing LVDT	76
Figure 6.3: Öhlins TTX shock absorber	77
Figure 6.4: Linear potentiometer fixed on the monoski	78
Figure 6.5: Linear interpolation of the signal from the potentiometer	78
Figure 6.6: Calibration of the height of the seat. In red are the measurement points	79

Figure 6.7: Results of the calibration of the height of the seat and their linear interpolation	79
Figure 7.1: Gyroscope and reference system	80
Figure 7.2: signal after being integrated, lines of the two methods to cancel the drift.....	81
Figure 7.3: signal after using the line method	82
Figure 7.4: Signal after using the interpolation method.....	82
Figure 8.1: Accelerometers and reference system of each.....	83
Figure 8.2: Accelerometers and gyroscope fixed on the monoski	83
Figure 9.1: NI USB-6210 module	84
Figure 10.1: Acquisition setup for an outdoor test	85
Figure 10.2: LabVIEW program part 1.....	86
Figure 10.3: LabVIEW program part 2.....	87
Figure 10.4: LabVIEW program part 3.....	88
Figure 10.5: LabVIEW program	89
Figure 10.6: Front Panel of LabVIEW after an acquisition	90
Figure 10.7: Example of file produced	91
Figure 11.1: Tester on the monoski	92
Figure 11.2: Main results of the test of dropping 15 kg on the knees of the skier	94
Figure 11.3: Main results of the test of jumps on the seat	96
Figure 11.4: Load cell channels of the test of jumps on the seat.....	97
Figure 11.5: Comparison between load cell channels and roll moment.....	98
Figure 11.6: Main results of the test of leaning left and right.....	99
Figure 11.7: Main results of the test of leaning forward and backwards.....	100
Figure 11.8: Results of the FFT of the.....	101
Figure 11.9: Results of accelerometers.....	101
Figure 11.10: Tester before strapping the accelerometer and gyroscope	103
Figure 11.11: Results of leaning left and right test.....	104
Figure 11.12: Results of leaning forward and backwards.....	104
Figure 12.1: Sensors used in the instrumented monoski in Padua	105
Figure 12.2: Bike bench with roller shakers and hydraulic actuators.....	106
Figure 12.3: Detail of the articulated parallelogram.....	106
Figure 12.4: Monoski test bench	107
Figure 12.5: MTS Smart Station main interface.....	108
Figure 12.6: Bindings load cells and reference system.....	110

Figure 12.7: View of the potentiometer fixed on the monoski	111
Figure 12.8: Uni-axial piezoelectric accelerometer	112
Figure 12.9: Tri-axial piezoelectric accelerometer	113
Figure 12.10: SoMat Data Logger and its modules	114
Figure 12.11: TCE® (test control environment) main interface.....	115
Figure 12.12: HBM SoMat InField® main interface	115
Figure 12.13: Reference system.....	116
Figure 12.14: Calculation of torque from the forces.....	117
Figure 12.15: Conventions of segments and absolute angles	119
Figure 12.16: Dempster normalized parameters and resulting values for the subject tested	119
Figure 12.17: Description of the skier's posture leaning forward.....	120
Figure 12.18: Angles measured from image analysis and COM of each link calculated.	121
Figure 12.19: Position of hip joint with respect to the reference system	121
Figure 12.20: Description of the skier's posture leaning backwards.....	122
Figure 12.21: Angles measured from image analysis and COM of each link calculated.	123
Figure 12.22: (a) My when leaning forward (b) My when leaning backwards	124
Figure 12.23: (a) X _{COP} when leaning forward (b) X _{COP} when leaning backwards ..	125
Figure 12.24: Posture when leaning right and left.....	126
Figure 12.25: (a) Mx when leaning right (b) Mx when leaning left.....	126
Figure 12.26: (a) Y _{COP} when leaning right (b) Y _{COP} when leaning left.....	127
Figure 12.27: Loads due to dynamic movement of the skier.....	129
Figure 12.28: COP coordinates due to dynamic movement of the skier.....	130
Figure 12.29: Weights and sandbag strapped in the seat.....	132
Figure 12.30: Sinusoidal excitation at 1Hz results, ±30 mm amplitude	133
Figure 12.31: Sinusoidal excitation at 2 Hz results, ±30 mm amplitude.....	133
Figure 12.32: Sinusoidal excitation at 3 Hz results, ±30 mm amplitude.....	134
Figure 12.33: Force and stroke of the cylinder measured by the MTS Station Manager.	135
Figure 12.34: Step excitation of 20 mm amplitude.....	135
Figure 12.35: Step excitation of 40 mm amplitude.....	136
Figure 12.36: Step excitation of 60 mm amplitude.....	136
Figure 12.37: Loads due to compression of the shock absorber.....	137
Figure 12.38: Stroke of the potentiometer due to compression of shock absorber.....	137
Figure 12.39: Foot load cell channels of the test of compression of shock absorber.....	138

Figure 12.40: (a) Position of the joints respect to the reference system.....	139
Figure 12.41: Example of angles in relation to shock absorber length.....	140
Figure 12.42: Angles of arms and shock absorber in function of the stroke.....	140
Figure 12.43: Force-stroke plot of the compression of shock absorber test	141
Figure 12.44: Forces on the arms and shock absorber of the compression of shock absorber test	141
Figure 12.45: Results of the sinusoidal forced vibrations tests	142
Figure 12.46: FRF of the sinusoidal excitation at 1 Hz results, ± 30 mm amplitude	144
Figure 12.47: FRF of the sinusoidal excitation at 2 Hz results, ± 30 mm amplitude	144
Figure 12.48: FRF of the sinusoidal excitation at 3 Hz results, ± 30 mm amplitude	145
Figure 12.49: FRF of the step excitation of 40 mm amplitude	146
Figure 12.50: FRF of the step excitation of 20 mm amplitude	146
Figure 12.51: FRF of the step excitation of 60 mm amplitude	147

1 MONOSKI: MAIN FEATURES

Monoskis, also called sit-skis, consist of a molded seat (1) mounted on a metal frame (2), an adjustable shock absorber (3) as well as a conventional ski binding (4) and a ski (5) as in figure 1.1.

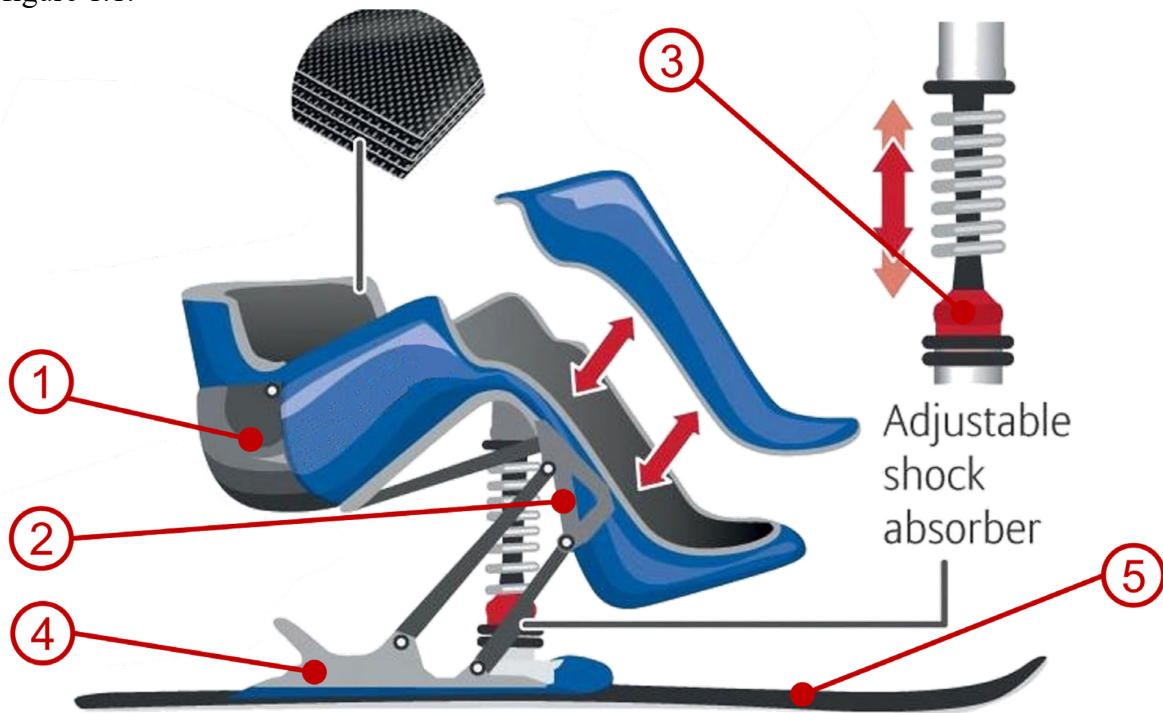


Figure 1.1: Monoski main parts

Change of direction: turns are made by shifting the upper body to the side; special outriggers featured by small skis at the bottom are used to support stabilization and to steer.



Figure 1.2: Change of direction

The molded seat (1) is usually customized to the specific requests in size and inclination of each athlete depending on the disability. It is usually made of carbon fiber, or carbon fiber

and Kevlar, on the external part to reduce the weight and give stiffness to the monoski. In the inner part of the seat, there is a damp-proof foam layer that takes the shape of the skier. The skier inside the seat can protect his legs with a rigid cover or with a soft fabric cover. The skier is strapped in with belts. The main goal of the seat is to rigidly connect the skier with the gear giving to the athlete the right feeling and control.

The frame (2) and the suspension system are usually made of aluminium and steel, and their assembly permits different settings of the monoski. The suspension structure is a complex system of arms and plate supports that carry the skier's weight and interact with the shock absorber (3) transmitting the forces to the ski through the foot (4). In the more developed models, the suspension is a quadrilateral mechanism.

The damper (3) permits different set-up in terms of length, stiffness of spring, speed of dampening and rebound to allow the athlete to find the best set-up related to his/her skiing technique, his/her weight and the slope condition.

The aluminium foot (4) is a piece adopted by all the producers and consists of 2 parts: the base and the handle.

- The base is the part that guarantees the connection to the ski, clamping on the bindings, and it operates as a normal ski boot. It is a standardized part 325 mm long.
- The handle is one of the most stressed parts of the sit-ski because it channels all the loads from the skier into a small cross-section area. This is not a standardized part, and each brand has got its one. The handle usually has on it a numbered scale to help the skier choose his/her skiing position. The seat part can slide on the handle on a guide, and once the position is selected, it gets fixed by one or more bolts, depending on the model of monoski.

The choice of the ski (5) depends on the type of practice, weight, and skiing level of the skier. With uni-ski, total weight is evenly distributed over one single board, so experience has shown that it has to be used a ski with an identical size as the one used by an able-bodied skier of the same weight and ability.

1.1 Survey

The starting point for identifying performance parameters and for new ideas and improvements to a monoski, is the opinion of skiers. The users, thanks to their experience, can give important hints to the design. Through an interview with Lasse Ericsson, coach of the Swedish Para-Alpine Ski Team and a discussion with a professor of Mid Sweden University, Jonas Danvind, a list of the most important quality requirements for sitskis has been prepared (Table 1). Lasse has great experience in Paralympic skiing and worked for many years in this field and with different Teams.

The discussion took place at the Para Winter Camp in Åre Sweden. The event was organized by the Swedish Paralympic Committee on 7-10 April 2022.

Functionality	1. Light
	2. Durable
	3. Stiff
	4. Seat height
	5. Easiness ride on tow lifts
	6. Easiness of taking the chairlift
Safety	7. Impact resistant
	8. Stability skiing
Comfort	9. Comfort in chairlift position
	10. Fits comfortably when skiing
	11. Adjustable seat
	12. Adjustable seat belts
Usability	13. Maintenance
	14. Handling during transport to and from ski resorts
	15. Customization of suspension kinematics
	16. Customization of shock absorber
Pleasure	17. Brand
	18. Style and color
	19. Material (of seat and frame)
	20. Price

Table 1: Quality requirements divided in categories

The four most used monoskis were selected and in a questionnaire a large number of users were asked first to rate the importance of the quality requirements, then to evaluate how much their sitski meets their needs on the characteristics described before.

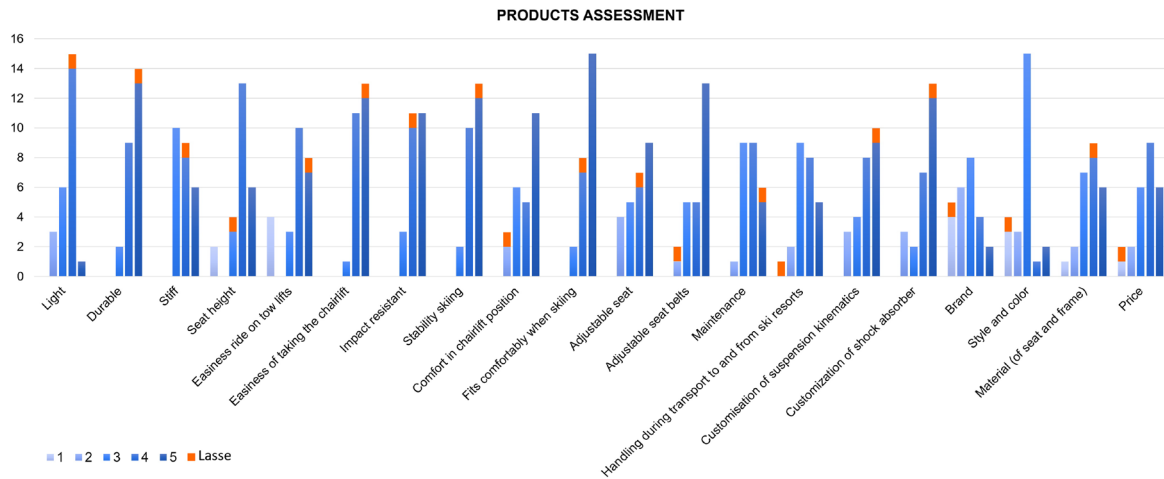


Figure 1.3: In blue the results from online form, in orange the answers of Lasse Ericsson

The open question showed that a requirement is to allow for many adjustments so that changes to the riding position can be performed depending on the different disciplines in alpine racing.

Big adjustments are required on forward/backward position, setting of seat height and of the movement of the frame when compressing the shock absorber; also, the seat height is disability influenced. The adjustments should be simple to understand and straightforward, in particular for the suspension, which seems very tricky and complex to set up. Some skiers also stress the importance of lightness.

The four most used respondents' sitskis were selected and compared on the basis of the scores.

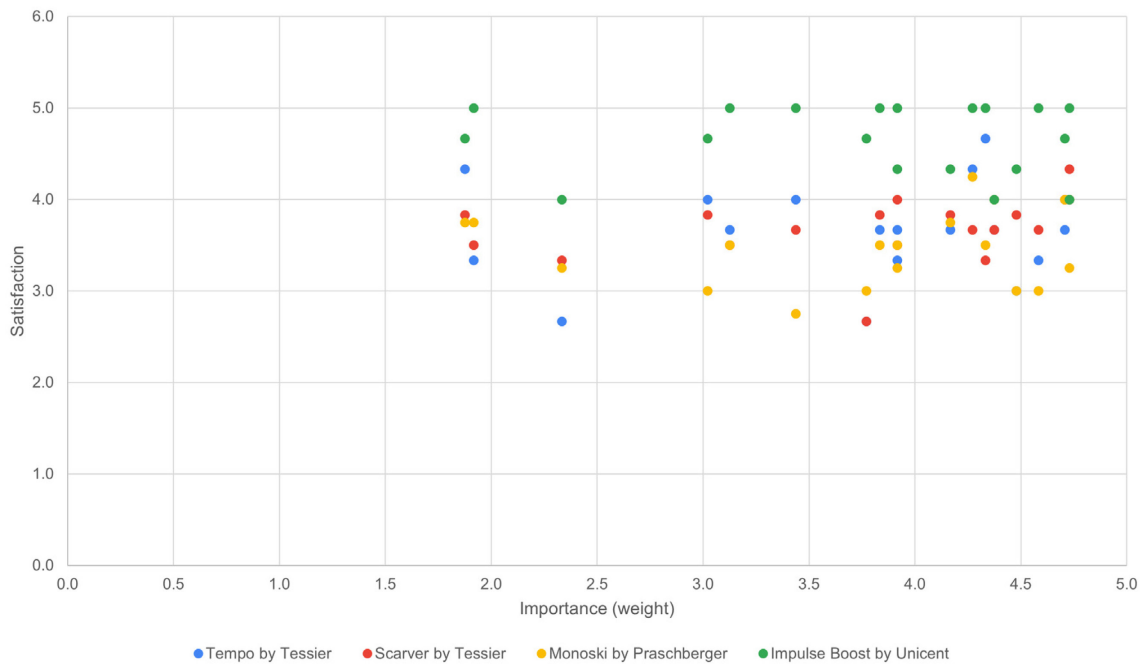


Figure 1.4: Importance – satisfaction results

It must be stressed that the preference of a monoski to another is influenced not only by the type of disability and its severity, but it also depends on the discipline in which one wants to compete.

The most significant limitation of this questionnaire is that respondents should have tried more than one model of monoski in order to make reliable comparisons, which was not always the case.

Tempo’s respondents were few, mostly beginners and, as stressed by Lasse, this rig is not suitable for high level competitions.

Scarver has lower ratings than the others, despite being the most used in competitions and by experienced skiers. This can be explained because the requirements of more experienced skiers are higher than the beginner’s, and are more specific and extreme.

Impulse Boost seems overall to satisfy their skiers as pointed out in the graph.

The questionnaire doesn’t consider the services and support of the different companies because of the variety of origin of respondents but it can be an important factor.

1.2 Interesting features

Some models on the market have interesting and innovative characteristics such as:

- Reticular frame structure as in DynAccess Hydra and Tensor to reduce the weight of the system while maintaining its stiffness. In these models the frame is designed in a Topology Study by knowing the loads at the connections with seat, wishbone arms, and the best stiffness to weight ratio as goal.

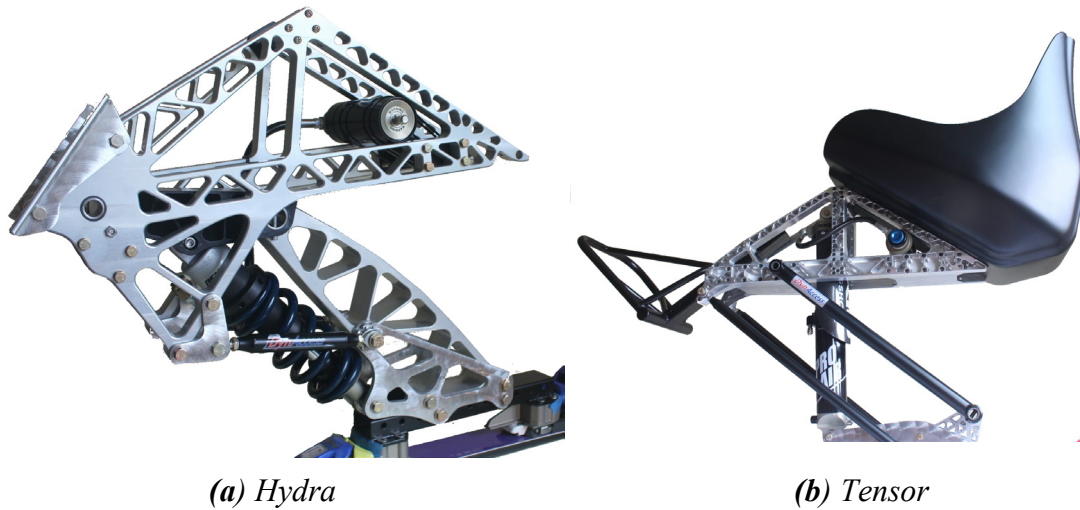


Figure 1.5: DynAccess monoskis

- Lever arm for the shock absorber to reduce its length and, as a consequence, its weight. It is a solution inspired by the Linkage driven single pivot rear suspension of mountain bikes. The gain is the use of smaller shocks absorber, as in the prototype Aggressor by Ableway AB [1].

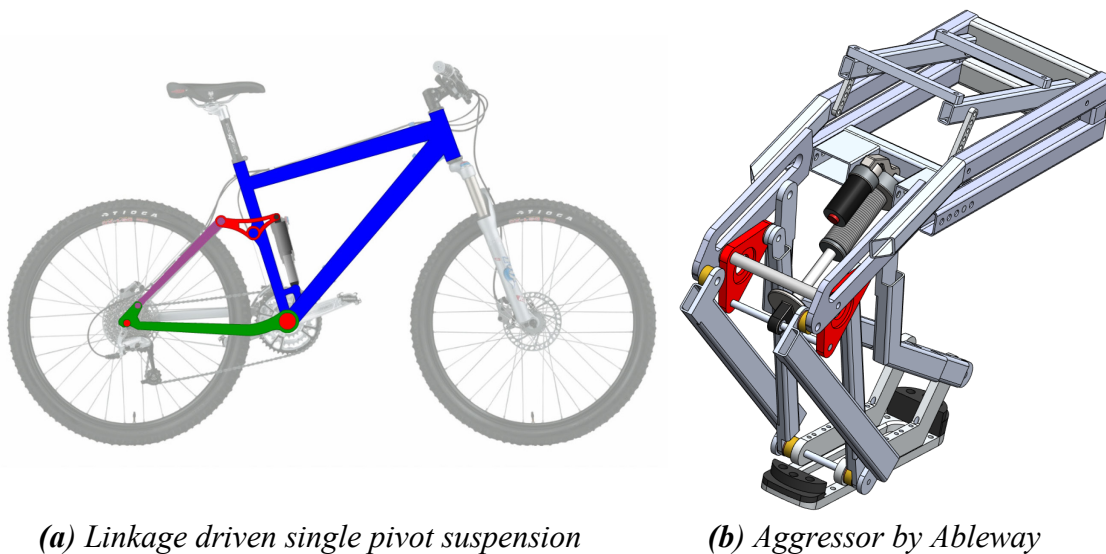


Figure 1.6: Is highlighted in red the triangular arm of the suspension

2 MONOSKI PROJECT

The project started from the foundations previously laid down by Davide Piccinin [2], Matteo Ferrari [3] and Dario Vanzetto [4] in their thesis called respectively “*Kinematic and kinetic analysis of a Paralympic skier during slalom - 2016*”, “*Design and validation of a dynamometric load cell for the measurement of loads acting on a Paralympic monoski – 2016*” and “*Acquisition and analysis of kinematic and kinetic data on a top Paralympic skier during giant slalom – 2017*”.

Ferrari developed and created the load cell (called Dynafoot) during his thesis work; Piccinin conducted validation tests comparing it with the force plates (called Dynaplate) created by Paride Gardin [5] during his thesis “*Analisi del comportamento strutturale del Sistema complesso sci-attacco scarpone – 2007*”. Vanzetto successfully tested the force plates with a Paralympic athlete with interesting findings from which an article was later published [6].

2.1 Matteo Ferrari

Ferrari in his thesis work designed the Dynafoot: a dynamometric multicomponent load cell with the aim of measuring external forces and moments produced by a Paralympic monoski during a downhill run.

The aluminium foot structure is the part of Scarver by Tessier that was chosen to be transformed into a dynamometric load cell by integrating it into the monoski without changing its geometry. Using the same geometry of the foot, four holes were created, two in the left side and two in the right side. In this way, it was possible to create four vertical channels and two lateral channels, using strain gauges system. The dimension of the holes is chosen to produce high local stress to have a good sensitivity of the cell, and not to exceed the yield stress of the material.

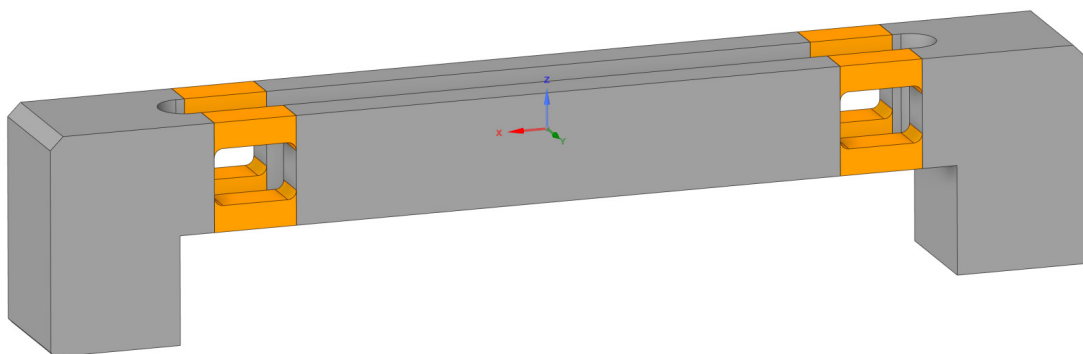


Figure 2.1: Dynafoot

Unfortunately the finite elements simulations were performed on only half the structure without considering that the pitch moment is antisymmetric.

In any case, the tests carried out show that the load cell with this geometry has good sensitivity.

Has been performed the calibration and was derived the calibration matrix with the same procedure used at chapter 5.6.

The load cell has been tested during the winter 2016 in Folgaria. For the data acquisition was chosen a light and portable system: BTS pocket. Of the four runs performed only two had reliable results.

To better understand the intensity of the forces acting on the ski the forces are normalized to the Total Weight of the skier + Scarver + clothes + devices: $TW = 885 \text{ N}$.

It can be appreciated that the mechanical behaviour of dynamometric load cell gave a good signal as regards to vertical force, roll and pitch. Regarding lateral signal intensity, it is much lower than vertical load due to the lower sensibility than the other channels and because during downhill runs the lateral loads are low.



Figure 2.2: Result of Ferrari’s test

2.2 Davide Piccinin

The work conducted by Davide Piccinin started with the validation of Dynaplate (Fig. 2.3) to use it as an instrumentation to analyse different skiing techniques. He organized two tests on the slopes to compare athletes with different skills (amateur and professional) and to compare different dynamometric systems (Dynaplate and Dynafoot).

The monoski used by the athletes was the Scarver by Tessier.

The first series of tests took place during the ISEA WinterCamp 2016, held in San Martino di Castrozza, Italy, from February 28th 2016, to March 4th 2016.

In two days of testing, Andrea Stella, an amateur Paralympic skier, performed 6 runs, the day. Later Alessandro Varotto, a professional Paralympic monoskier, in a similar modality, performed 5 runs.

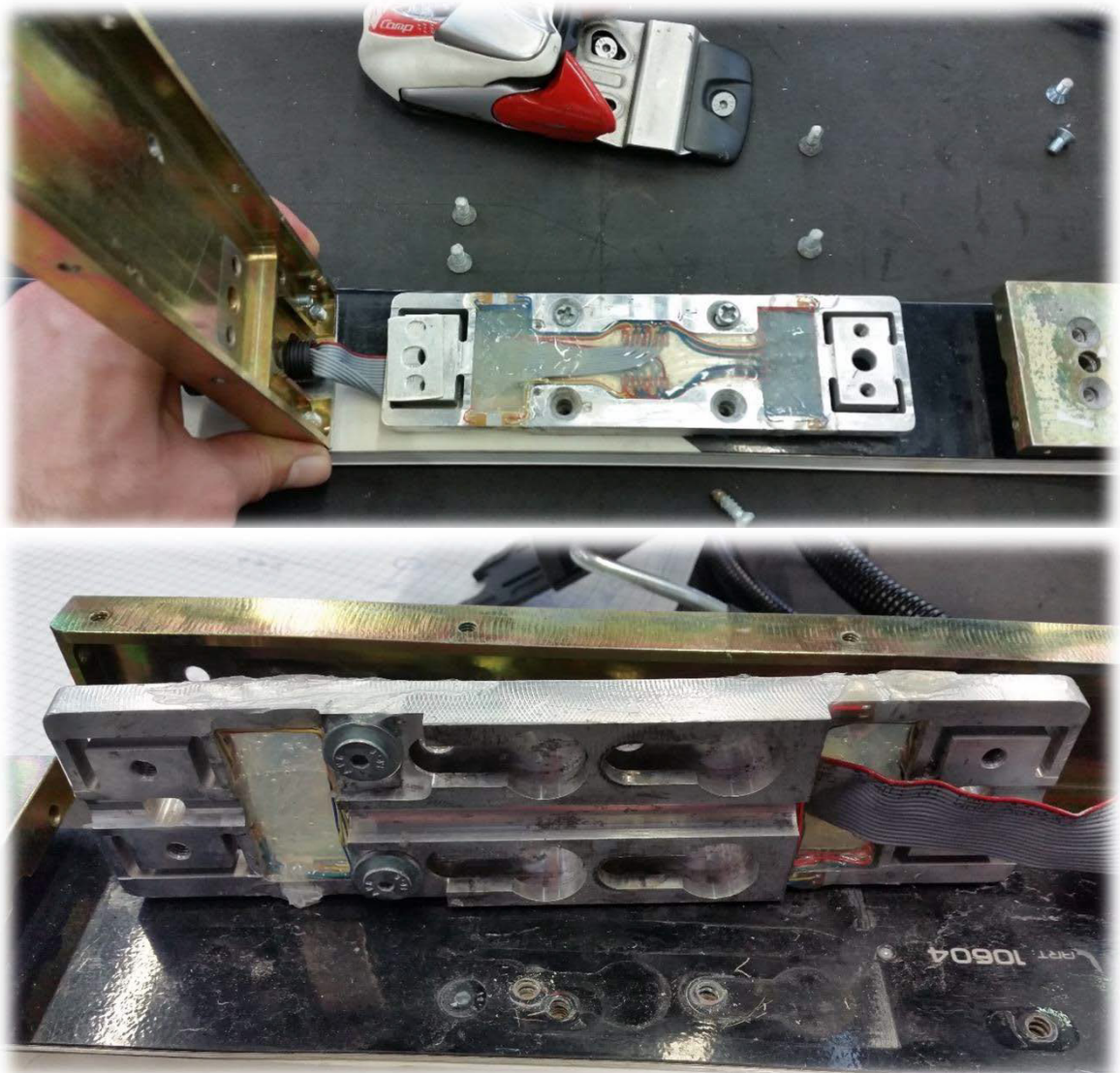


Figure 2.3: Dynaplate

The devices used were:

- Xsens suit: MVN motion capturing system (brought by Aalborg University)
- Leica GNSS: high precision Global Navigation Satellite System (brought by Ljubljana University)
- Dynamometric Force Plates: load cell measuring F_z , M_x , M_y (brought by Padova University)

The results are again normalized on the Total Weight of the skier + equipment. Stella and Varotto's weights were respectively 65 kg and 77 kg, the monoski was 17.09 kg.

Piccinin started comparing the parameters with the variables: 2 skiers performing some runs with 2 different styles so a within-within 2x2 study chart could be created. He focused on these key parameters: Z-axis peak force, maximum ΔX of COP, mean value of COP and time.

The forces applied to the ski raised switching from a wide slalom to a narrow slalom for both athletes, but if for Stella, the increase was quite significant +13.11%, for Varotto the increase was almost negligible +0.42%. Comparing the two measures, it is possible to point out that

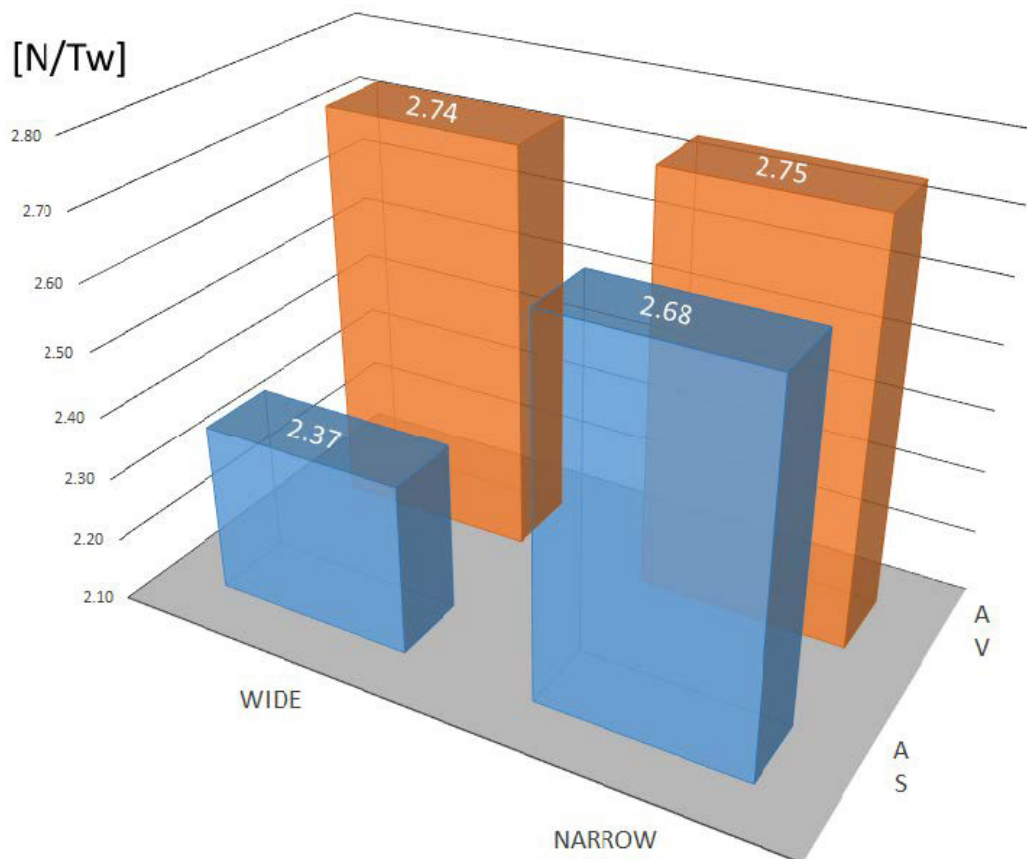


Figure 2.4: Mean values of force peaks

Varotto, who is a professional skier, applied 15.55% more force than Stella on the wide slalom, and 2.58% on the narrow.

Comparing the techniques, just by looking at the forces, it is clear that Varotto had more control over the Scarver, constantly producing more force and keeping it more uniform than Stella.

Looking at the runs performed by Stella and those performed by Varotto, both athletes on the 4th and 7th curve push more on the ski, and less on the 5th and 6th. This might be due to the slope shape and snow condition but, while Stella seems to struggle to keep a uniform skiing from most of the time passing from 4th to 5th pole, Varotto kept it more stable, sometimes also not even showing any difference. In Figure 2.5 and Figure 2.6 are reported

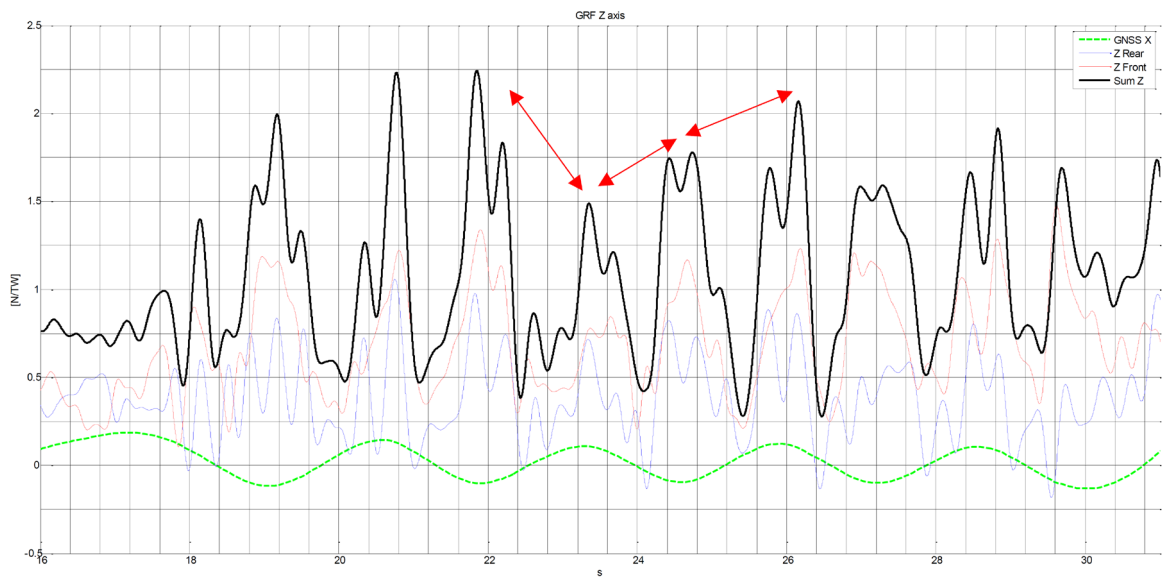


Figure 2.5: Stella's 3rd wide run

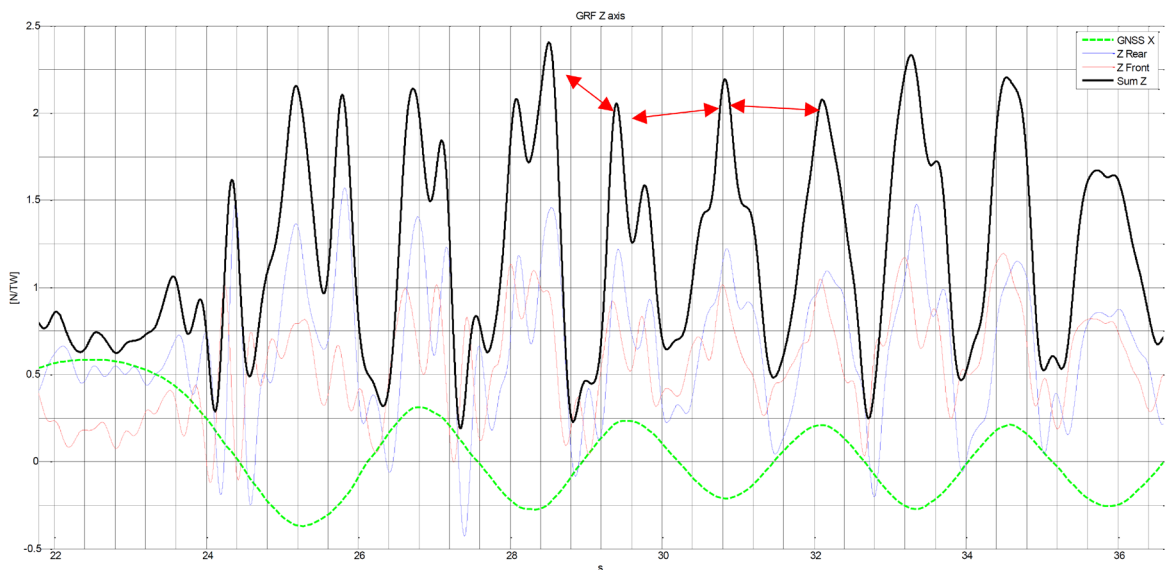


Figure 2.6: Varotto's 2nd wide run

the differences between wide run 3 from Stella's test and wide run 2 from Varotto's since they have the same course time.

The pattern of the skiing, though, seems pretty much the same for both the skiers: the maximum force is reached at the turn climax with a 2 peak-shaped trend, while the minimum value of force appears on the straight part between two curves and, most likely, identify the moment when the skier changes the edge "jumping" or unloading a little bit due to the rebound force from the damper.

Another difference between the two skiers is the distribution of the forces. Until now the focus was on the total force on the Z-axis but, as it can be clearly seen in Figure 2.5 and Figure 2.6, Stella pushes more on the front, while Varotto pushes more on the rear.

The tendency that's possible to observe, dealing with COP data, is an increase of ΔX passing from wide to narrow slalom. Also, the mean value of the COP increases, which means that the skier tends to be more leaned forward. In fact, switching from wide to narrow slalom, the mean COP position along the X-axis increases from 35.28 mm to 49.6 mm (+40.59%) for Stella and from -1.63 mm to 14.70 mm (+1000.86%) for Varotto.

Between Andrea Stella (AS) and Alessandro Varotto (AV) there's a clear difference of balance. Stella is more on the front in either case in respect of Varotto: on the wide

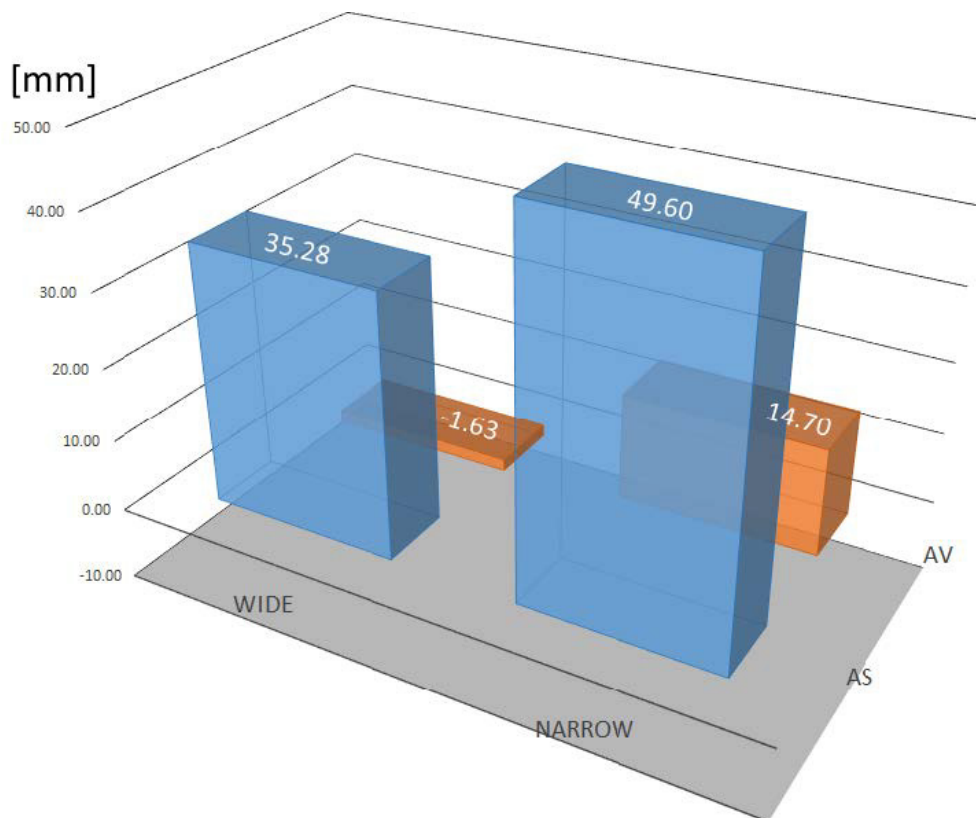


Figure 2.7: Mean values of X_{COP}

respectively they had a mean X_{COP} position of 35.28 mm and -1.63 mm, while on the narrow 49.60 mm and 14.70 mm. This is still compatible with what just said about the forces.

Technique differences are clear in this case. As written above, shifting from wide to narrow means moving the COP slightly on the front, and it is confirmed looking at the whole chart. The reason why the average value of COP moves forward is because there are higher peaks while the valleys stay almost the same. Stella passes from a range of, roughly, 20:100 mm of movement to a 20:130 mm; Varotto from -40:90 mm to -40:140 mm.

Varotto's technique of skiing, also, followed the same pattern as the COP. Moving his body on the front before entering the curve, keeping it mostly steady at the climax of the curve and moving on the rear during the straight phase.

Stella's technique, on the other hand, didn't have a recognizable pattern between the different runs: that's probably the basic difference between a PRO athlete, Varotto, and an amateur, Stella.

In the same season, it was possible to perform another test on March 24th in Folgaria, Italy, to compare two dynamometric systems: Dynaplate, by Paride Gardin, and Dynafoot, by Matteo Ferrari.

Initially, the purpose was to compare the data gathered from these two systems by connecting them both to the same BTS pocket; this would have given two points of view of the same identical run, one from the Dynafoot and the other from the Dynaplate, avoiding repetitiveness problems and technical variations within different runs. This, though, wasn't possible because of the not uniform current supplied to the bridges when too many channels were connected to the DAQ. For this reason, were performed tests with first the Dynaplate and then with Dynafoot connected one at a time to the BTS pocket; but this would have meant neglecting the differences between the runs on the technical level, concentrating just on a quantity level.

The two load cell systems show consistent results even though a direct comparison is not possible.

Unfortunately, the Dynaplate had some issues during the tests, spoiling almost every data collected. Some water filtered through the silicon that covers the plate altering the signal from the strain gauges. So, it was possible to save just one run out of three.

2.3 Dario Vanzetto

Vanzetto for his thesis work made few tests with the alpine skier and World and Olympic champion Christoph Kunz. The test took place in Adelboden, Switzerland in March 2017.

The monoski used by the athlete was this time Impulse Boost by Unicent GmbH.

Vanzetto took up the Dynaplate system, designed and realized by Paride Gardin in 2006 to measure the Ground Reaction Forces. To measure the damper stroke and speed used a magnetostrictive potentiometer produced by Athena.

Unfortunately, connecting all 10 channels resulted in a decrease in the voltage supplied by the amplifiers. As a result, only three channels had to be used and were measured only Vertical forces, Pitch and Roll moments.

The weakness of this load acquisition system was the instability of the amplifier used to connect the load cells to the data logger. This brings issues in terms of reliability of the signal since the variation of temperature causes the drift of the signal acquired during the run. This trouble was solved by implementing a test protocol: to obtain a perfect “zero” the athlete was lifted from the ground for 10 seconds in order to identify the “unload” situation both before and after each run.

Were recorded 6 runs during which the setup of the monoski (in terms of variations of COP position) was changed every two runs. Unfortunately, during the 7 th run, some cables of the Dynaplate were punched by the suspension mechanism of the monoski.

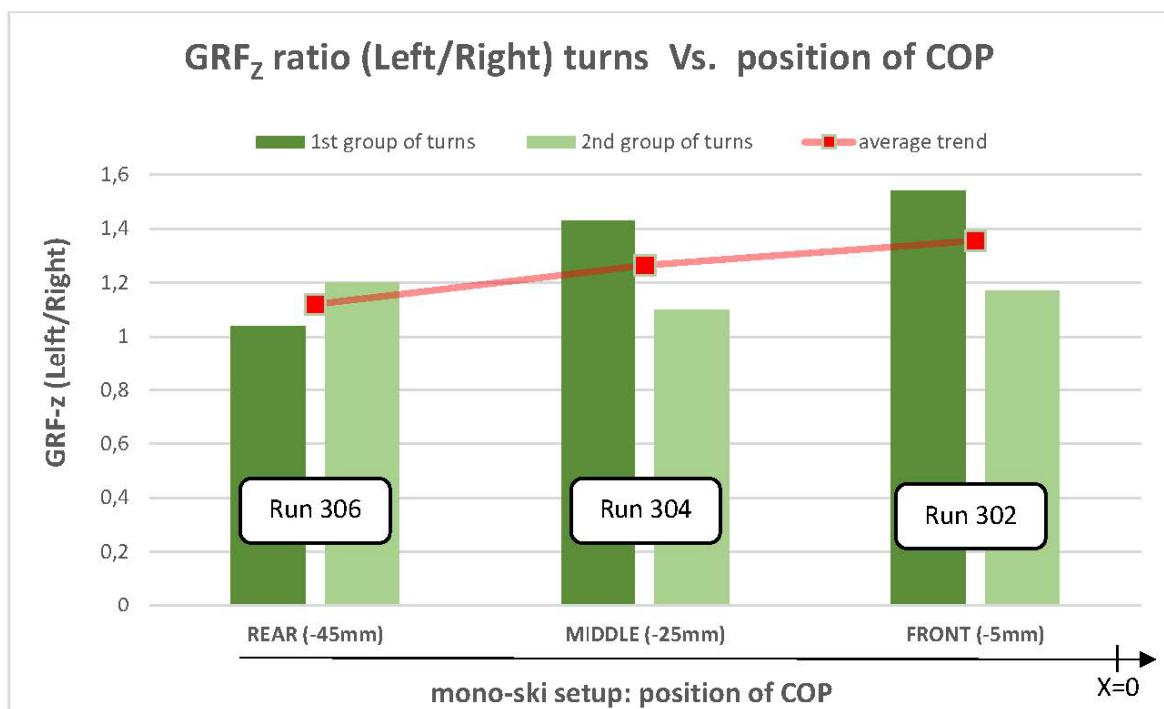


Figure 2.8: GRF (left/right) – position of COP

Few considerations were made, in particular, the following were chosen as key parameters: Z-axis peak force, variation of X_{COP} , mean value of COP and damper stroke and speed peaks and the purpose is to study them in relation to the different phases of the turn.

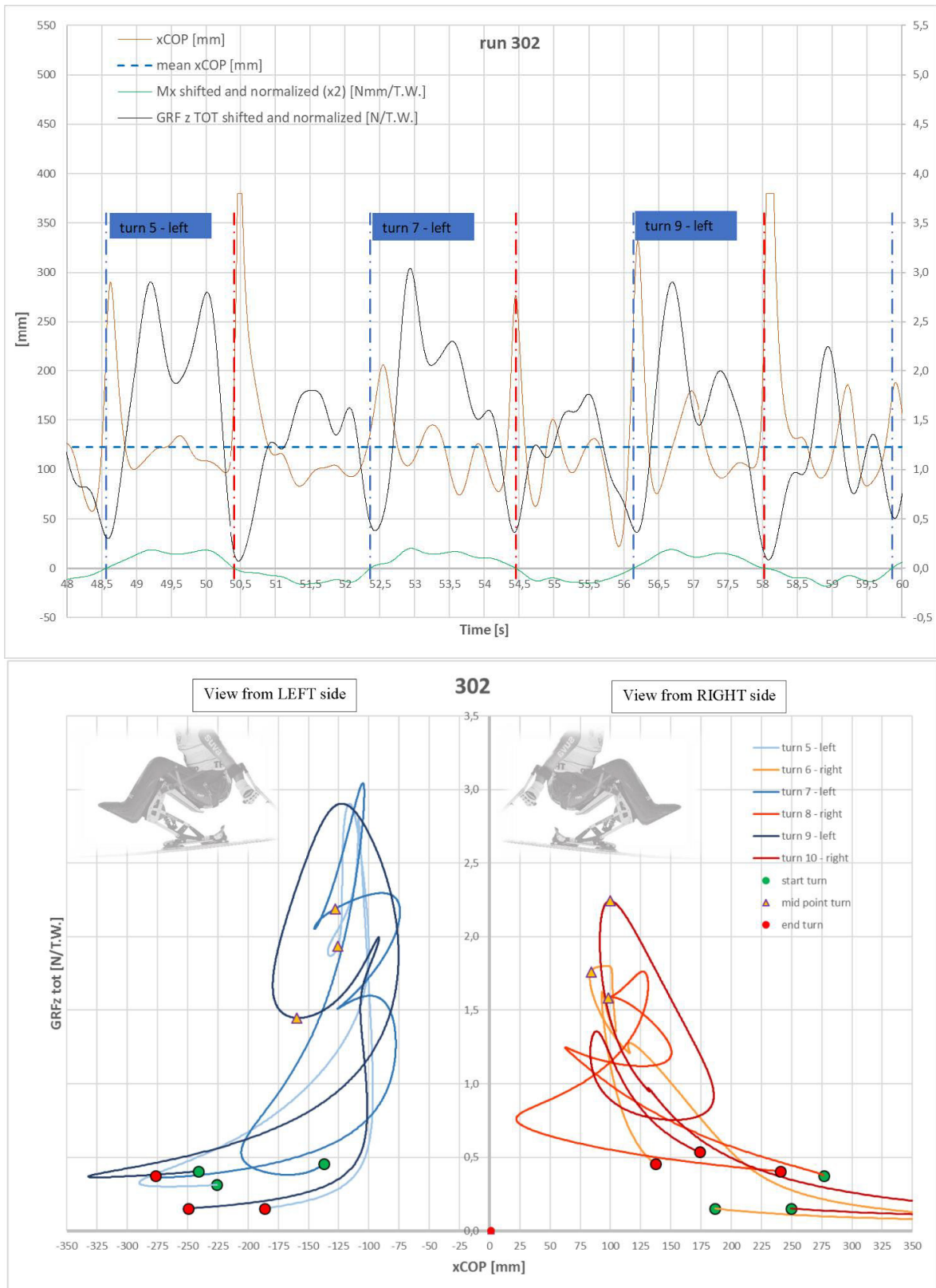


Figure 2.9: Results from run 302

The pattern shows that moving backwards the position of the COP, the peaks of GRF-z total decrease. It means that the more the COP of the monoski is set backwards, the less the athlete is able to push on the ski. This preliminary remark is consistent with Kunz's subjective ratings and with the lap time analysis, since run 302 is the fastest one, and it has the highest rating.

The athlete's skiing technique is not symmetric: from data analysis it is possible to see that GRF-z peaks are higher during left turns than right ones. This phenomenon does not seem related to a possible lateral steepness of the slope because it is clear quite at each point of the track, from start to finish, and the ratio (Left/Right) changes with different average speeds. It is likely that Kunz is more confident to turn on the left. This could be an interesting hint for the athlete and his trainers to improve his skiing technique on the right turns.

It is possible to observe that, looking at the right side of these graphs, for the right turns the peak of GRF-z is always reached at the mid-point of the curve (yellow triangle). For the left turns, on the other side, the peak of vertical force is often reached before the mid-point of the curve.

The phenomena just pointed out is more evident when the loads (GRF-z total) are high, as for the group of turns in Figure 2.9. This means that the athlete was able to take in advance the left turns.

The influence of the position of the Center Of Pressure (COP) along the longitudinal X axis is very important: the more the COP is set forward, the higher are the vertical forces reached. It is clear, from lap time analysis and from athlete's subjective ratings, that the best performances are reached when the base of the monoski is set in the most anterior position with respect to the foot (boot of the monoski).

3 INSTRUMENTATION

The following chapters present the materials and methods used in the construction of an Instrumented Monoski for kinematic and kinetic data collection.

Instruments were chosen from a sensor fusion perspective, to describe the complex monoski system combining multiple complementary data sources.

A solution was searched to achieve the ambitious goal of describing the system in both slow and fast dynamics.

4 SCARVER BY TESSIER

For this Thesis work the monoski Scarver by Tessier © [7] was chosen as the platform for the measurements given its success in competitions. It can be considered the benchmark product for the monoski since it is the model most paralympic winners use. At the Paralympic Games of Beijing 2022 it scored 19 medals, including 5 Gold.

The decision to use this model was also dictated by the will to use a particular load cell designed by Matteo Ferrari in 2015 (Cap. 5). The sensor in, fact, is designed to be integrated into the monoski instead of the original foot without altering the geometry of the system. Since the sensor is designed to be part of this particular model, it is not possible without changes in the dimensions of the system, to use this particular load cell in a different model other than the Scarver. This represented the main issue in the first part of my work since this specific model was not available.

4.1 Components and main features



Figure 4.1: Monoski Scarver

<i>ITEM NO.</i>	<i>DESCRIPTION</i>
1	Seat
2	Aluminium frame with Plastic cover for the contact with the chairlift
3	Higher suspension arm
4	Straight lower suspension arm
5	Aluminium base
6	Damper
7	Leg protection in composite material
8	Low part (aluminium boot with graduated rail)
9	Anti-sliding ear
10	Foot aluminium structure

Table 3: Components of the Scarver

The Table 3 describes the components from which the Scarver is made:

- Weight: thanks to its design in high-strength aluminium and steel Scarver frame offers a good stiffness-to-weight ratio (frame + Öhlins shock absorber: 9,9 kg).
- Chairlift use: the unlocking button is very easily accessible and its handling is done without any effort. When the frame is unlocked it is possible to rise up just pushing on outriggers. The slab of polyethylene in contact with the seat gives stability to the athlete and makes easier the chairlift's off-loading.
- Customizable: Three possible suspension kinematics: the aluminium frame has three different settings depending on the style and discipline.
 - Position 1: when the damper compresses, the suspension movement is almost vertical, which is ideal for slalom, freeride and Dual-ski use.
 - Position 2: is an intermediate, versatile position that will suit most of the skiers.
 - Position 3: the centre of gravity of the frame moves forward when the shock absorber compresses. This compensates the rear imbalance produced by skiing in a “carving” style and recharges the tip of the ski to improve the grip all along the ski.

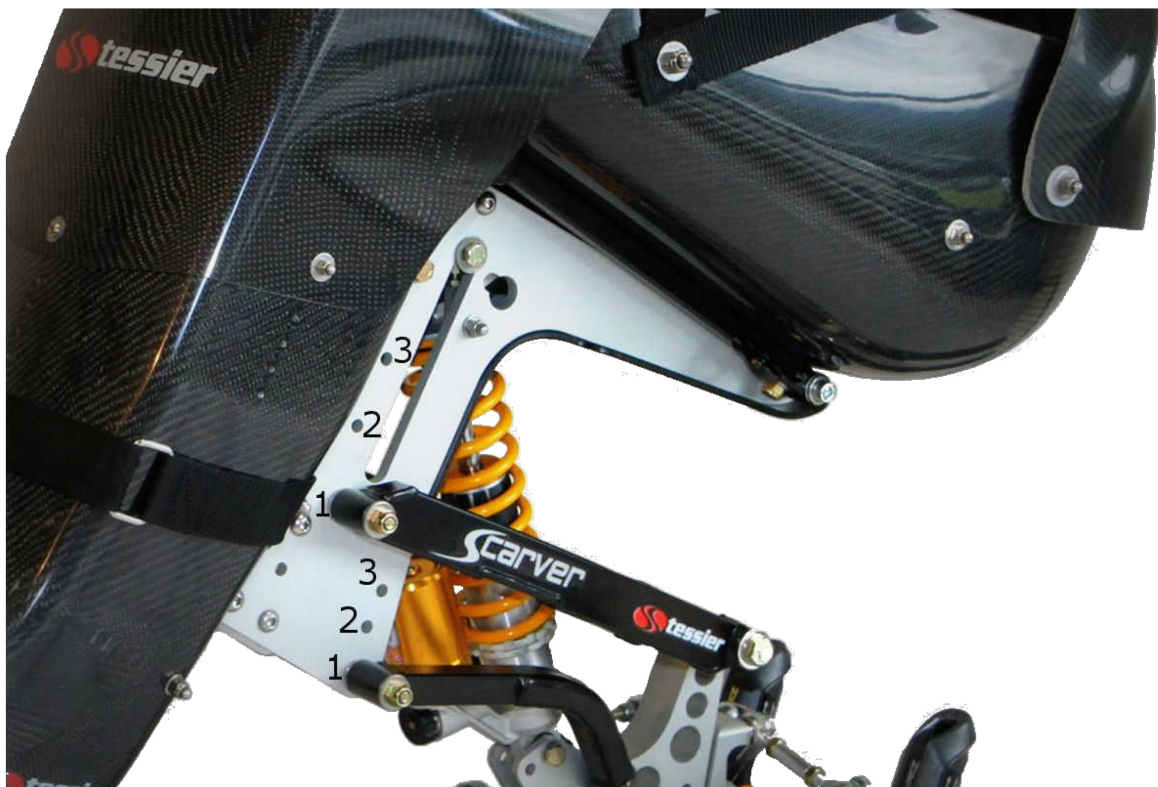


Figure 4.2: Suspension kinematics settings

- Customization: in addition to the suspension kinematics, other parameters can be adjusted.
 - o The seating angle can be set from 30° to 40° and from 15° to 20°, every 2°, to provide the best position to the athlete.
 - o The center of pressure (COP) can be adjusted moving the foot aluminium structure (part 10) of ± 35 millimetres forward or backward to get the best skiing comfort.

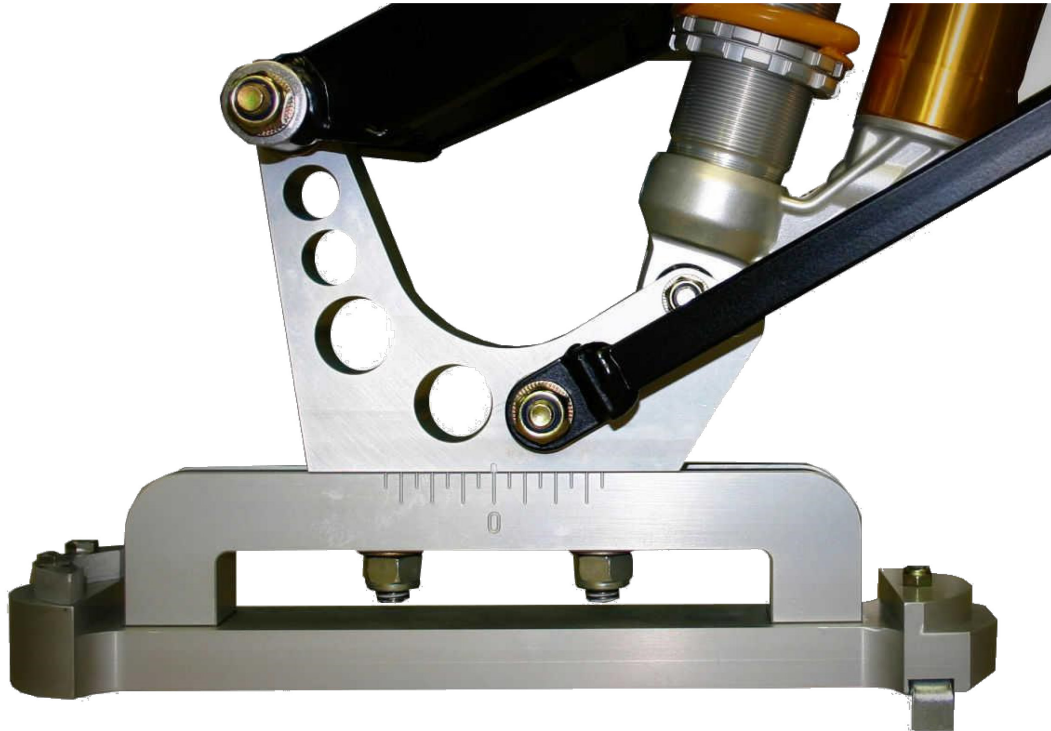


Figure 4.3: COP setting

- Versatility: the Scarver can switch from Mono-ski to Dual-ski in few minutes just changing the foot aluminium structure (part 10 Figure 4.1)

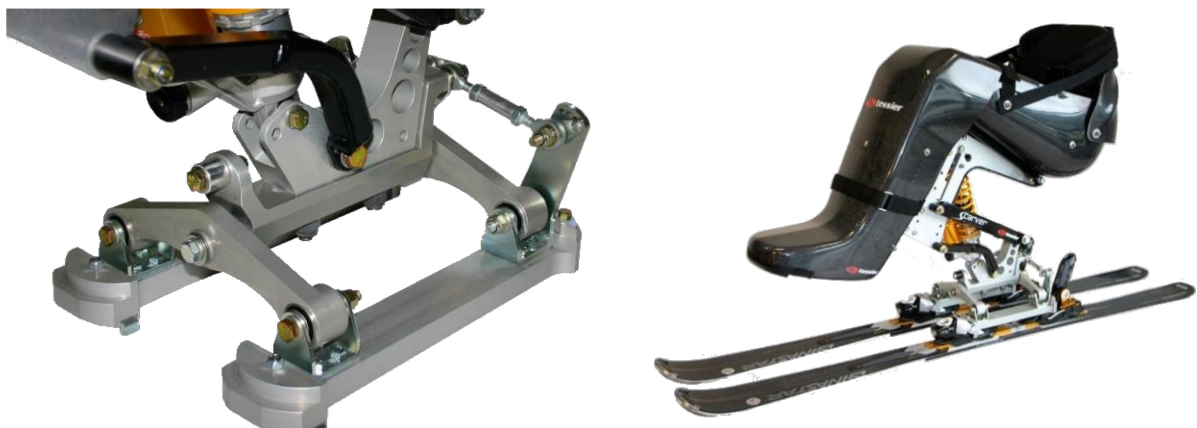


Figure 4.4: Aluminium foot for Dual-ski

5 DYNAMOMETRIC LOAD CELL

To collect kinetic data are measured the Ground Reaction Forces (GRF) using a load cell. The contribution of the outriggers is neglected as the main role of outriggers is not to transfer force between the snow surface and the body, but rather to maintain balance [8].

The dynamometric load cell system called Dynafoot was designed and realized by Matteo Ferrari in 2016 during his Master thesis [3].

Since the aluminium foot receives all the forces and moments from the ski has been decided to use this part as a load cell.



Figure 5.1: Dynafoot by Matteo Ferrari

5.1 Strain gauges

There are several methods used for measuring strain. The most common is the use of strain gauges. It consists of a grid of conductive material on a polymeric carrier that, once glued to the surface of the material, varies its electrical resistance in proportion to the amount of local deformation derived from the strain. It is possible then to determine the relationship between

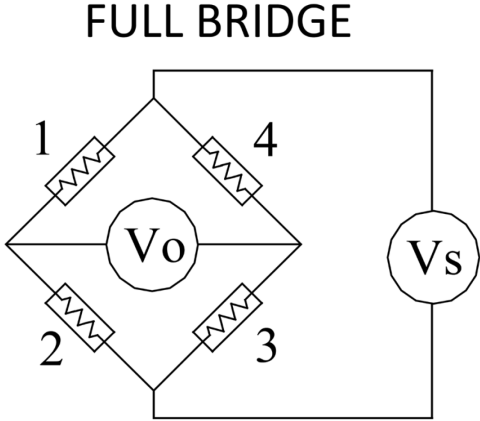


Figure 5.2: Wheatstone full bridge

the variation of resistance and the deformation. It is a linear and reversible relation that, after some calibrations, permits to transform variations of resistance into variations of force.

The variation of resistance is very small so is used a special circuit to measure it: the Wheatstone Bridge (Figure 5.2).

The strain gauges are almost always used in a bridge configuration with four resistive arms and an excitation voltage V_s applied across the bridge.

The disposition of the strain gauges chosen is the full bridge because it gives the maximum sensitivity (output signal 4 times bigger than the single bridge) and compensates the temperature sensitivity due to the thermal expansion.

It is known from the literature that for a full-bridge system, it is possible to express the output signal as

$$V_o \approx V_s \frac{K}{4} (\varepsilon_1 - \varepsilon_2 + \varepsilon_3 - \varepsilon_4)$$

where V_o is the output voltage of the bridge, V_s is the excitation voltage given by the instrumentation used for acquisition, K is the gauge factor (for metallic strain gauges it's typically around 2) and ε_i identifies the strain the on the strain gauges. Furthermore, remembering that Young Modulus E that for Ergal Alloy T6 temper 7075 is equal to $70000 \div 72000 \text{ MPa}$ and Hooke Law $\sigma_i = \varepsilon_i E$, it's possible to explain last equation as

$$V_o \approx V_s \frac{K}{4 E} (\sigma_1 - \sigma_2 + \sigma_3 - \sigma_4)$$

In the specific case, the strain gauges applied on the aluminium plate are HBM 1-LY43-3/350 and for the channels measuring the lateral force HBM 1-LY43-3/120.

The measurements with strain gauges is, in theory, very accurate, but there are few important sources of error that must be considered.

One of the most important sources of error is the positioning of the strain gauges: they must be perfectly bonded in order to deform like the supporting material. Furthermore, the centring of the strain gauges in the place where they are to be glued and their angle greatly influence the measurements.

Must be considered also the influence of the connecting cables with their different resistance due to the bending and coiling, temperature gradience, attenuation of measurement signal and many other parameters.

5.2 Design of the load cell

The sensor has been designed so that it can be integrated into the monoski without changing its geometry in particular the height of the seat. For this reason, has been chosen to reproduce the foot of the Scarver monoski with four windows on the sides in order to create a stress concentration zone. This is necessary to produce a part of the system sensible to the loads: on the thin beams that are thus created there is a local deformation produced by the external forces or moments that is big enough to be measured.

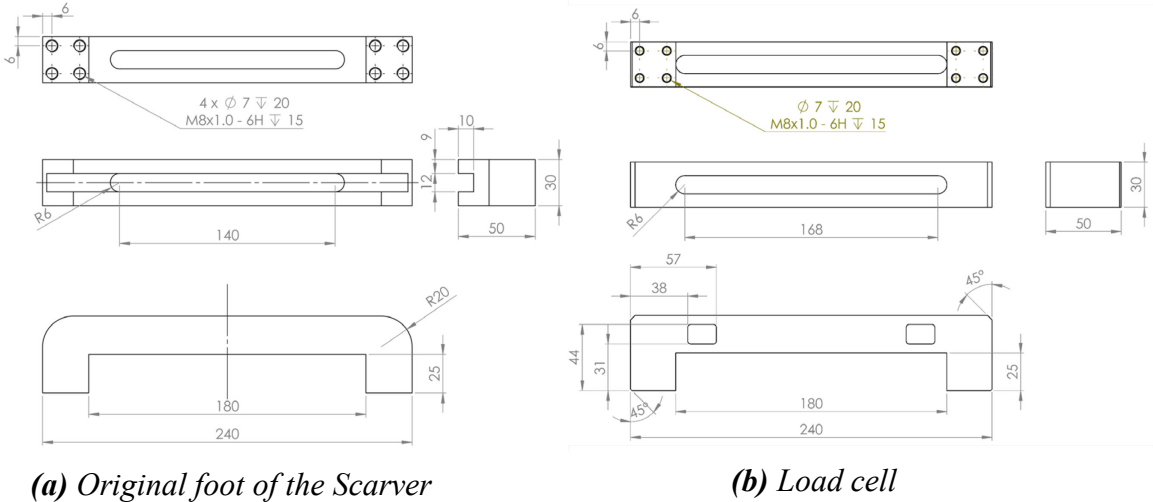


Figure 5.3: Comparison between foot and load cell

The load cell has been designed to measure the main GRF acting on the monoski: thanks to a specific placement and connection of the strain gauges on the beams is possible to measure the loads. More specifically full bridge strain gauges were glued onto the beams as in Figure 5.4. A full bridge makes a Channel so and output. A limit of this design is that the skier normally sets the aluminium base (part 5 Figure 4.1) in their comfortable position. The presence of the strain gauges limits the position of the base on the zero position only.

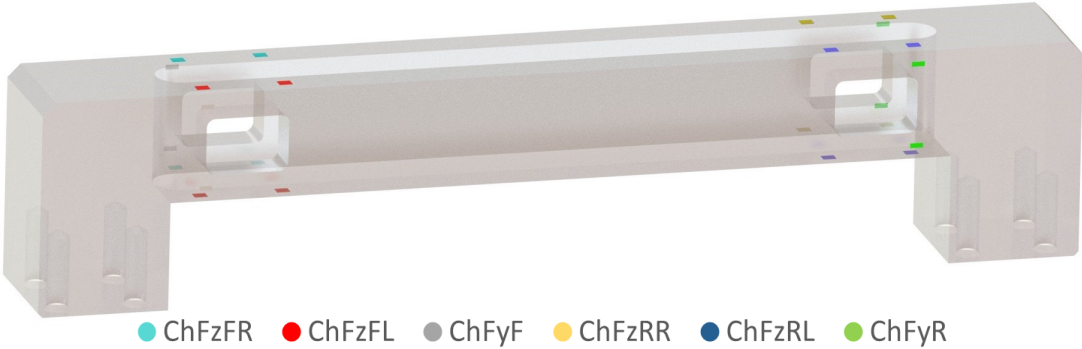


Figure 5.4: Placement of the strain gauges

The reference system is located at the center of the cell; the loads that can be measured are shown in figure.

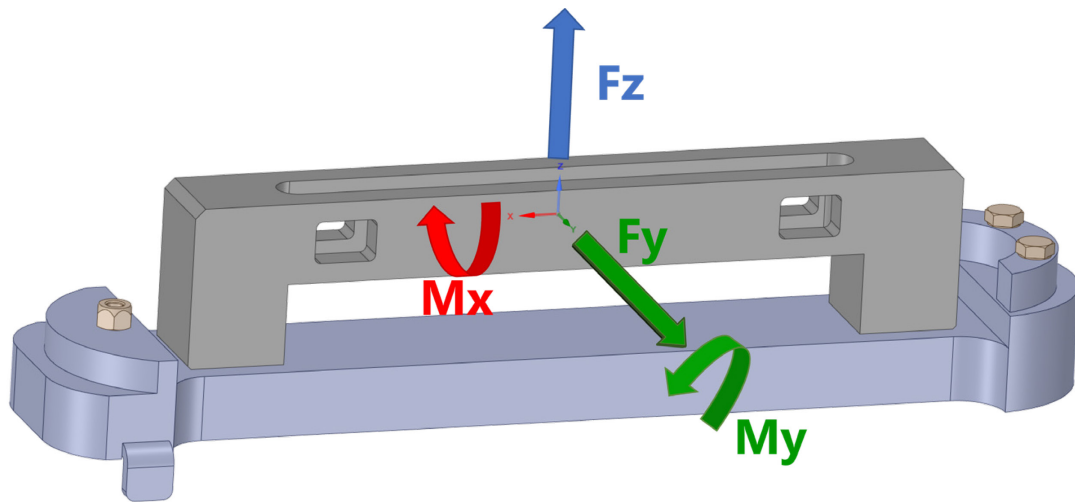


Figure 5.5: Multicomponent indirect load cell

Reference system and positive direction of loads

5.3 Amplifiers

As stated in the previous paragraphs the connecting cables influence the measure especially if, as it was in the original load cell, the cables of the legs of the bridge circuit were a pair of meters long and exposed to a harsh environment like the foot of a monoski skiing down a slope. The connecting cables can have different electrical resistance due to the bending and coiling, temperature gradient, mechanical effects, attenuation of measurement signal and many other parameters. The effect is to decrease the signal-to-noise ratio and increase the drift and uncertainty in general. This becomes an issue when the signal is amplified because if the input is already affected by the noise, is difficult to extract the input from the signal. Therefore it is necessary to have the amplification stage closer to the signal source, before it is affected by noise.

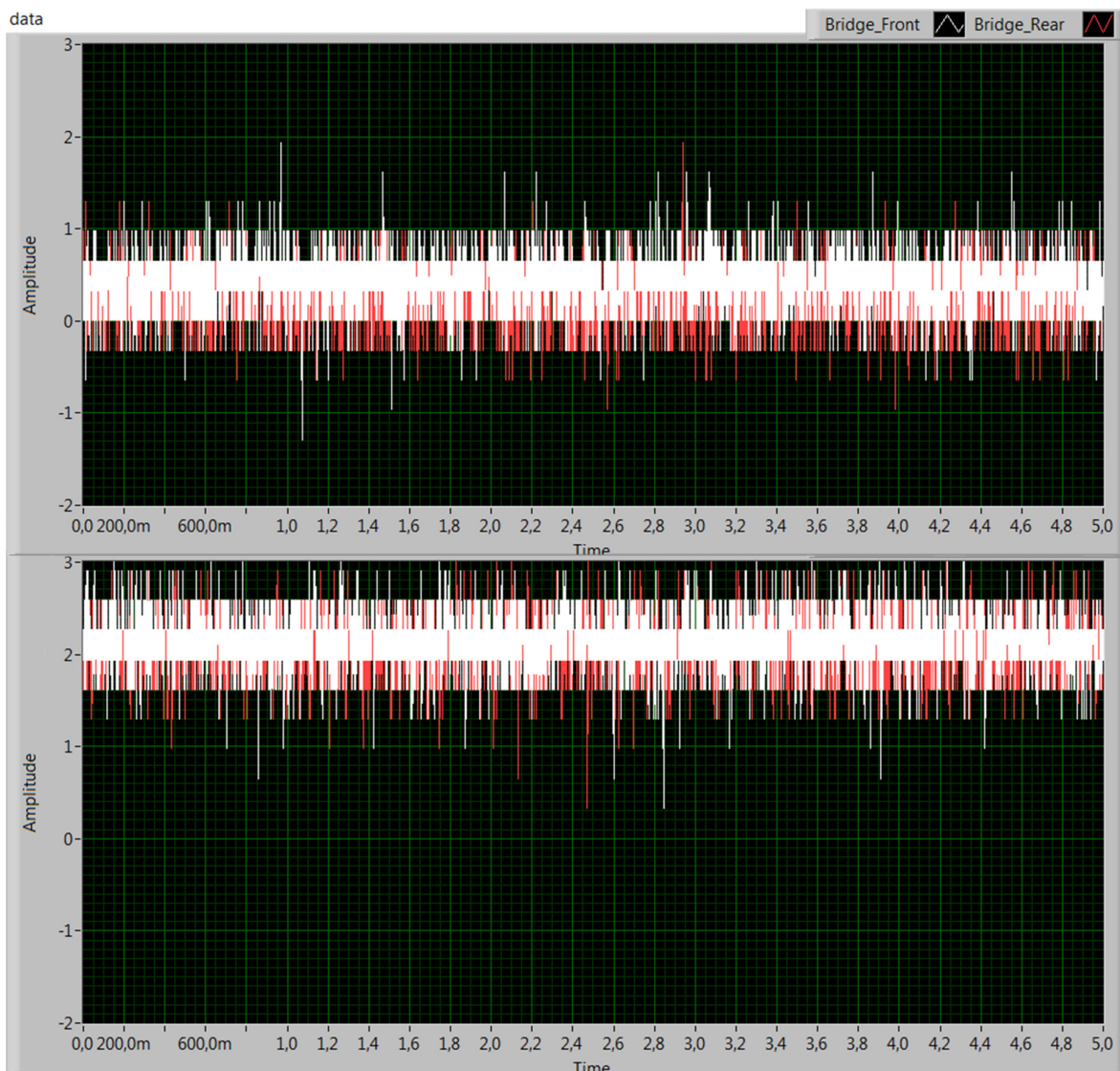


Figure 5.6: Example of signal from not amplified vertical channels first when load cell unloaded, second when a vertical load of 65 kg is applied. Amplitude is in mV.

In order to increase the reliability and to decrease the noise it has been decided to move closer to the origin of the signal, the strain gauges, the amplification stage. Thanks to the opportunity to build compact amplifiers it has been decided to fit them directly on the foot of the sitski.

It has been decided to use for each channel an amplifier with a fixed gain of 160 that is thought to be enough magnification for the signal. As can be seen in Figure 5.6, applying 65kg of vertical load on the load cell produces an increase of the output voltage approximately of 1 mV. This explains why has been chosen to use an amplification of 160. It's also possible to appreciate the noise of the signal.

There is also a second stage amplifier per channel set with a gain around 1. This stage has the function of allowing it to be modified to change the gain (more or less than 1 by changing one resistance on the circuit) in case it is needed and to filter out signal noise.

To reduce the noise has been used an RC circuit as an active low pass filter, passing low frequency signals while attenuating the high frequencies.

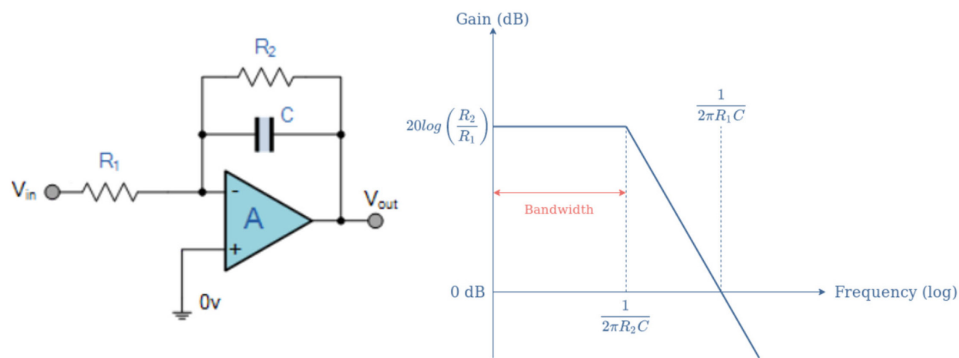


Figure 5.7: Amplifier with low pass filter

By choosing the correct capacitor C is possible to set the cutting frequency. Has been decided to cut at very high frequency (5 kHz) just to filter a bit the noise.

R_2 is fixed and is the amplifier's internal resistance: $R_2 = 3,2 \cdot 10^5 \Omega$

C chosen to have the desired frequency: $C = 100 \text{ pF}$

$$f = \frac{1}{2 \pi C R_2} \cong 5 \text{ kHz}$$

The amplifiers are powered by a 5 V power supply and receive the 2,5 V reference to offset the signal. Therefore, for every channel, since the specific amplifiers used have rail to rail output, the signal after the amplification stage goes from 0 to 5 V maximum and when there is no load applied is around 2,5 V.

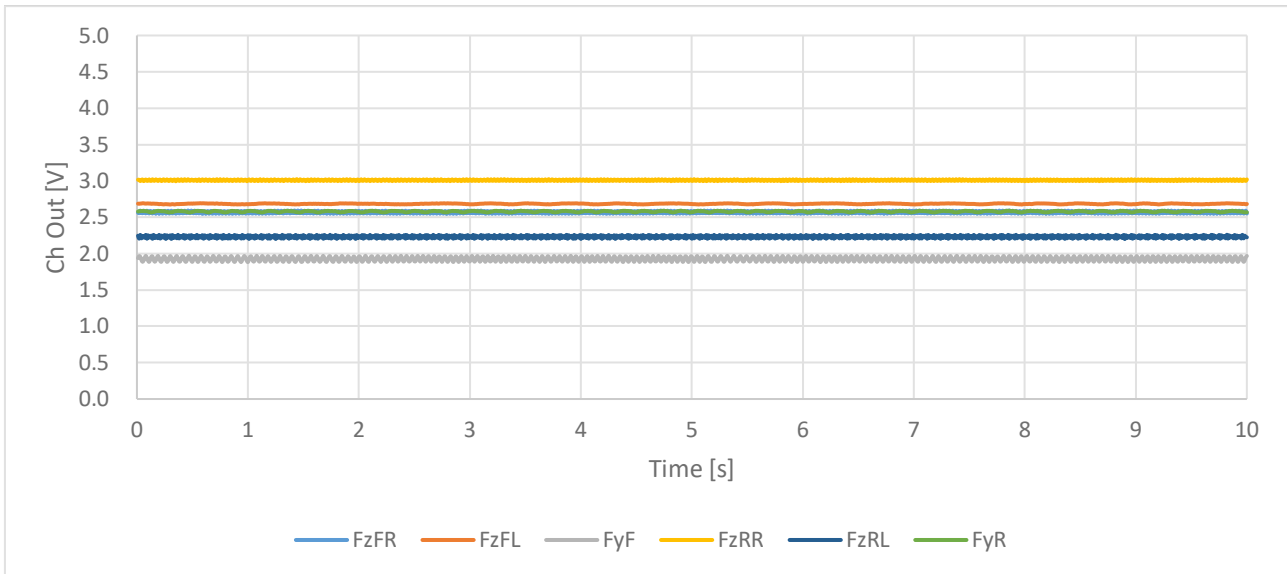


Figure 5.8: Example of signal from the channels with the amplifiers when the load cell is unloaded

In Figure 5.8 is shown is the output signal when the load cell is unloaded. It is possible to see some noise in the signal but it has negligible amplitude. There is an offset of the channel signal that shifts the output from the 2,5 V reference due to the reality of the circuit. This is very difficult to manually remove (a small input offset when amplified gets bigger) so it was preferred to correct it later analytically. The offset, although significant (0.5 V), was considered insignificant: given the low amplification of the signal, it was considered never to reach the limits of the measurement range (0 - 5 V).

After tests in the laboratory, these assumptions proved to be wrong because the excessively high amplification together with the offset, caused the signal to reach the limits of the range.

Given that the boards were manufactured before the boot of the monoski was available, the size of the boards did not allow the load cell to fit in it. It has been necessary to move and cut them. In future developments, the boards should be designed to be more compact, with a shape closer to the one of the load cell to allow a less exposed placement.

Once calibrated, the load cell is completed and ready to be used on the ski slopes after being made waterproof with a layer of lacquer and sealed in a silicon layer. The silicon was applied in three successive casts to make it bond with the board and to make it bulky, where the boards are more exposed to impacts.

Specifics of the amplifiers boards are in Appendix pag. 152 (Load cell amplifiers boards design).

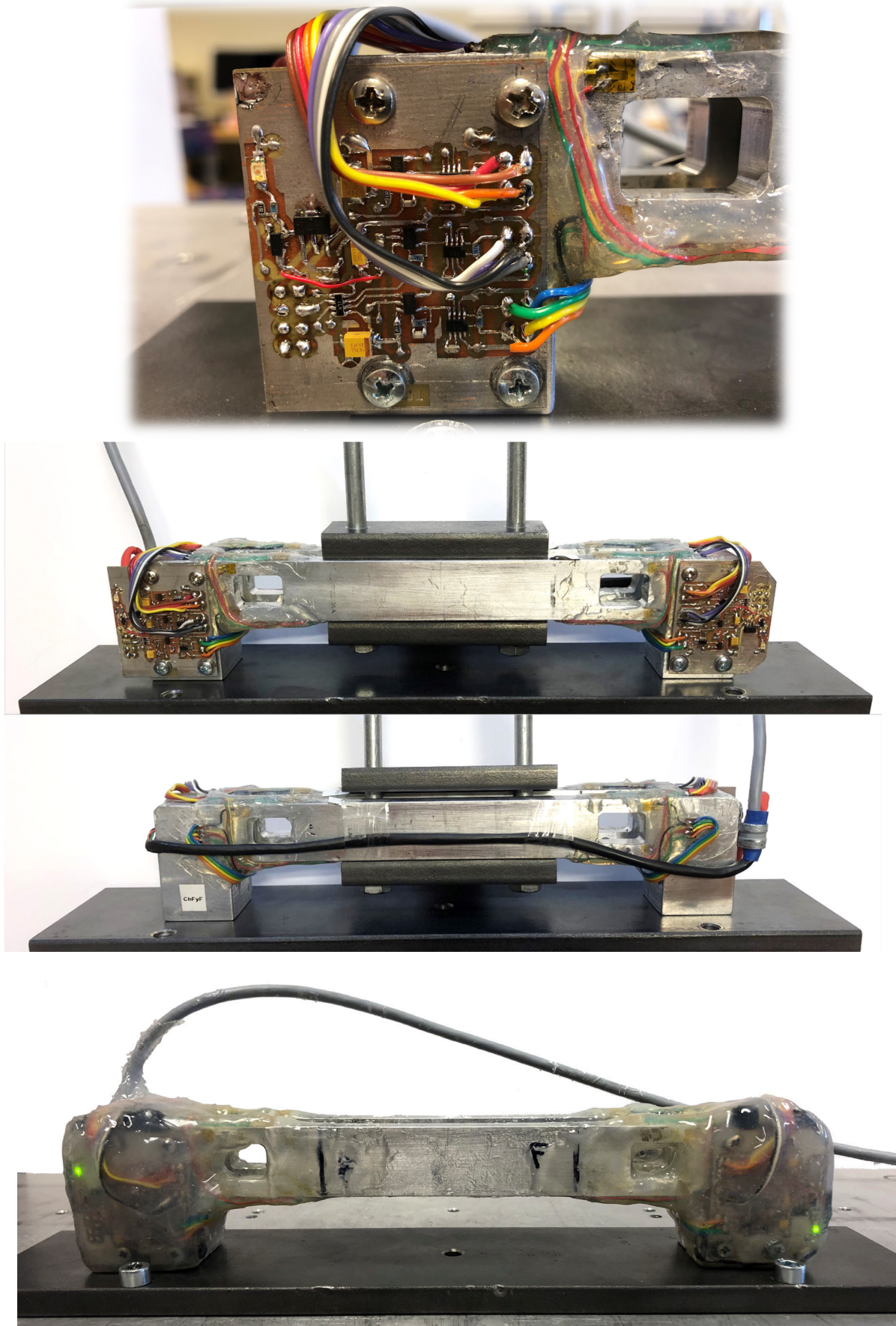


Figure 5.9: Construction stages of the load cell

5.4 Calibration of load cell

In order to use the load cell is necessary to do the calibration procedure.

Because of all the changes to the original, the load cell cannot use its original calibration, so it is necessary to redo the whole process. The goal of the calibration procedure is to establish a relationship between the six voltage outputs and the four load components.

The process consists of applying to the sensor known static forces at known positions, measuring the results in Volts given by the sensor and relating the two in a mathematical process.

To calibrate the Load Cell is necessary to calibrate each load that can be measured separately. It is therefore necessary to apply static loads that are as “pure” as possible so with only one load component. The calibration has been divided into four test sessions: F_z , F_y , M_x , M_y , one for each pure force/moment. The instruments and materials used in the process were chosen and designed, given these assumptions.

5.4.1 Calibration instrumentation

To perform the process, few instruments were used. These can be divided in:

- Kistler force plate
- Materials
- Data acquisition instruments and software

For good calibration quality, the loads (input to the load cell) and volts (output) are measured with high precision.

Loads applied using weights were measured in two ways to doublecheck their values: by knowing dead weights (and arm for the moments) and with the Kistler Force Plate.

A Kistler Multicomponent Force Plate for Biomechanics Type 9281EA [9] was used to measure the GRF. It provides a dynamic and quasi-static measurement of the 3 orthogonal components of a force (F_x , F_y , F_z) acting from any direction on the top plate. With the aid of the software system BioWare Type 2812A [10] can also be measured: the moments M_x , M_y and M_z , the coordinates a_x and a_y of the point of application of force on the force plate surface (Center of Pressure), the torque T_z (free moment) about an axis normal to the force plate surface, center of mass displacement and acceleration, physical power and work, coefficient of friction.




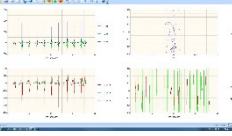

				
Force plate with charge amplifier Type 9281 EA	Connection cable Type 1759 A	External Control Unit Type 5233A2	BioWare® Type 2812 A	PC

Figure 5.10: Kistler force plate connections with Built-In Amplifier

Is important that the components used to apply loads on the load cell deforms as little as possible to avoid influencing the loads. For this reason, to fix the load cell to the force plate has been necessary to build a robust plate that could connect the two because the original Scarver foot did not allow fastening on the Kistler force plate.

Since a prototype monoski (Aggressor by Ableway AB [1]) was available and there was a plan of the stakeholders to eventually use it for future tests, a new foot was designed (Appendix pag.156: Load cell amplifiers boards design) that would allow the load cell to be mounted on both the Scarver and the Aggressor. The new foot also allowed easy fastening on the Kistler platform for indoor tests.

Using the same foot for the calibration and the testing could also improve the quality of results.

Due to time pressure the new foot was not manufactured and instead was used for the calibration a 1 cm thick steel plate (Figure 5.11 (b)).

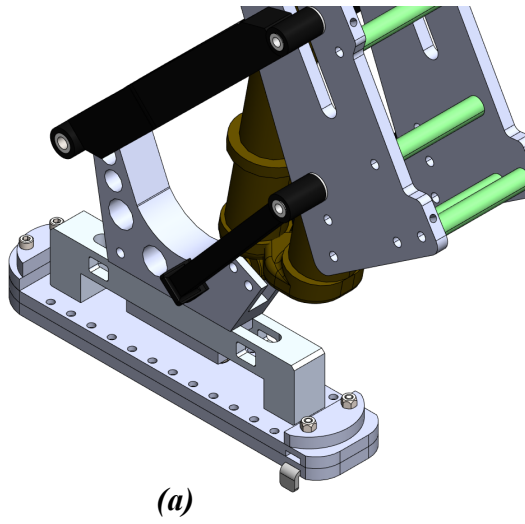
Were also manufactured other 3 smaller plates (1 cm thick steel) of the same size of the one used in the FEM simulations in Ansys in the previous chapters to reproduce the same load condition on the load cell.

A weight set was available with 20 kg (2x), 15 kg (1x), 10 kg (1x), 5 kg (4x) weights. Another set of smaller weights was available (1 kg, 0.5 kg). The weights were measured using a high precision scale.

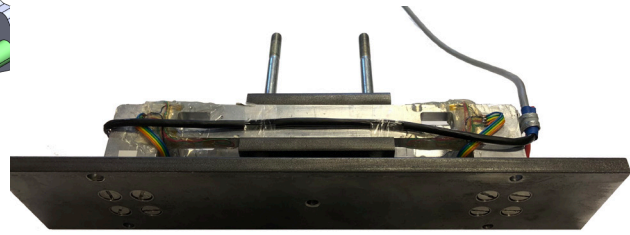
The rest of the material used consists of aluminium bars, pulleys, ropes, screws and bolts. In particular a 1.46 m bar was used to produce the moments. An aluminium cage was used to hang the pulleys.

In addition to these, it was used as an acquisition system to record the signals from the Load Cell of the module NI USB-6210 controlled by LabVIEW (Cap. 10).

For the calibration has been used a simple LabVIEW program featuring: the setting of a number of samples and rate [Hz] and file name, triggering physical analog button, automatic average calculation, and autosave of all data and results.



(a)



(b)

Figure 5.11: (a) New foot CAD drawing (b) The plates manufactured for the calibration

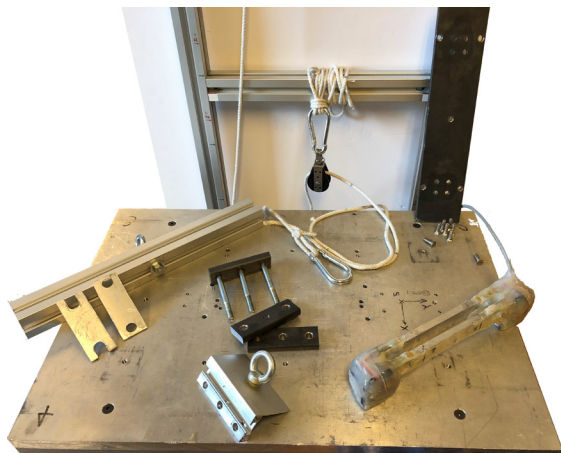
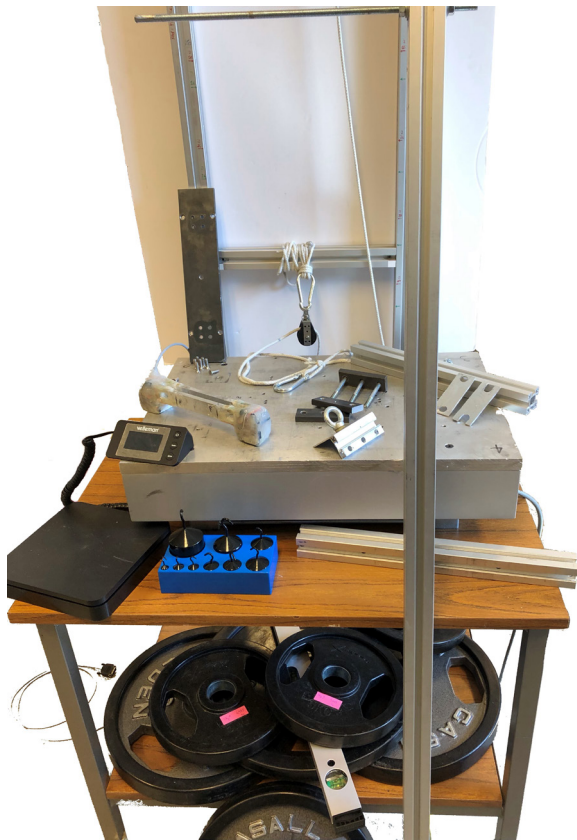


Figure 5.12: Material used in the calibration

5.4.2 Calibration procedure

Before each session were set the materials and the acquisition systems. For this calibration were set a sampling of 10 seconds at a rate of 1000 Hz for both Kistler and Load Cell. After these settings, to apply the desired load, the procedure described below is repeated the same for each measure.

- With no weights applied, only the weight of the materials, the Kistler is zeroed (zeroing of the internal amplifiers by reading the voltage offset)
- The weights are applied and wait for the time when the weights stop swinging
- The acquisitions with Kistler and LabVIEW are started simultaneously
- Measurement
- Saving of the Kistler results in .txt format
- Remove all weights

The procedure includes putting on and then removing all weights for each measure. This avoids the drift problem of both the Kistler force platform and the load cell. Offset drift is the drift in output voltage over time. Instead, resetting to 'zero' each time partially avoids this problem that seemed to affect the Kistler when it was under load for long periods of time. This issue is accepted since it is due to the operating principle of the force plate, in fact the force sensors embedded are piezoelectric type.

The measurements of the Kistler and the results of the load cell are averaged on the 10 seconds of sampling since the calibration is static.

Calibration along z-axis has been executed by placing the weights on an aluminium bar bolted on the load cell. The centring was performed by passing the weights through a round bar fixed to the center of the dynamometric load cell to avoid creating any moment so producing a “pure” vertical load.

Calibration along the y-axis has been executed by anchoring a wire to the L-shape plate fixed on the top of the dynamometric load cell. The eyebolt in which has been fixed the wire is located exactly at the center of the cell reference system. The reason is to produce only lateral load. The wire fixed into the L-shape structure passes around a pulley, fixed on a cage so the weights are left hanging.

Calibration of the moment around x-axis has been executed using a long aluminium bar (1,46 m) bolted on the load cell. At one end of the bar there is an eyebolt with a wire fixed, at the other end, there is a round bar to centre the weights. The two ends are exactly opposite to the centre of the bar, symmetrical to the longitudinal axis. The wire passes around a pulley

fixed on a cage and the weight is left hanging. On the other side, the weights are passed through the round bar. By summing the moments on one side and the other, this produces the pure rolling moment.

Calibration of the moment around y-axis has been executed with the same method used for M_x but with the load cell rotated to produce the pure pitch moment.

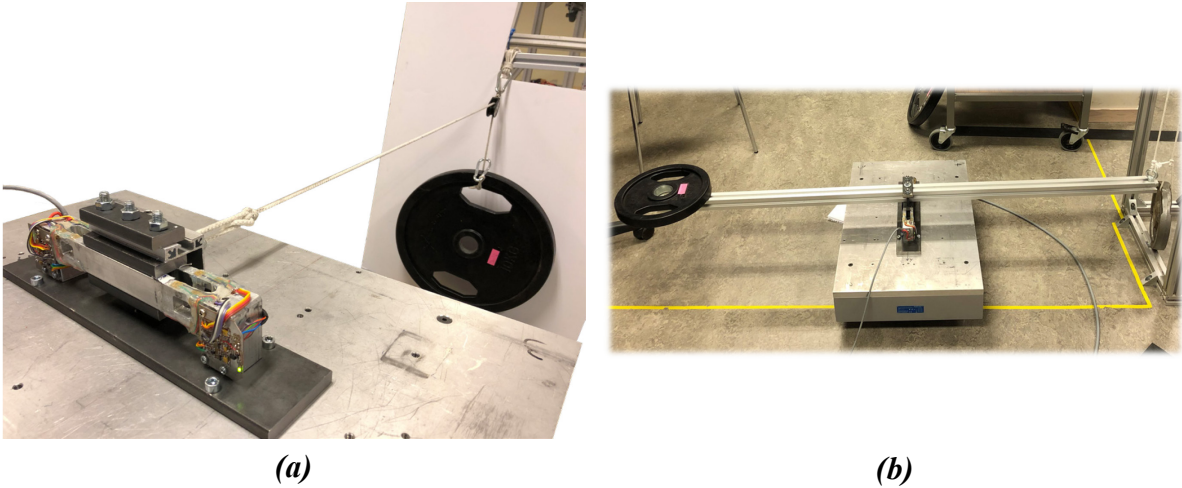


Figure 5.13: (a) Calibration of F_y

(b) Calibration of M_x

Only the values for the calibration with a vertical load, F_z , are reported and described here. The values of the other calibrations are given in the Appendix pag.162 (Calibration of the load cell).

Loads [N]		Ch output averages [V]									
Fz Kistler	Fz Weight	FzFR	FzFL	FyF	2.5V F	5V F	FzRR	FzRL	FyR	2.5V R	5V R
-0.1	0	2.570	2.685	1.927	2.557	5.006	3.009	2.231	2.579	2.556	5.011
98.9	98	2.619	2.703	1.932	2.557	5.007	3.054	2.270	2.627	2.556	5.012
147.3	148	2.645	2.716	1.930	2.557	5.007	3.085	2.279	2.631	2.556	5.012
198.4	199	2.667	2.735	1.930	2.557	5.007	3.103	2.302	2.631	2.556	5.012
295.5	297	2.715	2.758	1.933	2.557	5.007	3.152	2.339	2.630	2.556	5.012
391.2	395	2.779	2.776	1.932	2.557	5.007	3.210	2.363	2.604	2.556	5.013
491.5	495	2.848	2.780	1.935	2.557	5.007	3.283	2.384	2.611	2.557	5.013
588.0	593	2.875	2.834	1.936	2.557	5.007	3.295	2.444	2.613	2.556	5.013
682.9	688	2.934	2.834	1.933	2.557	5.007	3.384	2.456	2.623	2.556	5.013
780.2	787	2.956	2.881	1.938	2.557	5.007	3.396	2.527	2.622	2.556	5.012
1011.3	1021	3.143	2.873	1.941	2.557	5.007	3.609	2.529	2.633	2.556	5.013
1143.9	1154	3.147	2.921	1.942	2.557	5.007	3.647	2.648	2.633	2.556	5.012

Table 4: Loads applied and channel response of the load cell

On the left are the loads measured by the Kistler force plate and by the sum of the weights applied. As can be seen, the values have a very small difference. Considering the high precision of the force plate, the value measured by the Kistler has been kept.

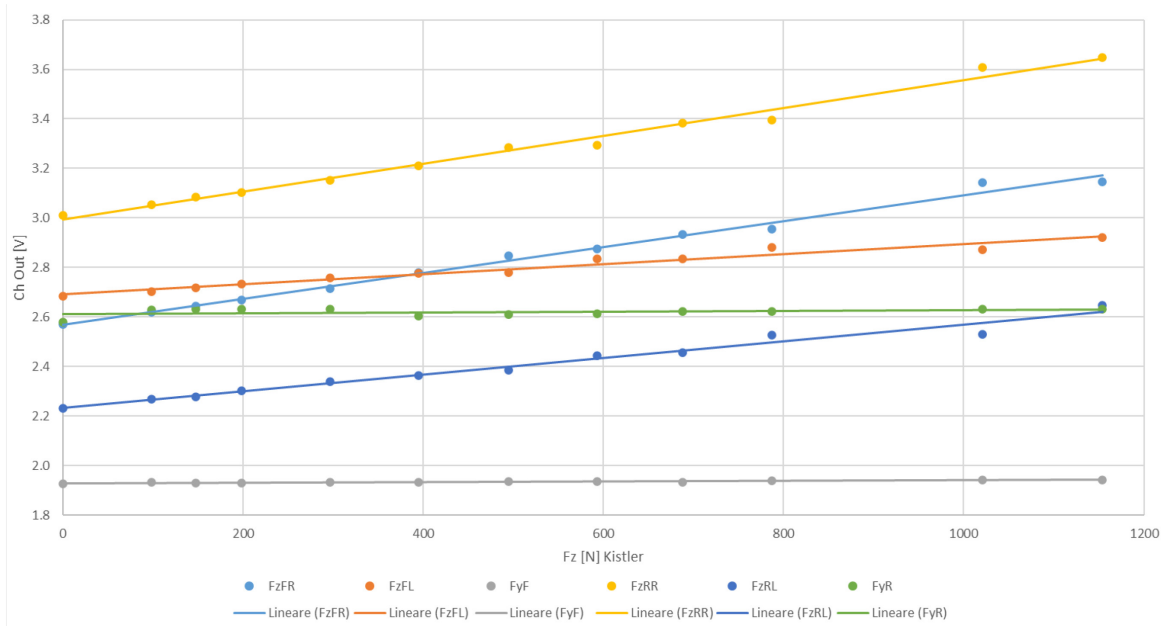


Figure 5.14: Load - Channel output for Fz Calibration

As expected, increasing the load on the sensor, the voltage output increases consequently in the channels sensible in that direction (vertical in this case) and remains stable on the other channels.

It is clear from the graph that different channels are subject to different offsets due to the physical reality of the components. In fact, it only takes the resistance of the strain gauge or of the cable or some extra amplification to get slightly different results from one channel to another. This offset is numerically corrected in the next steps of the procedure. As the test phase revealed, this offset is a very serious issue: since the possible range of output is between zero Volt and 5 Volt an offset of just 1V greatly reduces the measuring range of the load cell.

For the other load components, the procedure is the same, except for the two moments M_x and M_y : in this case, the measurements by the Kistler force platform revealed to be unreliable so were used the moments calculated by knowing the weights and the lever arm.

5.5 Data analysis

There are different possible approaches to the mathematical problem of the calibration. In addition each approach can be more complex or less sophisticated.

The approaches followed were:

- Calibration matrix model using first-order equations [11] [12] [13];
- Neural Networks part of the Deep Learning Toolbox of MATLAB [14] [15].

Was then conducted an investigation to identify which approach best fitted this particular case study giving more accurate results.

5.6 Calibration using calibration matrix

A strain gauge is sensitive to its grid area deformation $\varepsilon_{\mu m}$ in microstrain caused by a generical load $L_{N,Nm}$. The relationship is linear, so the sensitivity is a constant. The load cell used in this thesis is a Multicomponent Load Cell, in fact has multiple strain gauges so it can measure multiple loads in different directions at the same time. Consequently, the calibration process will be a matrix system:

$$\{\varepsilon\}_{\mu m} = [S_{L,\varepsilon}] \cdot \{L\}_{N,Nm}$$

where $[S_{L,\varepsilon}]$ is the sensitivity matrix.

The output signal of the strain gauges is in milliVolt per Volt $\{\Delta V\}_{mV/V}$ but it can be written as function of generic channel vectors that, after being amplified, are in Volt per Volt $\{Ch\}_{V/V}$. Therefore, the previous expression can be written as:

$$\begin{aligned} \{Ch\}_{\frac{V}{V}} &= \begin{bmatrix} S_{\frac{V}{V}} \\ \frac{V}{N} \end{bmatrix} \cdot \{L\}_{N,Nm} \\ 6 \times 1 & \quad \quad \quad 6 \times 6 \quad \quad \quad 4 \times 1 \\ \{V\} &= \begin{bmatrix} \frac{V}{N,Nm} \end{bmatrix} \cdot \{N,Nm\} \end{aligned}$$

where $\{L\}_{N,Nm} = \{Fz, Fy, Mx, My\}^T$ is the Loads vector.

Although the channels $ChFy_F$ and $ChFy_R$ might measure lateral forces and the yaw moment, it has been decided to not consider the latter as not interesting for the loads on a monoski.

$\{Ch\}_{V/V} = \{ChFz_{FR}, ChFz_{FL}, ChFy_F, ChFz_{RR}, ChFz_{RL}, ChFy_R\}^T$ is the Channel vector with the six voltage outputs of the six bridges of the load cell.

In the calibration process the loads are known and applied with high accuracy, the voltages are measured and the objective of the procedure is to obtain the Sensitivity matrix $[R]_{6 \times 4}$.

$$\begin{Bmatrix} ChFz_{FR} \\ ChFz_{FL} \\ ChFy_F \\ ChFz_{RR} \\ ChFz_{RL} \\ ChFy_R \end{Bmatrix} = \begin{bmatrix} R_{11} & \cdots & R_{14} \\ \vdots & \ddots & \vdots \\ R_{61} & \cdots & R_{64} \end{bmatrix} \cdot \begin{Bmatrix} Fz \\ Fy \\ Mx \\ My \end{Bmatrix}$$

Because a Multicomponent Load Cell is used, a single load is measured by more than one Channel, as can be seen in the previous equation in fact the dimensions of the Channels and Load vectors is different. For this reason the procedure must first obtain a Channels vector with the same dimension of the Load vector.

It is necessary to use the Virtual Channels.

These can be derived from the geometry considering that the absolute reference system of the load cell is placed in the centre position of the beam, as shown in Figure 5.19 is known which force each channel is sensitive to and is possible to relate each load with the Channel's response as follows,

$$Fz \propto \{ChFz_{FR}, ChFz_{FL}, ChFz_{RR}, ChFz_{RL}\}$$

$$Fy \propto \{ChFy_F, ChFy_R\}$$

$$Mx \propto \{-bx \cdot ChFz_{FR}, bx \cdot ChFz_{FL}, -bx \cdot ChFz_{RR}, bx \cdot ChFz_{RL}\}$$

$$My \propto \{-by \cdot ChFz_{FR}, -by \cdot ChFz_{FL}, by \cdot ChFz_{RR}, by \cdot ChFz_{RL}\}$$

$$\begin{cases} Fz \propto \{ChFz_{FR}, ChFz_{FL}, ChFz_{RR}, ChFz_{RL}\} \\ Fy \propto \{ChFy_F, ChFy_R\} \\ Mx \propto \{-bx \cdot ChFz_{FR}, bx \cdot ChFz_{FL}, -bx \cdot ChFz_{RR}, bx \cdot ChFz_{RL}\} \\ My \propto \{-by \cdot ChFz_{FR}, -by \cdot ChFz_{FL}, by \cdot ChFz_{RR}, by \cdot ChFz_{RL}\} \end{cases}$$

bx and by are correspondingly the lever arm of the moment Mx , the second the lever arm of the moment My with respect to the reference system.

Considering the system as linear, then the virtual channels are:

$$\begin{cases} vChFz = ChFz_{FR} + ChFz_{FL} + ChFz_{RR} + ChFz_{RL} \\ vChFy = ChFy_F + ChFy_R \\ vChMx = -bx \cdot ChFz_{FR} + bx \cdot ChFz_{FL} - bx \cdot ChFz_{RR} + bx \cdot ChFz_{RL} \\ vChMy = -by \cdot ChFz_{FR} - by \cdot ChFz_{FL} + by \cdot ChFz_{RR} + by \cdot ChFz_{RL} \end{cases}$$

These can be written in a matrix system:

$$\begin{Bmatrix} vChFz \\ vChFy \\ vChMx \\ vChMy \end{Bmatrix} = \begin{bmatrix} 1 & 1 & 0 & 1 & 1 & 0 \\ 0 & 0 & 1 & 0 & 0 & 1 \\ -bx & bx & 0 & -bx & bx & 0 \\ -by & -by & 0 & by & by & 0 \end{bmatrix} \cdot \begin{Bmatrix} ChFz_{FR} \\ ChFz_{FL} \\ ChFy_F \\ ChFz_{RR} \\ ChFz_{RL} \\ ChFy_R \end{Bmatrix}$$

$$\begin{matrix} \{vCh\} = [H] \cdot \{Ch\} \\ 4 \times 1 \quad 4 \times 6 \quad 6 \times 1 \end{matrix}$$

The geometrical Transformation matrix $[H]_{6 \times 4}$ expresses the dependency of virtual channels $\{vCh\}$ on the sensor channels $\{Ch\}$.

The virtual channels can be then used to link the Load vector as follows

$$\begin{pmatrix} vChFz \\ vChFy \\ vChMx \\ vChMy \end{pmatrix} = \begin{bmatrix} S_{11} & \cdots & S_{14} \\ \vdots & \ddots & \vdots \\ S_{41} & \cdots & S_{44} \end{bmatrix} \cdot \begin{pmatrix} Fz \\ Fy \\ Mx \\ My \end{pmatrix}$$

Sensitivity matrix $[S]_{4 \times 4}$ in $\left[\frac{V}{V} / N, Nm\right]$

The Sensitivity matrix is used to derive the Calibration matrix which is the matrix needed to calculate forces and moments in the test sessions.

$$[C] = [S]^{-1}$$

To summarize the results are:

$$\begin{cases} \{L\} = [C] \cdot \{vCh\} \\ \{vCh\} = [H] \cdot \{Ch\} \end{cases}$$

Finally, the processing of the data from test sessions to obtain the Loads on the load cell is done by multiplying the Channel signals by H and C matrices.

$$\begin{matrix} \{L\} = [H] \cdot [C] \cdot \{Ch\} \\ 4 \times 1 \quad 4 \times 6 \quad 4 \times 4 \quad 6 \times 1 \end{matrix}$$

5.6.1 Results of the calibration

The data from the calibration tests has been imported in MATLAB for analysis.

For each calibration test (four in total) were built two matrices: one of the mean measures of every load step in Volt/Volt and one of the loads applied in N and Nm. (Table 4)

The matrices of the measures were normalized to the value of the first load step because for every test the first value is measured when there are no weights applied. In this way the negligible weight of the steel plate and aluminium bar or hooks are cancelled and zeroed. This allows also to compensate the offset of the Voltages in the signals which was clearly visible in Figure 5.8.

The linear interpolation of each Channel response in each calibration test allows to build the Sensitivity matrix $[R]_{6 \times 4}$. It has been done using the function “polyfit” of MATLAB.

The gradient of each interpolation line will be a matrix component of the Sensitivity matrix $[R]_{6 \times 4}$. The matrix is built column by column on each calibration test.

The results are shown in the following figures.

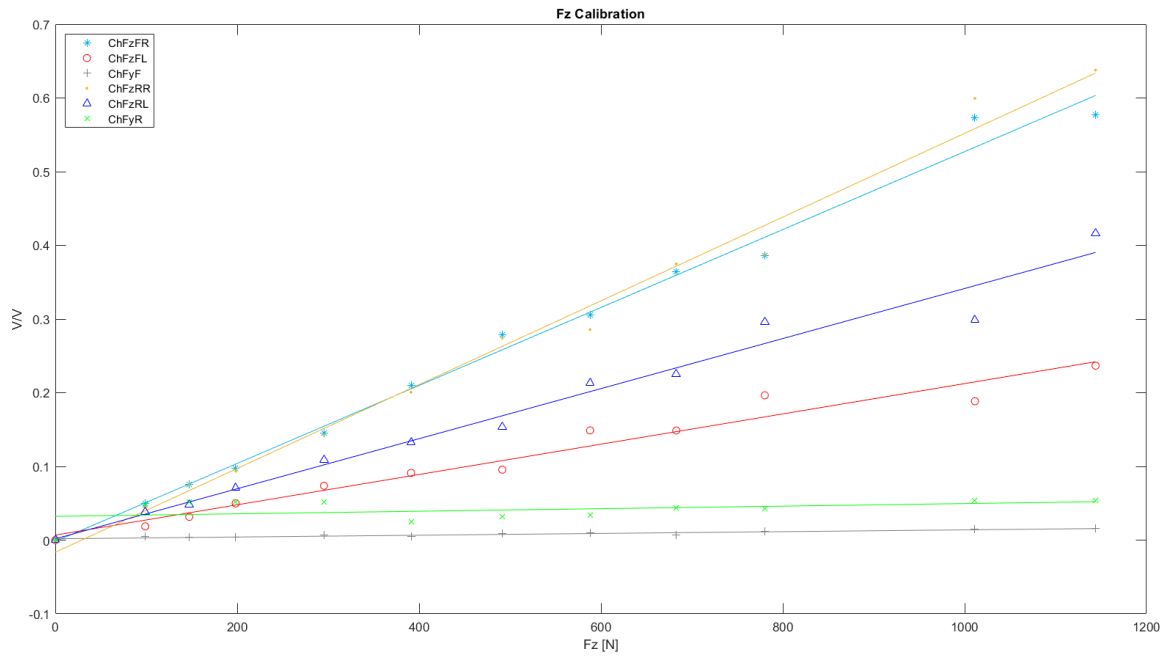


Figure 5.15: Load – Channel output for Fz calibration

First Column of Sensitivity matrix $[R]_{6 \times 4}$	
R_{11}	$5.289 \cdot 10^4$
R_{21}	$2.056 \cdot 10^4$
R_{31}	$0.121 \cdot 10^4$
R_{41}	$5.68 \cdot 10^4$
R_{51}	$3.397 \cdot 10^4$
R_{61}	$0.173 \cdot 10^4$

Table 5: Results of the Fz calibration

As can be seen in the figure above concerning the calibration of the Fz, the channels that show bigger responses, so have a greater slope of the line, are the vertical ones. This is correct in fact given the geometry of the load cell and the position of the strain gauges it is correct that the channels sensitive to vertical forces have a non-zero output and the channels sensitive to horizontal forces have outputs close to zero.

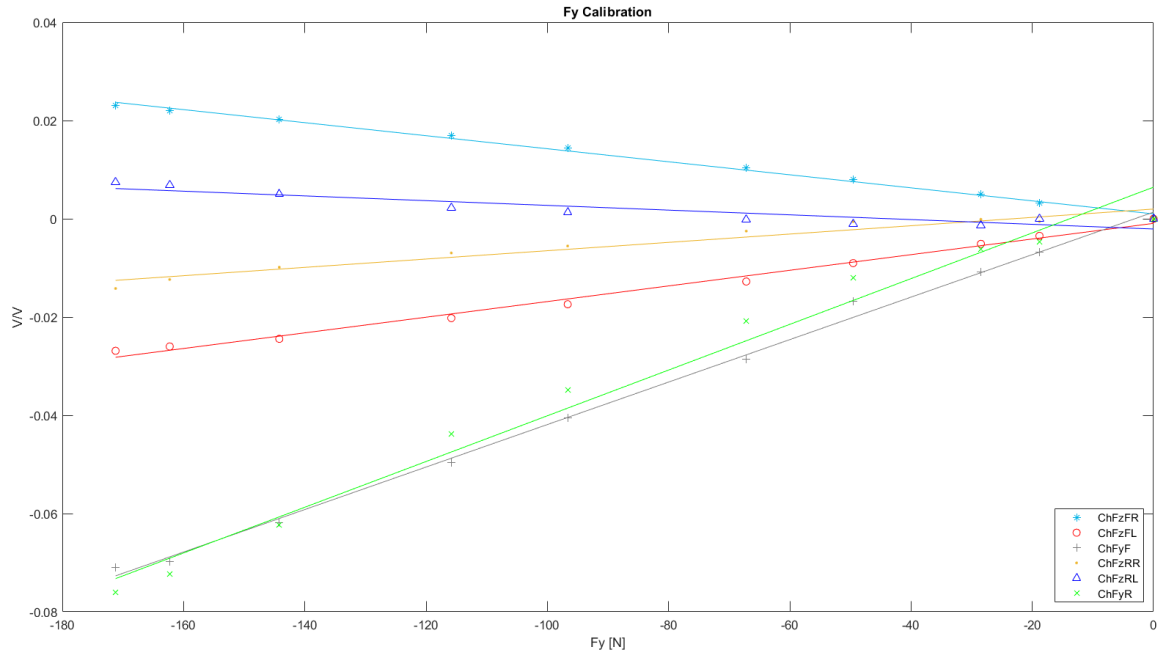


Figure 5.16: Load – Channel output for F_y calibration

Second Column of Sensitivity matrix $[R]_{6 \times 4}$	
R_{12}	$-1.327 \cdot 10^4$
R_{22}	$1.592 \cdot 10^4$
R_{32}	$4.324 \cdot 10^4$
R_{42}	$0.848 \cdot 10^4$
R_{52}	$-0.481 \cdot 10^4$
R_{62}	$4.654 \cdot 10^4$

Table 6: Results of the F_y calibration

As can be seen in the figure above concerning the calibration of the F_y , the channels that show bigger responses, so have a greater slope of the line, are the lateral ones. However, the vertical channels do not have all values close to zero. This is a sign that the calibration in this direction is not very good. In fact from the geometry of the load cell the lateral loading should not appear on the channels that are sensitive to horizontal forces.

Also, notice that the points are more scattered than the other measures and this badly impacts the quality of the results.

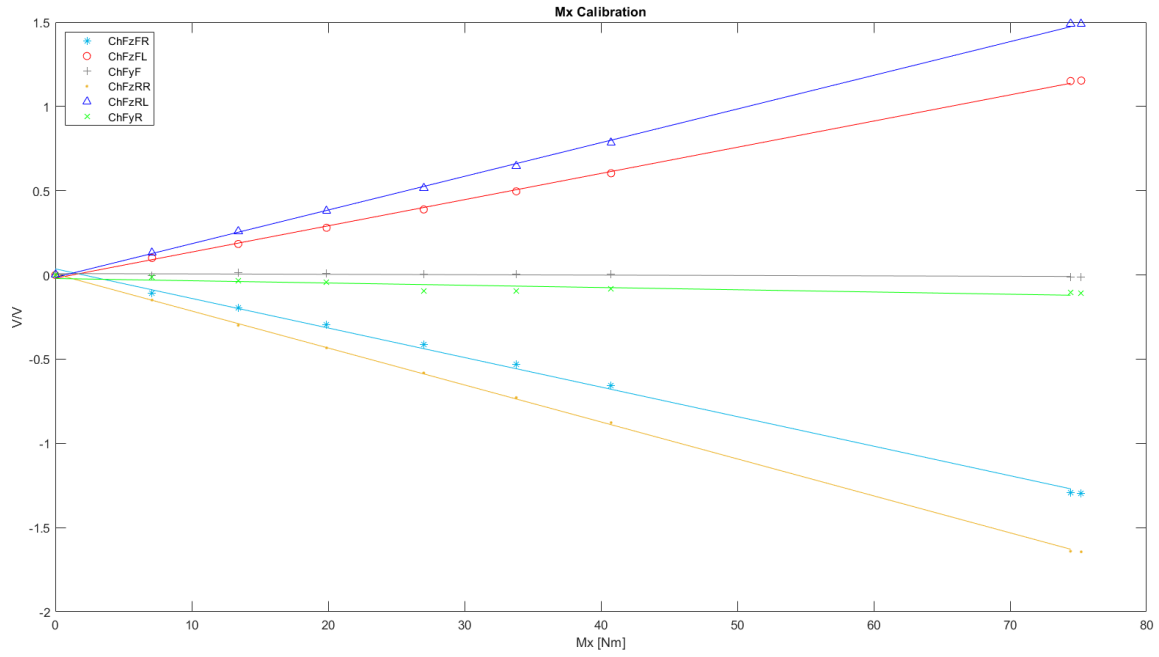


Figure 5.17: Load – Channel output for Mx calibration

Third Column of Sensitivity matrix $[R]_{6 \times 4}$	
R_{13}	$-175.442 \cdot 10^4$
R_{23}	$155.515 \cdot 10^4$
R_{33}	$-2.314 \cdot 10^4$
R_{43}	$-219.477 \cdot 10^4$
R_{53}	$199.931 \cdot 10^4$
R_{63}	$-13.352 \cdot 10^4$

Table 7: Results of the Mx calibration

The calibration of the moment on x-axis with the load cell shows a perfect symmetry between left and right. The lateral channels have values close to zero.

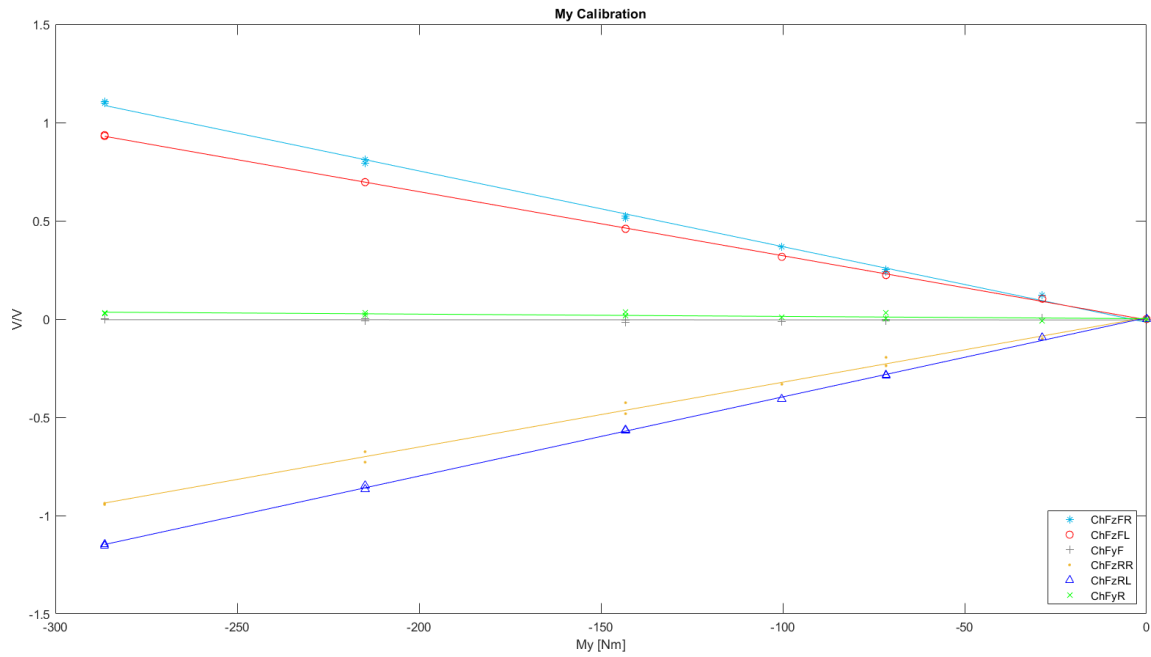


Figure 5.18: Load – Channel output for My calibration

Fourth Column of Sensitivity matrix $[R]_{6 \times 4}$	
R_{14}	$-38.528 \cdot 10^4$
R_{24}	$-32.598 \cdot 10^4$
R_{34}	$-0.055 \cdot 10^4$
R_{44}	$32.976 \cdot 10^4$
R_{54}	$40.286 \cdot 10^4$
R_{64}	$-1.153 \cdot 10^4$

Table 8: Results of the My calibration

The calibration of the moment on axis with the load cell shows a perfect symmetry between front and rear. The lateral channels have values close to zero.

The resulting Sensitivity Matrix $[R]_{6 \times 4}$ determined by assembling the columns previously obtained, is the following:

$$\begin{pmatrix} ChFz_{FR} \\ ChFz_{FL} \\ ChFy_F \\ ChFz_{RR} \\ ChFz_{RL} \\ ChFy_R \end{pmatrix} = \begin{bmatrix} 5.3E-4 & 1.3E-4 & -175.4E-4 & 38.5E-4 \\ 2.1E-4 & -1.6E-4 & 155.5E-4 & 32.6E-4 \\ 0.1E-4 & -4.3E-4 & -2.3E-4 & 0.1E-4 \\ 5.7E-4 & -0.8E-4 & -219.5E-4 & -33.0E-4 \\ 3.4E-4 & 0.5E-4 & 199.9E-4 & -40.3E-4 \\ 0.2E-4 & -4.7E-4 & -13.4E-4 & 1.2E-4 \end{bmatrix} \cdot \begin{pmatrix} Fz \\ Fy \\ Mx \\ My \end{pmatrix}$$

The values are in $\left[\frac{V}{V}/N\right]$.

Since the load cell is symmetrical with respect to the point of force application and the strain gauge bridges are positioned and connected to have the same output for a given force, the channels should give the same amplitude. As can be seen in every plot of the calibration test, the bridges are slightly unbalanced due to the physical reality of the components. In fact, it only takes the resistance of the strain gauge or of cable or some extra amplification to get slightly different results from one channel to another.

This is highlighted in the sensitivity matrix that shows different values for every channel.

The channels are numerically balanced normalizing the signals, as explained in the next chapter.

5.6.2 Virtual channels

Next step is to determinate the virtual channel vectors.

Referring to the Figure 5.19 is possible to measure the lever arms:

$$bx = 10.5 \text{ mm} \quad by = 72.5 \text{ mm}$$

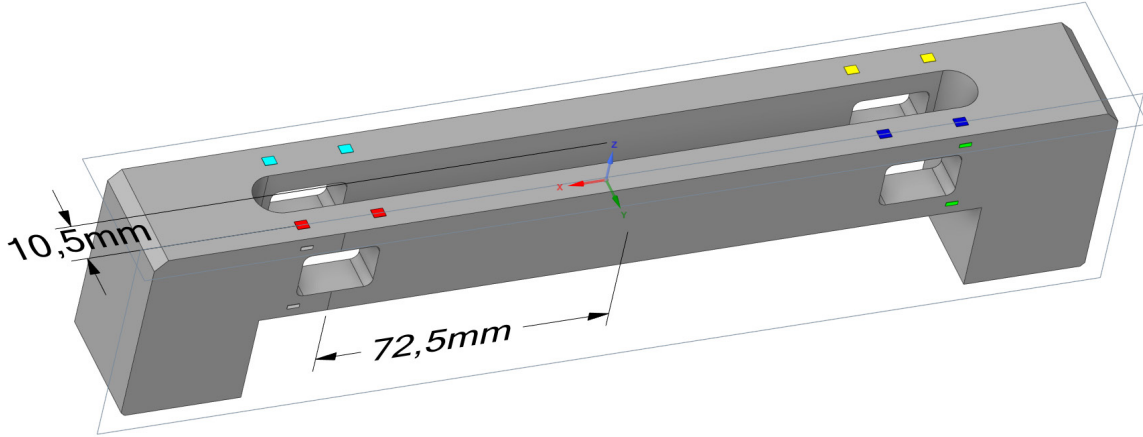


Figure 5.19: bx and by of the load cell

In this way it is possible to derive the geometrical Transformation matrix $[H]_{6 \times 4}$.

The matrix H is used also to correct the signals of the channels in order to balance their output. The results of each calibration test were normalized against the maximum value. Basically, each column of the Sensitivity matrix is normalized to its maximum absolute value to calculate the weights.

The result is the following.

$$[H] = \begin{bmatrix} 1.075 & 2.765 & 0 & 1 & 1.673 & 0 \\ 0 & 0 & 1.076 & 0 & 0 & 1 \\ -1.251 \cdot bx & 1.411 \cdot bx & 0 & -bx & 1.098 \cdot bx & 0 \\ -1.046 \cdot by & -1.236 \cdot by & 0 & 1.222 \cdot by & by & 0 \end{bmatrix} =$$

$$= \begin{bmatrix} 1.075 & 2.765 & 0 & 1 & 1.673 & 0 \\ 0 & 0 & 1.076 & 0 & 0 & 1 \\ -0.013 & 0.0148 & 0 & -0.011 & 0.012 & 0 \\ -0.076 & -0.0896 & 0 & 0.089 & 0.073 & 0 \end{bmatrix}$$

Now the Virtual Channels can be calculated using the relation:

$$\{vCh\}_i = [H] \cdot \{Ch\}_i$$

The linear interpolation of each Virtual Channel response in each calibration test allows to build the Sensitivity matrix $[S]_{4 \times 4}$. The gradient of each interpolation line will be a matrix component of the sensitivity matrix $[S]_{4 \times 4}$. The matrix is again built column by column on each calibration test.

The results are the following.

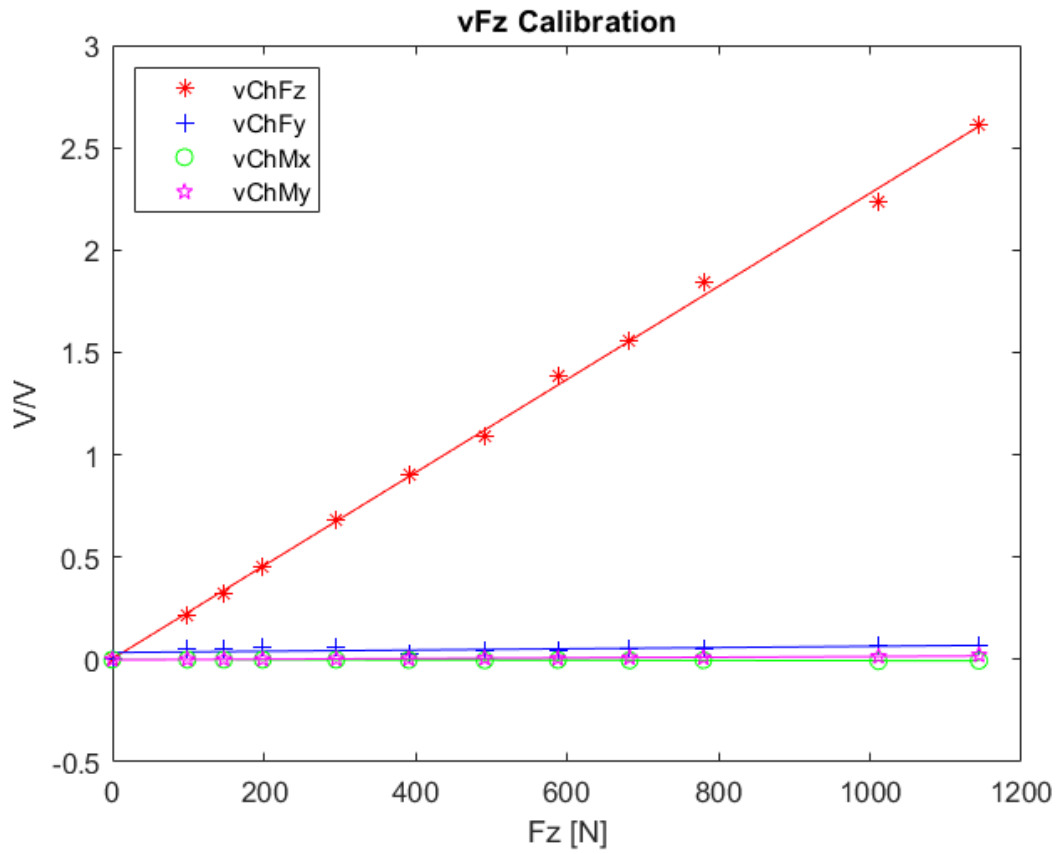


Figure 5.20: Virtual channels for Fz calibration

First Column of Sensitivity matrix $[S]_{4 \times 4}$	
S_{11}	$22.738 \cdot 10^4$
S_{21}	$0.304 \cdot 10^4$
S_{31}	$-0.060 \cdot 10^4$
S_{41}	$0.165 \cdot 10^4$

Table 9: Results of the virtual channels for Fz calibration

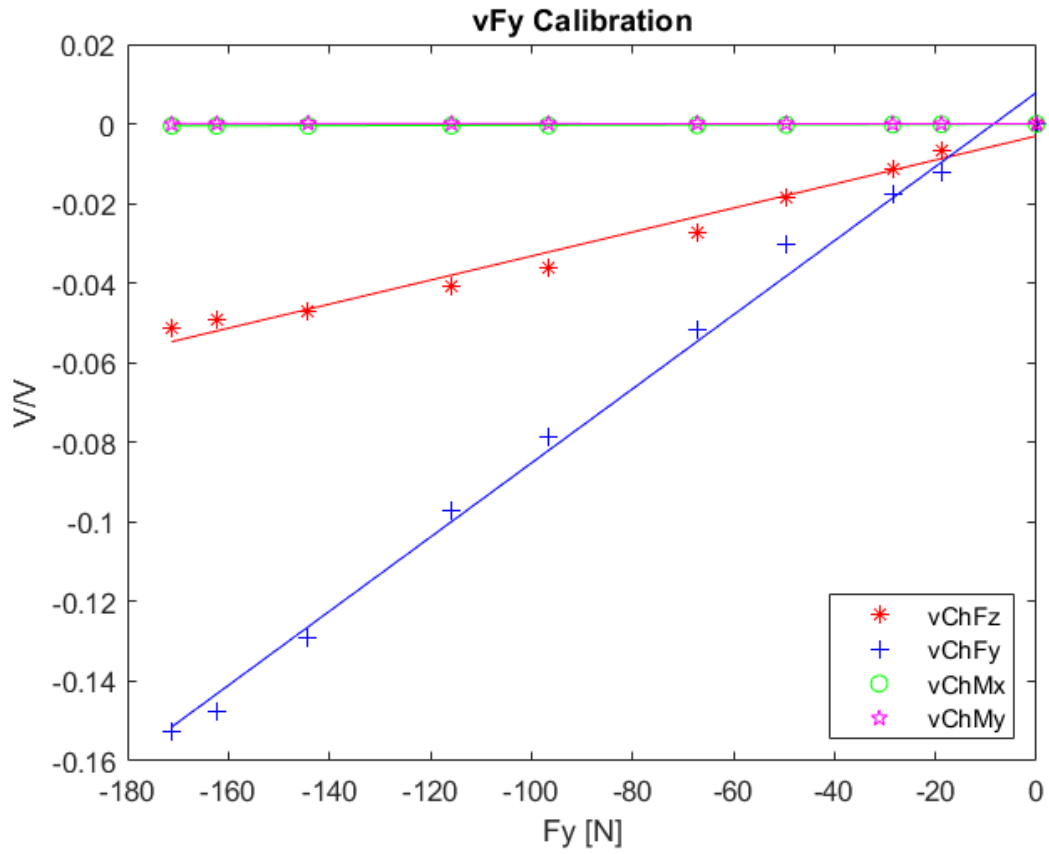


Figure 5.21: Virtual channels for F_y calibration

Second Column of Sensitivity matrix $[S]_{4 \times 4}$	
S_{12}	$3.017 \cdot 10^4$
S_{22}	$9.307 \cdot 10^4$
S_{32}	$0.027 \cdot 10^4$
S_{42}	$-0.002 \cdot 10^4$

Table 10: Results of the virtual channels for F_y calibration

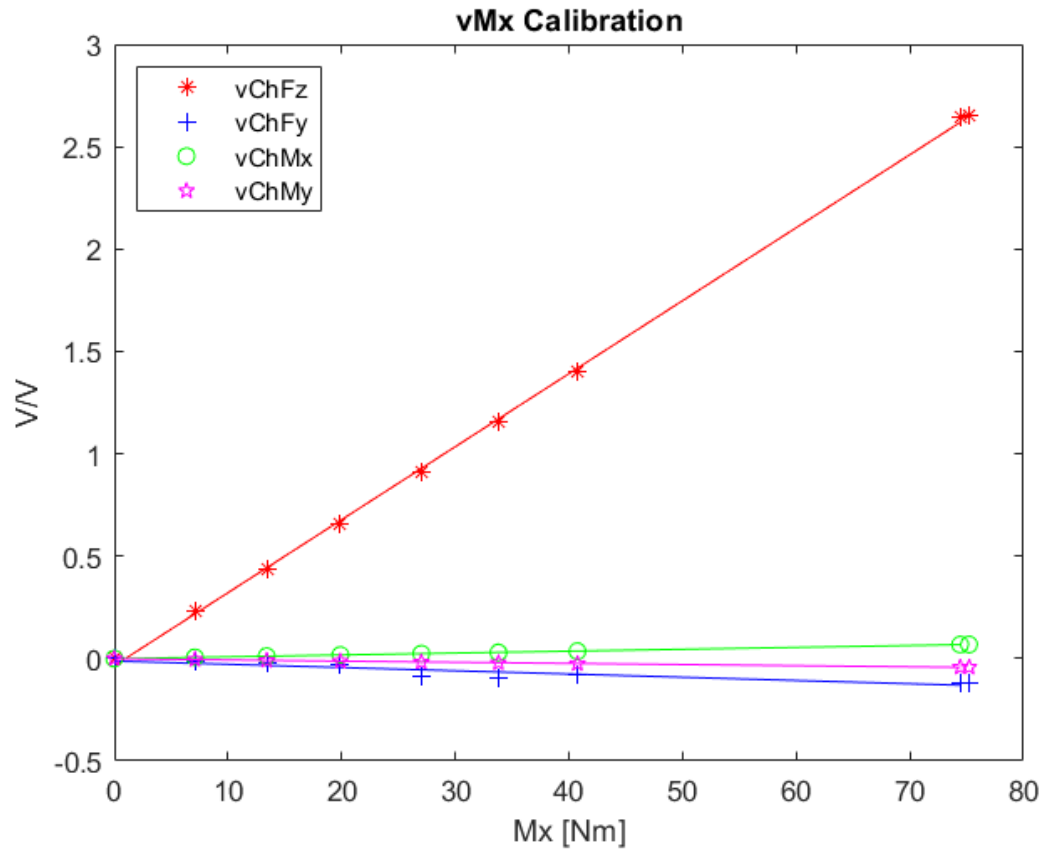


Figure 5.22: Virtual channels for M_x calibration

Third Column of Sensitivity matrix $[S]_{4 \times 4}$	
S_{13}	$356.525 \cdot 10^4$
S_{23}	$-15.843 \cdot 10^4$
S_{33}	$9.218 \cdot 10^4$
S_{43}	$-5.578 \cdot 10^4$

Table 11: Results of the virtual channels for M_x calibration

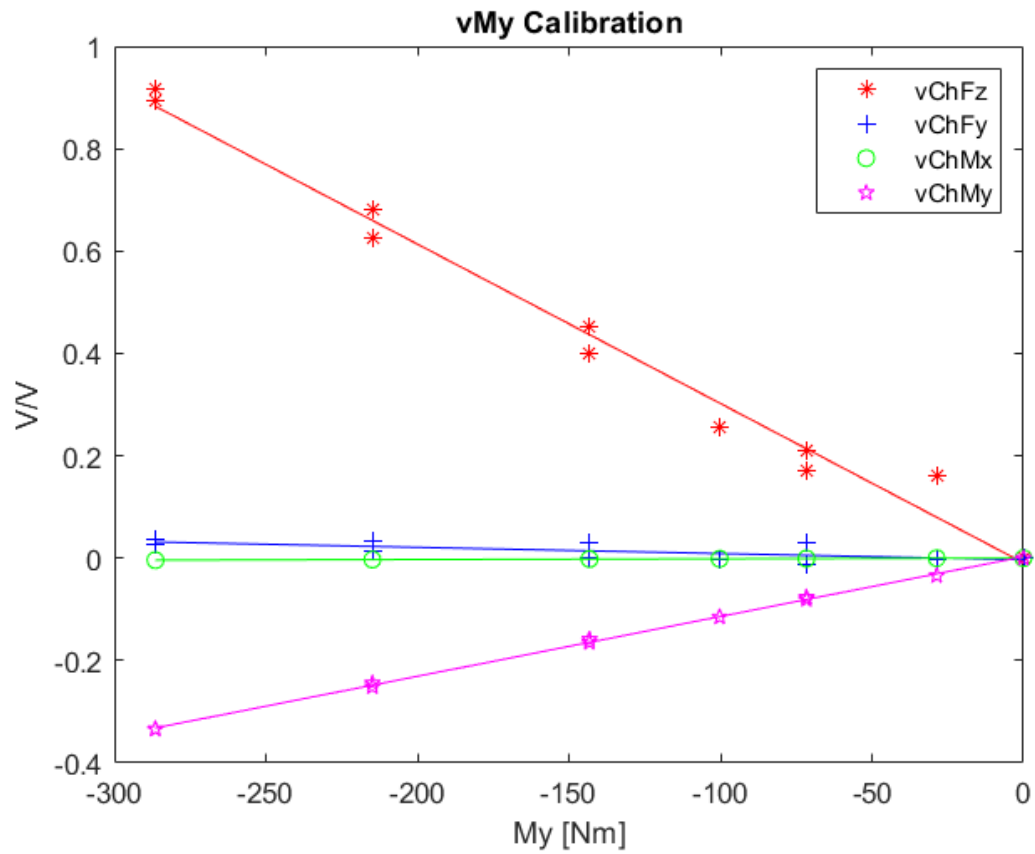


Figure 5.23: Virtual channels for My calibration

Fourth Column of Sensitivity matrix $[S]_{4 \times 4}$	
S_{14}	$-31.143 \cdot 10^4$
S_{24}	$-1.212 \cdot 10^4$
S_{34}	$0.141 \cdot 10^4$
S_{44}	$11.683 \cdot 10^4$

Table 12: Results of the virtual channels for My calibration

The resulting Sensitivity Matrix $[S]_{4 \times 4}$ determined by assembling the columns previously obtained, is the following:

$$\begin{Bmatrix} vChFz \\ vChFy \\ vChMx \\ vChMy \end{Bmatrix} = \begin{bmatrix} 0.00227 & 0.00030 & 0.03565 & -0.00311 \\ 0.00003 & 0.00093 & -0.00158 & -0.00012 \\ -0.0001 & 0.00000 & 0.00092 & 0.00001 \\ 0.00002 & 0.00000 & -0.00056 & 0.00117 \end{bmatrix} \cdot 10^4 \cdot \begin{Bmatrix} Fz \\ Fy \\ Mx \\ My \end{Bmatrix}$$

It is possible to observe that the values outside the main diagonal are insignificant compared to those into it.

Finally, is possible to calculate the inverse of the Sensitivity Matrix and get the Calibration Matrix $[C]_{4 \times 4}$.

$$[C]_{4 \times 4} = \begin{bmatrix} 393.78 & -85.63 & -14640.62 & 1217.68 \\ -8.92 & 1071.01 & 2222.41 & 60.52 \\ 2.64 & -3.63 & 973.57 & -5.11 \\ -4.29 & -0.35 & 671.46 & 836.37 \end{bmatrix}$$

Values are in $[N/\frac{V}{V}]$.

Then, to calculate the forces and moments applied to the dynamometric load cell from the Voltage output, the calculations to be performed are as follows:

$$\{L\} = [H] \cdot [C] \cdot \{Ch\}$$

$$\{L\} = \begin{bmatrix} 523.21 & 762.70 & -92.16 & 655.36 & 578.50 & -85.63 \\ -43.37 & 2.84 & 1152.73 & -26.90 & 15.08 & 1071.01 \\ -9.57 & 22.17 & -3.91 & -8.04 & 15.26 & -3.63 \\ -76.83 & -76.85 & -0.38 & 62.74 & 61.20 & -0.35 \end{bmatrix} \cdot \{Ch\}$$

To check if the Calibration Matrix works and to evaluate the quality of its results, has been plotted the loads used for the calibration and the loads calculated with the Calibration Matrix from the Channels output voltages. The loads are constant in each interval because has been used the theoretical force estimated from the weights stretched in 1000 points.

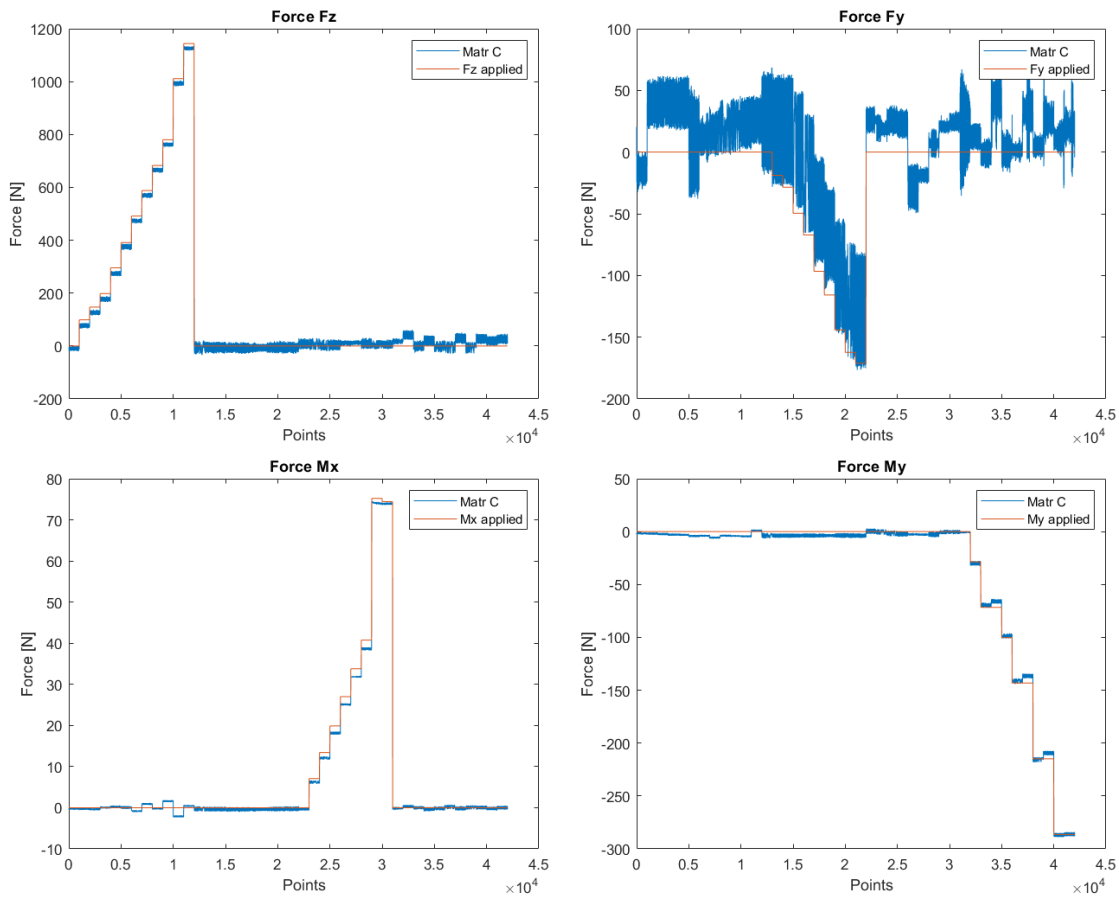


Figure 5.24: Calibration loads rebuilt using the Calibration Matrix

It can be seen from the comparison that the results from the matrix are not always precisely following the applied forces. In the plot of the calibration of the lateral force, F_y , there is a lot of scattering of the data. The latter is not due to the calibration matrix but from data received from the acquisition system: the output voltages of the lateral Channels are affected by more noise than other channels. This suggests using a capacitor with higher capacitance for the lateral channels in the amplifiers boards to reduce the noise.

5.7 Calibration using neural networks

Since the forces from the Calibration Matrix are not perfectly overlapping those applied experimentally, a second calibration method was carried out using the Neural Networks.

The software used to implement the neural nets, and for the subsequent analysis of the data, was the Deep Learning Toolbox of MATLAB R2022a.

Artificial neural networks, also called neural networks (NN) are computing systems inspired by the biological neural networks that constitute animal brains.

With neural networks, an attempt is made to bypass the linear mathematical process used in the previous chapter: the neural network itself finds a link between input and output in an initial training phase of the network.

The main advantage of using the NN consists in the capability of training not only on the data from the calibration with pure Forces and pure Moments but also from the calibration with coupled loads. Another important advantage consists in the handling of non-linearities, an intrinsic aspect of reality.

Additional calibrations were carried out with coupled loads. In particular, four tests were performed:

- (Fy&Fz) where Fy was variable and Fz constant
- (Fz&Mx) where Fz was variable and Mx constant
- (Mx&Fz) where Mx was variable and Fz constant
- (My&Fz) where Mx was variable and Fz constant

The calibration procedure was the same as previously described.

Another important aspect that has not been explored in this thesis is that having a sufficiently reliable load cell that can be used as a reference, it is possible to calibrate another simply by rigidly connecting them together and applying static and dynamic loads, pure and coupled. In this way, several coupled loads can be applied at the same time, and a large amount of data that can be considered 'exact' directly from the load cell used as a reference is available to train the network. This is in a short time and with low effort.

Unfortunately, in the case of this thesis, the force plate did not prove to be sufficiently reliable, and loads had to be applied with weights.

5.7.1 Neural Net Theory

A neural net is a structure for calculations made of multiple layers.

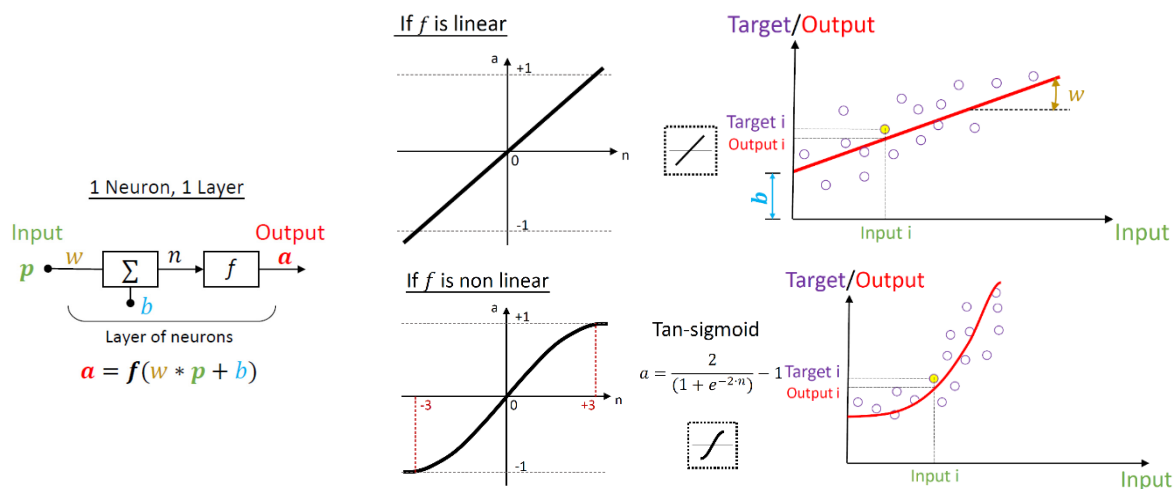


Figure 5.25: Example of NN

Considering this example of the simplest neural net possible. A layer is structured as in figure, it has an input and an output. Given p as the input, w is the weight given to the input, b the bias or offset. The transfer function f can be of different types (linear, tan sigmoid...) depending on the purpose. In this case, the NN is used for function approximation and, as suggested by MATLAB, the function used is the tan sigmoid.

During the training session, known inputs and outputs are given; the training algorithm is used to calculate the correct values to w , and b to best fit the data. Output is usually different from the target since is performed an interpolation of the data.

The way the training algorithm is structured is faster to use normalized data in a range from -1 to +1 so the NN performs a normalization of the inputs before the hidden layer and a back normalization of the outputs after the output layer.

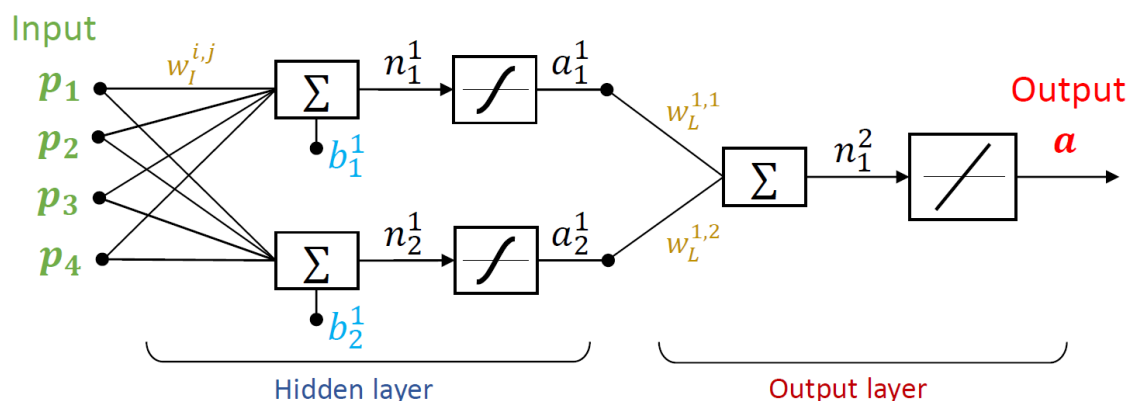


Figure 5.26: Scheme of NN with 4 inputs, 2 neurons in the hidden layer and an output layer of 1 neuron so one output only

In this case there is a matrix of the weights; each weight is multiplied with its input and the results are summed. The result is fitted in a tan-sigmoid function and the output are summed. The output layer is linear.

The user can only set the number of neurons in the hidden layer, the number of neurons in the output layer depends on the number of outputs.

The number of neurons in the hidden layer is chosen in order to fit the data. Too many neurons risk to result in overfitting of the data and the NN risks to lose plasticity (flexibility) on the output (different input sets give the same output). There is no rule to calculate the right number of neurons for the hidden layer, several attempts must be made to find the best value. The best value is the one that best estimates the output of the neural network but avoids the problem of overfitting. To overcome this issue is suggested to start solving the problem with a low number of neurons and in the later attempts increase it step-by-step.

Are described below the steps for the creation of a neural net:

- Data collection: must be known a set of inputs and their outputs (called target for the training);
- Creation of the structure of the NN (creation of the object)
- Configuration of NN defining number of inputs, outputs, number of neurons of the hidden layer;
- Weights w and bias b are initialized with random values;
- Training: the algorithm iterates and calculates the values of weights and bias in order to minimize the error between output and target;
- Validation or testing: are given to the NN new inputs and known outputs (not used during the training) and is calculated the error;
- The NN is ready to predict unknown outputs.

Training

Neural networks learn (or are trained) by processing datasets, each of which contains a known "input" and "target," forming probability-weighted associations between the two, which are stored within the data structure of the net itself. The training of a neural network is an iterative process conducted by determining the difference between the processed output of the network (a prediction using the weights and bias) and the target output. Is calculated the Mean Squared Error (MSE) between the two. If the MSE is higher than the one of the previous cycle, then the training must continue. The network then adjusts its weights and bias according to a learning rule (in this case is used Levenberg-Marquardt) and using this error value. Successive iterations will cause the NN to converge, producing output which is increasingly similar to the target output, reducing the MSE. There are two stopping criteria of the training: the number of validation checks and of epochs. Number of validation checks: when is found a possible minimum of MSE is stopped the training algorithm but the training continues by trying other values of weights and bias and this way evaluating if the minimum of the MSE is absolute or relative. If is found a lower MSE than the training algorithm is used again. The Number of epochs is the maximum number of iterations beyond which the NN is considered trained (can occur when convergence is slow).

When one of the two stopping criteria are satisfied, the training can be terminated, and the values of w and b are saved in the structure of the net.

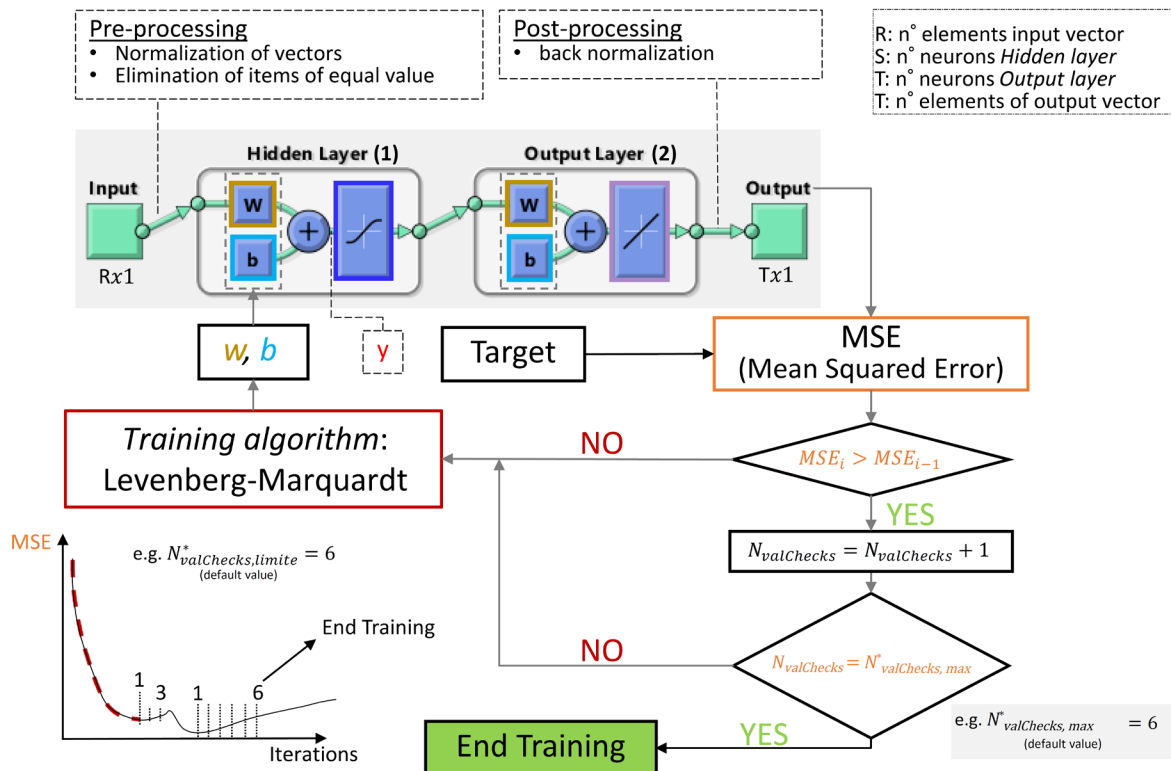


Figure 5.27: Training process

5.7.2 Implementation of the NN

Were followed two different methods:

- One NN to calculate all the loads using as input the four Virtual Channels;
- Four different NN, one per load to be calculated, using as input of every net the four Virtual channels.

It has been decided to give as input to the NN the four Virtual Channels instead of giving directly the six Channel voltages because the experience shows that for the NN is easier to find a pattern and solve the problem starting from less inputs more clearly connected to the outputs.

For this reason, for both methods were calculated, as previously explained, the Virtual Channels: using the geometrical Transformation matrix $[H]_{6 \times 4}$ previously calculated, from the product with the vectors of the Channels, were derived the Virtual Channels for each calibration test.

$$\begin{aligned} [vChFz] &= [H] \cdot [ChFz] & [vChFy\&Fz] &= [H] \cdot [ChFy\&Fz] \\ [vChFy] &= [H] \cdot [ChFy] & [vChFz\&Mx] &= [H] \cdot [ChFz\&Mx] \\ [vChMx] &= [H] \cdot [ChMx] & [vChMx\&Fz] &= [H] \cdot [ChMx\&Fz] \\ [vChMy] &= [H] \cdot [ChMy] & [vChMy\&Fz] &= [H] \cdot [ChMy\&Fz] \end{aligned}$$

Furthermore, as the NN requires a large amount of data to be trained and should also train on the noise of the input, all channel values for each load step were used (64000 values) and not just their average for every calibration test (as was the case with the calibration matrix where a load step is a point in the graph).

The matrix of Virtual Channels is then assembled in a matrix $[p]_{4 \times 64000}$ input to the NN.

The targets for the NN are different for the two methods: to the single NN are given as target all the loads together in a matrix; to the four NN were given as target one vector of loads each.

To exploit the capabilities of the machine learning were performed four additional tests with couple loads to train the NN to the behaviour of the load cell not only in “pure load cases”. The vector of the loads includes the additional calibrations with coupled loads: as can be seen in the figure before the 42000th point the loads are applied one at a time, after there are two loads at a time.

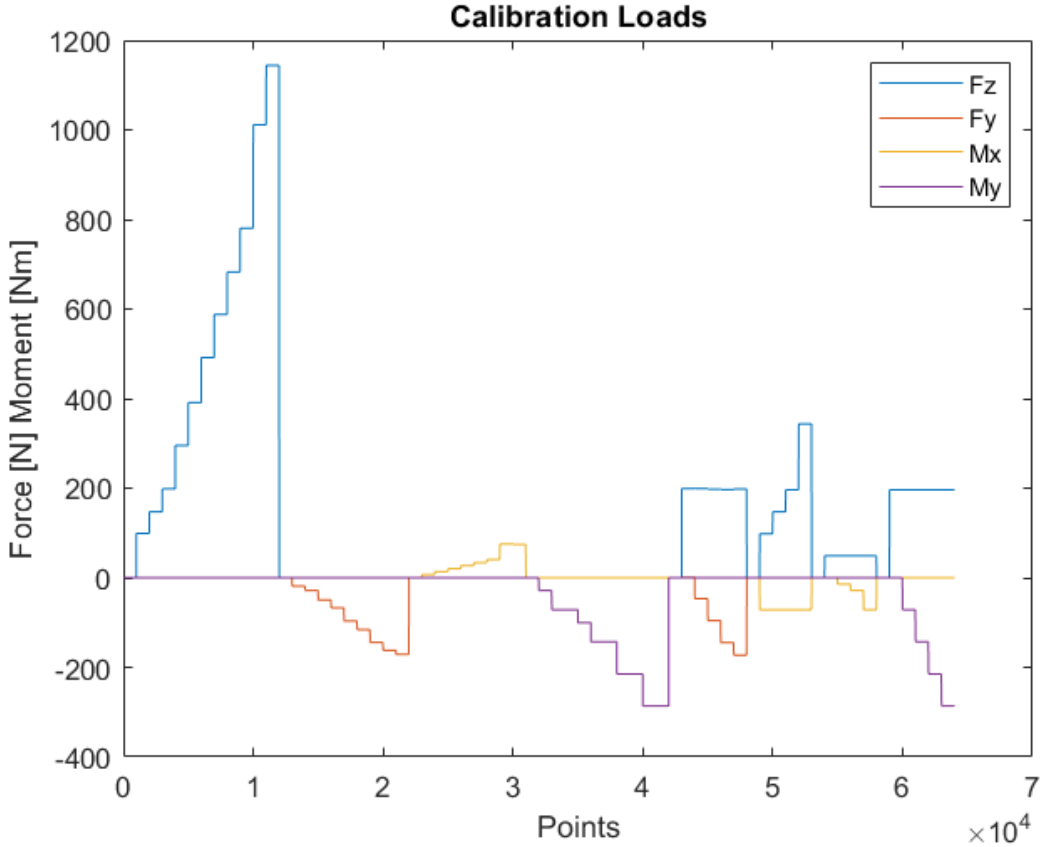


Figure 5.28: Loads used for the calibration with the NN approach

It is important to know that when a neural network is created the weights and bias are random values. These are changed during the training to minimise the MSE values. Since, these numbers are random, each network that is created is different from the previous ones (assuming equal network settings and equal input and target), therefore one network can reach the absolute minimum of the MSE and another can reach a relative minimum. For this reason, given the large volume of data, were generated a large number of networks (more than 30) and then picked the one with the lowest MSE on the validation data.

The code used to generate the Four neural networks case is described below.

```

599 % Matrix of the input to the NN (n°rows matr = n°input values)
600 p = [vChFz; vChFy; vChMx; vChMy; vChFy_Fz; vChFz_Mx; vChMx_Fz; vChMy_Fz]';
601 q=30; %Number of NN generated for each load
602 n=3; %Number of neurons of the Hidden Layer
603
604 z=0; %index
605 for w = ['1' '2' '3' '4'] % Create four NN. One for each load F1=Fx, F2=Fy, F3=Mx, F4=My
606     z=z+1; % For z=1 than Fz. For z=2 than Fy...
607     %% Input & target NN: matrices p & t
608     % Training with mask
609     t = Fcal_all(z,:); % Matrix of targhets for the NN (n°rows matr = n°targhet values)
610
611     for i= 1:q
612         %% Create Neural Network Object
613
614         net = feedforwardnet; %Generate NN of type feedforward
615
616         net.divideFcn = 'dividerand'; % Randomly divided dataset (default)
617         net.divideParam.trainRatio = 0.7; % Division of datatset (default)(use 70% of the data for the training)
618         net.divideParam.valRatio = 0.15;
619         net.divideParam.testRatio = 0.15;
620
621         % Setup parameters nntraintool
622         net.trainParam.max_fail = 6; % Number of validation checks to end training
623         net.trainParam.epochs = 1000; % Number max of epochs to end training
624
625         %% Configure and Initialize Shallow Neural Network Inputs and Outputs
626
627         net.biasConnect = [0 ; 0]; % Zeroing of the bias in Hidden and Output Layer
628
629         net.layers{1}.name = "Hidden";
630
631         net.inputs{1}.processFcns = {'removeconstantrows'}; %pre-processing configured net
632         net.layers{1}.size = n; % Number of neurons Hidden Layer
633
634         net.layers{2}.name = "Output";
635         net.outputs{2}.processFcns = {'removeconstantrows'}; %post-processing rete configurata
636
637         eval(['net' num2str(i) '= configure(net , p , t);']); % Initialisation w, b: net ready for training
638

```

Figure 5.29: Code for the creation of a NN part 1

Is first assembled the vector p , then set the number of neural networks to be generated and the number of neurons of each.

At line 605 is started a “for” loop, which will close at line 674 of the script. This will cycle for four times changing w from “1” to “4”. The output of this “for” loop will have four neural networks which will then be used for the estimation of loads.

At line 609 the load vector ‘t’ is created. This target vector will be for the NN that has to calculate vertical forces, Fz ; for the NN that has to calculate horizontal forces, Fy and so on. At line 611, a 'for' loop is opened, which closes at line 649. This loop will create 30 NN with the same settings, input and target. This loop is within the loop that is opened on line 605, so this will create 30 NN for each " w " equals to "1" "2" "3" "4" (the Four NN).

From line 612 to 638 the NN is created and set up. It is created the object NN and the dataset is divided randomly using the 70% of the data to perform the training (calculate in the iterations w and b), 15% is used for the validation (note that this data is different from the one used in training), 15% used for testing the performance of the NN out of the training phase. The number of validation checks and of epochs are defined. These two are the stopping criteria of the training.

On line 627, parameters called "bias" are removed. The bias in fact, as presented in the NN theory, are mainly responsible for the fact that null inputs ($v_{Ch_i} = 0$) correspond to non-zero load outputs. The neural network should therefore respect as much as possible the physical reality in which if the measured voltages are constant and equal to those of when the load cell was zeroed, then this is associated with the zero of the forces.

The network is then configured setting the number of neurons in the hidden layer, eliminating the items of equal values and giving to the network object the inputs 'p' and the target 't'.

```

638
639     %% Training Neural Network
640
641     eval(['net' num2str(i) ', 'tr' num2str(i) '] = train('net' num2str(i) ', p , t);]);
642
643     % Print Bias and Weights
644     eval(['net' num2str(i) '.b;']); % Bias NN
645     eval(['net' num2str(i) '.IW;']); % Weights of Hidden Layer NN
646     eval(['net' num2str(i) '.LW;']); % Weights of Output Layer NN
647
648     % doc net %To the Matlab Reference
649 end
650
651 %% Select NN with lower MSE
652 % Create vector of MSE of each NN generated
653 for j = 1:q
654     eval(['mse_f' num2str(w) '_v(j) = 'tr' num2str(j) '.best_vperf;']);
655 end
656
657 % Find lower MSE in the vector
658 eval(['mse_f' num2str(w) '_v_buono = min(mse_f' num2str(w) '_v);']);
659
660 % Change the name to the net with lower MSE
661 mse_v_f = eval(['mse_f' num2str(w) '_v']);
662 mse_v_buono_f = eval(['mse_f' num2str(w) '_v_buono;']);
663
664 for k=1:q
665     eval(['k' num2str(w) '=k; ']);
666
667     if mse_v_f(k)==mse_v_buono_f;
668         eval(['k' num2str(w) '=k; ']);
669         eval(['net_F' num2str(w) ' = 'net' num2str(eval(['k' num2str(w) ']) ' ');]);
670         eval(['k' num2str(w) '=k; ']);
671     end
672 end
673
674 end
675 %% Save the 4 neural nets and H matrix
676 save("neural_netsF.mat", 'net_F1','net_F2','net_F3','net_F4','H2');
677
678 %% Use Neural Network

```

Figure 5.30: Code for the creation of a NN part 2

At line 641 the NN is trained on the "t" vector.

The "for" loop on line 653 saves the validation MSEs of the 30 previously calculated networks in a vector of 30 rows. On line 658, the minimum value of this vector is taken, and in the "for" loop starting on line 664, with an "if" loop inside it, only the network with the lowest MSE of those calculated is saved in the MATLAB workspace. In line 675, a "neural_netsF.mat" is saved in the workspace with the four best NN inside, and the H matrix used to calculate the virtual channels.

The output from this script is then four NN for estimating one of the load components each.

This was the code to generate the four neural networks, one per load component.

The code to generate one NN to calculate all the loads differs only for the training vector: “t” is a matrix 4x64000 and gives for training the NN all four loads together.

```

599 % Matrix of the input to the NN (n°rows matr = n°input values)
600 p = [vChFz; vChFy; vChMx; vChMy; vChFy_Fz; vChFz_Mx; vChMx_Fz; vChMy_Fz]';
601 % Matrix of targhets for the NN (n°rows matr = n°targhet values)
602 t=Fcal_all;
603
604 q=30; %Number of NN generated for each load
605 n=3; %Number of neurons of the Hidden Layer
606 z=0; %index
607 for i= 1:q
608
609     %% Create Neural Network Object
610
611     net = feedforwardnet; %Generate NN of type feedforward
612
613     net.divideFcn = 'dividerand'; % Randomly divided dataset (default)
614     net.divideParam.trainRatio = 0.7; % Division of dataset (default)(use 70% of data for training, 30% for validation)
615     net.divideParam.valRatio = 0.15;
616     net.divideParam.testRatio = 0.15;
617
618     % Setup parameters nntaintool
619     net.trainParam.max_fail = 6; % Number of validation checks to end training
620     net.trainParam.epochs = 1000; % Number max of epochs to end training
621
622     %% Configure and Initialize Shallow Neural Network Inputs and Outputs
623
624     net.biasConnect = [0 ; 0]; % Zeroing of the bias in Hidden and Output Layer
625

```

Figure 5.31: Code for the creation of a NN part 3

Are generated 30 NN and of these 30 only the one with the lowest MSE is saved.

For the neural network with One network for all the loads, trying different numbers of neurons for the Hidden Layer, it was found that the optimal number of neurons is 2. This outcome resulted from the calculation of the MAE: for higher values of neurons the MAE increased greatly.

The MAE can be calculated according to the following relationship:

$$MAE = \frac{\sum_{i=1}^n |y_i - x_i|}{n}$$

where y represents the vector of 'true' values, x the vector of estimated values and n the dimension of the two.

For the Four neural networks it was found out, for the same reason, that the optimal number of neurons is 3.

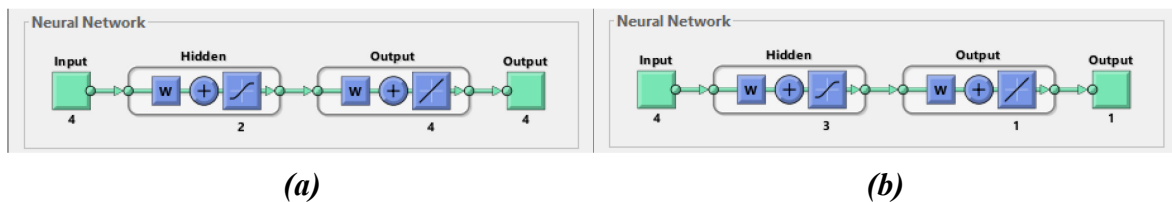


Figure 5.32: NN structure. (a) One NN for all the loads (b) Four NN: one for each load

5.8 Comparison between the calibration methods

To numerically assess the quality of the solutions three methods, Calibration Matrix, One NN for all Loads and Four NN, are compared.

It is necessary to compare the methods on new data, which has never been used for the generation of neural networks. It would be a conceptual error to use the same data used for training, because it is not correct to use the same data on which the networks were generated and optimised for evaluation.

A final test was carried out in which forces and moments were applied. The loads are all coupled to simulate the actual forces acting on the monoski foot. Moreover, these complex loads highlight the errors and weaknesses of each method much more than the 'pure' loads.

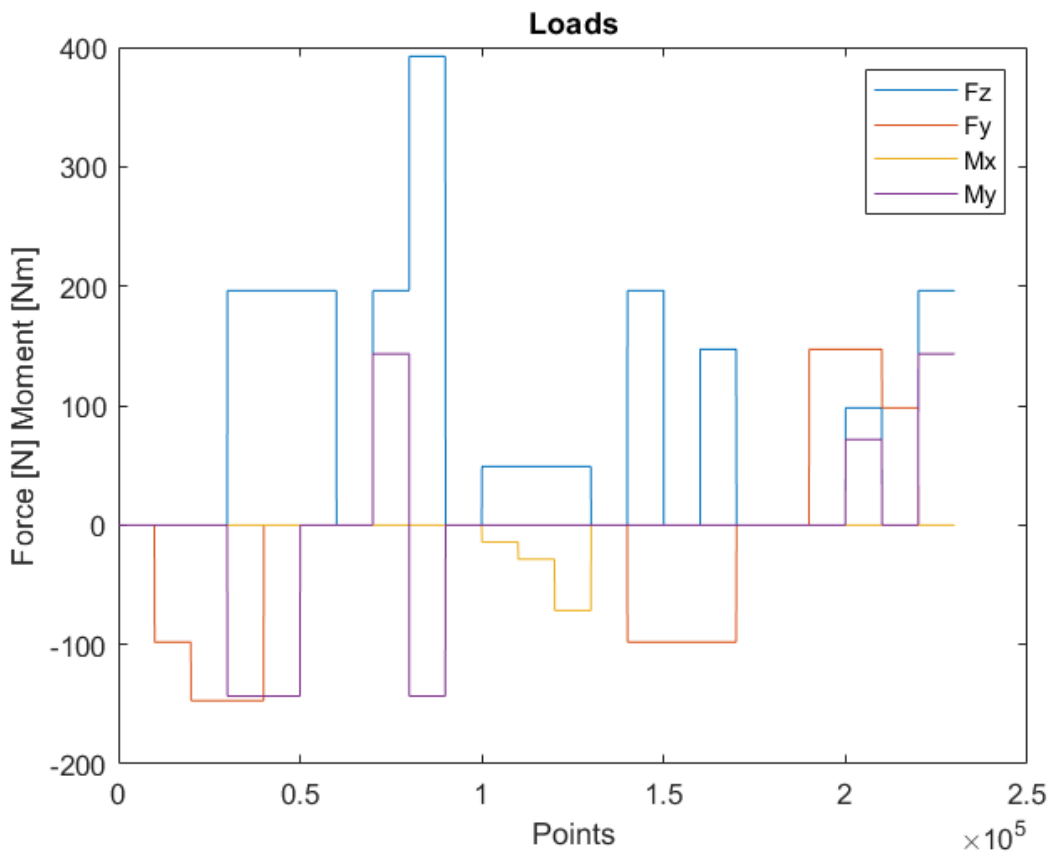


Figure 5.33: Loads to test the calibration methods

Is than asked to each method to rebuild the load components starting from the voltages of the Channels.

Another MATLAB programme was written to compare the different methods.

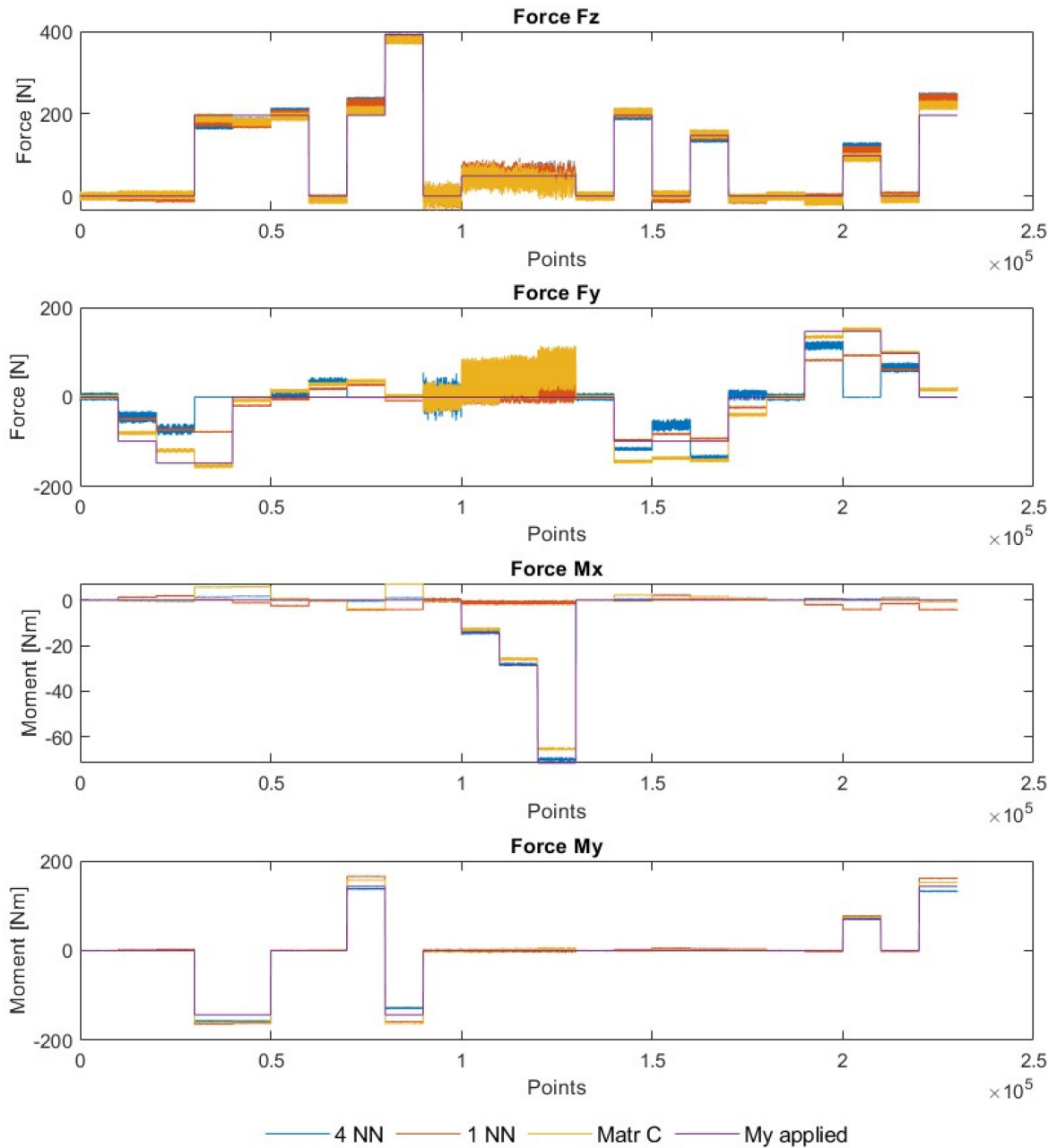


Figure 5.34: Results filtered using function 'movmean' value 5;

Fy due to the high noise is filtered using value 15

The graphs underline the complexity of extracting loads when there are several loads acting simultaneously.

From the Mx graph, it is obvious that the neural network with only One NN for all loads cannot follow the real pattern of loads. This is probably due to the fact that it is too complex for a single network to combine four inputs into four different outputs.

Overall, the load cell represents the acting forces well, except for the lateral load. For this load component, as already pointed out during calibration, the data are scattered and, in some cases, not representing the actual loads.

It can also be seen that between point 0.2×10^5 and 0.5×10^5 , when are applied all together Fz, Fy, My, that not only the different solution methods struggle to follow the loads applied, but also the lateral Channel is loaded when the force Fz is added. It shows that probably due to the bending of the load cell beams, vertical deformations are also transferred on the strain gauges applied on the side.

To numerically assess the quality of the solutions, the MAE (Mean absolute error) parameter can be used.

This indicator is often used in statistics to measure the error between two different data sets (predicted and observed) describing the same phenomenon as time varies.

	<u>MAE_Fz_[N]</u>	<u>MAE_Fy_[N]</u>	<u>MAE_Mx_[Nm]</u>	<u>MAE_My_[Nm]</u>
4 NN	9.1209	28.146	0.53486	2.7799
1 NN	10.806	24.382	6.239	5.7344
Matr C	9.2365	22.042	1.823	4.3417

Table 13: MAE results for each load component using the calibration methods

As can be seen from the table, the MAEs numerically confirm what is seen visually in the graphs; the NN with Four networks has lower errors than the calibration matrix, while the neural network with One network has higher deviations. The MAE are average deviations in N or Nm from the applied loads so it can be said that these errors, if compared to the magnitude of the loads, are negligible.

In the future, further data and more coupled loads can be used to train the network to try to improve the results and especially to analyse its behaviour on completely new loads (and thus inputs).

Thanks to the NN can be obtained better results than with traditional methods (in this case first order calibration equations); in addition, even unexperienced users can quickly perform the calibration using NN using ready-made code achieving good high-quality results.

This innovative method has not yet been widely used in the field of mechanics, but in the future there will probably be widespread use as already happens in other fields.

5.9 Limits of the load cell

Since the original design of the foot has been changed, has been decided to verify the maximum loads that the load cell can withstand.

Verification was carried out by simulating in ANSYS Workbench the loads conditions. [16] Were considered the maximum loads measured in the tests on the slopes by Matteo Ferrari (2015) and Dario Vanzetto (2017).

Vanzetto tested a high-level Paralympic skier doing giant slalom. Since the accelerations and thus forces produced by the skier are key factors in the performance, then as expected Vanzetto had bigger values of loads. Vanzetto could not measure M_y with his instrumentation so was used the data from Ferrari.

Considering these characteristics of the material of the cell.

Ergal Alloy 7075-T6		
Density	2.81	[g/cm ³]
Tensile strength, Yield (Proof)	430 ÷ 480	[MPa]
Ultimate tensile strength (UTS)	510 ÷ 540	[MPa]
Elastic modulus / Young's modulus	72	[GPa]
Poisson's ratio	0.33	[g/cm ³]

Table 14: Mechanical properties of the material of the load cell

The loads used in the simulation are:

- $F_z = 2500 \text{ N}$
- $F_y = 160 \text{ N}$
- $M_x = 80 \text{ Nm}$
- $M_y = 300 \text{ Nm}$

The structure of the load cell is symmetric but the moment is an antimetric load. Therefore is not possible to conduct the simulations on only half structure. As can be seen in Figure 5.35, to consider the additional stiffness due to the frame of the sitski is added the cubic-shape part bolted on the load cell.

Applying all the loads together on the load cell simulates the maximum load that might occur during normal skiing.

The loads were applied at the reference system of the load cell. The results show that the maximum principal stress is reached in the chamfer of the windows on the sides of the load cell. The peak of the stress is about 390 MPa.

This value is very close to the yield stress of the aluminium.

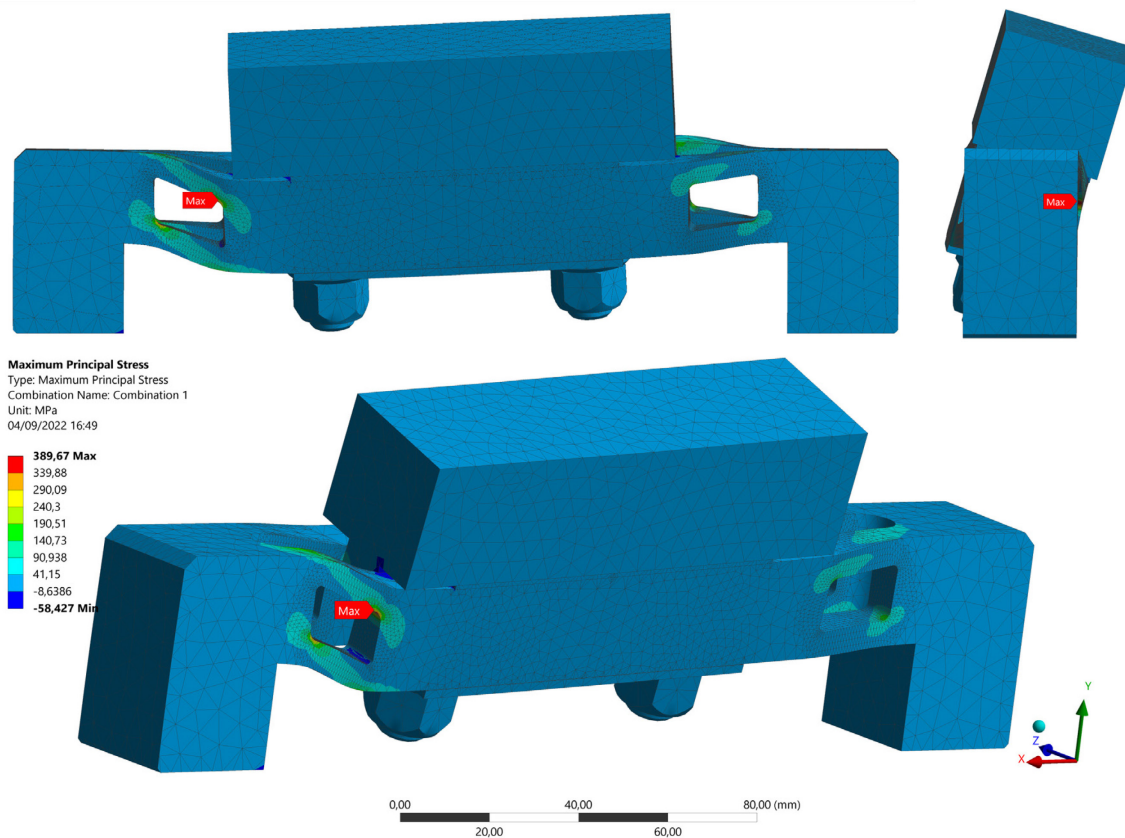


Figure 5.35: Results of FEM simulation

This shows that a competitive skiing almost reaches the maximum possible stress before producing a permanent deformation of the cell.

The loads produce a maximum deformation of 0,34 mm on the top of the cubic part.

Thanks to the linearity of the analysis is possible to calculate the maximum deformation of the lower part before it becomes permanent. This could be useful to design a load cell saver: a structure to avoid yielding the material when overloading the cell.

A possible future improvement of the load cell to solve this issue can be to rebuild the load cell in a stronger material in order to be able to measure extreme jumps performed by heavy skiers without deforming the structure. This is very important to know the maximum loads that can happen in extreme conditions.

A valid solution can be using titanium: it has much higher yield strength so can resist higher stresses. Titanium also would not affect the sensibility of the cell because thanks to an elastic modulus not much higher than the one of the aluminium, provides sufficient deformability to be measured by the strain gauges. This makes the titanium perfect for a future load cell (without changing the geometry) [17]. Since it is a metal very difficult to machine, the geometry would be 3D printed using an electron beam melting machine.

6 ACQUISITION OF DAMPER STROKE AND SPEED

To measure kinematic data of the suspension in field tests has been considered to use a position sensor. Since the mechanism is a four-bar linkage with a damper, the measure of an angle of a beam or a distance between two joints is enough to solve the rigid system.

Has been decided to measure the stroke of the damper because meaningful.

Were considered three possible types of sensors and technologies to measure the stroke:

- Magnetostrictive potentiometer (LVDT);
- Resistance potentiometer;
- Laser.

The use of the laser system was excluded first due to its fragility and sensitivity to vibration. Is a non-contact sensor but has the issue that an object (like the snow) can block the laser beam.

6.1 Resistive potentiometer

A slider potentiometer consists of a resistive element and a sliding contact (wiper) that moves along the element making electrical contact. In this device, the resistance between the contact and one end terminal is proportional to the distance between them. In the acquisition system the potentiometer is than considered as a variable resistance

Potentiometers however have the issue to be hardly waterproof when used for high speed movements. Since for this thesis having waterproof instruments is mandatory, the resistance potentiometer has been set aside.

6.2 Magnetostrictive potentiometer

A linear variable differential transformer (LVDT) measures the distance between a position magnet and the head end of the sensing rod. The sensing rod is mounted along the motion axis to be measured, and the position magnet is attached to the member that will be moving. The head includes an electronics module, which reports the position information to a controller in the appropriate analog or digital format.

The linear variable differential transformer has three solenoidal coils placed end-to-end around a tube. The center coil is the primary, and the two outer coils are the top and bottom secondaries. A cylindrical ferromagnetic core, attached to the object whose position is to be measured, slides along the axis of the tube. An alternating current drives the primary and

causes an electromotive force to be induced in each secondary proportional to the length of the core linking to the secondary due to the mutual induction.

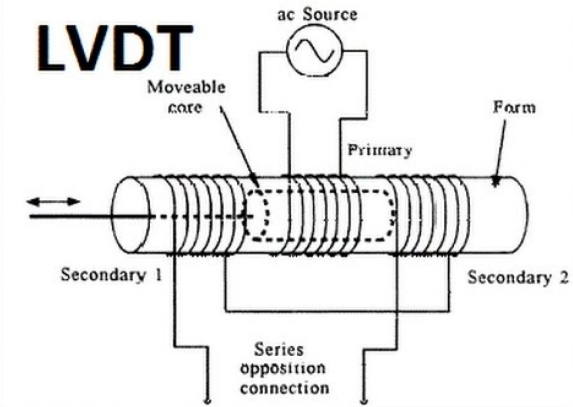


Figure 6.1: LVDT construction

The signal processing to obtain the output is explained in figure:

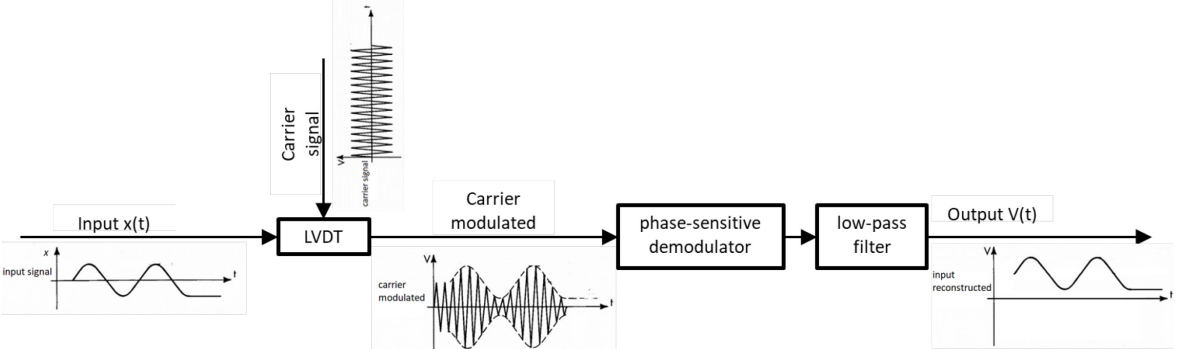


Figure 6.2: Signal processing LVDT

An advantage of the LVDT sensor, over other types of linear position sensors, is the ability to read the position magnet even when there is a barrier between the position magnet and the sensing rod. This is why this technology is preferred to the resistive for the ability, of the first one. This is the main advantage of the LVDT and it allows to use it in every condition, even with snow colliding the sensor, as in this thesis work case.

The LVDT transducer should be protected from ice as it could at the least cause the transducer to seize but could in extreme cases cause the transducer to be damaged. The sensor can be used well below freezing but it must be dry.

As can be seen in the signal processing (Figure 6.2), few processing functions are needed. To have a more portable sensor and eliminate the need for calibration and additional equipment, reduce the setup time as well as overall system cost the DC models were selected. Also all the other sensors on the monoski are DC.

6.3 Model used

The TTX race shock absorber model is custom made by Öhlins for Tessier. Research revealed that the maximum stroke is 100 mm [18]. To put the sensor in parallel with the shock absorber, the latter must have the same or greater stroke.



Figure 6.3: Öhlins TTX shock absorber

Due to the difficult availability and high cost of an LVDT with these characteristics, a cheaper resistance potentiometer was chosen. Water resistance is ensured by placing the sensor inside a waterproof box or bag.

A potentiometer with a smaller stroke (80 mm) was available at Mid Sweden university (KTC Pulling Rod Type) [19]. Having a smaller stroke of the damper meant that, in order to avoid damaging the sensor, it could not be fixed in parallel with the damper but on another point of an arm using a clamp (Figure 6.4). This setting furthermore creates a new issue: the sitski cannot be opened to get the lifter with the potentiometer fixed in that position.

The first few times they were used, the potentiometers presented a signal with some noise in dynamic measures. This is due to dust and dirt that can accumulate on the sliding contact over time and produces the wiper to vibrate on the contact. The noise became negligible after a few days of use.

The possible drops of tension due to the uneven contact between the wiper and resistive element were not present, as can often happen with fast movements: usually with slow potentiometers there are lost signals when the tension drops to 0 V.

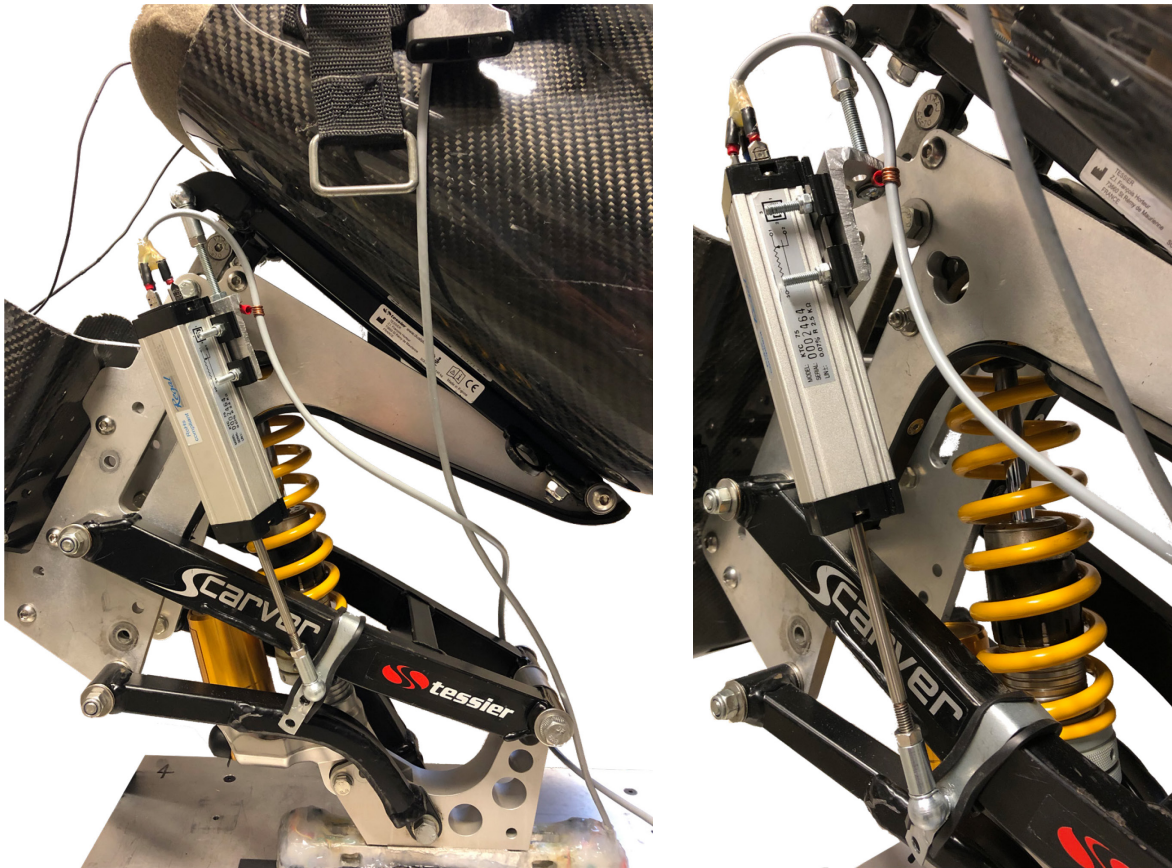


Figure 6.4: Linear potentiometer fixed on the monoski

6.3.1 Calibration of linear potentiometer

The resistive potentiometers the way they are constructed they have a linear behaviour by definition. This has been verified measuring the stroke with a calibre and acquiring the output, the results are shown in this graph.

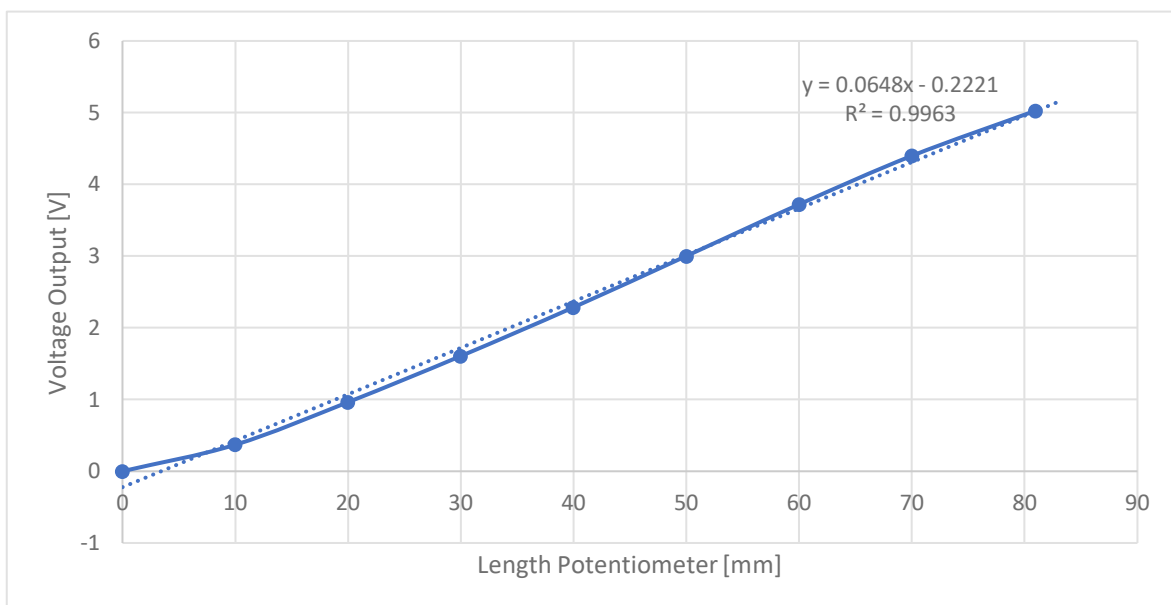


Figure 6.5: Linear interpolation of the signal from the potentiometer

The function was then used in MATLAB to calculate the stroke from the acquired signal. In order to describe the kinematics of the monoski, the relationship between the ground clearance of the seat bottom and two points of the frame was also measured.

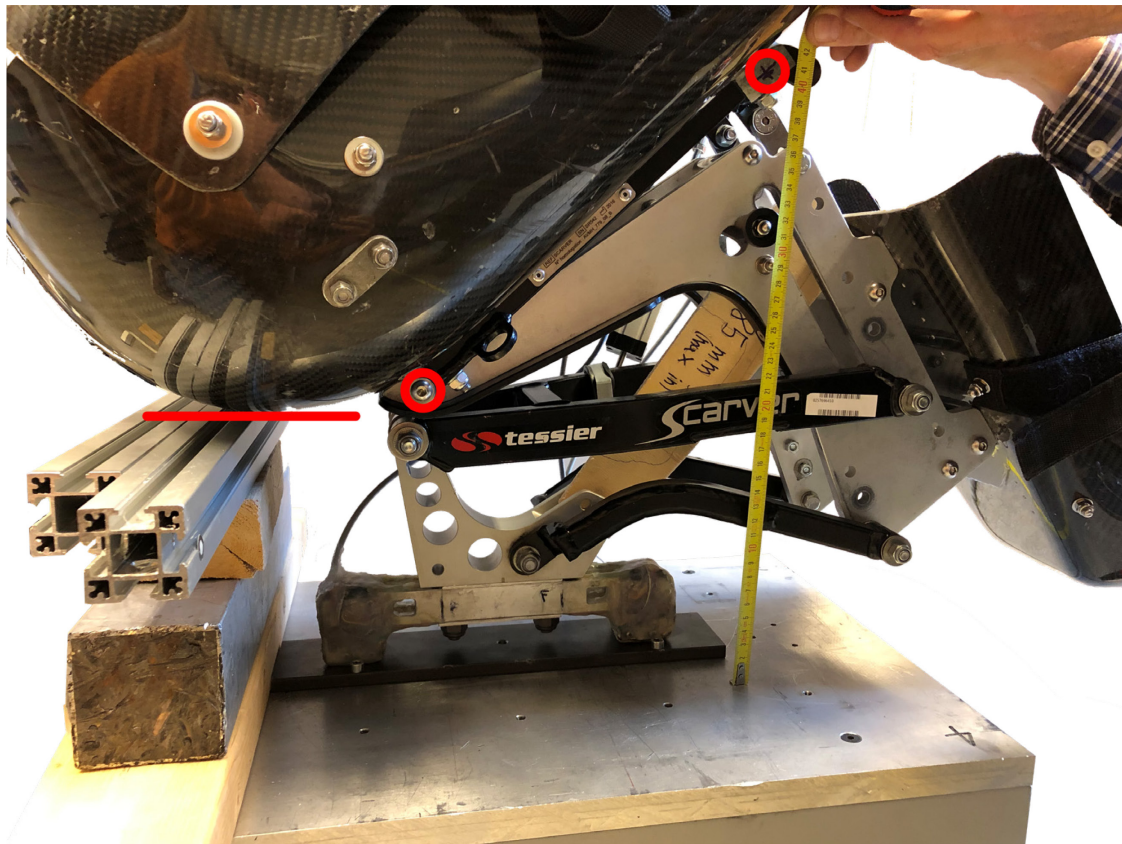


Figure 6.6: Calibration of the height of the seat. In red are the measurement points

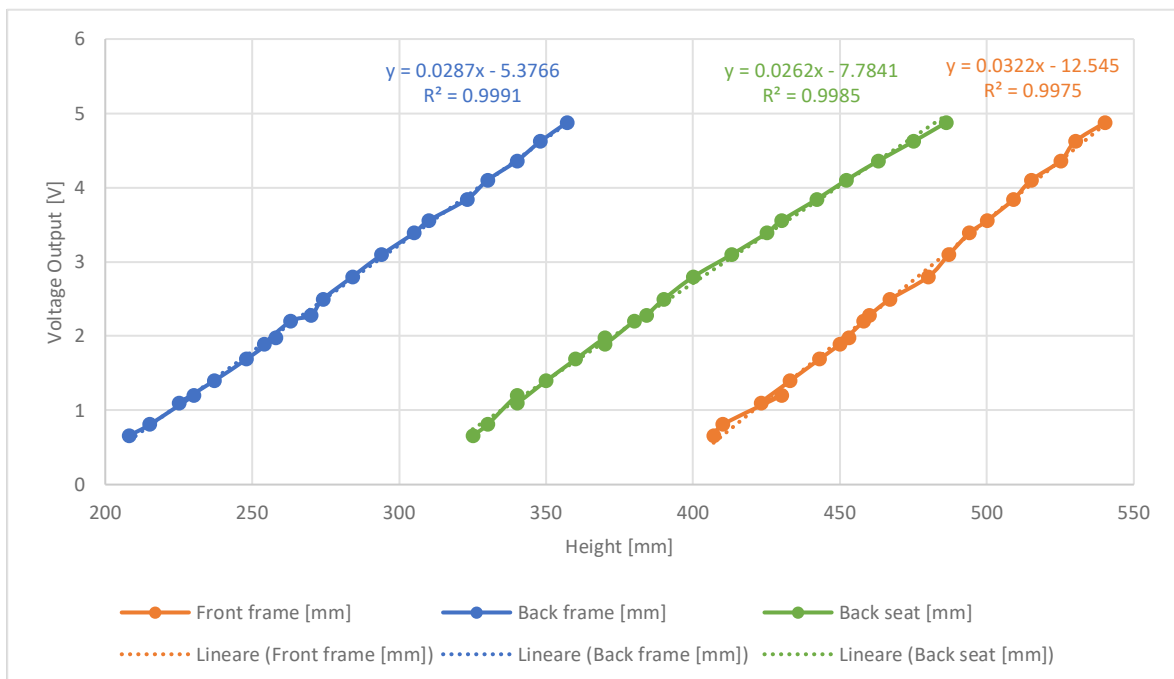


Figure 6.7: Results of the calibration of the height of the seat and their linear interpolation

7 GYROSCOPE

A MEMS analog dual-axis gyroscope is used to measure the rotational speed [dps] of the seat or skier (LPY4150AL) [20].

This sensor was introduced to measure the lateral inclination of the monoski (roll) during the run to recognise the various phases of skiing.

The gyroscope has four outputs: dual-axis rotational speed amplified and not.

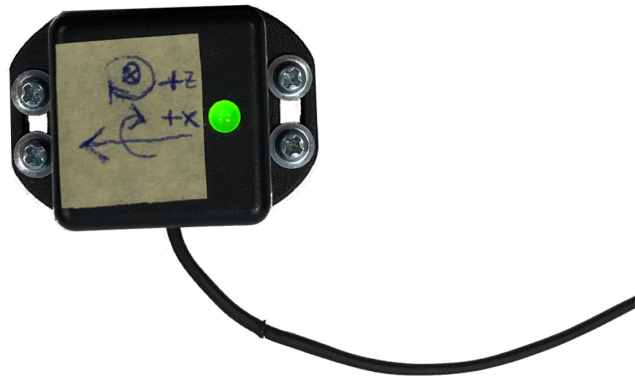


Figure 7.1: Gyroscope and reference system

The calibration constants are found in the datasheet.

Since the gyroscope measures rotational speeds and not rotations, it is necessary, in order to obtain the desired information, to integrate the data.

This processing of the results has been done in MATLAB: once cancelled the offset, the rotational speed [dps] is numerically integrated using the function `cumtrapz` obtaining a rotation [deg].

By numerically integrating noise in the signal, however, it can happen that it adds up: since integrating corresponds to adding areas, even a small offset or noise (which in the case of a gyroscope can be a vibration, for example), can lead to an uncontrolled drift of the result.

Gyroscopes should theoretically not be subject to accelerations but, due to the reality of sensors, accelerations (and in particular vibrations) produce noise in the signal.

During testing, it was realised that this is a serious problem with the gyroscope.

Two methods were tried to correct the drift of the signal, considering that the sensor thus starts and finishes the acquisition with the same orientation:

- use a line between the first and last data points. However, this method only works well when the offset from zero is low, and the drift is constant.
- Linearly interpolate all points to follow the trend of the data. However, this method has the problem that the drift is sometimes not constant, so a linear interpolation cannot follow this trend. In these cases, attempts have been made to use higher degrees for the interpolation.

An example is given here where neither method gave good results: the skier moved in the seat of the monoski introducing vibrations and accelerations that are read as false rotations by the gyroscope. The sensor started and finished in the same position than with the same angle.

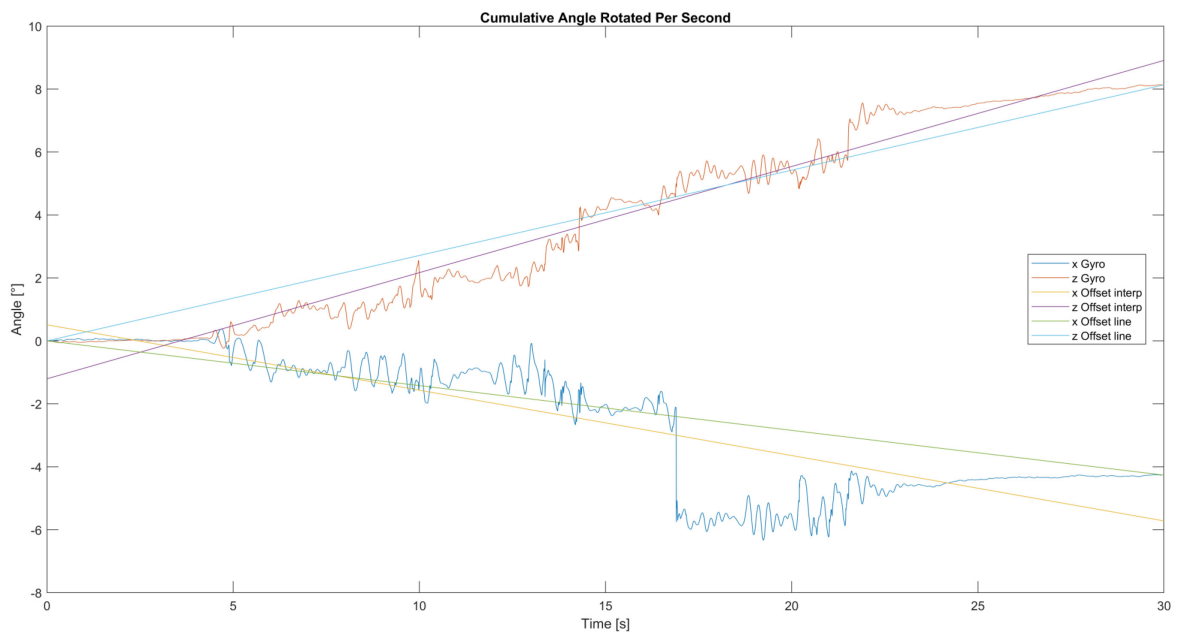


Figure 7.2: signal after being integrated, lines of the two methods to cancel the drift

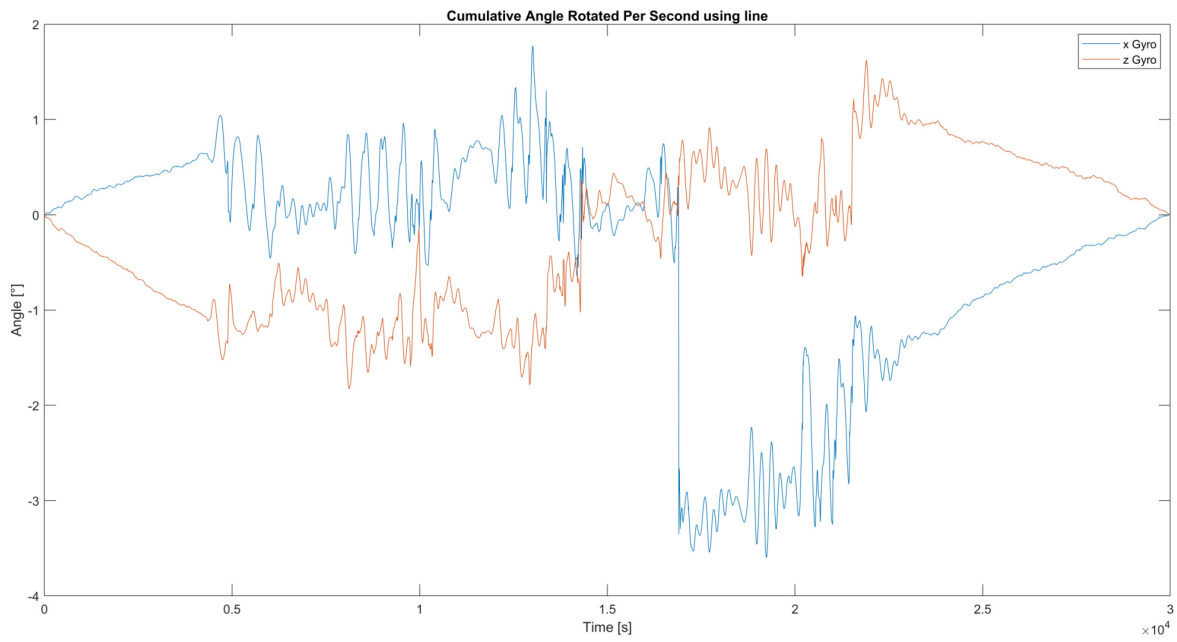


Figure 7.3: signal after using the line method

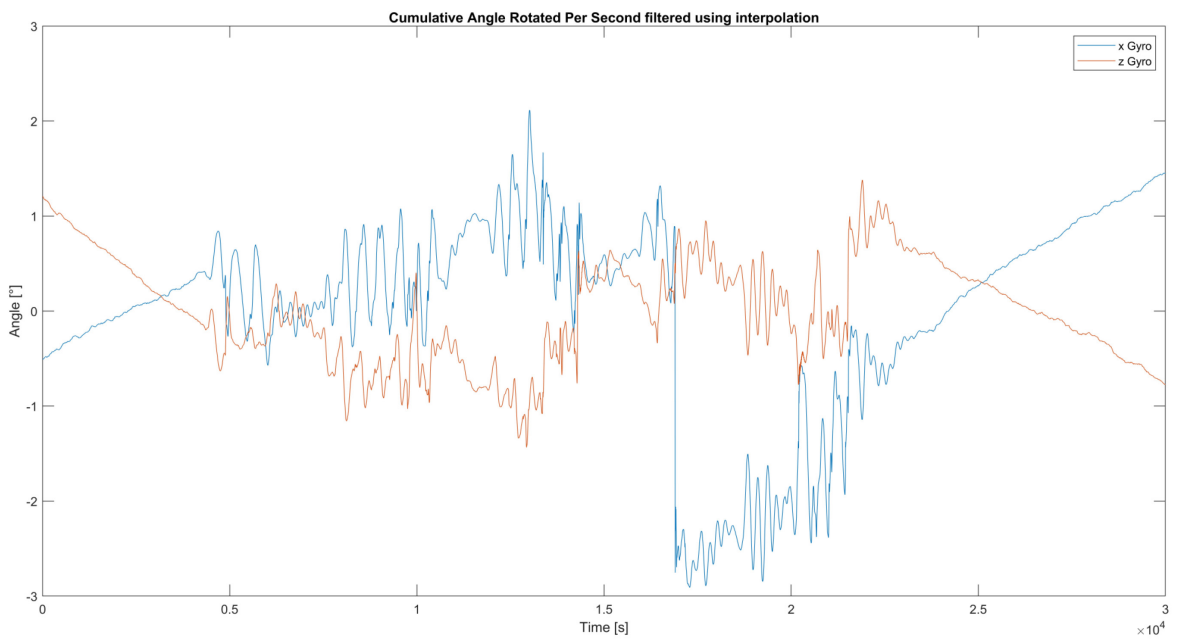


Figure 7.4: Signal after using the interpolation method

8 ACCELEROMETERS

Two triaxial accelerometers were used to measure kinematic data of the seat and the skier. To achieve good sensitivity and, at the same time, a high range, two capacitor MEMS accelerometers were used, one 3-axis with a range of ± 2 or ± 6 g (LIS344ALH) [21], the other with a range of ± 200 g (ADXL377) [22].

The first has a dynamically user selectable full-scale of ± 2 g / ± 6 g by changing an external resistance. In this work has been chosen to use the wider range of ± 6 g.

The two accelerometers are placed in a box with a Red Led.



Figure 8.1: Accelerometers and reference system of each

The calibration constants are found in the datasheet.

To fix the accelerometers and the gyroscope was used an aluminium plate bolted on the frame of the monoski.

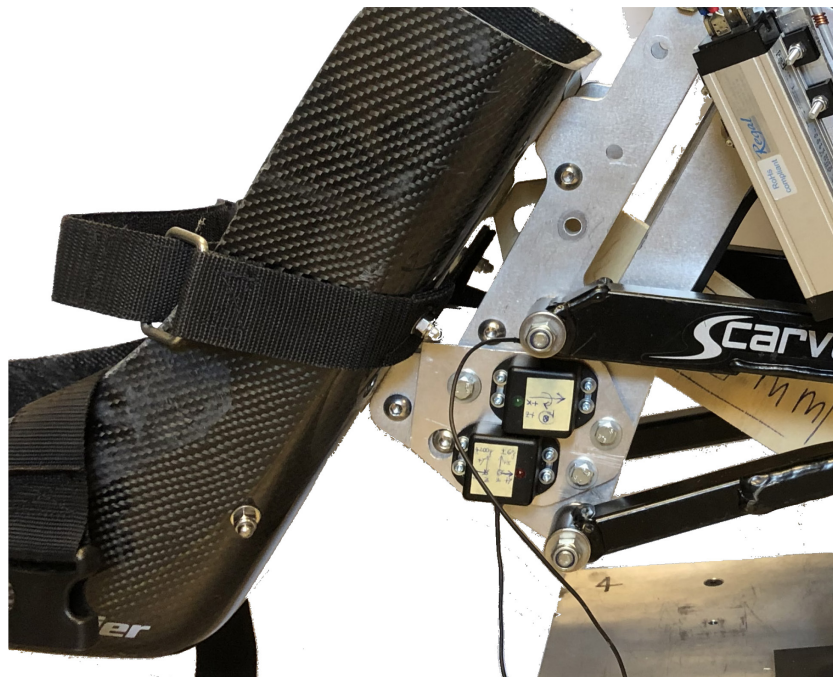


Figure 8.2: Accelerometers and gyroscope fixed on the monoski

9 DATA ACQUISITION HARDWARE

Given the need for a portable system, it was thought to use a modified Arduino board. However, due to the large amount of data acquired and to be saved, this option was discarded because the Arduino does not have enough computing power.

It was therefore decided to use the NI USB-6210 [23] module connected to a laptop as the DAQ.

The NI module is compact and portable; however the issue with this setup is that the NI module needs to be constantly connected to the computer, so, for the field tests, both the laptop and the module must be in the backpack of the skier.



Figure 9.1: NI USB-6210 module

The sampling rate is 250 kS/s and the maximum number of analog inputs is 16.

The number of analog inputs revealed to be not enough to connect all the channels of all the sensors used. Only because the tests were carried out in the controlled environment of the laboratory, it was decided not to check the power at the bridges of the load cell (5 V) and the reference voltages of the load cell (2.5 V), so that all other channels could continue to be acquired.

For the field tests, four setups were prepared by not acquiring some channels or disconnecting a sensor. In field tests, it is recommended to check the voltages of the load cell because any drift in these due to the draining of the battery or other issues could spoil all the data.

10 DATA ACQUISITION SOFTWARE

LabVIEW 2019 SP1 was used to programme and acquire the data.

The National Instruments module was programmed using LabVIEW [24]. It is a visual programming platform with functional modules. In the programs the actual functionality of the acquisition system is designed, and has a user interface like a control panel of a hardware device (Front Panel).

In addition, to the sensors, a box with a triggering button and two LEDs (Green and Red) was also connected to the digital input and output ports of the module. It is needed to start the acquisition without having to take the laptop out of the backpack on the ski slopes.

The black box with the red light connected to the external battery (7.5 V) is a voltage regulator to power all the sensors (5 V) besides the load cell with its own internal regulators. It was necessary in order not to connect all sensors to the DAQ, as this would have drained the laptop's battery very quickly.

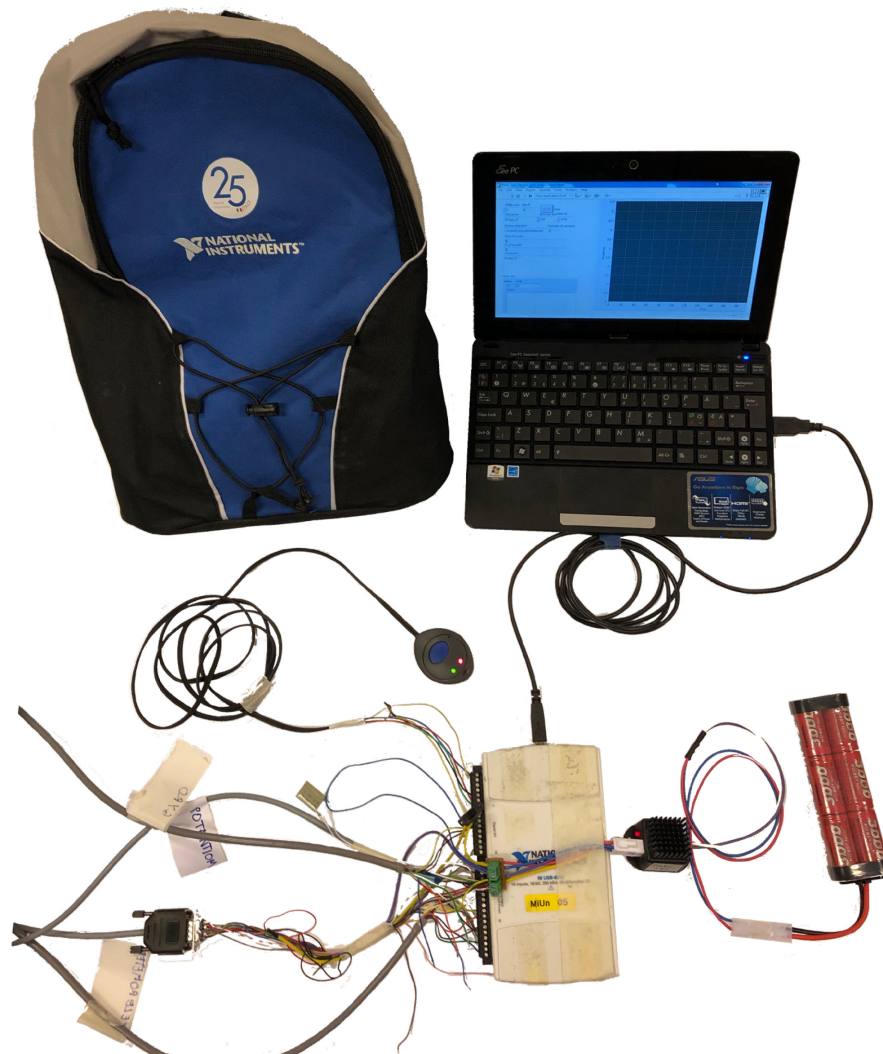


Figure 10.1: Acquisition setup for an outdoor test

Four programs were prepared, one for each different setup of sensors, then channels connected to the module.

Here is the description of the program designed to connect the load cell, potentiometer, accelerometers, gyroscope.

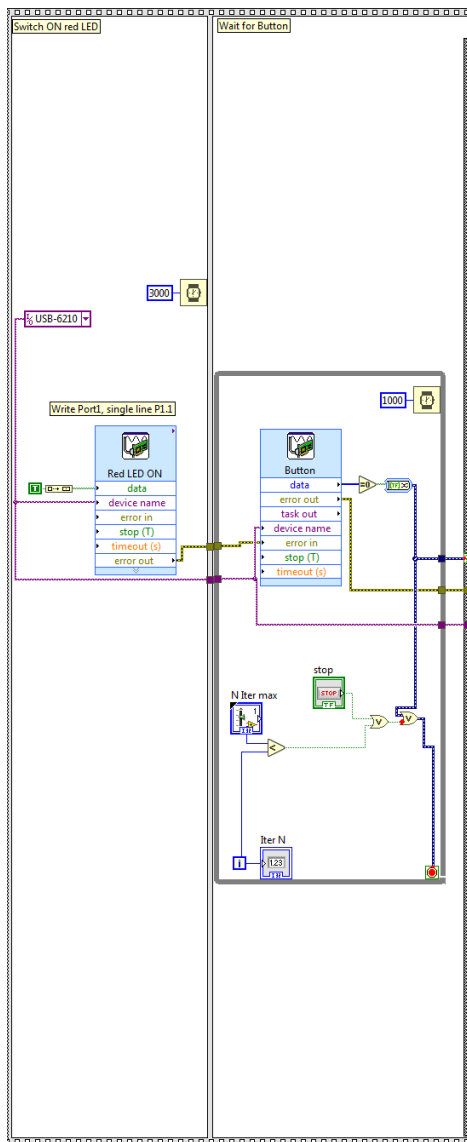


Figure 10.2: LabVIEW program
part 1

The program has been organized in boxes for greater clarity. LabVIEW uses a visual programming language so each operation is an object that can be taken from the library.

In the first box, the name of the module is set and the Red LED light up to inform the user that the programme is running properly.

The small blue box is a so called DAQ Assistant and is used to communicate (read or write analog or digital signals) with the DAQ module. In this case is producing a digital input. (digital 1 on Red LED line)

In the second box there is a 'while' loop that waits for the button to be pressed (digital input TRUE) to start the acquisition.

Stopping can be done either by pressing the button, or when the button has not been pressed for too long, or with an emergency stop button on the front panel.

All the following part is contained in an 'if' box so that if the trigger button has been pressed than the rest of the programme is executed, otherwise, the program stops, the LED turns off and displays an error message on the laptop.

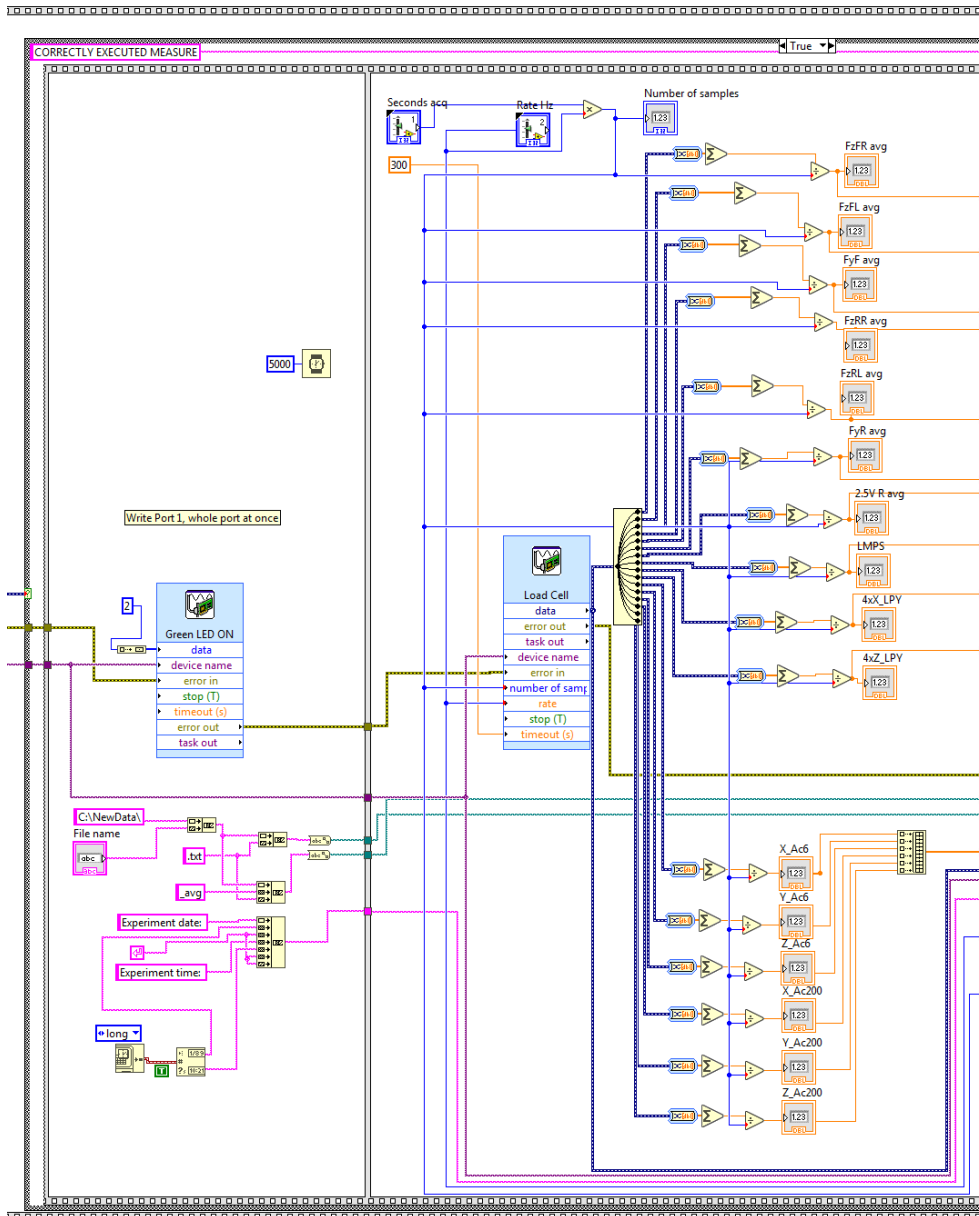


Figure 10.3: LabVIEW program part 2

In the third box only the Green LED is turned on to inform the user that the DAQ is acquiring. The name of the file is built using the name of the file typed by the user in the front panel, the date and time is registered and will be printed in the header of the file.

The next box is the main of the program: the DAQ acquires the signals for the time and at the rate set by the user. The ports to be acquired are set in the DAQ Assistant configuration. The signals (in Volt) acquired are split to calculate and display the average of each.

To keep the programme simple has been decided to stop the acquisition with the time and not using the button. This also avoids having to check the status of the button at each acquisition cycle, saving computing power.

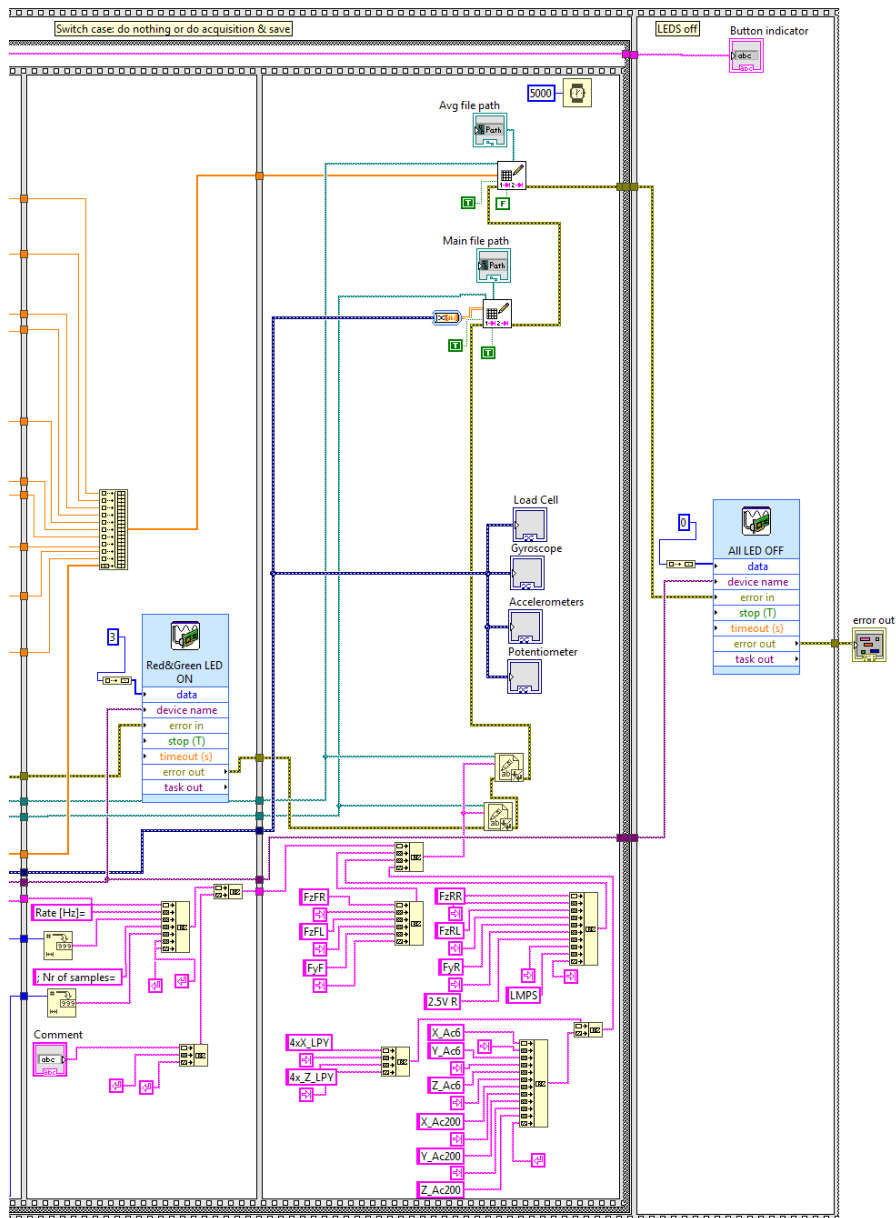


Figure 10.4: LabVIEW program part 3

In the fifth and sixth box the header of the file is automatically created and assembled with the date and time, the rate used, the number of samples and the comment typed by the user.

Is created the header of the table of the data with the name of the channels.

The Red and Green lights are on to inform the user that the acquisition is ended and the DAQ is busy saving the data. Are created two separate files .txt in the same folder, one with all the data, the other with the average of the measurement in the time. This last function speeded up the calibration of the load cell.

On four graphs are plotted the raw data of the channels.

Finally, the LEDs are switched off and any errors that may have occurred are displayed.

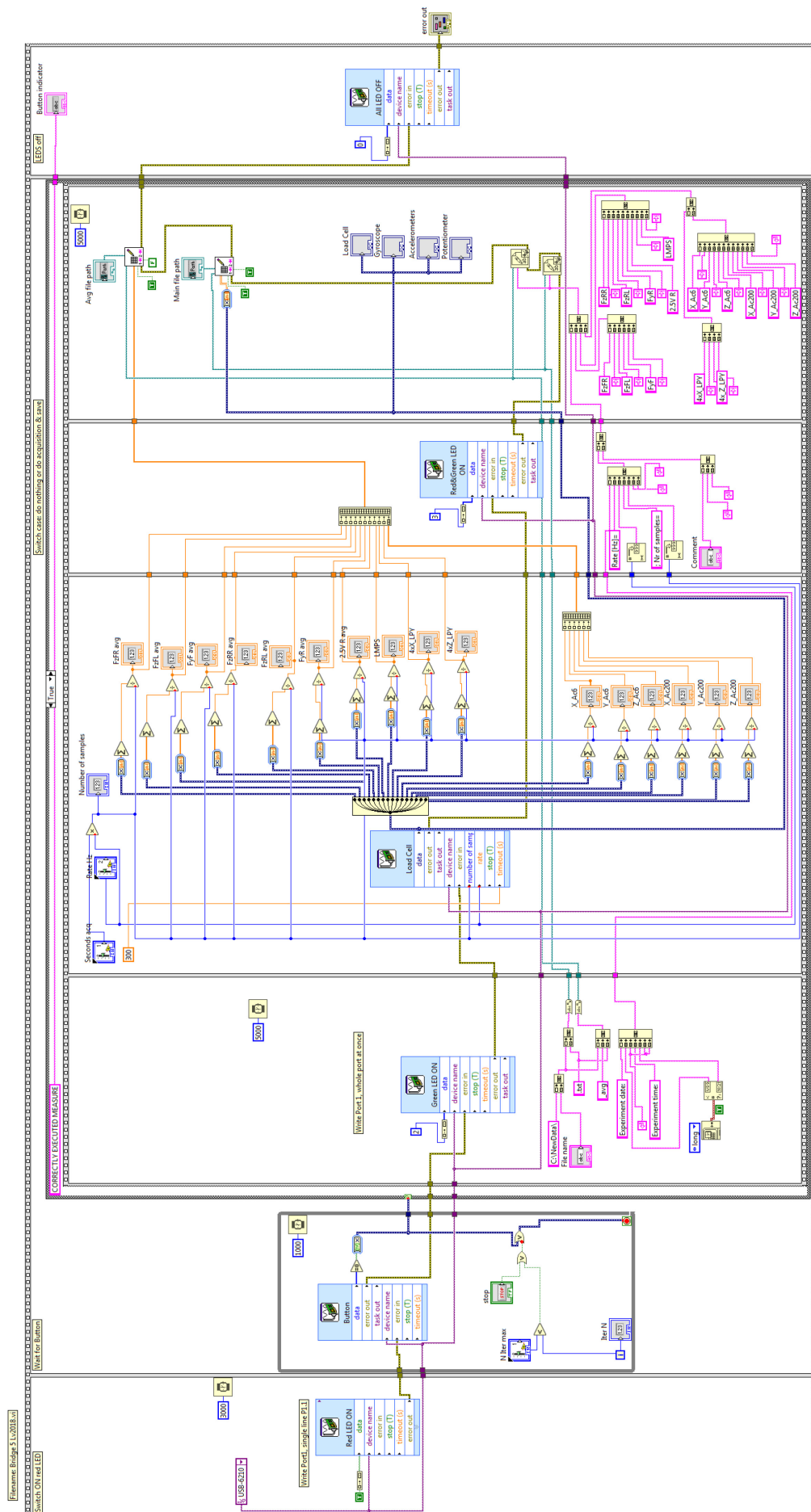
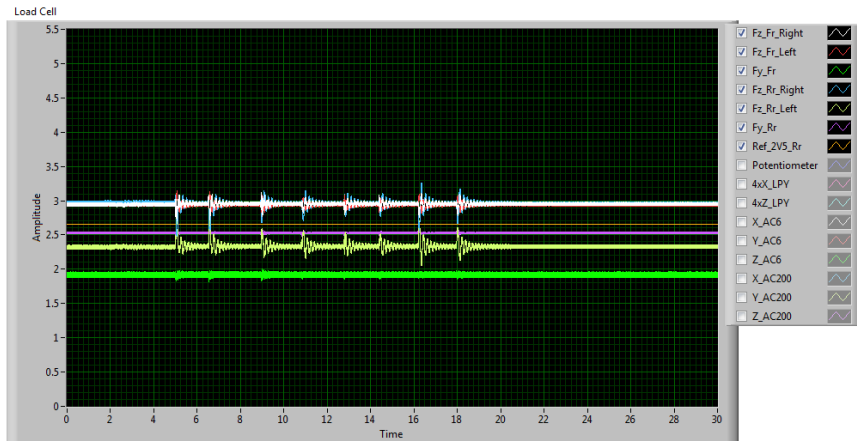


Figure 10.5: LabVIEW program

N Iter max Iter N **STOP** stop
 File name Seconds aco Rate Hz
 Button indicator Number of samples
 Main file path
 Avg file path
 Comment
 error out
 status code
 source
 FzFR avg FzRR avg
 FzFL avg FzRL avg
 FyF avg FyR avg
 2.5V R avg
 Mancano:
 2.5V F avg
 5V F avg
 5V R avg
 perche'scollegati



LMP5 4xX_LPV X_AC6 X_AC200
 4xZ_LPV Y_AC6 Y_AC200
 Z_AC6 Z_AC200

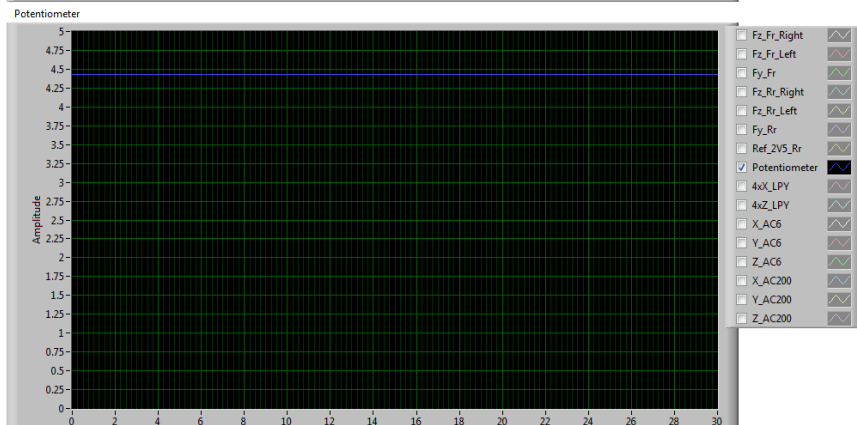
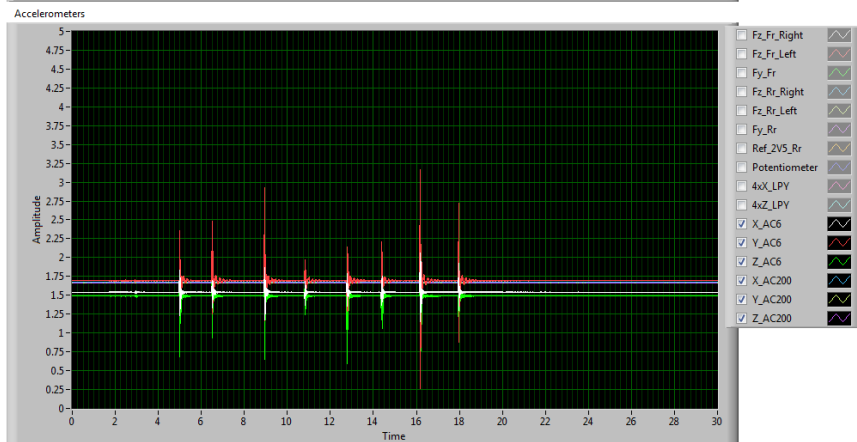
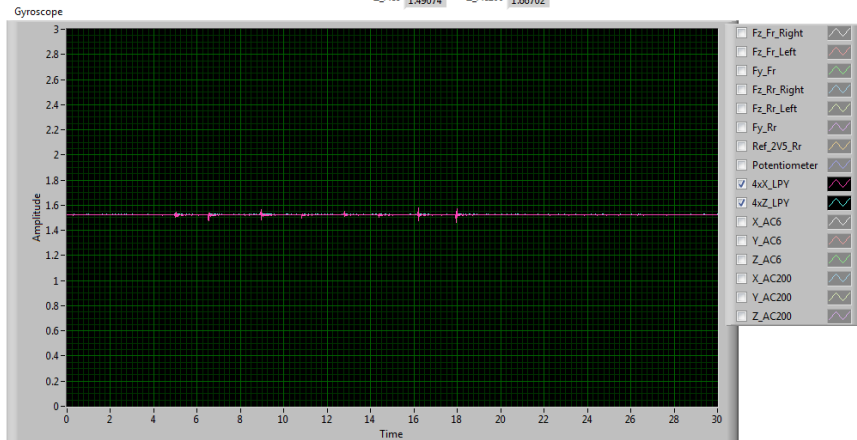


Figure 10.6: Front Panel of LabVIEW after an acquisition

vibrations_empty_seat - Notepad

File Edit Format View Help

Experiment date: 6/2/2022
 Experiment time: 6:03 PM

Rate [Hz]= 1000; Nr of samples= 30000

vibrations due to hammering th empty seat with a wooden stick

FzFR	FzFL	FyF	FzRR	FzRL	FyR	2.5V R	LMPS	4XX_LPY	4X_Z_LPYX_Ac6	Y_Ac6	Z_Ac6	X_Ac200	Y_Ac200	Z_Ac2	
2.943	2.936	1.909	2.981	2.317	2.529	2.654	4.428	1.522	1.525	1.541	1.693	1.491	1.678	1.671	1.667
2.940	2.935	1.955	2.991	2.348	2.538	2.654	4.428	1.521	1.526	1.541	1.693	1.490	1.677	1.671	1.666
2.958	2.933	1.936	2.973	2.331	2.537	2.653	4.428	1.522	1.527	1.541	1.694	1.491	1.678	1.670	1.666
2.926	2.937	1.887	2.997	2.298	2.534	2.654	4.428	1.522	1.526	1.542	1.693	1.492	1.677	1.671	1.665
2.967	2.931	1.898	2.973	2.314	2.524	2.654	4.429	1.522	1.526	1.541	1.693	1.491	1.678	1.670	1.667
2.925	2.939	1.949	2.992	2.348	2.520	2.654	4.428	1.522	1.526	1.541	1.693	1.492	1.678	1.670	1.666
2.959	2.928	1.948	2.979	2.335	2.530	2.653	4.428	1.523	1.525	1.542	1.694	1.492	1.678	1.669	1.667
2.941	2.940	1.895	2.983	2.300	2.538	2.654	4.428	1.522	1.526	1.542	1.693	1.490	1.677	1.669	1.666
2.942	2.928	1.887	2.986	2.310	2.537	2.654	4.428	1.523	1.526	1.542	1.693	1.490	1.678	1.670	1.666
2.958	2.941	1.939	2.974	2.345	2.534	2.654	4.428	1.522	1.526	1.541	1.694	1.491	1.678	1.669	1.666
2.928	2.925	1.957	2.996	2.339	2.523	2.654	4.428	1.523	1.526	1.542	1.694	1.490	1.678	1.669	1.667
2.967	2.940	1.907	2.973	2.305	2.520	2.653	4.428	1.523	1.525	1.542	1.693	1.491	1.678	1.670	1.666
2.923	2.929	1.880	2.995	2.305	2.531	2.654	4.428	1.523	1.525	1.542	1.693	1.490	1.678	1.669	1.668
2.962	2.938	1.928	2.977	2.340	2.539	2.654	4.428	1.523	1.524	1.542	1.693	1.491	1.678	1.669	1.667
2.940	2.930	1.960	2.986	2.343	2.536	2.653	4.428	1.523	1.525	1.542	1.694	1.490	1.678	1.670	1.666
2.943	2.937	1.918	2.985	2.308	2.533	2.654	4.428	1.523	1.525	1.542	1.694	1.490	1.678	1.669	1.668
2.956	2.934	1.880	2.978	2.301	2.522	2.654	4.428	1.523	1.526	1.542	1.694	1.491	1.679	1.669	1.667
2.928	2.936	1.915	2.995	2.336	2.522	2.654	4.428	1.522	1.525	1.542	1.693	1.490	1.679	1.668	1.667
2.967	2.935	1.957	2.972	2.346	2.532	2.654	4.428	1.522	1.525	1.542	1.694	1.491	1.677	1.669	1.667
2.924	2.931	1.932	2.996	2.313	2.539	2.654	4.428	1.523	1.524	1.542	1.694	1.491	1.678	1.670	1.668
2.962	2.939	1.885	2.976	2.300	2.536	2.654	4.428	1.522	1.525	1.541	1.694	1.490	1.678	1.670	1.667
2.937	2.930	1.902	2.988	2.331	2.532	2.654	4.428	1.522	1.527	1.542	1.694	1.491	1.678	1.670	1.666
2.944	2.939	1.951	2.982	2.348	2.521	2.654	4.428	1.523	1.526	1.541	1.693	1.491	1.678	1.671	1.667
2.953	2.928	1.943	2.978	2.319	2.522	2.654	4.428	1.522	1.525	1.542	1.693	1.492	1.678	1.670	1.666
2.929	2.941	1.894	2.993	2.298	2.533	2.654	4.428	1.522	1.524	1.542	1.693	1.491	1.678	1.670	1.666
2.965	2.927	1.889	2.973	2.326	2.539	2.654	4.428	1.522	1.525	1.541	1.694	1.491	1.678	1.671	1.668
2.924	2.940	1.942	2.996	2.351	2.536	2.654	4.428	1.523	1.524	1.542	1.693	1.491	1.678	1.671	1.667
2.965	2.927	1.956	2.975	2.324	2.531	2.654	4.429	1.522	1.525	1.542	1.693	1.491	1.678	1.670	1.667
2.934	2.939	1.905	2.990	2.296	2.521	2.653	4.428	1.523	1.526	1.542	1.693	1.491	1.678	1.670	1.666
2.948	2.930	1.881	2.981	2.322	2.523	2.654	4.428	1.523	1.526	1.541	1.694	1.491	1.678	1.670	1.667
2.951	2.937	1.931	2.981	2.350	2.534	2.654	4.428	1.521	1.525	1.541	1.694	1.491	1.678	1.671	1.667
2.922	2.930	1.861	2.980	2.320	2.520	2.654	4.428	1.523	1.525	1.541	1.693	1.491	1.678	1.670	1.667

Figure 10.7: Example of file produced

11 TEST AT SPORTS TECH RESEARCH CENTRE, ÖSTERSUND

Due to the time spent in the preparation of the instrumented monoski, it was not possible to perform a field test in the winter season. The equipment was therefore tested in the laboratory in order to verify its functioning, evaluate the quality of the measurements, the selection of sensors, their placement to assess possible improvements. In total 10 tests were performed in the laboratory.

The instrumented monoski was fixed on the Kistler force plate using the same steel plate built for the calibration. This is to have a reference for the load cell to check its correct functioning.



Figure 11.1: Tester on the monoski

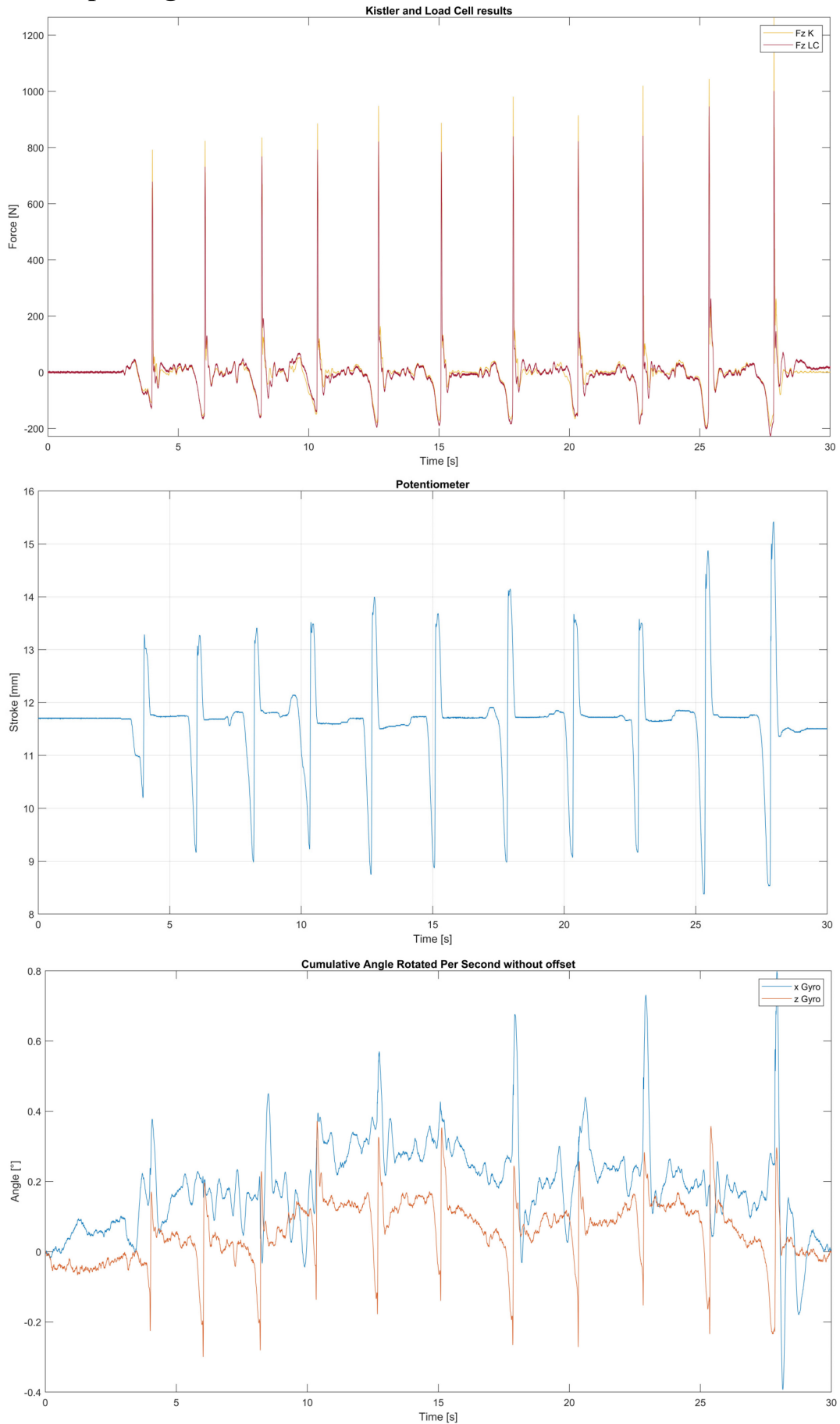
The most interesting results are discussed below.

The results of the load cell and Kistler are referred to the load cell's reference system and are zeroed with the skier already in the seat (weight of the skier = 72 kg, weight of the monoski and equipment = 16,5 kg).

The load cell results refer to calibration using traditional calibration matrix methods to simplify data analysis.

The results of the potentiometer are referred to the stroke of the sensor, using the calibration (Figure 6.5).

11.1 Drop 15 kg on the knees of the skier



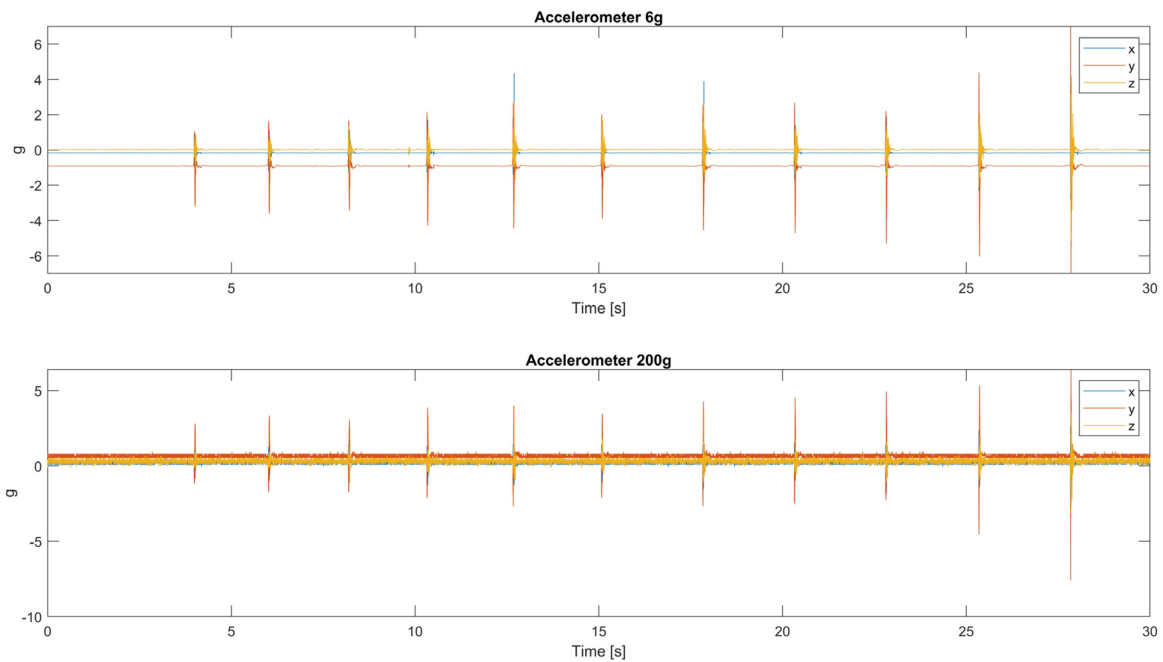


Figure 11.2: Main results of the test of dropping 15 kg on the knees of the skier

In this test, the skier had a 15 kg weight and lifted and dropped it onto his knees. This produces very high and short impulse forces and also triggers vibrations in the frame.

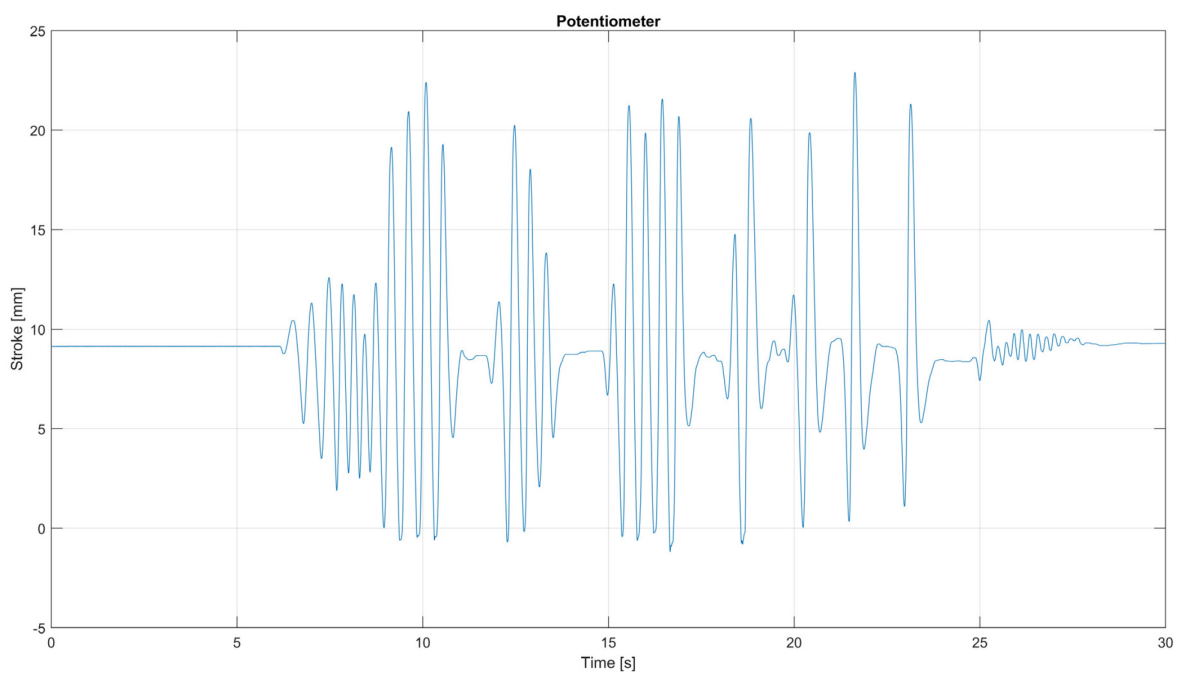
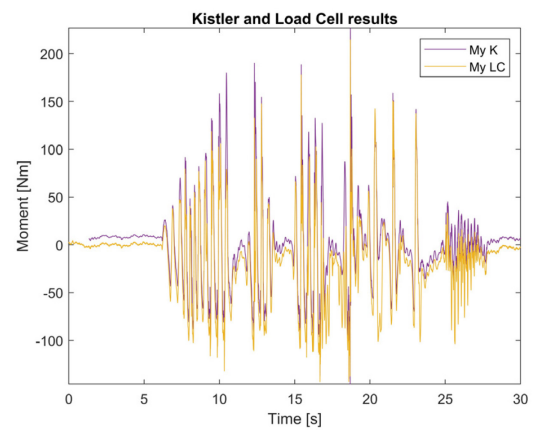
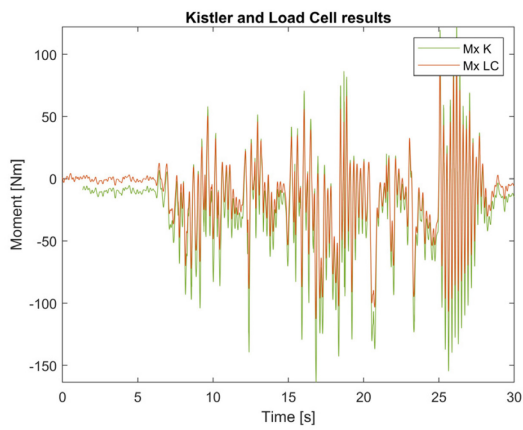
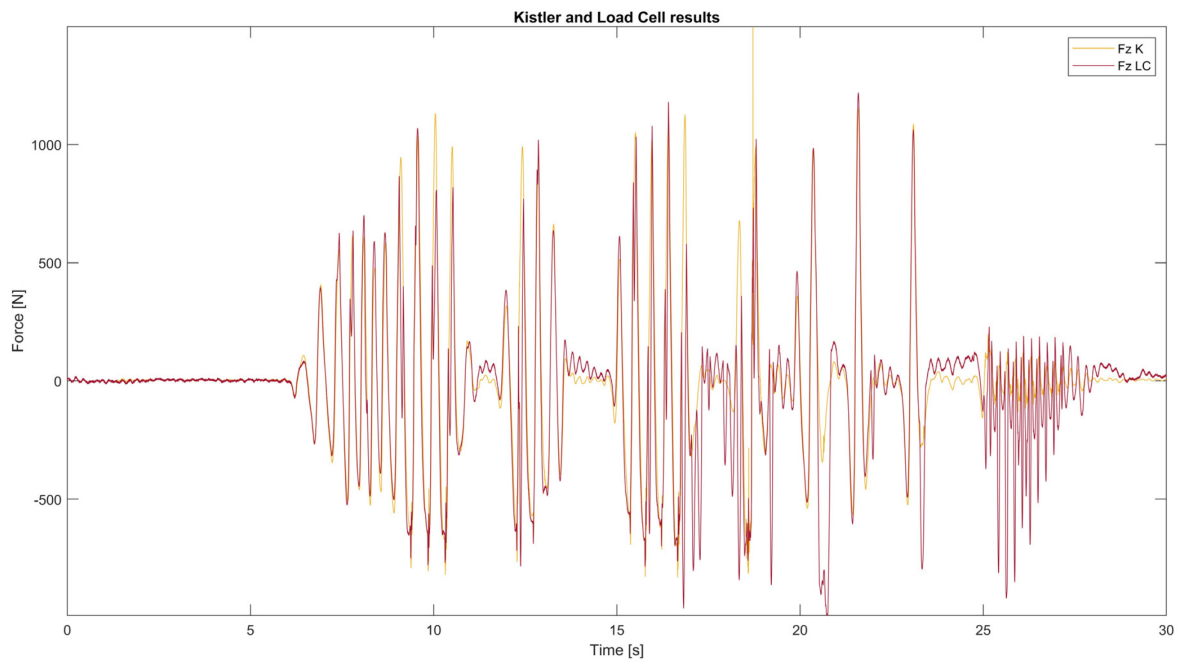
The result of the tests shows that the load cell has good sensitivity and gives results close to the one of the Kistler force plate. The vertical channel in particular follows perfectly the data from the force plate.

The potentiometer shows no noise at all and can follow very well the movement of the frame perfectly describing the kinematics of the frame.

The accelerometer, in particular the ± 200 g well represents the peaks of acceleration due to the hit by the weight. However, it is clear that the ± 200 g cannot be used to measure small accelerations due to the noise in the data. The ± 6 g accelerometer has more sensitivity and well represents the 3D accelerations of the seat but saturates very easily. In a field test it would be useless because it would saturate most of the time due to the vibrations that can easily reach up to 6 g.

The gyroscope shows an undesirable sensibility to accelerations but in this test is negligible: the rotations of the monoski are very small as expected since the frame is bolted on the Kistler force plate. The signal shows little noise as well.

11.2 Jumps on the seat



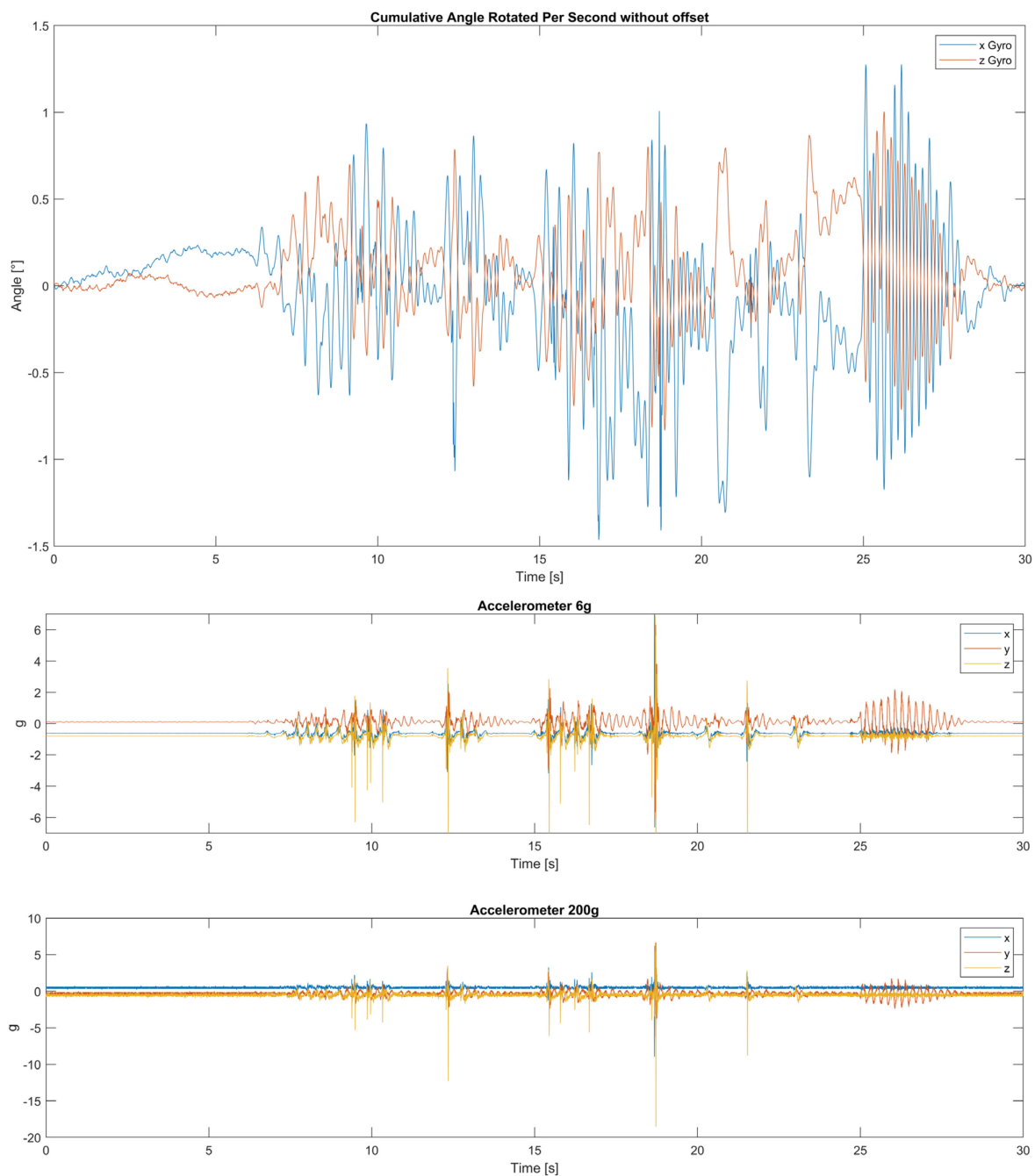


Figure 11.3: Main results of the test of jumps on the seat

In this test the skier was standing with his feet in the bucket of the seat and performed a few vertical jumps until seconds 25, then moved both vertically and laterally.

The potentiometer again has a good quality signal and can describe the movement of the frame even in the sharp peaks. It is also not affected by vibrations.

The gyroscope shows small rotations due to the small rotations that occur in the kinematic motion by compressing the shock absorber.

The accelerometer, in particular the $\pm 200g$ well represents the peaks of acceleration.

In this case the load cell cannot represent the peaks of the force: the force is cut because the range of the load cell is exceeded. This can be seen by looking at the channel's voltages.

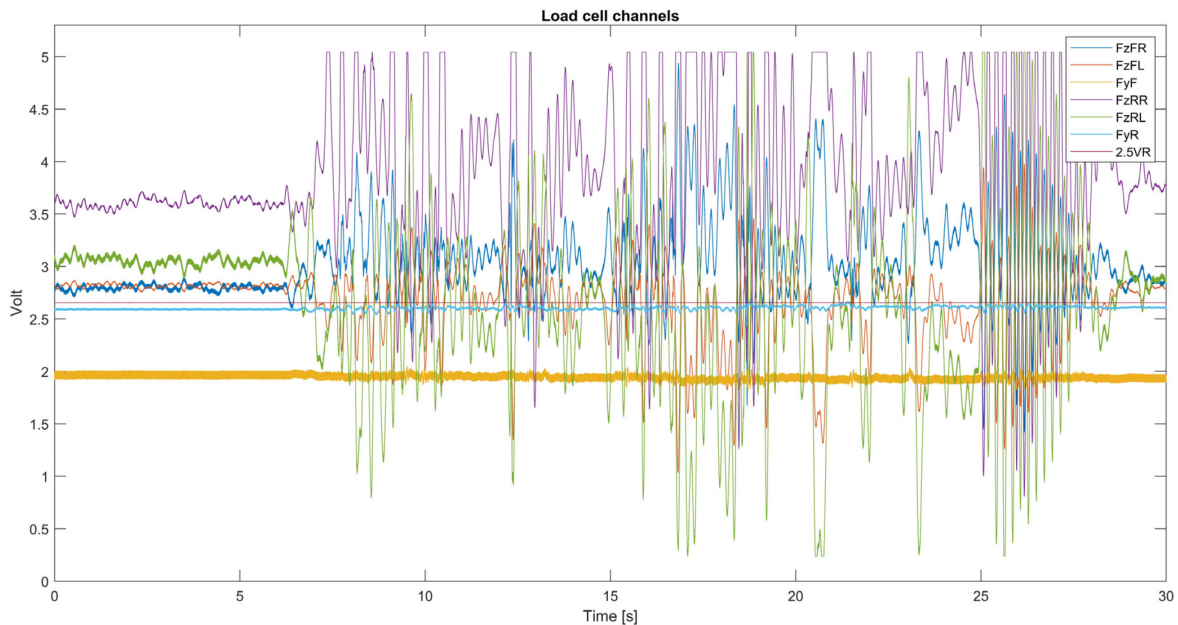


Figure 11.4: Load cell channels of the test of jumps on the seat

The channels reach the maximum value (equal to 5V of the power) and as consequence cut the data in those instants. In particular, the FzRR and FzRL channels happen to reach the upper limit of 5 V. This is due to excessive signal magnification in the amplifier board, which cannot be changed unless the amplifiers are changed. The FzRR channel also easily reaches 5 V due to the initial offset of 1 V compared to the theoretical 2.5 V

This magnification represents the major limitation of the load cell because much higher vertical loads would easily be reached during field tests. It can be seen, however, by looking closely at the load cell channel graph (Figure 11.5), that the FzRight and FzLeft channels are always opposite when 5 V is reached. This, therefore, means that it is not the vertical force that has saturated the amplifiers (the Right and Left channels would increase at the same time), and it is instead the moment M_x . It can be seen that the moments achieved in this test are much greater than those achieved in a ski run. In fact, the Centre of Pressure when skiing is within the area of the bindings [25]. Consequently, this limits the moment that can be generated. In the laboratory test, on the other hand, the monoski is fixed on the force platform; this greatly increases the width of the contact base compared to a ski and allows even higher moments to be produced. During some tests, in fact, happened that the base of the platform lifted off the ground and tilted to one side.

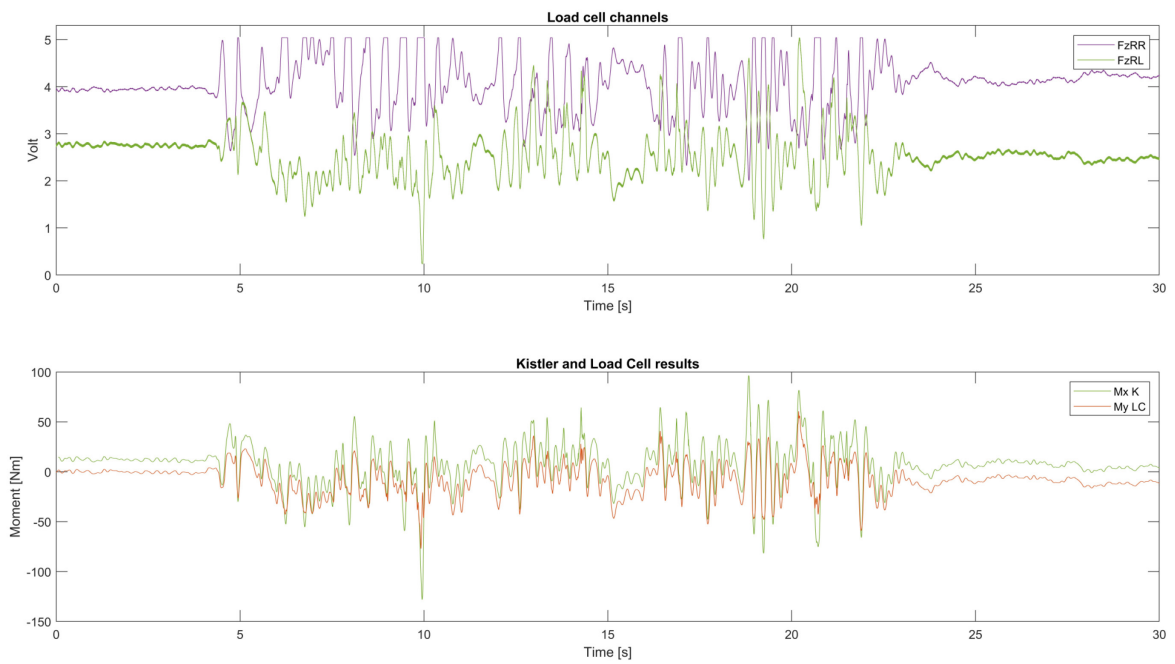


Figure 11.5: Comparison between load cell channels and roll moment

11.3 Leaning left and right

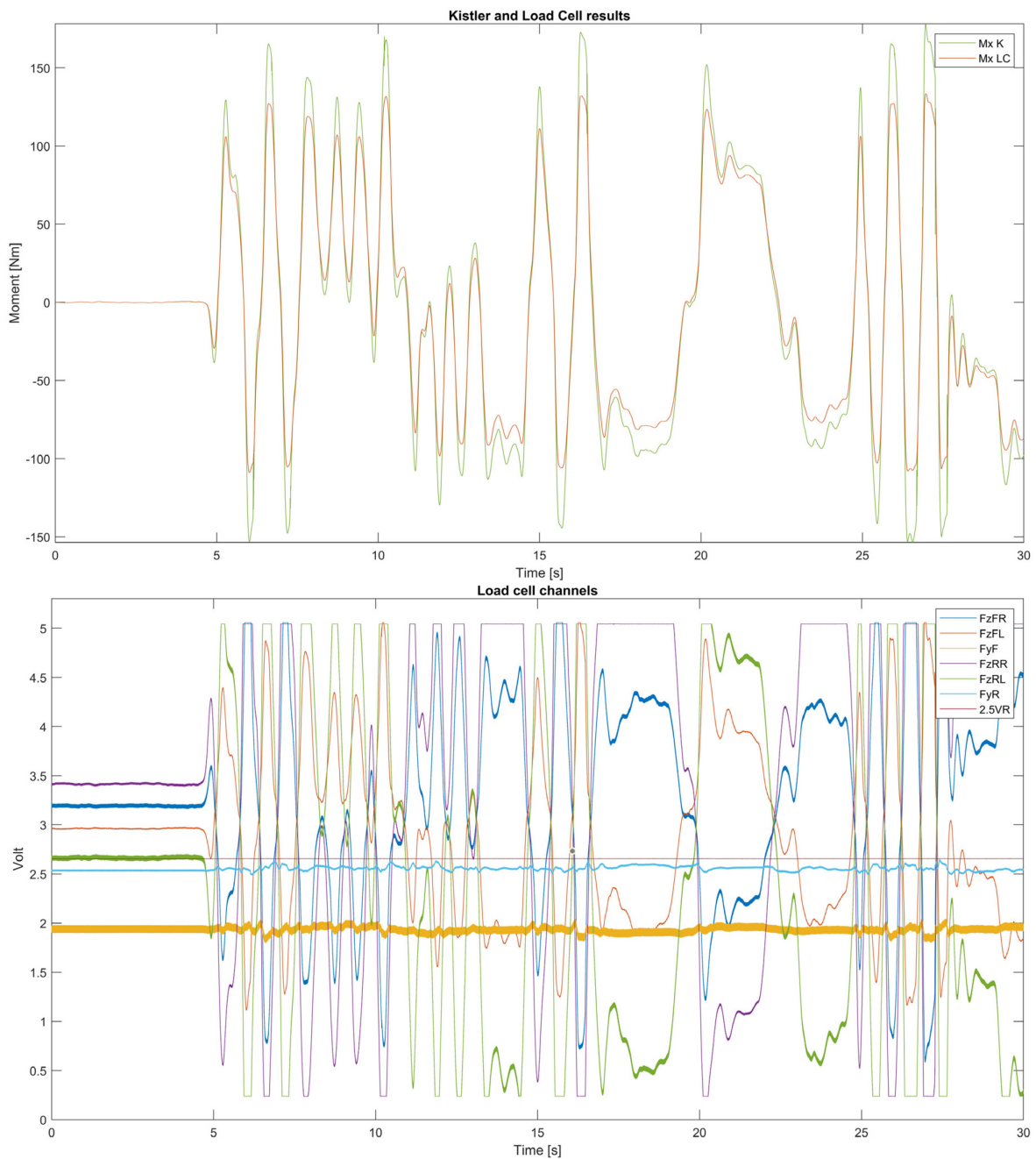


Figure 11.6: Main results of the test of leaning left and right

In this test is confirmed that the load cell can correctly measure the roll moment M_x until it saturates at around +40 Nm or -50Nm.

The test confirms that easily on the force platform can be reached very high moments, unlike on the ski.

11.4 Leaning forward and backwards

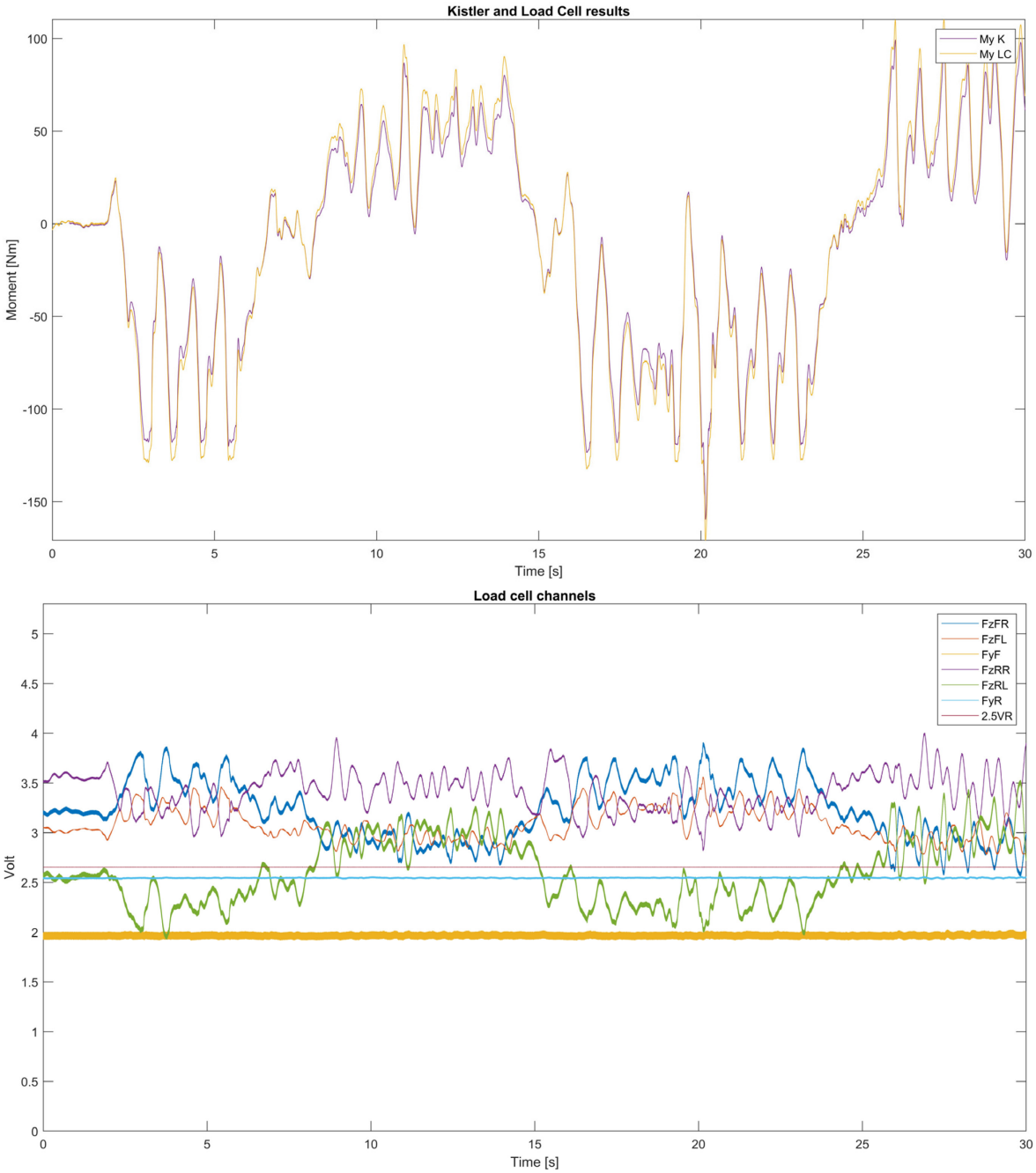


Figure 11.7: Main results of the test of leaning forward and backwards

This test confirms the perfect functioning of the load cell in measuring the pitch moment.

11.5 Study of vibrations

A simple vibration study was carried out; this can be useful to know the frequency of vibrations in order to decompose them from the accelerations produced by the actual motion of the seat. In a field test in fact the results are complicated and is difficult to identify the source of a signal.

Vibrations are also important for the health of the person and the fatigue life of the system. With the skier in the seat, the system was excited on different points of the frame and arms and the response of the accelerometers analysed. An impulse is analysed below.

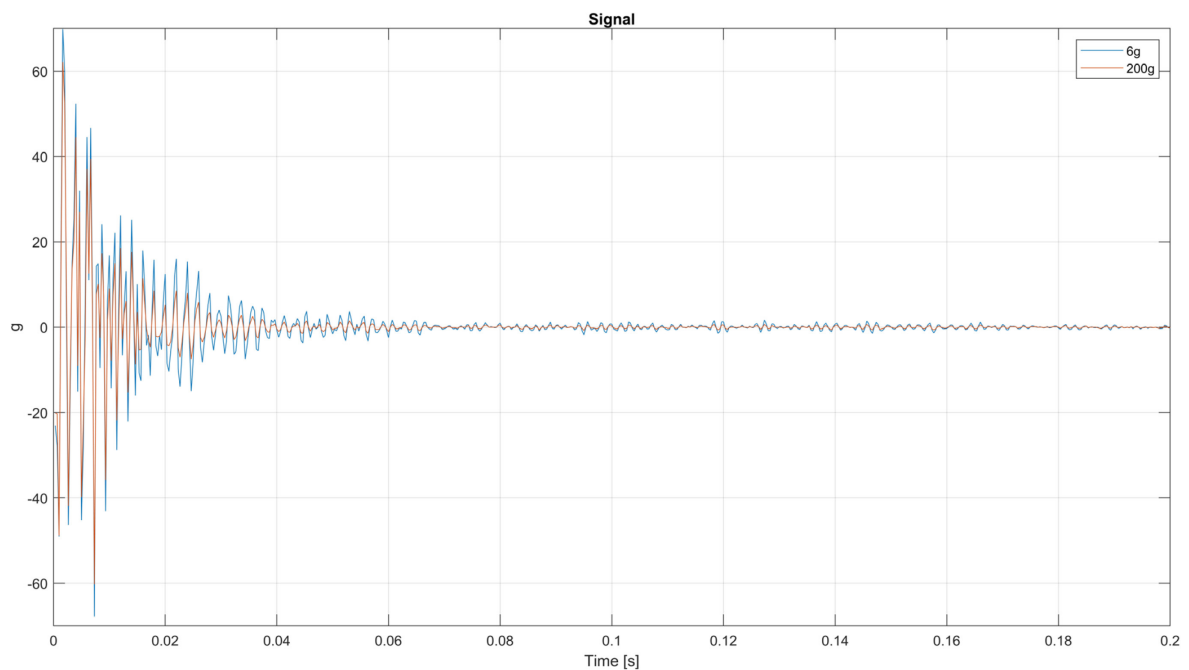


Figure 11.9: Results of accelerometers

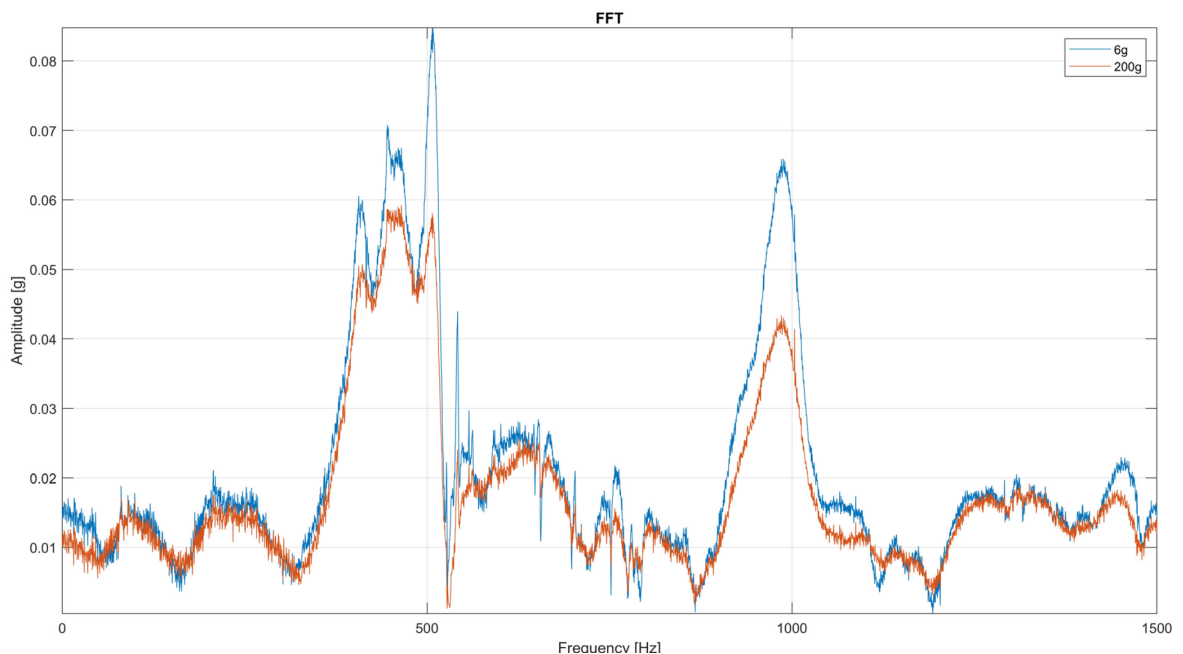


Figure 11.8: Results of the FFT of the

Since the test is not so focused on amplitude but more on the frequency distribution of vibrations, it was possible to excite the system by striking it with a wooden hammer.

During the test was noticed that after the sound of the hit (very intense but with fast decay), there was for few seconds the stale ringing, probably of the spring. This can be seen in the graph of the acceleration: the initial peaks are due to the sound propagating thru the frame, the following slow decay vibrations is the acoustic ringing of the spring.

The Fourier transform of the signals of the accelerometers shows two peaks in the frequency representing the resonance. The plot is cut at 1500Hz because the sampling rate used is 3000Hz.

The resonance frequency of the system is than around 500 Hz and the 1000 Hz peak is the second harmonic.

11.6 Tests with acc. and gyro attached to the chest of the skier

Given the results of previous tests on accelerometers and gyroscopes, where vibrations could spoil the data, a different positioning of these was tried: instead of mounting them rigidly on the frame, they were mounted on the skier's body.

An attempt was made to see if the accelerometer and gyroscope could give more meaningful and less noise-affecting results by attaching them to the person's chest. In the case of a ski run, the rotations of the athlete's body and the accelerations to which he or she is subjected may indeed be of interest for safety and comfort.



Figure 11.10: Tester before strapping the accelerometer and gyroscope

Two tests were performed: the first by leaning left and right and the second by leaning front and back.

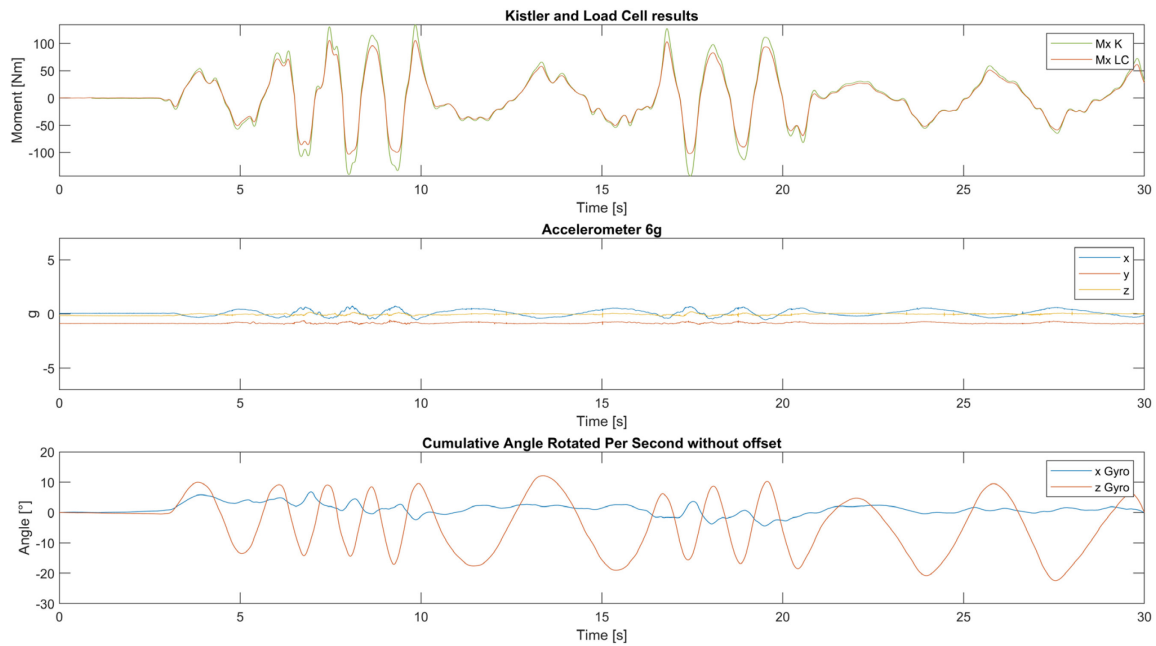


Figure 11.11: Results of leaning left and right test

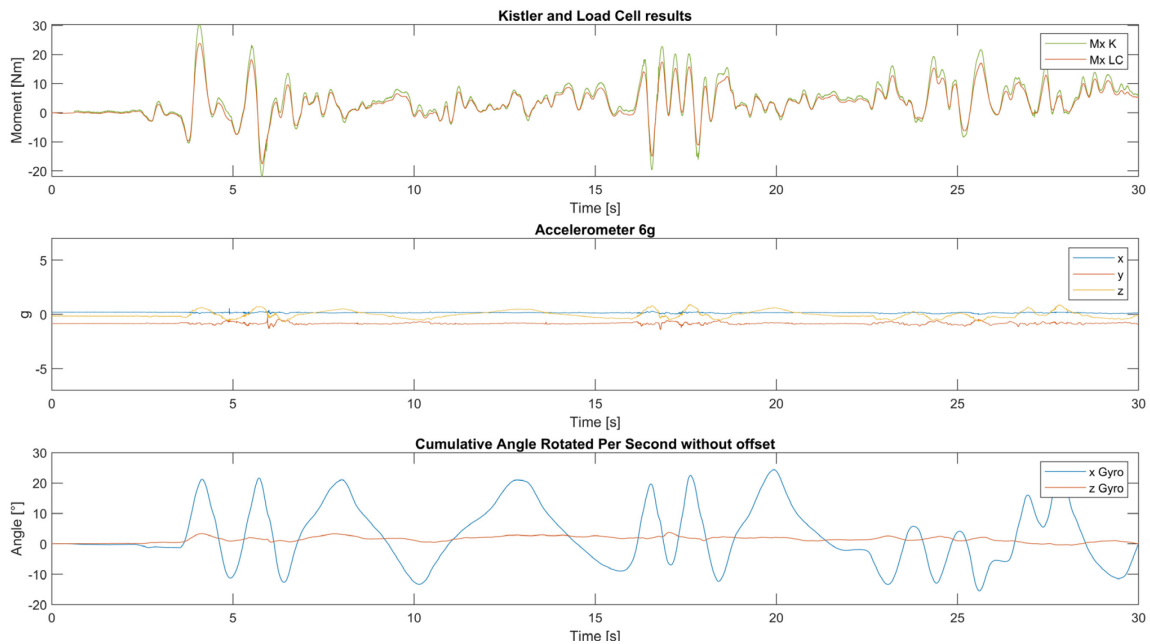


Figure 11.12: Results of leaning forward and backwards

The gyroscope shows that it could represent a way of measuring the movement of the skier but the problems in the processing of the data (Cap. 7) makes it unreliable. Since the interest is to measure angles, in the future could be used angular potentiometers instead of gyros. In fact, the potentiometer shows no peaks or noise even from vibrations. It also does not have the problem of having to integrate the signal

The ± 200 g accelerometer is useless on the skier due to too low sensitivity. The ± 6 g accelerometer instead could give interesting data of the skier because the body of the skier would dampen most of the vibrations (high frequency) and the accelerations due to the actual movement would be clear.

12 VALIDATION TEST AT PADOVA UNIVERSITY

Further tests took place at the University of Padua to further verify the set of sensors used to describe kinetic and kinematic data. The correct functioning of the load cell and the accuracy of the calibration were again verified. A study was also carried out on how the complex monoski system, and in particular the shock absorber, responds to dynamic loads and vibrations.

Since it was not possible to bring the instrumented monoski and the DAQ to Italy, the system had to be recreated using different sensors. Only the load cell was retained.

A new instrumented monoski was built, taking into account the problems that had arisen in the construction of the previous one and the results of the tests carried out in Sweden.

12.1 Materials

Another copy of Scarver monoski was found and the load cell and other sensors were applied. It was decided not to use a gyroscope because of the difficulty of obtaining good data and because rotations are of little interest in laboratory tests.

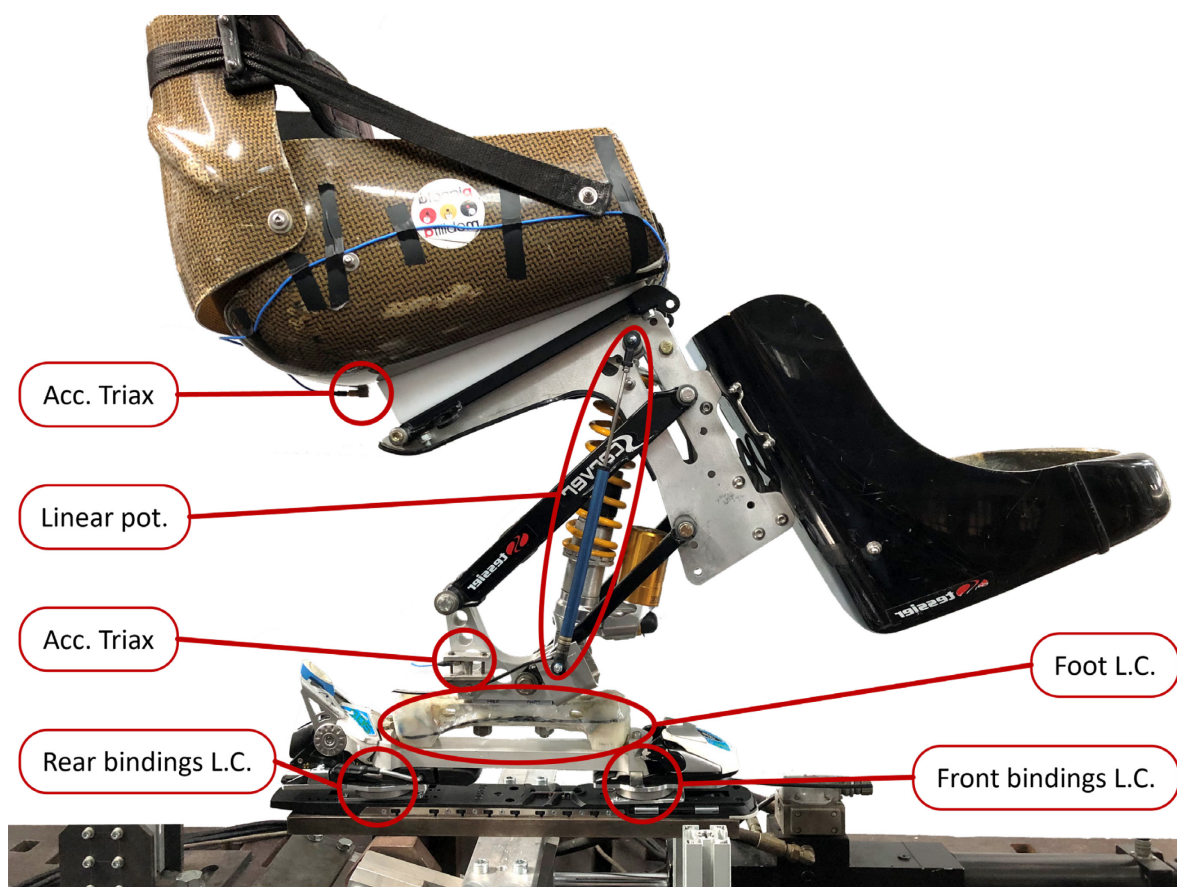


Figure 12.1: Sensors used in the instrumented monoski in Padua

12.1.1 MTS test bench

A test bench was used to produce the loads and vibrations on the monoski. The test bench is designed for testing bicycles [26] [27], but with the right adaptations it can also be used for monoskis.

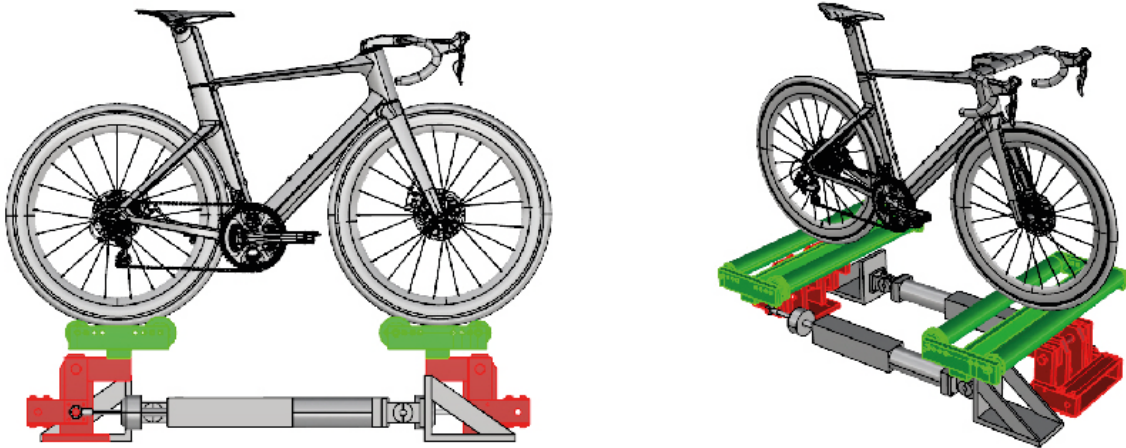


Figure 12.2: Bike bench with roller shakers and hydraulic actuators

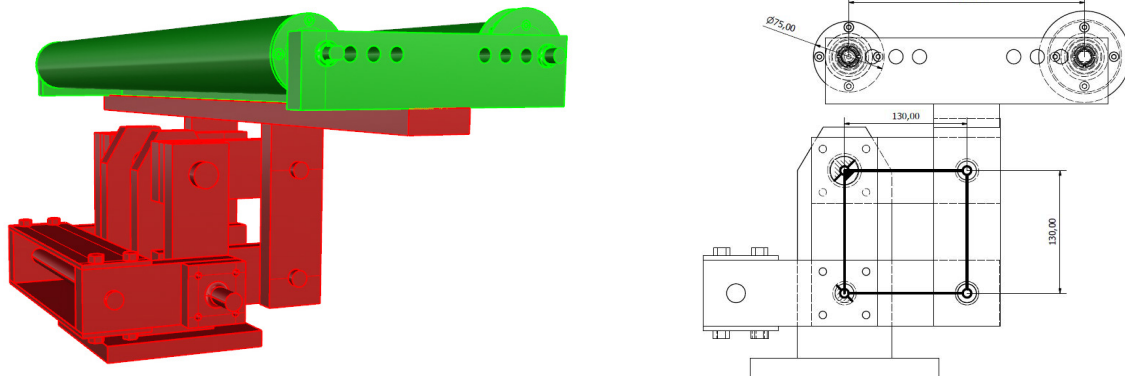


Figure 12.3: Detail of the articulated parallelogram

Only the rear articulated parallelogram was used in the monoski test, the rollers were replaced with a steel plate holding the ski piston plate as in figure.

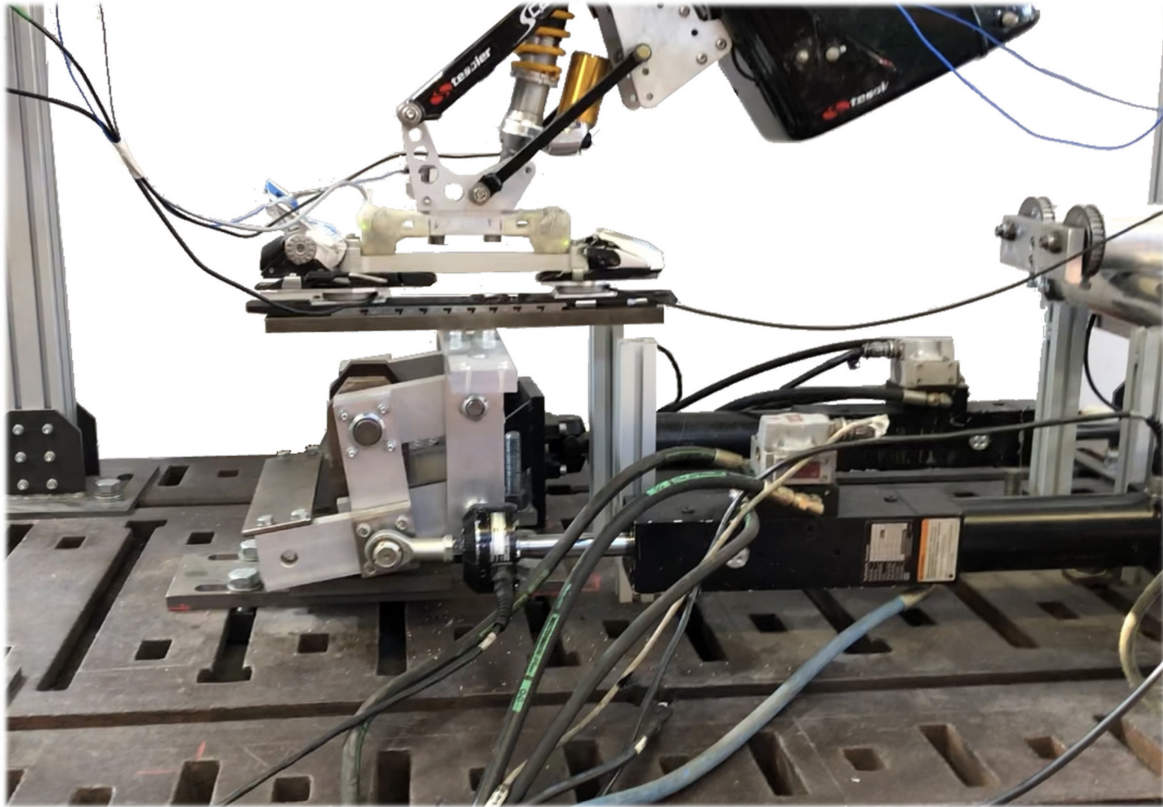


Figure 12.4: Monoski test bench

The bench is divided in:

- Hydraulic pump and control panel.
- Two MTS® servo-hydraulic actuators used to command the mechanisms. The hydraulic actuators used in this study are made by MTS System Corporation®, with a maximum force of 14.7 kN, frequency range 0-100 Hz, an effective area of 7.60 cm², a static stroke of 209.6 mm and a dynamic stroke of 203.2 mm. Each actuator is guided by a Moog® valve for its control.
- MTS Station Manager to set all parameters and to control each servo-hydraulic unit. This application allows to create the file set-up for carrying out the tests with a wide range of settings and use different control modes. Test's parameters such as the type of function (sine curve, square) wave, random etc... or the actuator control (force-displacement), PID and limits can be setup using the dialog window.

The interface of the software with main communication and control windows is showed in Figure 12.5 and it's composed by 5 dialog windows.

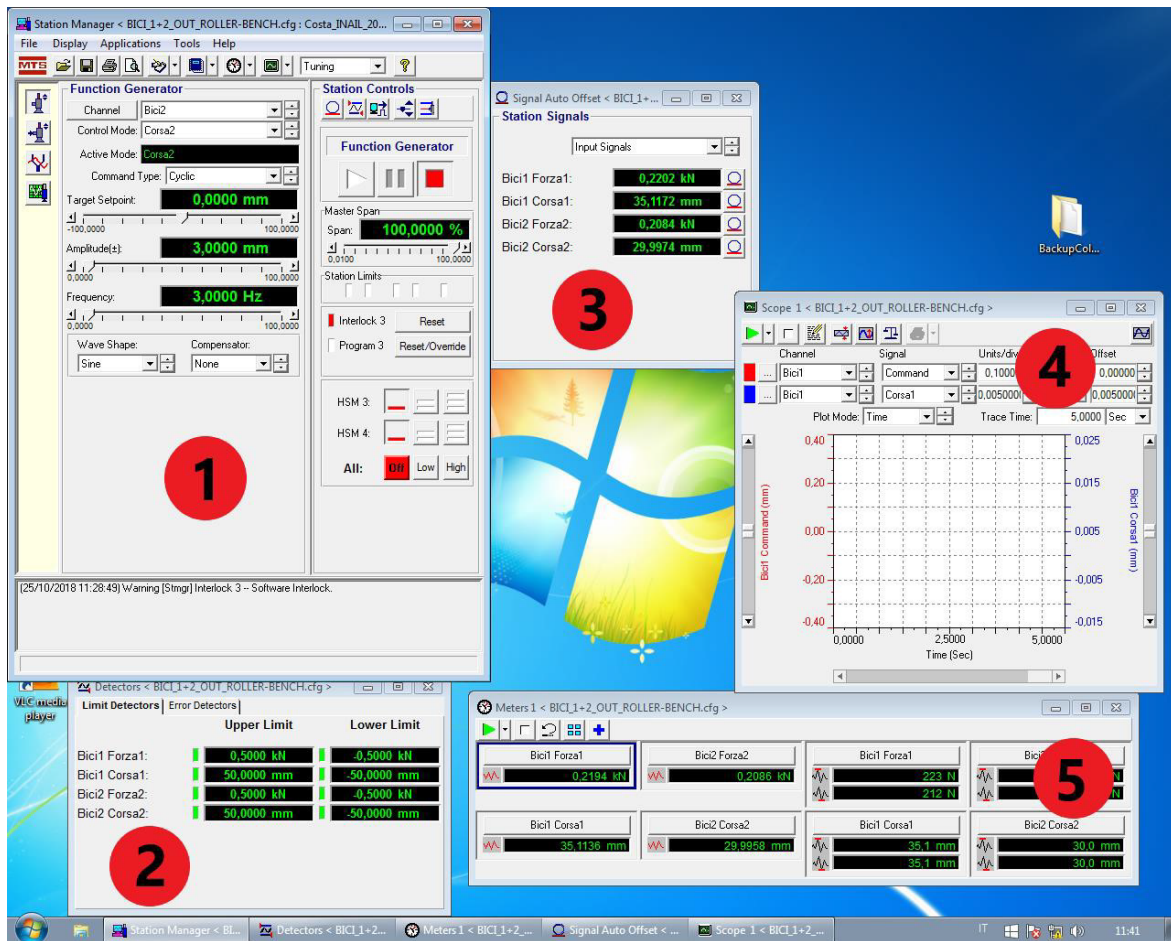


Figure 12.5: MTS Smart Station main interface

1. Command window: to set the input desired as the type of function, channels, frequencies, displacement amplitude.
2. Limits window: to define upper and lower limits of cylinders displacement and force (for test and safety reasons).
3. Offset window: to set new zero points of stroke and force. For example, for the definition of a zero position for the roller shaker.
4. Scope window: to plot different parameters as actuator force or stroke in real time; it's useful to compare applied force and output force to adjust the ability to follow the input curve using PID control.
5. Meters window: to view instantaneous values and peaks of forces and strokes.

MTS Function Generator®: Allow the complete control of the two servo-hydraulic actuators. With the function generator is possible to generate a digital function and control and correct the ability of the real system to follow the imposed signal.

Functions type are divided in three main groups:

- Cyclic functions: Sine, Square, ramp waves with constant amplitude and frequency;
- Random function: Random signal based on range of frequency and Root Mean Square;
- Sweep function: Sine waves with fixed amplitude and increasing frequency.

12.1.2 Load cells

In order to verify the correct functioning of the load cell attached to the monoski (henceforth called Foot load cell) and its calibration, two load cells (henceforth called Bindings load cells) were used as a reference.

The two six-axis load cells (SRI-M3564F) [28] are high-quality force sensors, so their measurements were considered as references. Unfortunately, it turned out that the two load cells do not work well when subjected to moments: from the tests carried out, the cells work correctly with only the applied forces, but if the lever arm is added to a force to create a moment, the force component is lower than expected, the lower the longer the arm, while the other two forces appear incorrectly different from zero.

In the case of the monoski, the load cells were used because the moments that can occur are low and we concentrate on analysing the vertical forces.

The load cells and the plates to fix them to the skis and bindings are part of the thesis by Pierluigi Cibir [29] studying the loads on mountaineering and downhill skis.

In these tests, the piston plate of the racing skis was screwed onto the steel plate of the articulated parallelogram. The load cells were mounted on the piston plate and the race ski bindings on these.

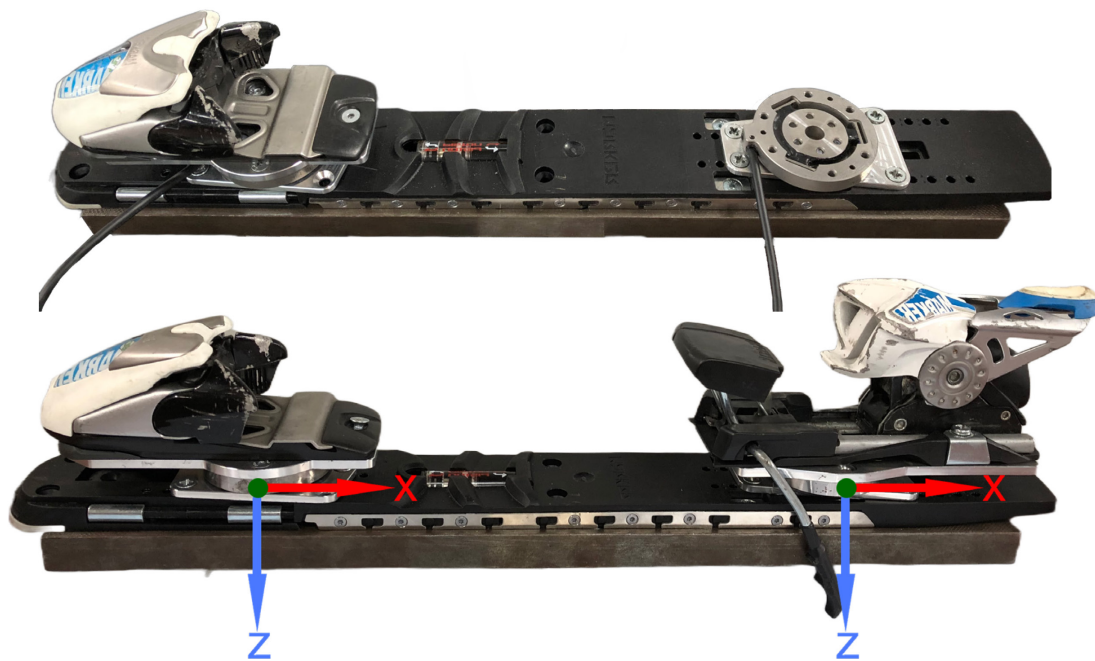


Figure 12.6: Bindings load cells and reference system

In the data processing of the loads were used the calibration matrix given in the datasheet of the cells.

12.1.3 Linear potentiometer

To measure the stroke of the shock absorber was again used a resistive linear potentiometer. The potentiometer (Penny and Giles SLS130/125/5k/L/50/1) [30] has a stroke of 125 mm enough to be placed in parallel to the shock absorber as originally intended. A leathed screw connected to the shock absorber head was used and an aluminium plate bent into a C shape at the opposite end as shown (Fig. 12.7). This way the measure of the potentiometer is the exact measure of the stroke.

The linearity of the sensor was verified. Since this was confirmed, the calibration was performed directly within the data acquisition software.



Figure 12.7: View of the potentiometer fixed on the monoski

12.1.4 Accelerometers

Two accelerometers were used: one rigidly fixed to the bindings, so the lower part of the monoski that moves with the mechanism of the bench, the other glued to the seat of the monoski.

The foot, due to the geometry of the articulated parallelogram of the bench, moves in the vertical direction only; for this reason, was used on the foot the uni-axial accelerometer.

The seat of the monoski is acting as a hanging load so there can be movements and vibrations also in the other directions; for this reason, the tri-axial accelerometer was used on the seat.

The uni-axial piezoelectric accelerometer is the model SoMat HSL 1100 (+/-50 g full scale, 0,3 15000 Hz bandpass).

The tri-axial piezoelectric accelerometer is the model SoMat triaxial ICP accelerometer, FS ± 1000 g.

For this application SoMat® Sensors Series IEPE (Integrated Electronics Piezoelectric) accelerometers are used. Each channel of the accelerometer is connected to an HLS port on the datalogger and is configured in TCE® software using the standard ICP Accelerometer setup with the specific calibration constant.

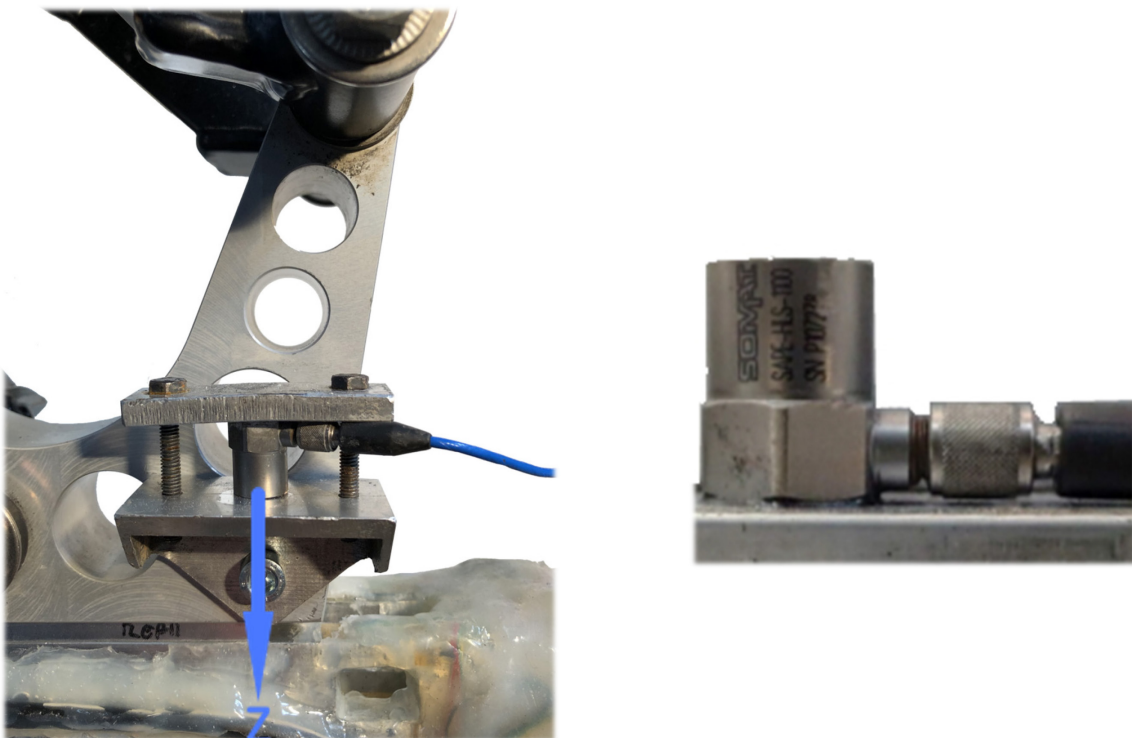


Figure 12.8: Uni-axial piezoelectric accelerometer

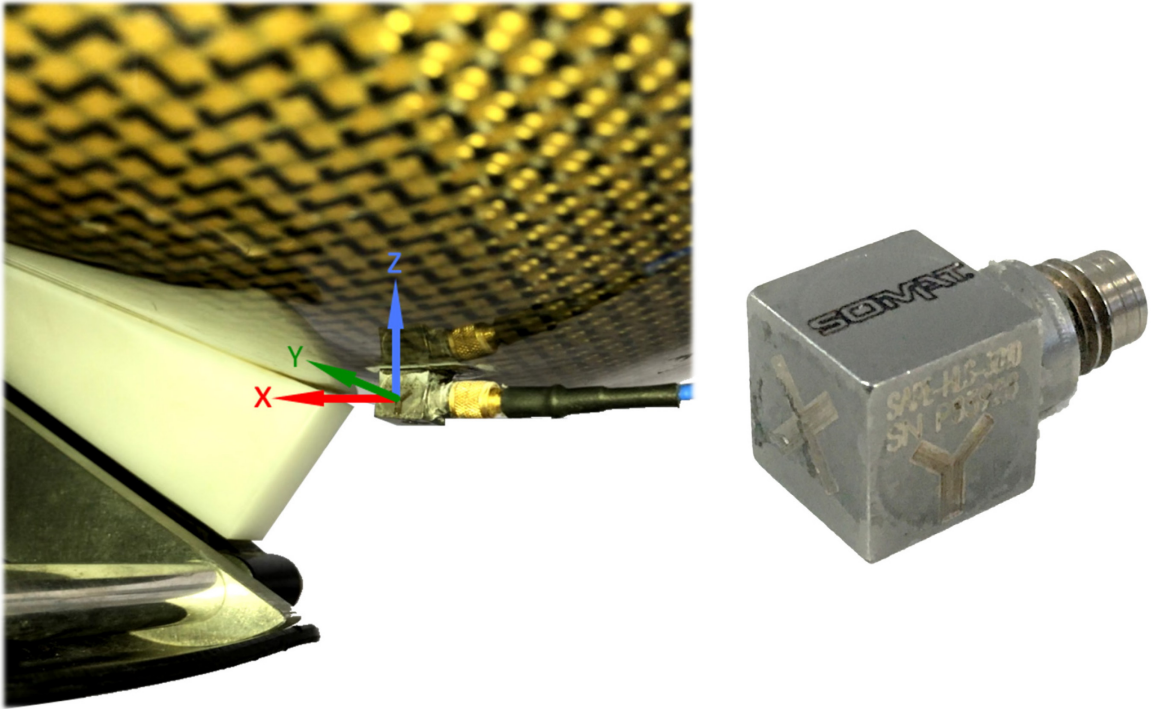


Figure 12.9: Tri-axial piezoelectric accelerometer

12.1.5 DAQ

HBM SoMat eDAQlite® is used to acquire analog and digital signals and data from sensors with a sample rate until 100 kHz.

The device is composed by different acquisition modules called layers (Each layer has four pins). There is the possibility to connect bridges strain gauges (acronym BRG) and other sensor, for example accelerometers or potentiometers (acronym HLS). In this study were used accelerometers, a potentiometer, two six-axes load cells and a four-axes load cell. Thus, were used all 12 available BRG channels for the six-axes load cells and 11 of the 12 available HLS channels for the other sensors.



Figure 12.10: SoMat Data Logger and its modules

12.1.6 DAQ software and data processing

SoMat Test Control Environment® (TCE) is used to configure this system. The software lets choose and setup the channel of each device, depending on its the properties. It's possible for example to set the calibration constant of accelerometers and potentiometer, to set the properties of the bridges of the bindings load cells.

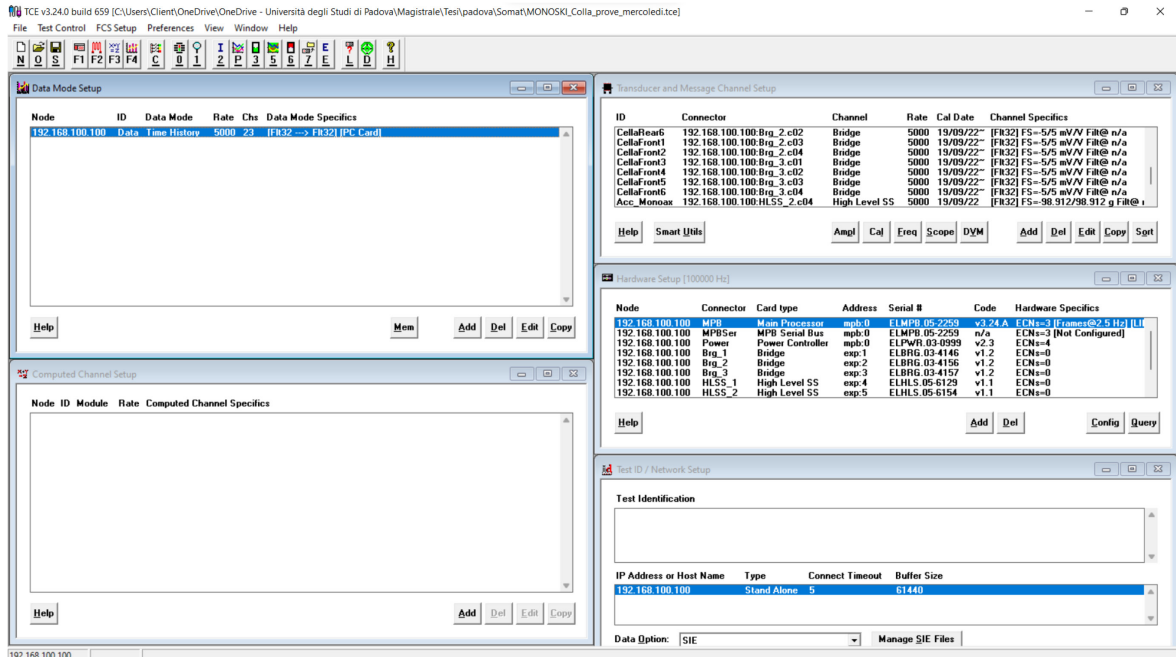


Figure 12.11: TCE® (test control environment) main interface

Data coming from the accelerometers and acquired with datalogger are stored in the system internal memory in .sie format. This file must be opened with HBM SoMat InField® software, that allow to plot and export an ASCII text file processable by other software for further calculation. The data was then processed in MATLAB.

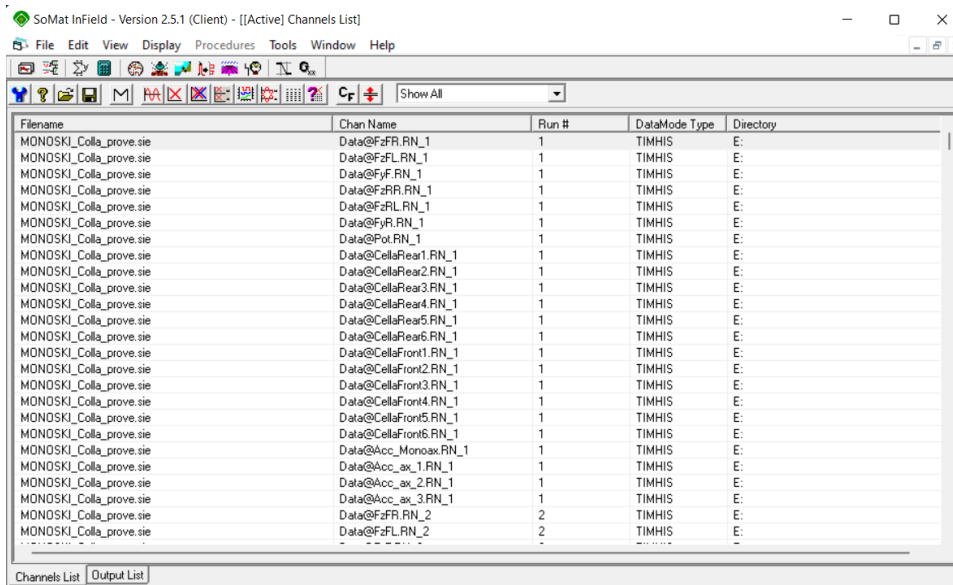


Figure 12.12: HBM SoMat InField® main interface

12.2 Reference system

To calculate the Ground Reaction Forces it was chosen to consider the same reference point of the foot load cell. The Dynfoot in fact is already set up to work with this system; the load cells on the ski binding and the uniaxial accelerometer on the other hand, each have their own reference system as explained before.

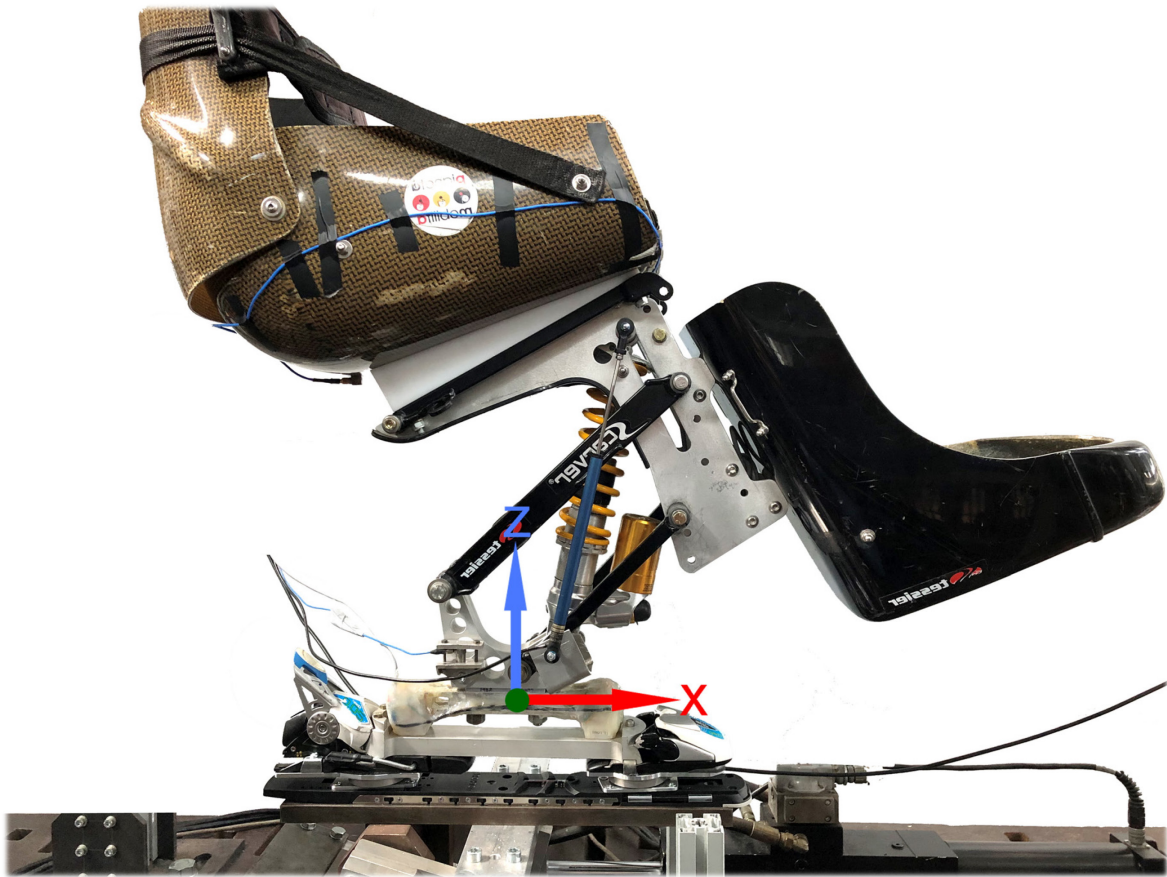


Figure 12.13: Reference system

For this reason, it is necessary to tilt the loads on some load cell axes and the axis of the uniaxial accelerometer.

Furthermore, due to the presence of two constraints on the boot (the two binding load cells), the forces and moments had to be added respectively.

$$F_{x_{binding}} = F_{x_{rear}} + F_{x_{front}} \qquad M_{x_{binding}} = M_{x_{rear}} + M_{x_{front}}$$

$$F_{y_{binding}} = F_{y_{rear}} + F_{y_{front}}$$

$$F_{z_{binding}} = F_{z_{rear}} + F_{z_{front}}$$

However, it is not possible to directly use the moment M_y around the y-axis measured by the binding load cells: it must be calculated from the forces F_z as follows.

The distance between the front cell centre and the reference point is $OF = 150$ mm, the distance between the rear cell centre and the reference point is $RO = 150$ mm. Considering the Ground Reaction Forces reference system, the pitching moment (torque around the y-axis) is positive in the clockwise direction.

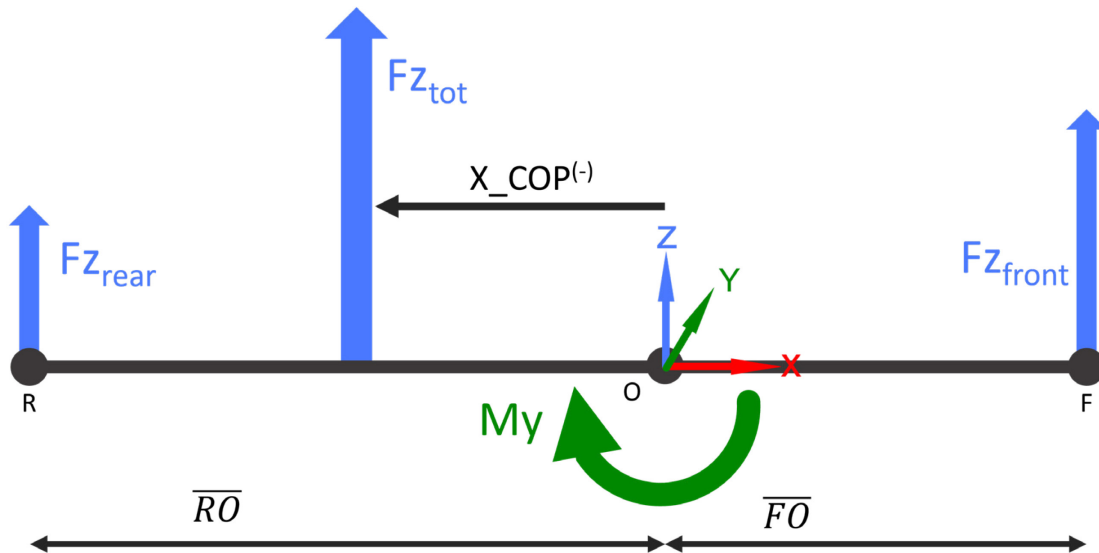


Figure 12.14: Calculation of torque from the forces

Is then possible to calculate the M_y moment knowing the vertical forces on the front and rear binding load cells and their lever arm with respect to the origin.

$$M_y = F_{z_{rear}} \cdot \overline{RO} - F_{z_{front}} \cdot \overline{OF}$$

12.3 Aims of the tests

The tests aim to answer these questions:

1. Is the foot load cell able to correctly detect static loads by taking the bindings load cells as a reference?
2. Is the foot load cell able to correctly detect dynamic loads by taking the bindings load cells as a reference?
3. How does the system and the shock absorber respond to forced static and dynamic loads and vibrations?

12.4 Static location of the Centre of Pressure

One of the tests to statically verify the correct functioning of the foot load cell is to check if it is able to trace the position of the Centre of Pressure (COP) on the ski binding. Two extreme positions of the skier's movement in the monoski were considered: skier leaning forward and skier leaning back. The results of the foot load cell were compared with those of the binding load cells and with the values calculated by the quantitative anthropometry. The extent of the displacement of the body posture along the x- and y-axes and the postures assumed have been noted in recent studies [31]. The postures assumed are the limit postures of a skier classified as LW 12. Furthermore, the COP of a skier in normal skiing conditions is always within the area between the bindings, so the moments, particularly M_x , are limited compared to those that could be performed with the ski fixed to the laboratory floor [25]. In these tests, the MTS test bench (Cap. 12.1.1) was stationary

12.4.1 COP by Quantitative Anthropometry

The quantitative anthropometry is a technique of non-invasive quantitative measurements of the body. It allows the evaluation of geometric and inertial parameters, such as the position of the Centre of Mass (COM) during static or dynamic postures.

In order to simplify the procedure, no complex motion capture systems were used, but only a camera was used for a 2D description of the posture in the sagittal plane.

The procedure starts with the identification of body segments (links) located between two joints. To highlight the joints during the test, were used reflective markers placed on the body or, when not possible, as in the case of the hip, ankle and ball of the foot, were placed on the seat.

Then the posture description was done following the absolute segments angles convention:

- The segment line connects the proximal and distal joint centres except for head and neck segments that go from C7 joint to the ear and except the foot that is parallel to the foot sole as in Figure 12.15.
- The absolute segment angle is the angle between the Z' axis (parallel to Global Z, passing through the Distal Joint) and the Segment Unit Vector. The sign is positive if counterclockwise from Z' to the Unit Vector. Exception for the foot: θ_{FOOT} is the angle between the X' axis (parallel to Global X, passing through the Heel) and the Foot sole Unit Vector.

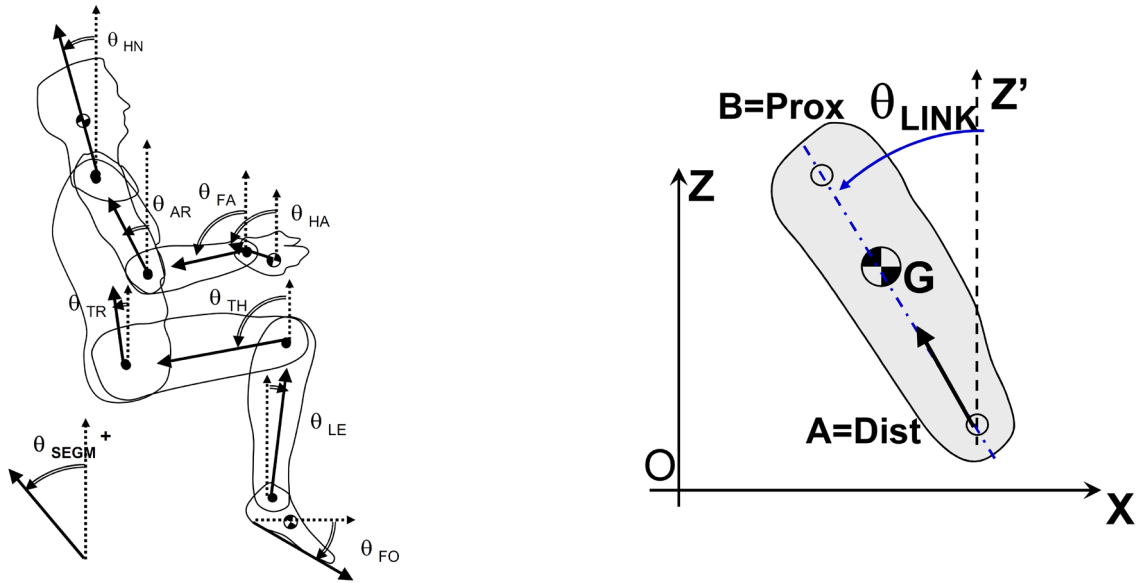


Figure 12.15: Conventions of segments and absolute angles

Is then possible to evaluate geometric and inertial parameters by means of the Dempster table. It is a table of statistical combination of a large number of subjects normalized to the height and total mass of the subject and allows to calculate the mass, length and COM position of each link. Finally using the segment's angles, length, mass, and position of the link COM is possible to calculate the full body COM.

The test subject weighs 60kg and is 1700mm tall.

Dempster table with this information can then be filled as follows:

	Link Mass [Kg]		Link Length [mm]		Link COM position [mm]	
Head & neck	7.90%	4.74	17.70%	300.90	56.70%	170.61
Trunk	51.10%	30.66	29.90%	508.30	46.70%	237.38
Arm	2.70%	1.62	17.20%	292.40	43.60%	127.49
Forearm	1.60%	0.96	15.20%	258.40	43.00%	111.11
Hand	0.60%	0.36	4.00%	68.00	100.00%	68.00
Thigh	9.70%	5.82	24.70%	419.90	43.30%	181.82
Shank	4.50%	2.70	23.20%	394.40	43.30%	170.78
Foot (Yankle)			4.60%	78.20	42.90%	33.55
Foot (Xtoe)			12.65%	215.05		
Foot (Xheel)			2.55%	43.35		
Foot total	1.40%	0.84	15.20%	258.40	26.40%	68.22
					rG	76.02

Figure 12.16: Dempster normalized parameters and resulting values for the subject tested

12.4.2 Skier leaning forward

The skier posture description is analysed below:

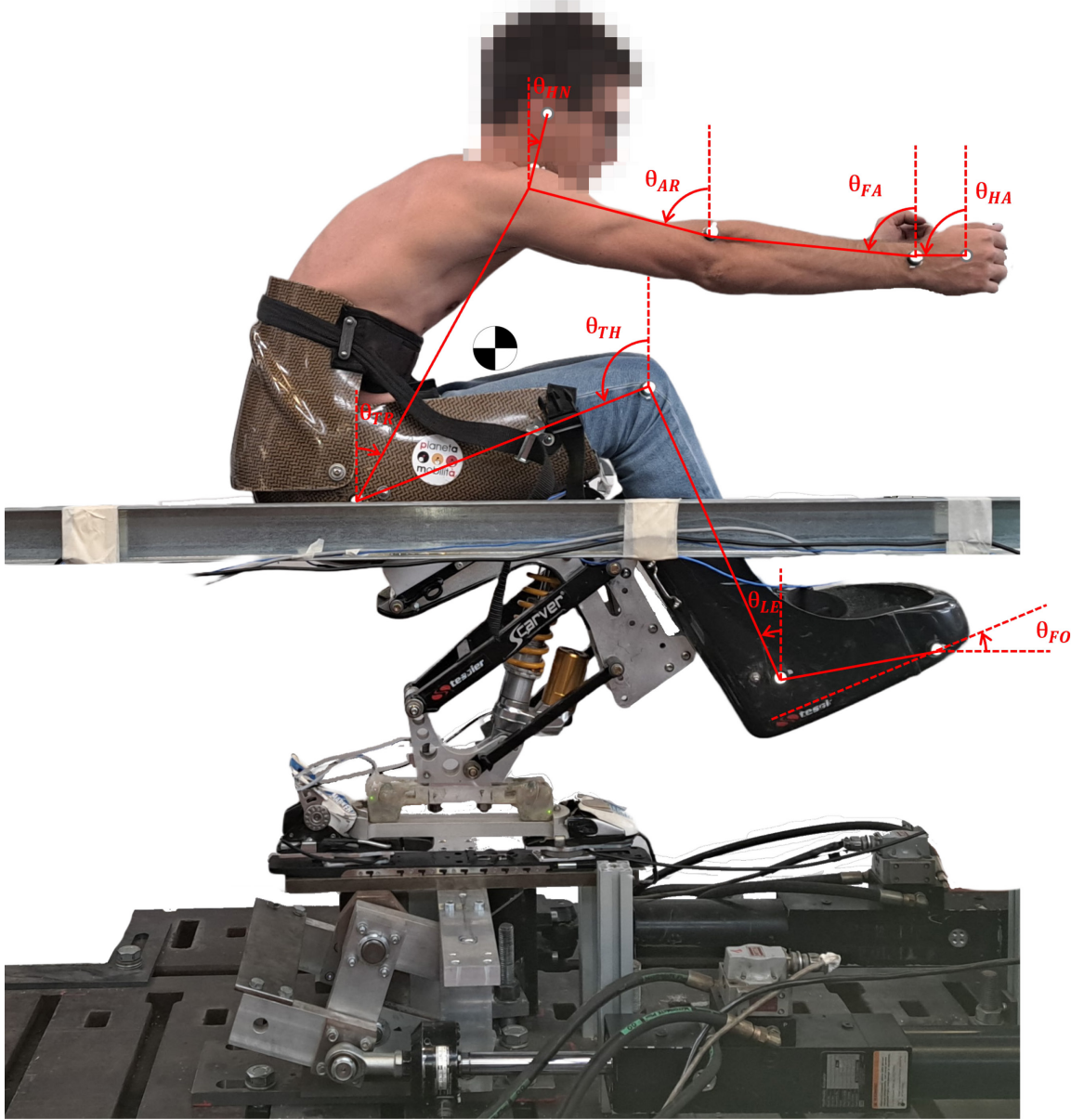


Figure 12.17: Description of the skier's posture leaning forward

Absolute angles [°]		
Foot	θ_{FO}	23
Shank	θ_{LE}	23
Thigh	θ_{TH}	68
Trunk	θ_{TR}	-29
Head and Neck	θ_{HN}	-14
Arm	θ_{AR}	75
Forearm	θ_{FA}	84
Hand	θ_{HA}	90

COM position in relation to the Hip	X [mm]	Z [mm]
Hand COM	854	342
Forearm COM	639	357
Arm COM	370	412
Head Neck COM	288	610
Trunk COM	131	237
Thigh COM	169	-68
Shank COM	456	-314
Foot COM	619	-524

Figure 12.18: Angles measured from image analysis and COM of each link calculated

The full body COM is located at the following coordinates on the sagittal plane with respect to the Hip joint: $X_{COM} = 231.6 \text{ mm}$ $Z_{COM} = 150.8 \text{ mm}$

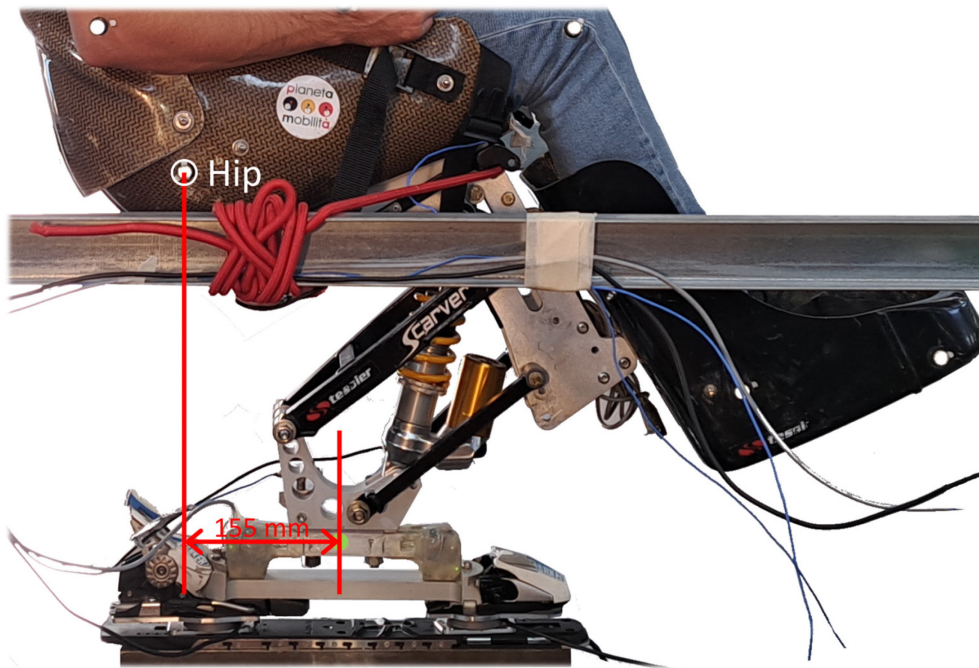


Figure 12.19: Position of hip joint with respect to the reference system

Since the test is quasi-static, the x-coordinate of the COM corresponds to the x-coordinate of the COP.

To calculate the coordinate of COP, it was decided to consider the same reference point of the foot load cell. The coordinate calculated with Quantitative Anthropometry must then be shifted by 155 mm obtaining the COP position relative to the reference system of the load cell.

$$X_{COP} = 76.6 \text{ mm}$$

12.4.3 Skier leaning backwards

A similar test was carried out with the skier leaning backwards. Even if this particular posture is not common in sit skiing, it is in any case useful to check the correct functioning of the load cells.

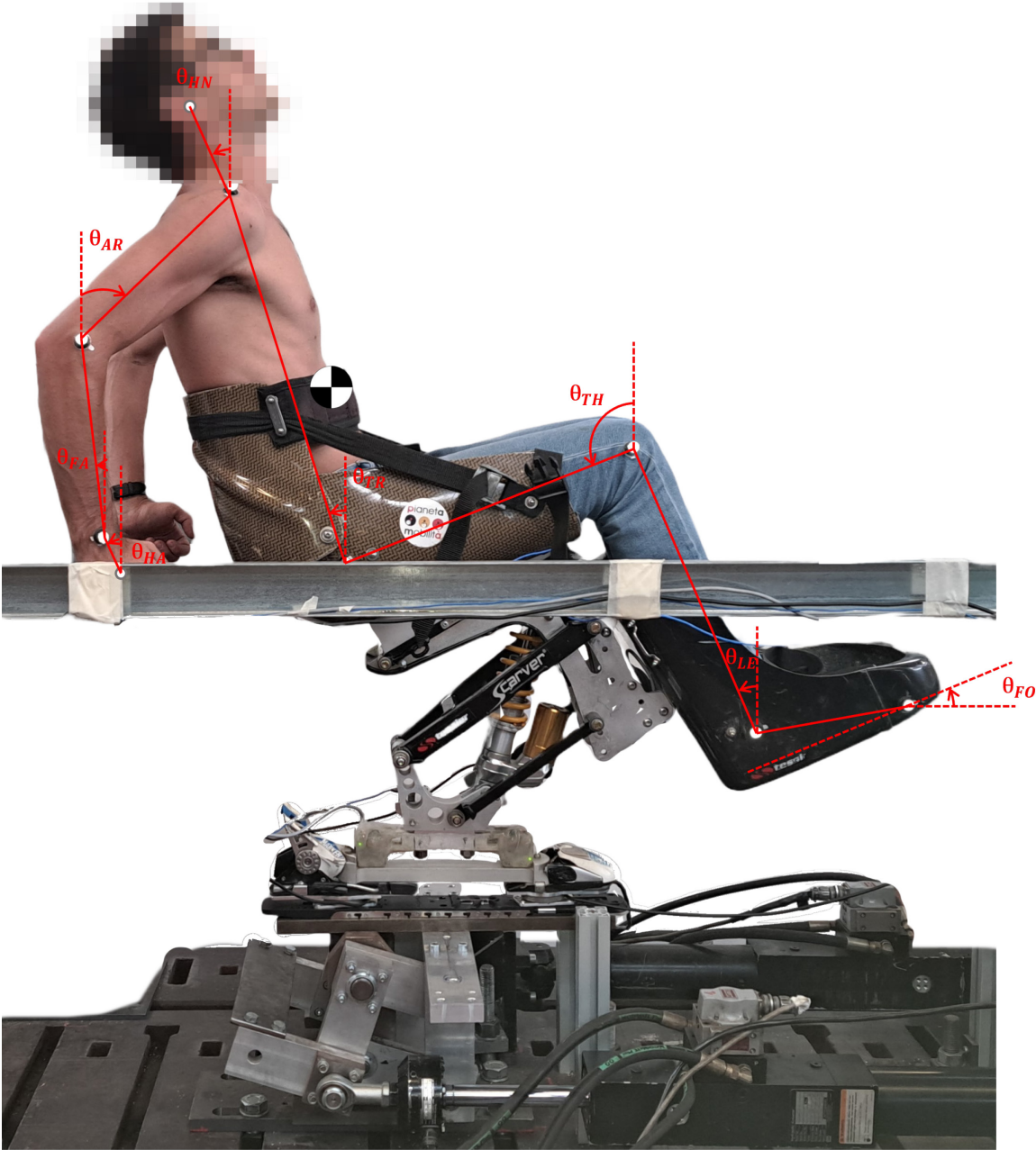


Figure 12.20: Description of the skier's posture leaning backwards

The posture is analysed below.

Absolute angles [°]		
Foot	θ_{FO}	23
Shank	θ_{LE}	23
Thigh	θ_{TH}	68
Trunk	θ_{TR}	18
Head and Neck	θ_{HN}	24
Arm	θ_{AR}	-46
Forearm	θ_{FA}	7
Hand	θ_{HA}	24

COM position in relation to the Hip	X [mm]	Z [mm]
Hand COM	-308	-38
Forearm COM	-354	170
Arm COM	-249	395
Head Neck COM	-226	639
Trunk COM	-84	258
Thigh COM	169	-68
Shank COM	456	-314
Foot COM	619	-524

Figure 12.21: Angles measured from image analysis and COM of each link calculated

The full body COM is located at the following coordinates on the sagittal plane with respect to the Hip joint: $X_{COM} = 2.0 \text{ mm}$ $Z_{COM} = 152.3 \text{ mm}$

The coordinate calculated with Quantitative Anthropometry must then be shifted by 155 mm obtaining the COP position relative to the reference system of the load cell.

$$X_{COP} = -153 \text{ mm}$$

12.4.4 COP by the load cells

The distance on the x-axis and y-axis between the centre of the reference system and the COP can be calculated from the loads measured by the load cells as:

$$X_{COP} = -\frac{My}{Fz} \qquad Y_{COP} = \frac{Mx}{Fz}$$

The cells were zeroed with the monoski fixed on the bindings, the before the tester sat in the seat, in order to measure only the loads produced by the body of the skier.

The graph of the moment My (pitch) clearly shows the change in value depending on posture. Are plotted the moment measured by the foot load cell and the moment measured by the bindings load cells. Also visible are the jumps (the spikes in the graph) performed to synchronise the data from the load cells and the video between each movement.

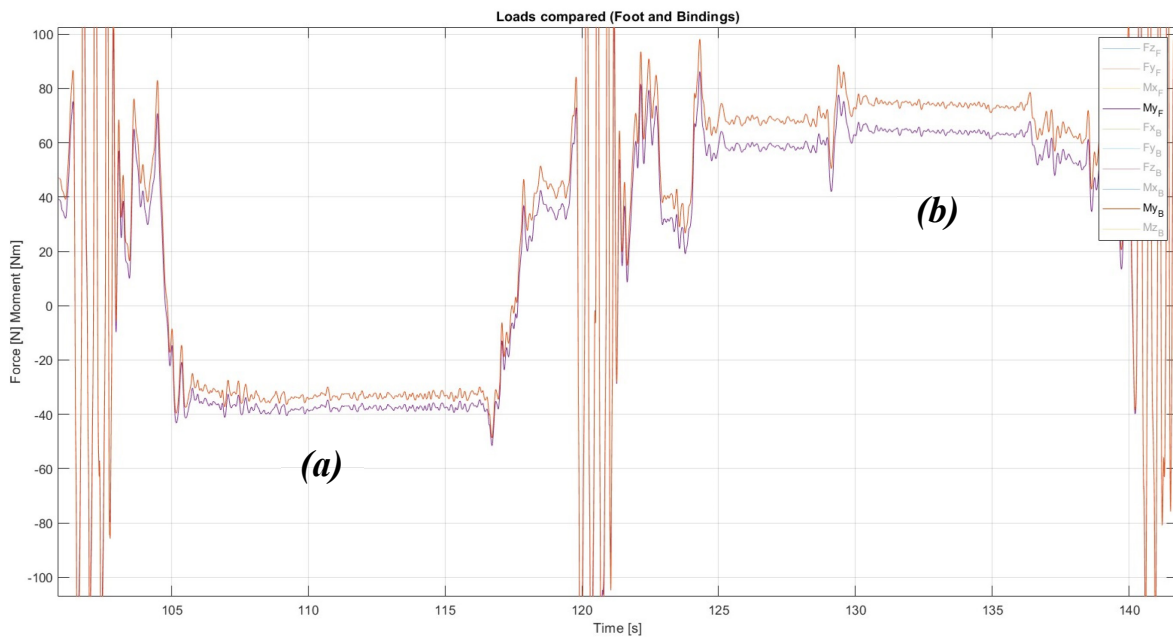


Figure 12.22: (a) *My when leaning forward* (b) *My when leaning backwards*

The COP calculated from the loads measured by the load cells is shown in Figure 12.23. A line shows where has been calculated the average. It corresponds to the instant in which the picture for the Quantitative Anthropometry has been taken.

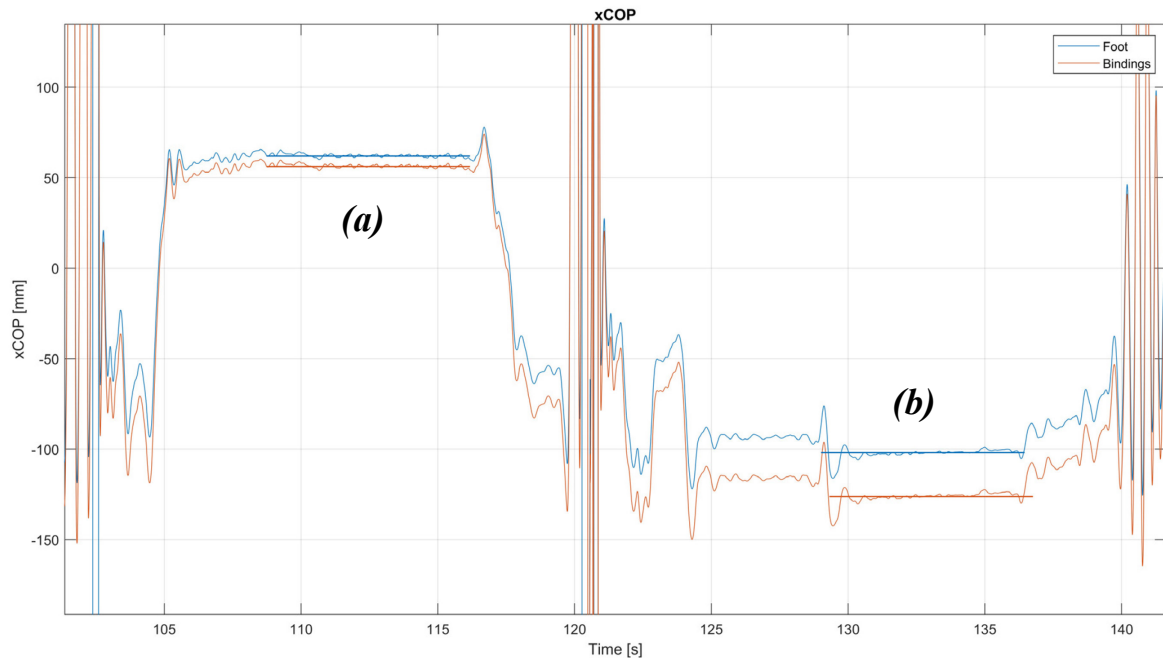


Figure 12.23: (a) X_{COP} when leaning forward (b) X_{COP} when leaning backwards

The results obtained from the three systems are compared here:

Comparison of X_{COP} [mm]

	Quantitative Anthropometry	Foot load cell	Bindings load cells
Leaning Forward	77	62	57
Leaning Backwards	-153	-102	-126
$\Delta X_{COP} = \text{Forw} - \text{Backw}$	230	164	183
Error % on ΔX_{COP}	25.7%	10.4%	\

Table 15: Comparison of COP coordinates

Already from the graph of the moment, it can be seen that the loads of the Foot and Bindings load cells have the same trend but are offset. This implies that the COP is also offset. Both load cells show a substantial displacement of the centre of pressure, as expected, but by comparing the results of the COP position, it can be seen that these deviate greatly from the results of the Quantitative Anthropometry study. This may be due to the approximations in the study such as considering the back as a linear segment.

Considering the result of the bindings load cells as exact, the average percentage error is 26% in the case of the Quantitative Anthropometry study and 10% in the case of the foot load cell.

A test was carried out to verify that the COP displacement could also be measured along the y-axis by leaning the skier to the right and left. In this case, however, the posture analysis according to Quantitative Anthropometry was not carried out because the movement does not take place in the sagittal plane. It is, however, a useful test to show that the foot load cell has similar behaviour to the more reliable bindings load cells.

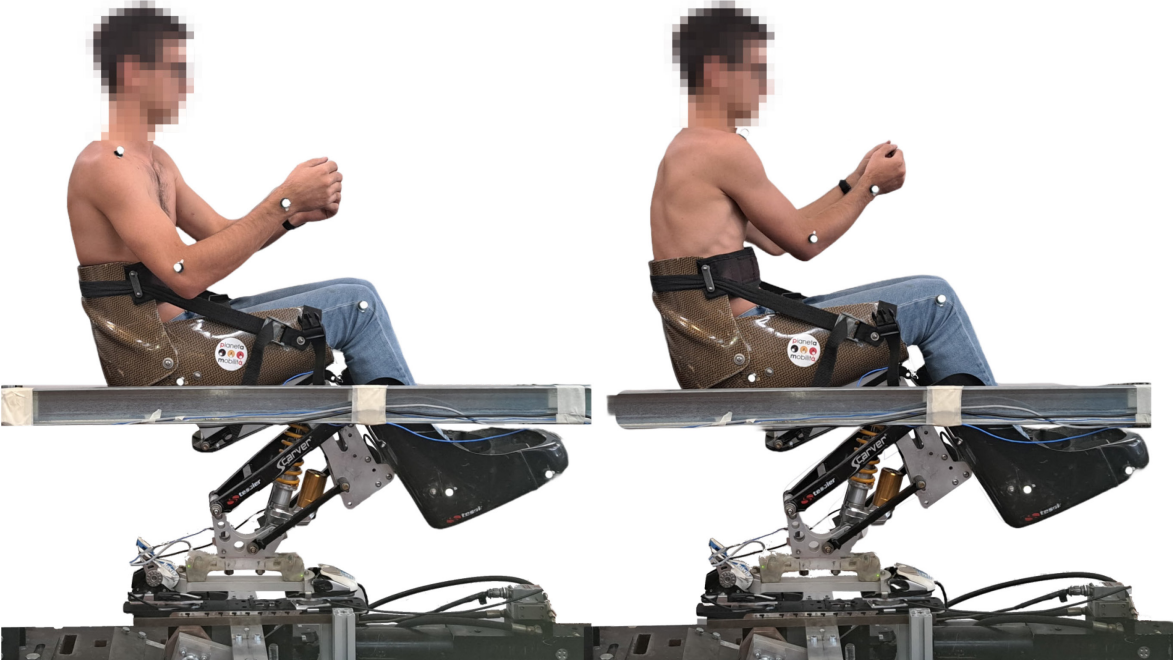


Figure 12.24: Posture when leaning right and left

The graph of the moment M_x (roll) shows that also on the x-axes the load cells have the same behaviour but with the values offset.

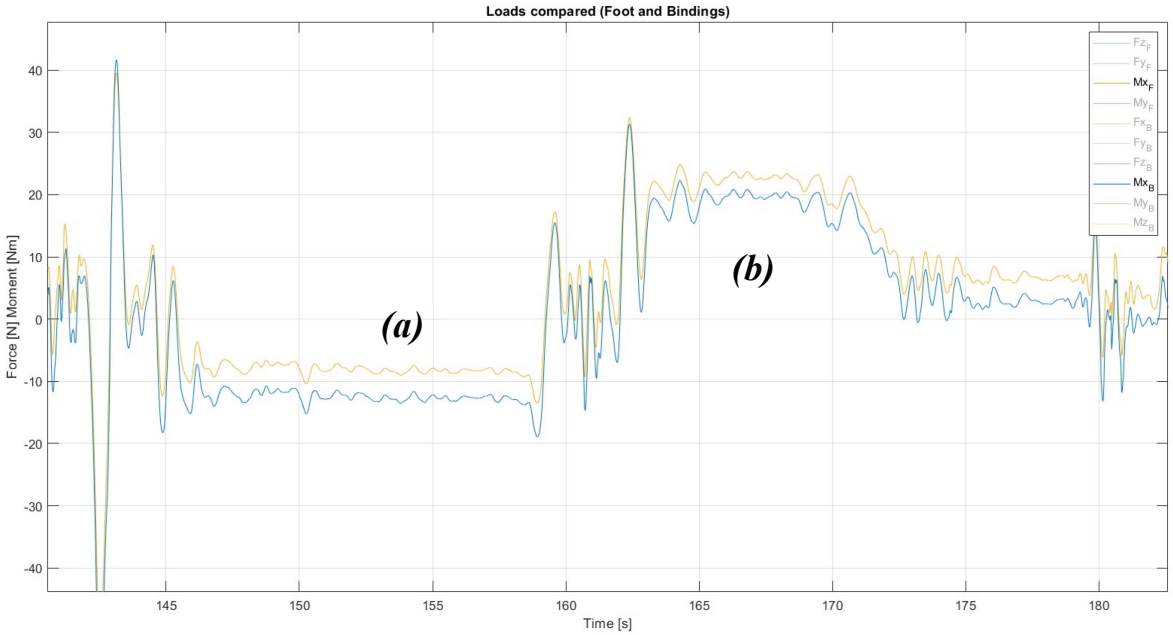


Figure 12.25: (a) M_x when leaning right

(b) M_x when leaning left

The COP calculated from the loads measured by the load cells is shown in Figure 12.26. A line shows where has been calculated the average.

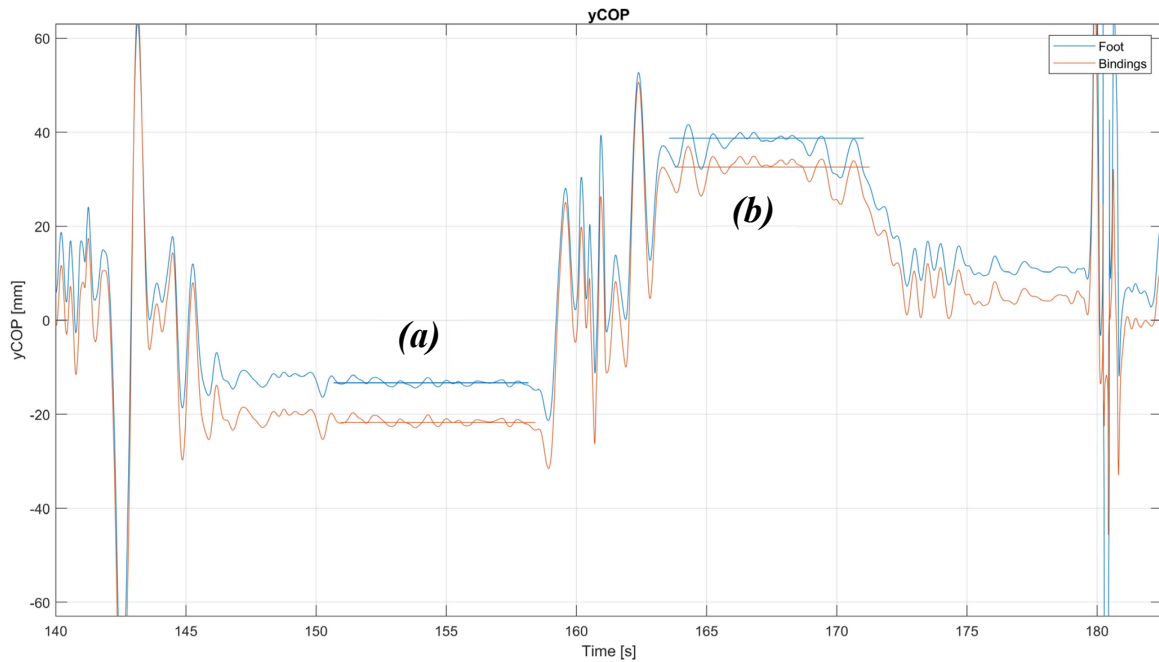


Figure 12.26: (a) Y_{COP} when leaning right

(b) Y_{COP} when leaning left

The results obtained from the three systems are compared here:

Comparison of Y_{COP} [mm]

	Foot load cell	Bindings load cells
Leaning Right	-13	-21
Leaning Left	39	34
$\Delta Y_{COP} = \text{Left} - \text{Right}$	52	55

Table 16: Comparison of COP coordinates

The COP displacement along the y-axis is correctly smaller than the one in the x-axis, as the COP must not exit the bindings area.

12.5 Dynamic location of the Centre of Pressure

Taking as reference the bindings load cells, it verified if the foot load cell is able to measure the same loads and trace the position of the COP during dynamic movements of the skier.

The two load cells systems have been zeroed with the monoski fixed on the bindings, before the skier sat in the seat.

Are performed the following movements:

- Three jumps lifting the body using the aluminium cage (seconds 180-181);
- Four violent leaning forward and backwards (seconds 182-190);
- Four vertical movements using the body to jump (seconds 191-195);
- Two times left and right leaning (seconds 196-209);
- Skier standing still in the seat position (seconds 210-215).

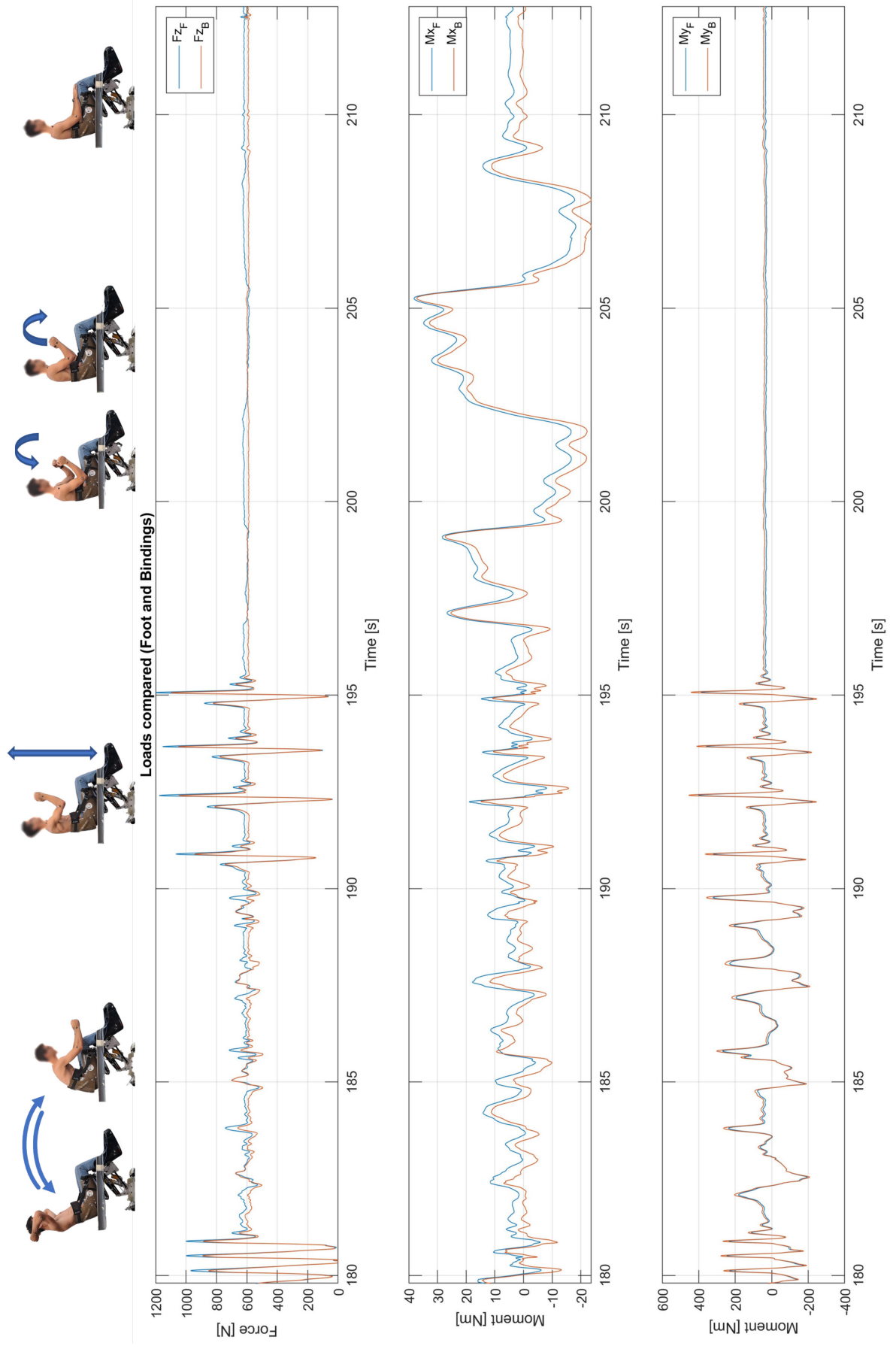


Figure 12.27: Loads due to dynamic movement of the skier

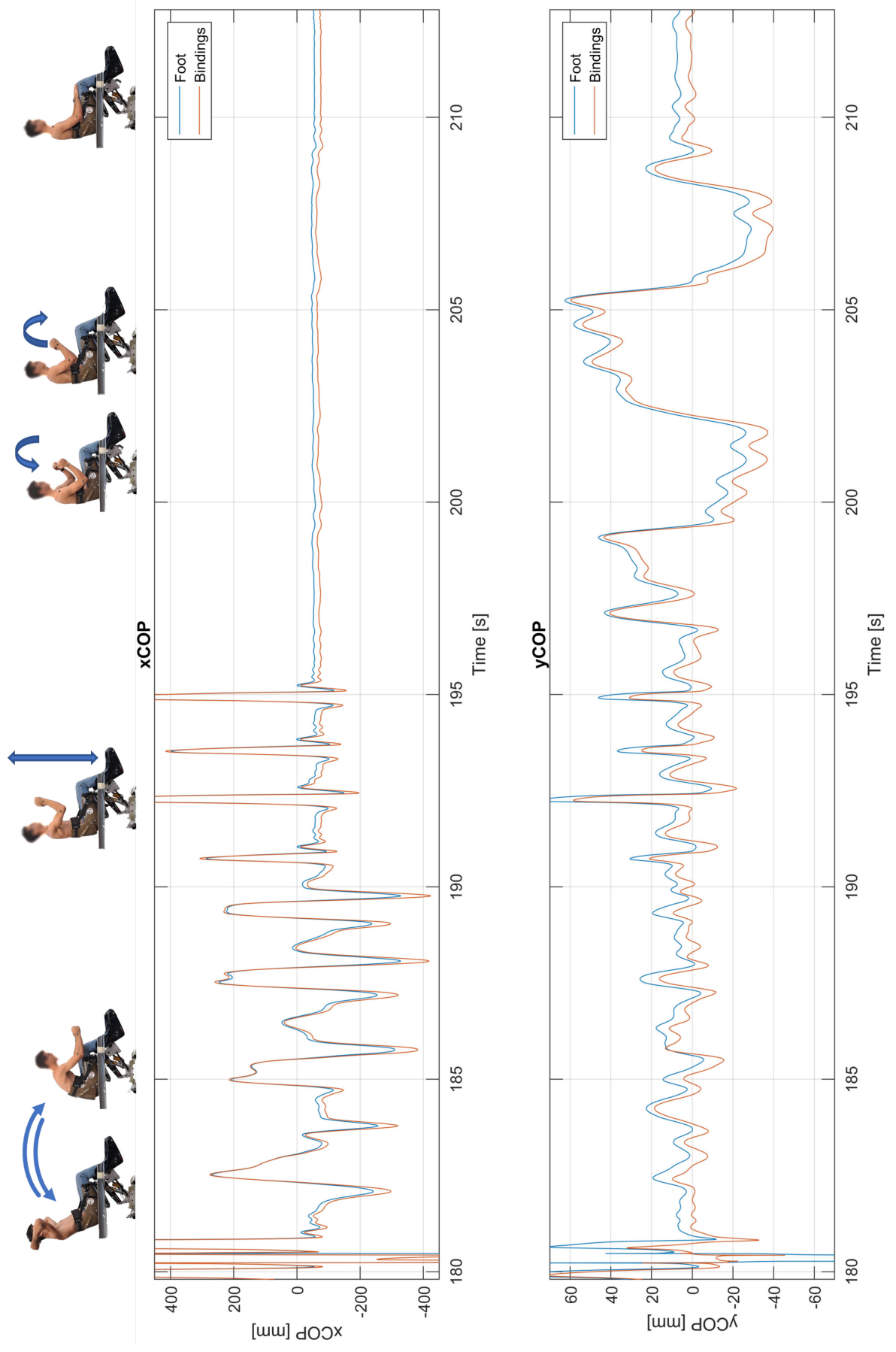


Figure 12.28: COP coordinates due to dynamic movement of the skier

12.6 Forced excitations

These tests aim to describe how the system and the shock absorber respond to dynamic forced loads and vibrations.

In addition, they verify the correct dynamic functioning of the foot load cell by comparing the results of the foot and bindings load cell.

Using the MTS test bench (Cap. 12.1.1) are produced sine forces and step displacements to study the response of the system to forced excitations.

Three different types of tests were performed:

1. Sinusoidal forced vibrations with dead weight and sandbag (Cap. 12.6.1);
2. Step forced vibrations with dead weight and sandbag (Cap. 12.6.2);
3. Static compression of the shock absorber with the seat and upper part of the frame tied with straps (Cap. 12.7).

Since the stresses would have been too dangerous for a human, an artificial model must be used. The dynamic behaviour of the dummy on the monoski was to be studied. Unfortunately, only a dummy of a size too large to fit in the anatomical seat was available. A model was therefore used consisting of three dead weights (30.8 kg in total) and a sandbag weighing 20 kg for a total of 50 kg. The owner of the monoski weighs 60 kg. It was not possible to reach this weight because the dead weight that should represent the legs and feet could not be tied down enough.



Figure 12.29: Weights and sandbag strapped in the seat

The dead weights and sandbags were strapped in the seat to prevent any movement and an elastic rope was added to avoid excessive lateral oscillations that could have led to system instability.

12.6.1 Sinusoidal forced vibrations

The MTS test bench (Cap. 12.1.1) is set in displacement control to produce the sine function at different frequencies (0.5, 1, 2, 3, 4 Hz) and amplitudes (± 10 , ± 20 , ± 30 mm).

Unfortunately, the 4 Hz test at ± 30 mm could not be realised due to the instability of the system.

Only the results of the ± 30 mm amplitude (60 mm of displacement) tests are analysed here. The test at 0.5 Hz is so slow that the monoski behaves almost statically. This test was not considered significant and therefore was discarded.

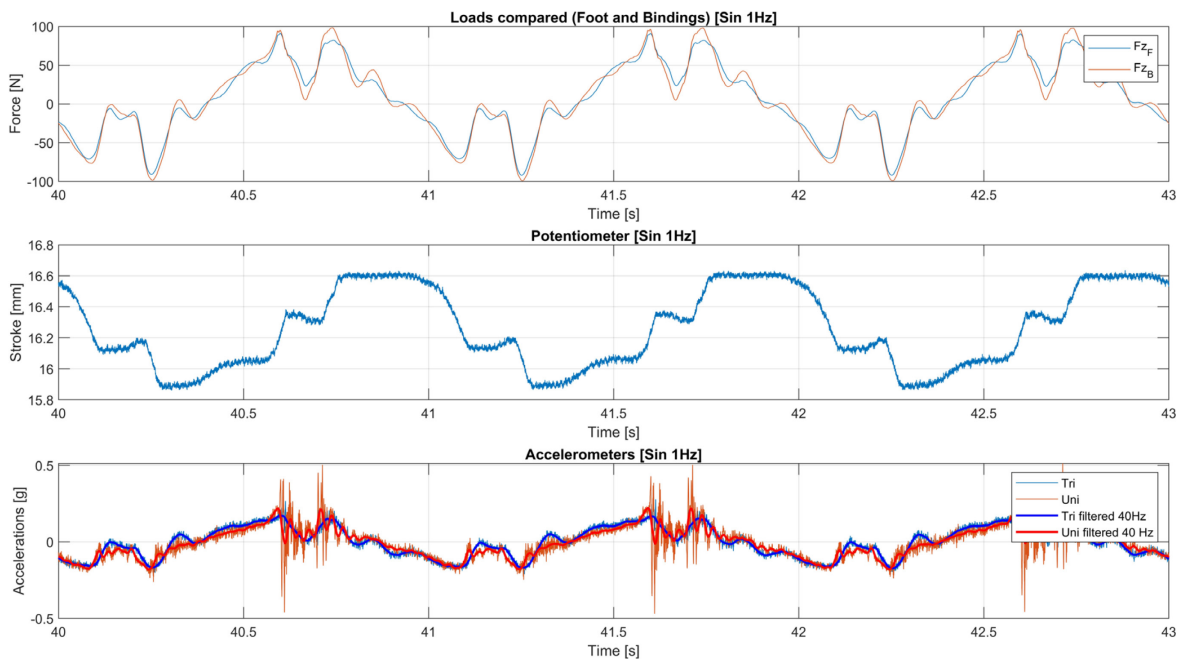


Figure 12.30: Sinusoidal excitation at 1Hz results, ± 30 mm amplitude

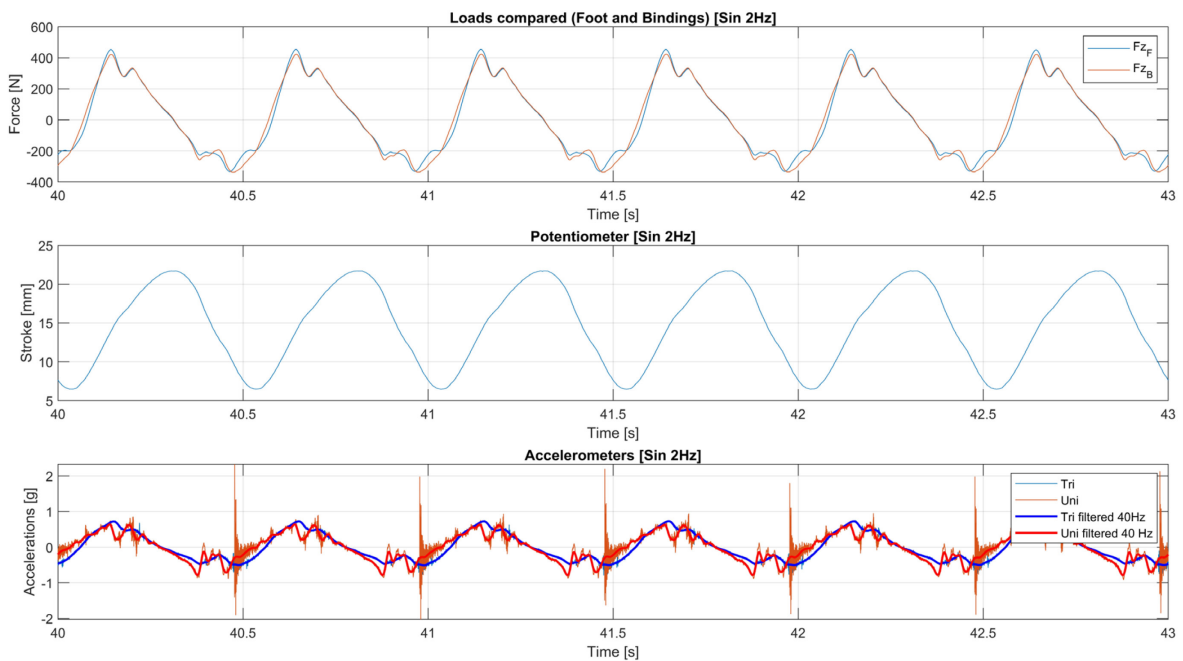


Figure 12.31: Sinusoidal excitation at 2 Hz results, ± 30 mm amplitude

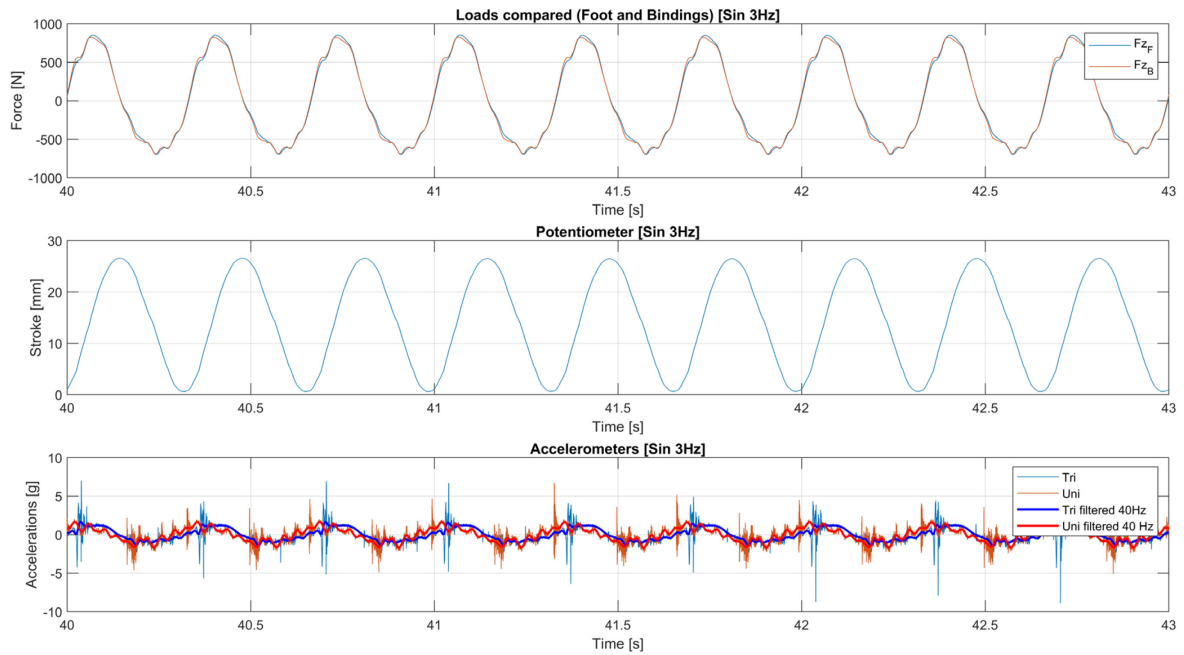


Figure 12.32: Sinusoidal excitation at 3 Hz results, ± 30 mm amplitude

The results show that the load cell again manages to reproduce the loads of the cells taken as reference.

The potentiometer responds correctly to the impulse with larger amplitudes as the force increases.

The uniaxial accelerometer measures the acceleration of the base of the monoski (the bindings). The triaxial accelerometer is placed under the seat and measures the accelerations of the top of the monoski and the skier; only the z-channel was plotted for clarity.

The uniaxial accelerometer often shows spikes and noise; this can be due to the vibrations of the test bench. The triaxial accelerometer, on the other hand, does not show these spikes because there is a damper between the two. In the 3Hz test, however, it shows abnormal spikes. This is probably due to one weight hitting the other in the seat or moving, due to the high loads.

12.6.2 Step forced vibrations

The MTS test bench (Cap. 12.1.1) is set in displacement control to produce vertical steps of different amplitudes (from 10 to 70 mm). An example of run is in Figure 12.33. In a very short time, the cylinder travels to the desired stroke and then remains stationary, slowly returns to its initial position, waits 5 seconds to be sure that the system is still before the next steps. Thanks to the geometry of the articulated parallelogram, the cylinder stroke corresponds almost perfectly to the vertical stroke of the ski bindings. The step is performed at the maximum technical speed possible for the cylinder.

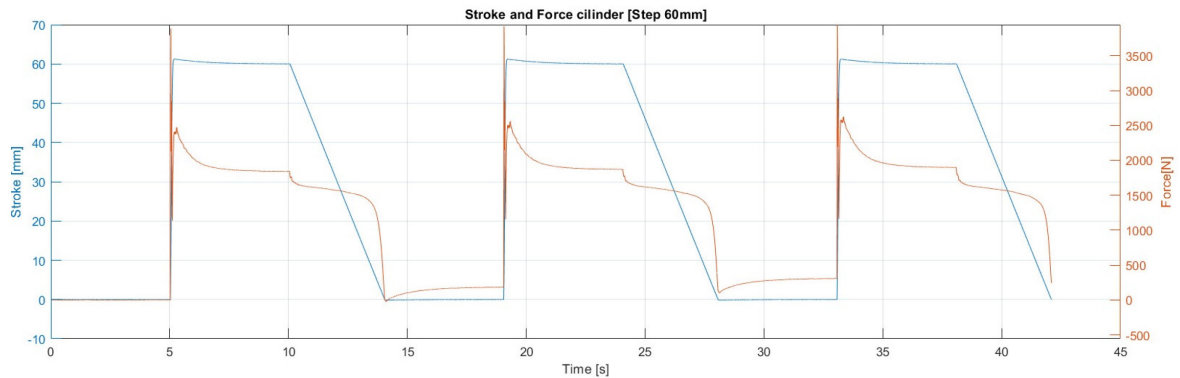


Figure 12.33: Force and stroke of the cylinder measured by the MTS Station Manager

Only the results of the 20, 40, 60mm tests are analysed here.

The forces are minus the weight of the sandbag and the weights in the seat.

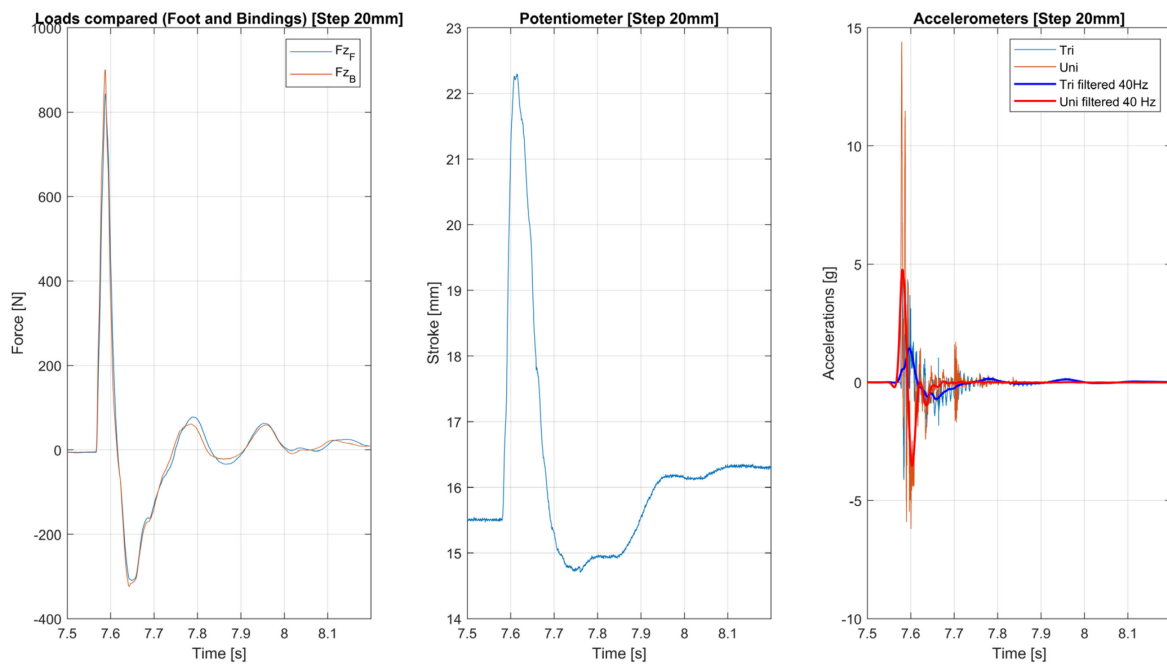


Figure 12.34: Step excitation of 20 mm amplitude

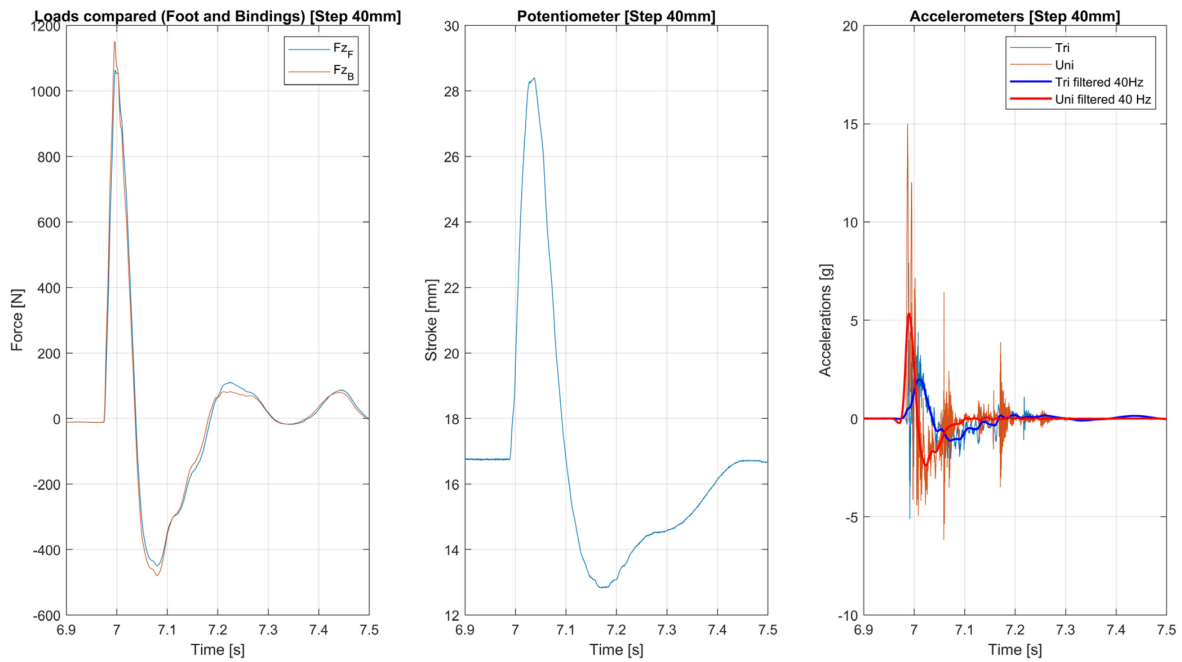


Figure 12.35: Step excitation of 40 mm amplitude

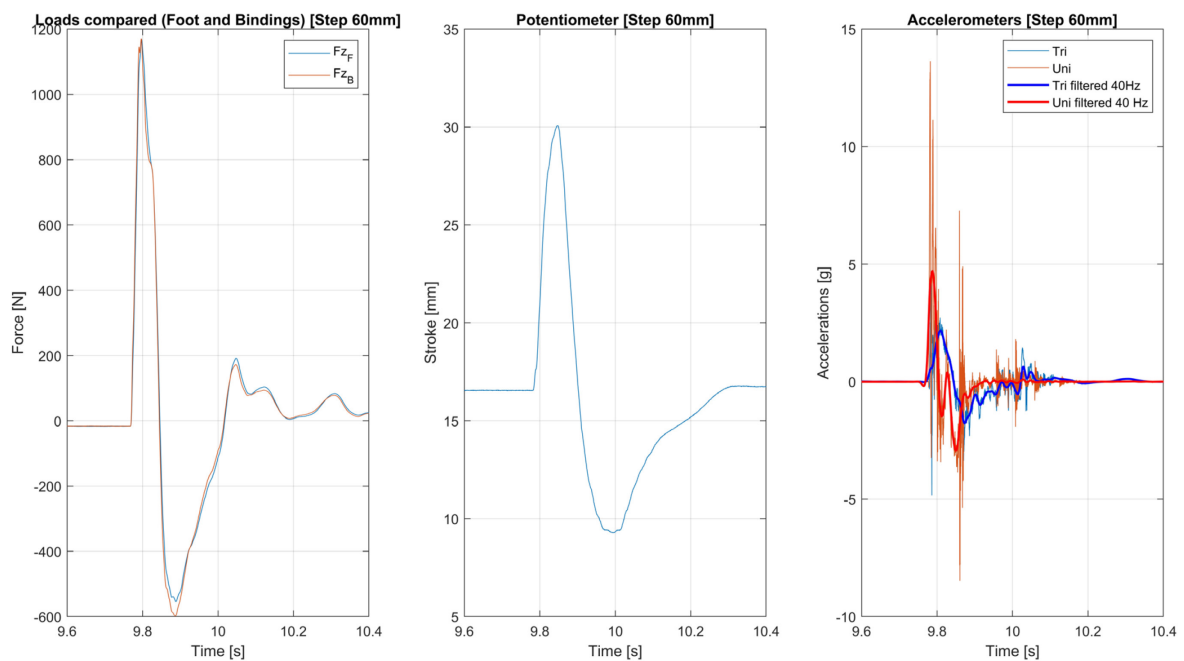


Figure 12.36: Step excitation of 60 mm amplitude

As can be seen in all the graphs, the force before the step is slightly negative because the elastic rope used to balance the monoski, when the articulated parallelogram is at its lowest point, produces a slight upward force. Vice versa when the parallelogram has pushed the monoski upwards.

Both the potentiometer and the accelerometers show a delay relative to the force, and the seat-mounted triaxial accelerometer shows a significantly smaller amplitude of acceleration than the acceleration on the bindings, proving that the shock absorber worked actively in these tests.

12.7 Compression of the shock absorber

A test was carried out to verify the operation of the cell at high loads and the maximum vertical load that the cell can measure. The kinematics of the frame was solved; the forces on each arm of the frame could then be calculated.

The seat weights used for the previous tests were removed and a method was planned to constrain the upper part of the frame with straps so as not to allow it to move upwards.

The test consists of moving the bindings upwards using the MTS test bench while the upper part is restrained.

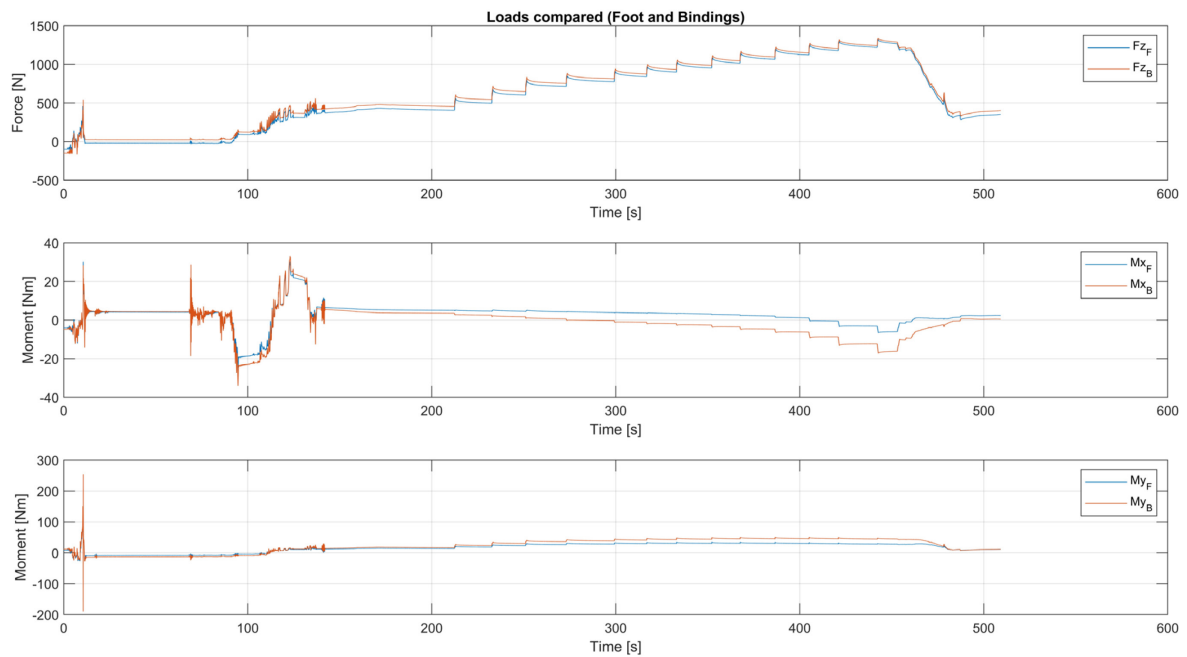


Figure 12.37: Loads due to compression of the shock absorber

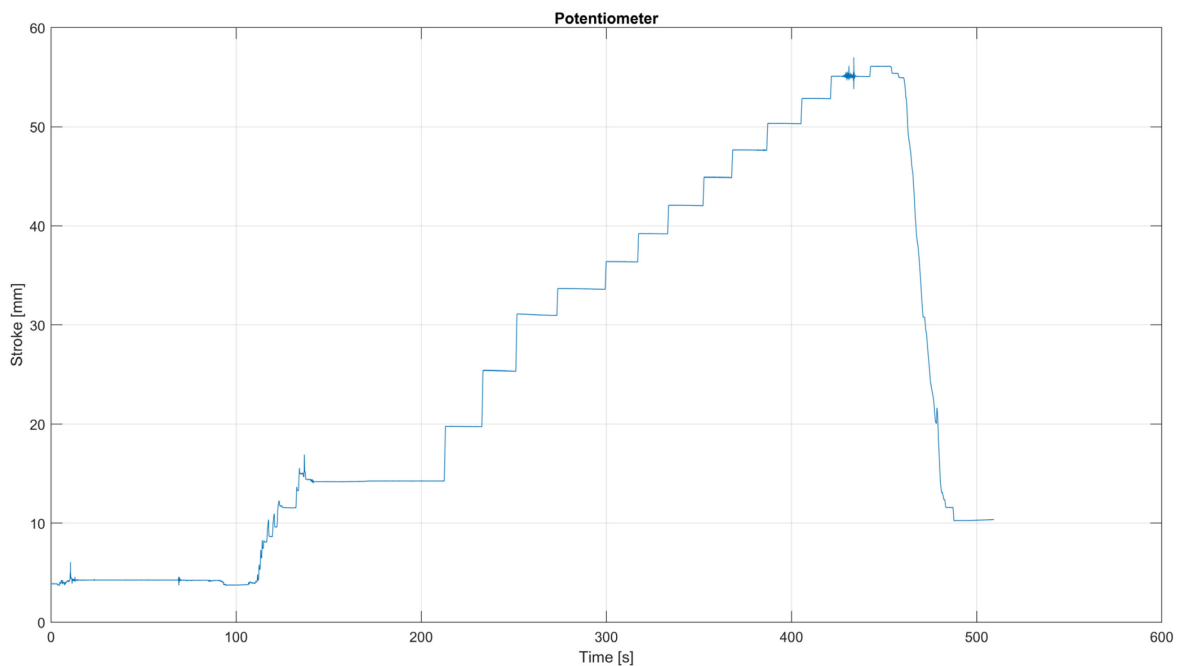


Figure 12.38: Stroke of the potentiometer due to compression of shock absorber

To measure the real compression of the shock absorber the test starts from the unloaded condition (zero stroke is reached when lifting the monoski from the ground).

The first 60 seconds of the test the monoski is fixed on the bindings standing still.

At 90 s the straps are attached to the upper part of the frame and fixed on the test bench. Then the straps are tensioned up to the second 150 to preload the system and thus compress the shock absorber before starting the test bench (this is to increase the total displacement achievable in the test). From second 200 the test bench increases step by step the vertical load.

Due to the uneven tensioning of the straps on the two sides, there is a small Mx moment. In addition, it can be seen that the straps after each elongation tend to lengthen, reducing the load slightly (this is why the forces are not constant but reduce slightly over time). The moment measured on the bindings load cells is greater because these are located lower down and therefore have a greater lever arm to the force of the straps.

The shock absorber compressed to a maximum of 56 mm. Unfortunately, the small vertical displacement of the test bench did not allow the shock absorber to be compressed by its full stroke (100 mm) and did not allow to reach higher loads on the load cell. However, a peak value of 1340 N was reached without any problems. Looking at the voltage trend in the channels (Figure 12.39), it can be seen that the mainly vertical load did not bring the channels too close to the 5 V limit. The channel FzRR, known to be at risk of reaching the limit of the range, in this test reached the value of 4 V at its peak.

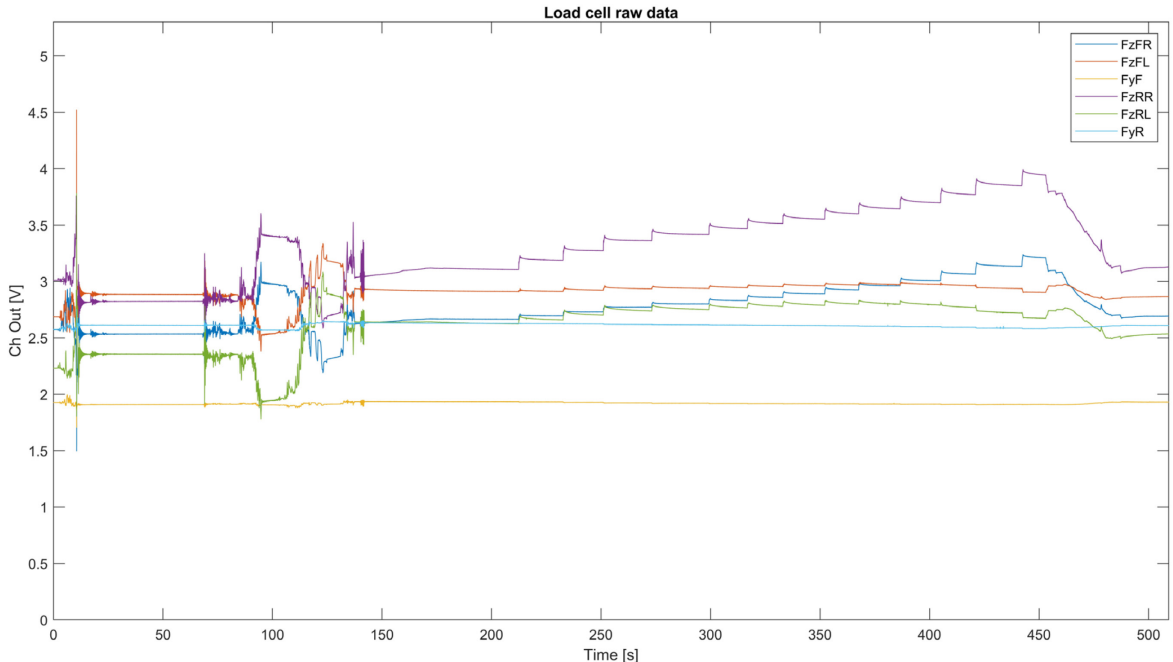


Figure 12.39: Foot load cell channels of the test of compression of shock absorber

12.7.1 Loads on the shock absorber

Knowing the loads measured by the load cells, it is possible to determine the loads acting on the shock absorber from the geometry using the following method.

Method for calculating shock absorber and arm loads

Considering the equilibrium of the aluminium base of the monoski, the functions expressing the loads on the arms and the shock absorber can be derived as a function of their angle. From the measurement of the shock absorber stroke it is then possible to determine the angles.

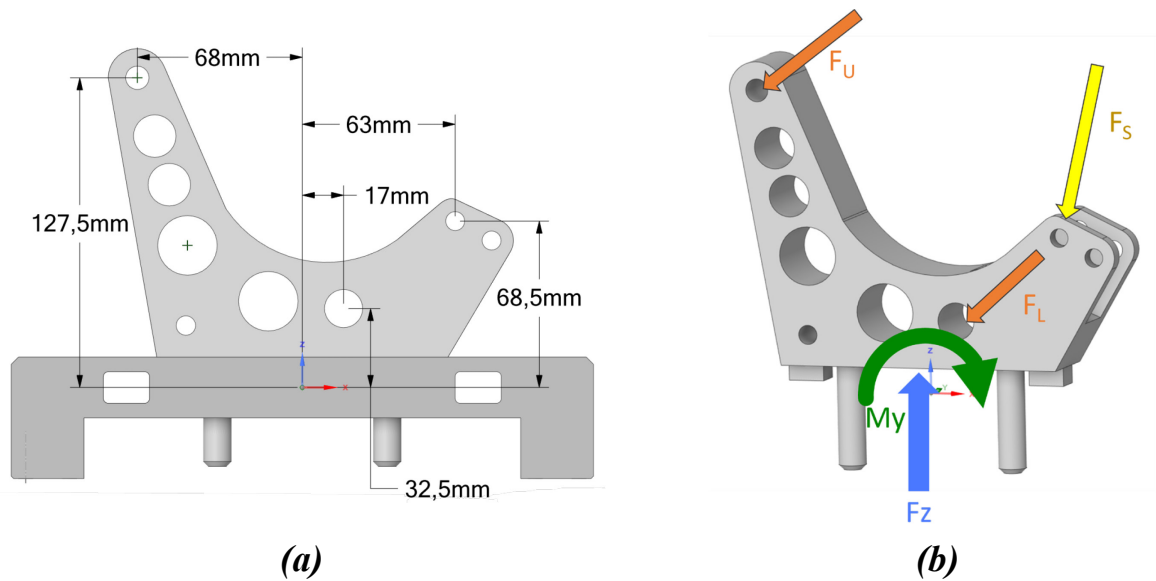


Figure 12.40: (a) Position of the joints respect to the reference system
(b) Equilibrium of the forces

Equilibrium equations of the forces on the aluminium base in the reference system of the load cell. (U = upper arms, S = shock absorber, L = lower arms)

$$\begin{cases} Fz = F_U \cdot \sin \theta_U + F_S \cdot \sin \theta_S + F_L \cdot \sin \theta_L \\ Fx = -F_U \cdot \cos \theta_U - F_S \cdot \cos \theta_S - F_L \cdot \cos \theta_L \\ My = -F_U \cdot \sin \theta_U \cdot 68 - F_U \cdot \cos \theta_U \cdot 127.5 \\ \quad + F_S \cdot \sin \theta_S \cdot 63 - F_S \cdot \cos \theta_S \cdot 68.5 \\ \quad + F_L \cdot \sin \theta_L \cdot 17 - F_L \cdot \cos \theta_L \cdot 32.5 \end{cases}$$

To calculate the forces on the structure, the loads Fz and My measured by the load cells are considered. Fx was assumed as equal to zero because there are no forces acting on the x-axis of the monoski when perfectly horizontal.

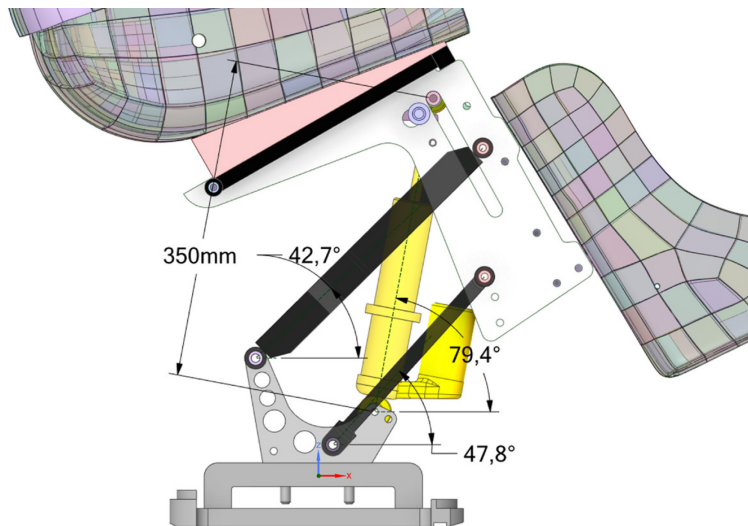


Figure 12.41: Example of angles in relation to shock absorber length

The angles of the shock absorber, upper arms and lower arms were derived from the geometric model of the monoski (Figure 12.41) by varying the length of the shock absorber. The results are in figure below.

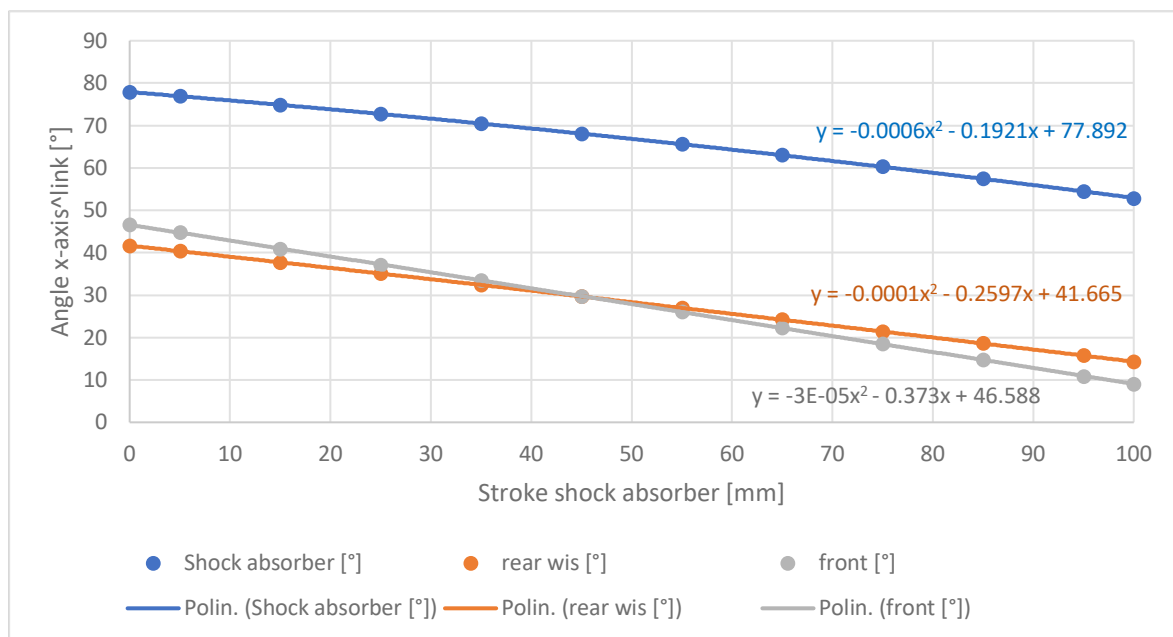


Figure 12.42: Angles of arms and shock absorber in function of the stroke

Using the interpolation equations can be calculated in each instant of each test the angles of the arms and shock absorber. Is then possible to solve the linear system using the operator 'mldivide' (" \") of MATLAB.

In the compression test of the shock absorber, these loads occur:

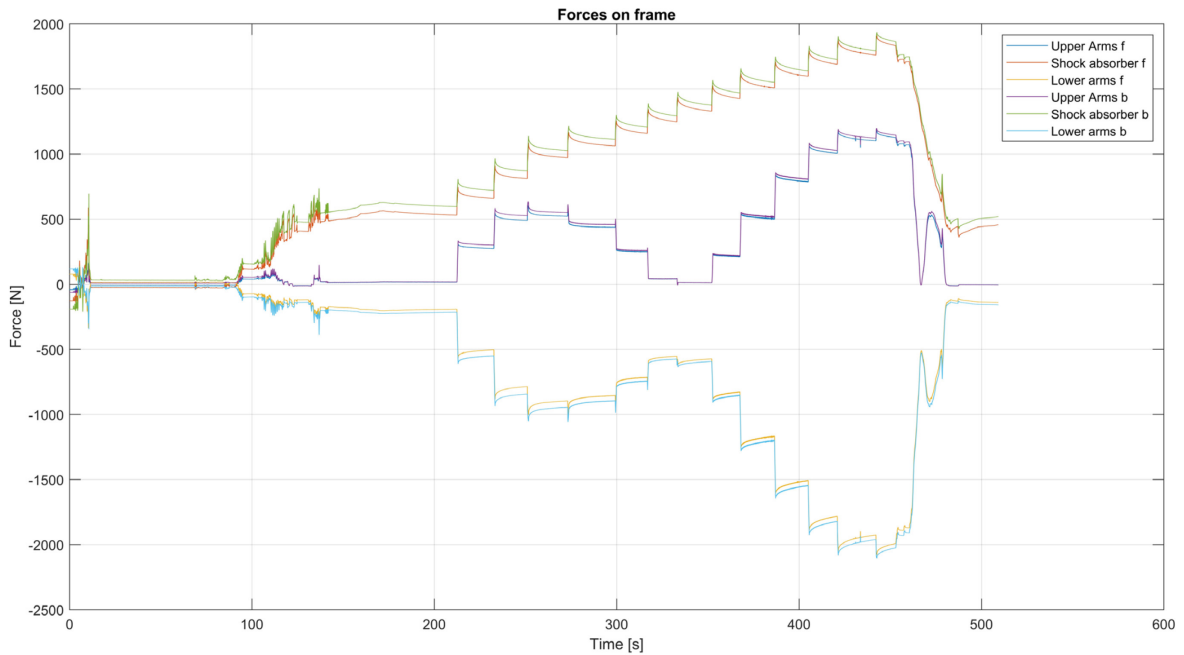


Figure 12.44: Forces on the arms and shock absorber of the compression of shock absorber test

Knowing the force and the stroke of the shock absorber is then possible to calculate the spring stiffness constant k .

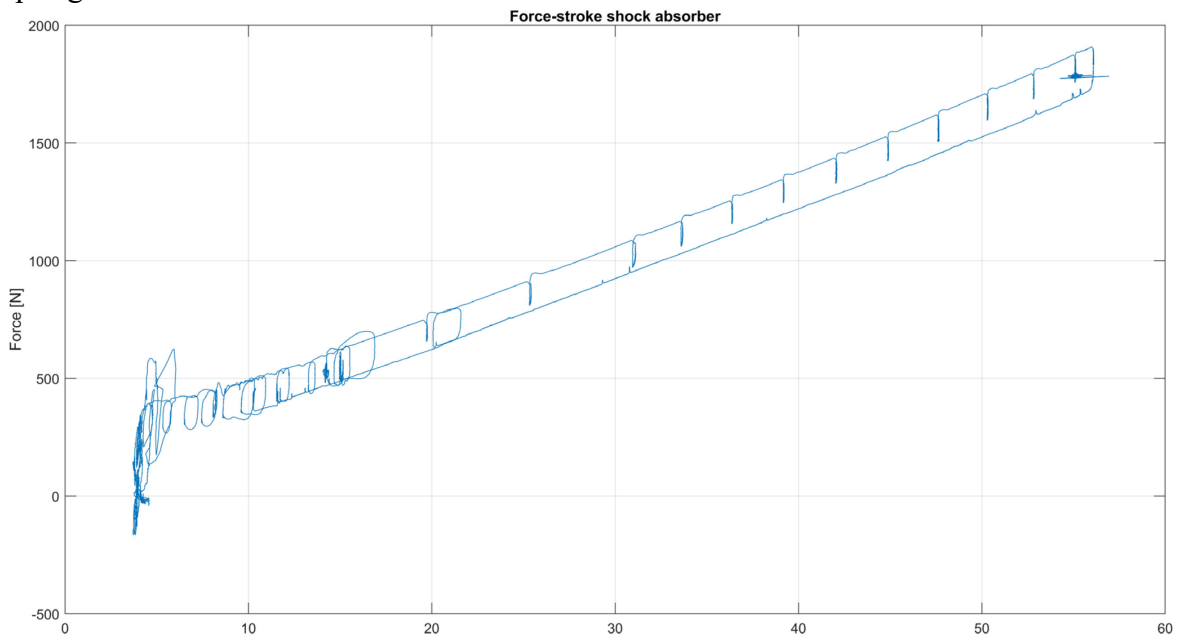


Figure 12.43: Force-stroke plot of the compression of shock absorber test

The elastic constant of the spring is the gradient of the linear interpolation of the results in Figure 12.43:

$$k = \frac{\text{Force [N]}}{\text{Stroke [m]}} = 31800 \text{ N/m}$$

Further developments may involve shock absorber-specific tests to confirm these results.

12.8 Dynamic behaviour of the shock absorber

From the dynamic tests obtained by testing the damper at load cycles with harmonic displacements, the viscous damper characteristic can be derived.

The force-displacement curve of a damper is a closed curve that contains the energy dissipated per cycle. Since the tested damper is not ideal and various phenomena (fluid dynamics, inertia forces, friction forces, elastic forces) are present, the curve produced is not an ellipse but resembles one.

The results of tests with sinusoidal forced vibrations (Cap. 12.6.1) are considered here.

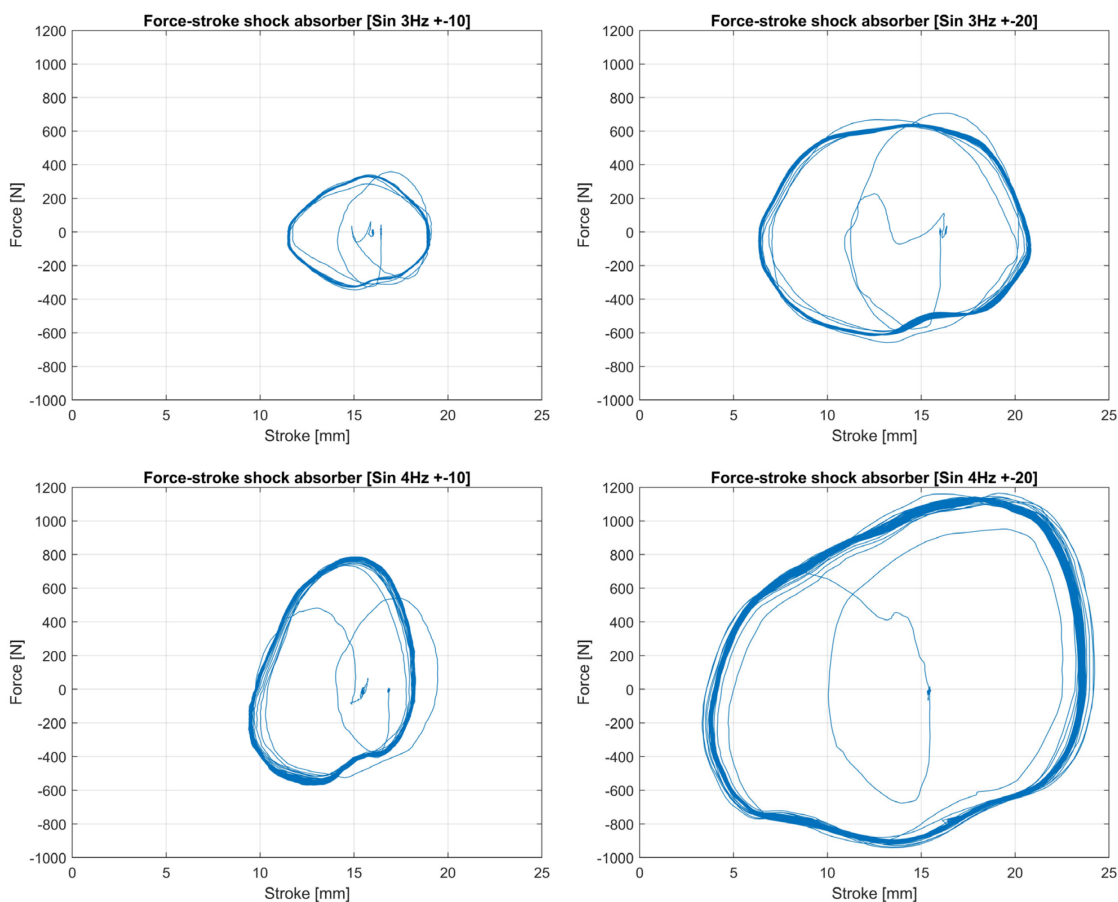


Figure 12.45: Results of the sinusoidal forced vibrations tests

It can be seen that the diagram is squarer than an ellipse. This may suggest that the force depends on the velocity with a power less than one.

The settings of the TTX by Öhlins shock absorber used in the test are:

- Precompression spring (free thread): 36.64 mm;
- Rebound: from each end 1 clockwise turn, 2 counterclockwise turn;
- Compression: from each end 2.5 clockwise turn, 1 counterclockwise turn.

12.9 Transfer function

Fourier Transform is a linear function used to analyse a signal in the frequency domain. In this way a complex time-based signal can be converted into its constituent frequencies.

Fourier Transform:

$$F(f(t)) = \int_{-\infty}^{+\infty} e^{-i\omega t} f(t) dt$$

Fourier Transform must be used with continuous analytical functions. Discrete function like signals obtained from sampling or from sensors (discrete signals stored in array) must be used Fast Fourier Transform (FFT).

To characterize the response of a mechanical system under external forces it is useful to define a Transfer function (FRF [32]) between input and output of the system. These outputs and inputs in the case under analysis are acceleration arrays. Transfer Function is a complex function defined in frequency domain and it's the ratio between Fourier transform of output signal and Fourier transform of the input one and it describes the behaviour of the system.

This function can be plotted through two diagrams. The first one represents the magnitude of output-input ratio in the frequency domain; the second diagram shows the phase in relation to frequency.

Transfer function is defined by the following equation

$$H(f) = \frac{Y(f)}{X(f)}$$

In this case, triaxial and uniaxial accelerometer accelerations are used respectively as outputs ($Y(f)$) and inputs ($X(f)$).

The uniaxial accelerometer is the input because it is fixed on the foot of the monoski and describes the vertical acceleration of the forcer. The triaxial accelerometer is fixed under the seat, considering only the z-channel, it is the output, i.e. the response of the system.

For the analyses, were used accelerations in figure 12.30, 12.31, 12.32 of Cap. 12.6.1 and figure 12.34, 12.35, 12.36 Cap. 12.6.2 respectively.

The analysis are carried out in HBM SoMat InField.

12.9.1 Sinusoidal forced vibrations

The results of the sinusoidal forced vibration tests (Cap. 12.6.1) are presented below. On the horizontal axis are frequencies [Hz], on the vertical axis is the Transfer function.

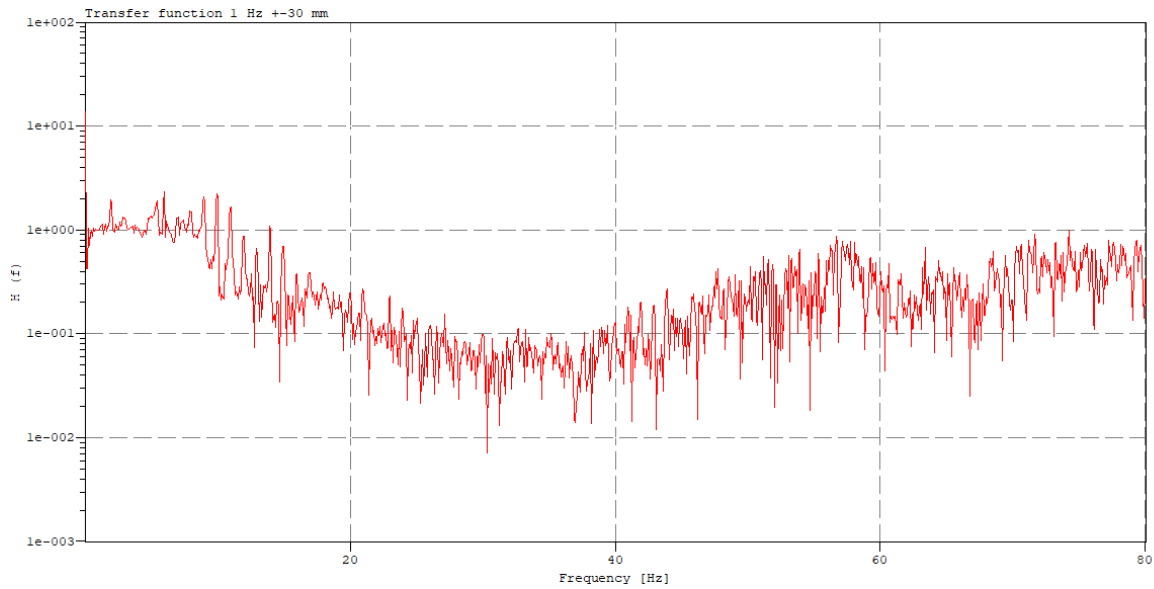


Figure 12.46: FRF of the sinusoidal excitation at 1 Hz results, ± 30 mm amplitude

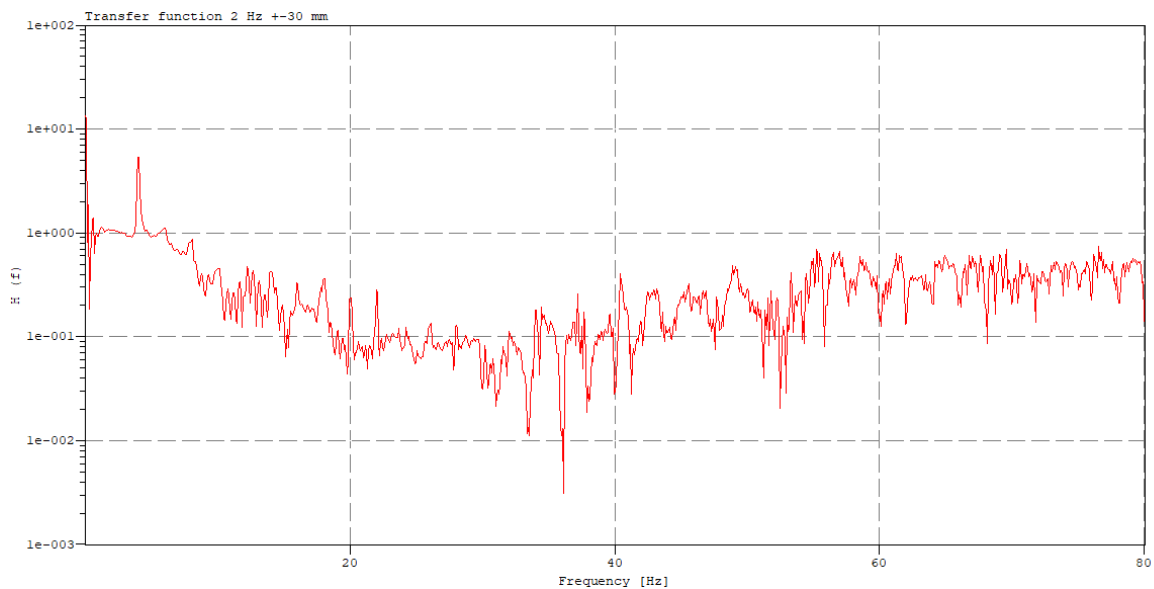


Figure 12.47: FRF of the sinusoidal excitation at 2 Hz results, ± 30 mm amplitude

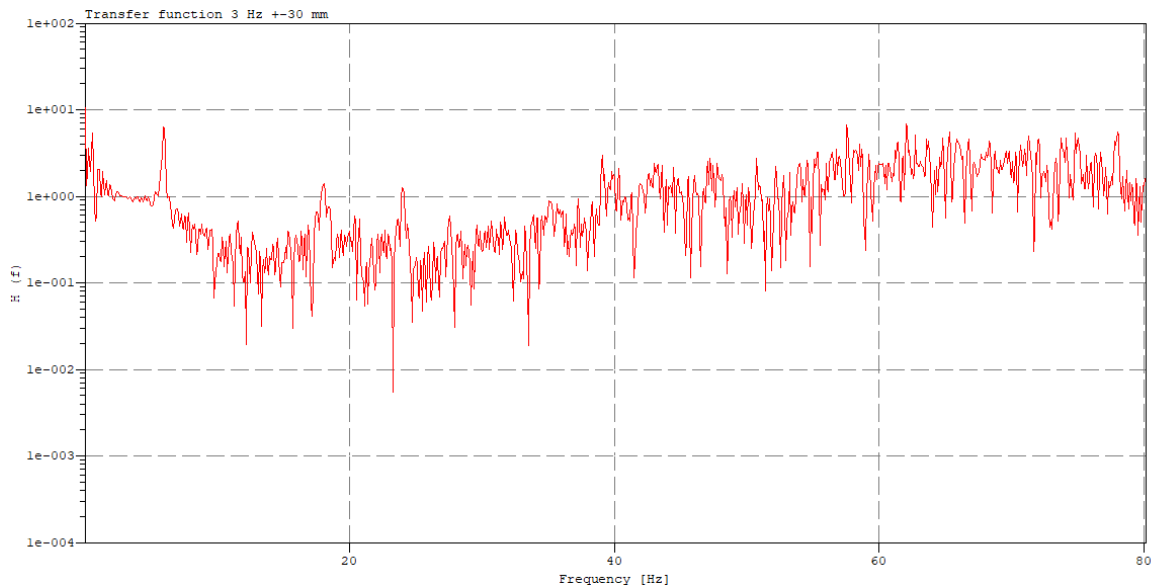


Figure 12.48: FRF of the sinusoidal excitation at 3 Hz results, ± 30 mm amplitude

Frequencies up to 80 Hz are plotted because the frequencies that are harmful to the human body are the low frequencies up to about 70 Hz.

The accelerations used to calculate the transfer function are not filtered since a filter would change the $H(f)$ only at the very high frequencies. If InField is set the maximum resolution in frequency, an Overlap of 33% and the type of domain as 'Hanning'.

It can be seen that accelerations are damped, in fact the transfer function is less than one for frequencies between about 10 and 50 Hz. This trend occurs in all tests and confirms that the shock absorber works to damp those frequencies that are the most harmful. Note that the y-axis is on a logarithmic scale, which means that the amplitudes of those particular frequencies are greatly diminished.

At very low frequencies the transfer function is above one, this means that the shock absorber is not dampening and is transmitting the slow movements to the skier. At 6Hz a resonance can be seen.

12.9.2 Step forced vibrations

The results of the step forced vibration tests (Cap. 12.6.2) are presented below.

Exciting the system with a step forcer excites a greater frequency spectrum than a sinusoidal excitation.

On the horizontal axis are frequencies [Hz], on the vertical axis is the Transfer function.

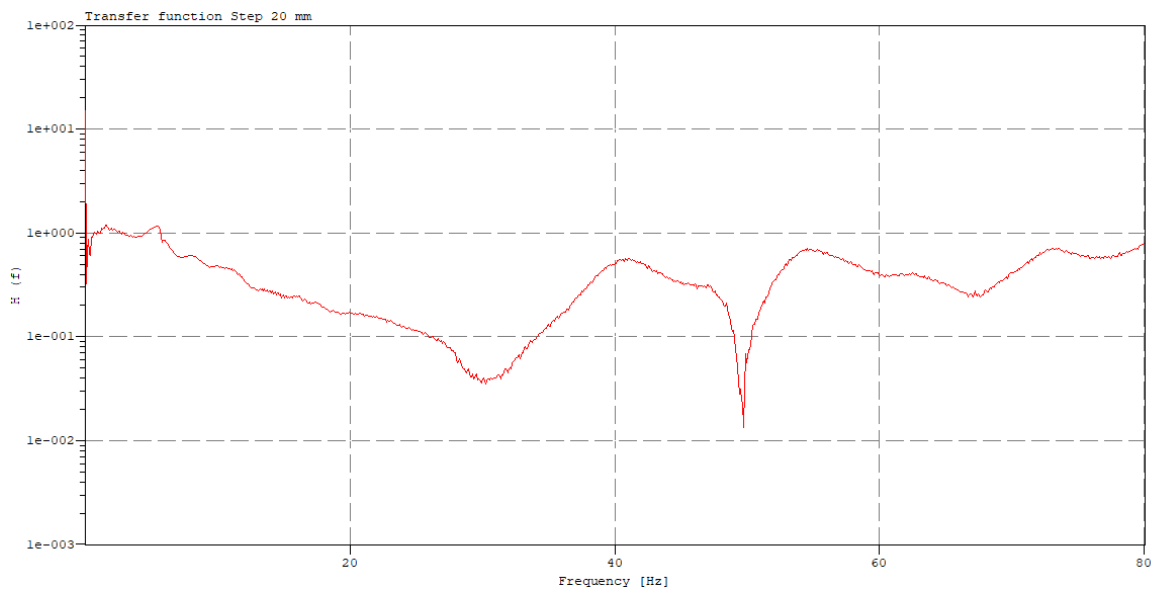


Figure 12.50: FRF of the step excitation of 20 mm amplitude

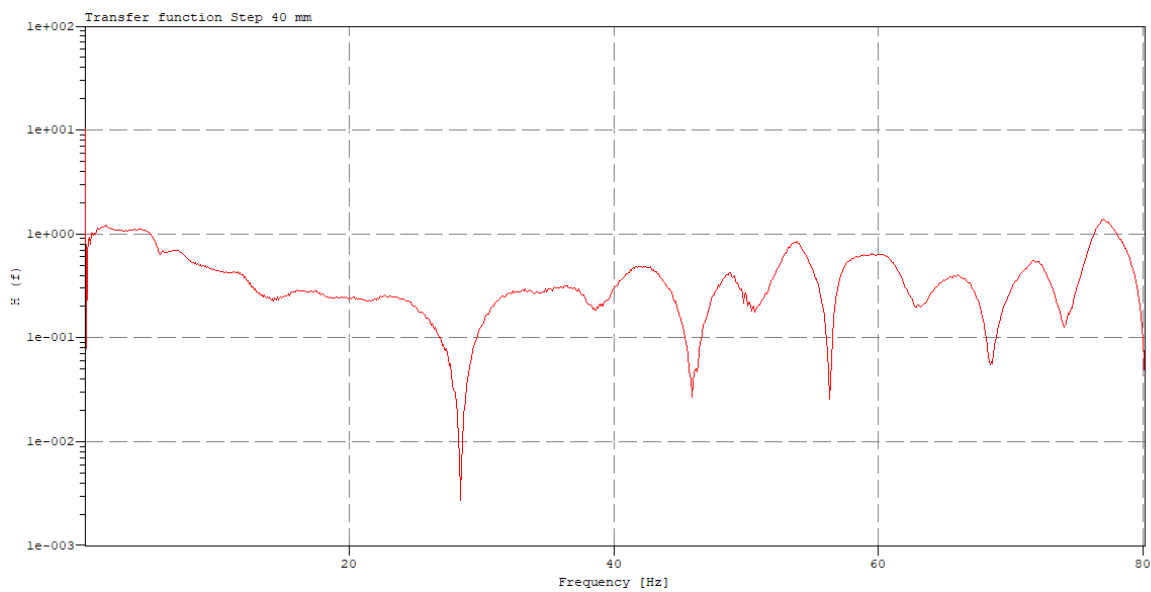


Figure 12.49: FRF of the step excitation of 40 mm amplitude

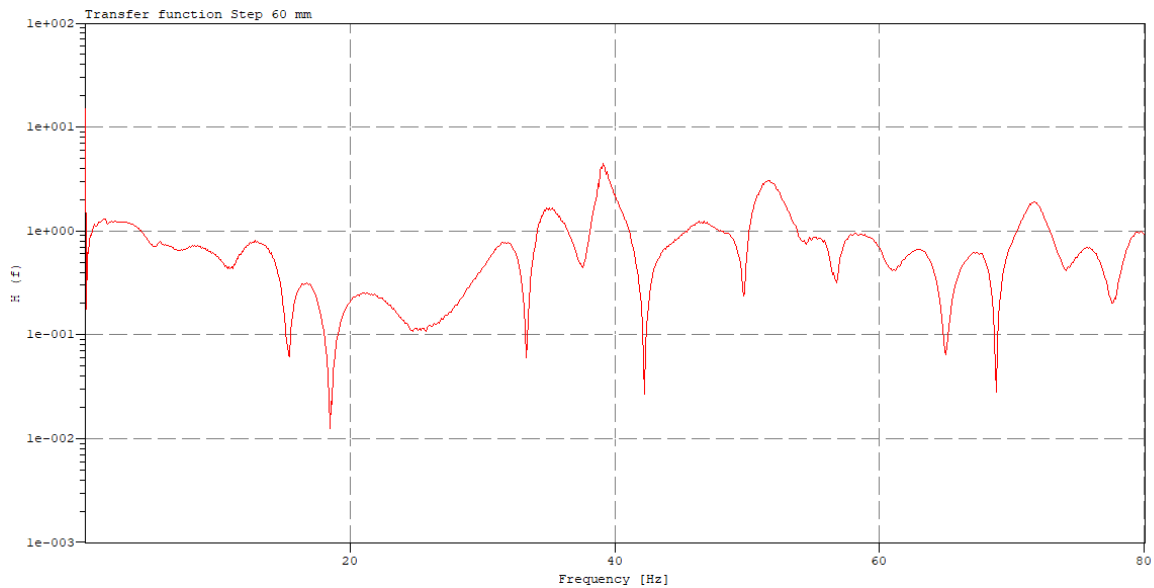


Figure 12.51: FRF of the step excitation of 60 mm amplitude

Again the plot is limited to 80 Hz.

The accelerations used to calculate the FRF are not filtered. If InField is set the maximum resolution in frequency, an Overlap of 33% and the type of domain as ‘Hanning’.

It can be seen that exciting with a step produces the damper to suppress the frequencies between 5 Hz and 30 Hz confirming the previous result.

The method adopted allows to study the dynamic behaviour of the system with a dummy or weights in the seat. Further tests could use a dummy seating in the monoski to study the transmission of bumps and vibration on the human body [33].

13 CONCLUSION AND FURTHER DEVELOPMENTS

The aim of the thesis was to find a methodology for studying the complex monoski system. Various solutions, models and sensors were evaluated in order to develop a monoski that would allow data acquisition. A lot of information, suggestions and improvements were gathered regarding the use, design and practicality of using the monoski.

The Instrumented Monoski that was developed proved to be a valuable platform for deriving the characteristics of this complex model. Future ski slope tests will provide useful experience for the following design stage.

The model and methods for indoor and outdoor testing were successfully developed. This was tested in the laboratory at Mid Sweden University, allowing strengths and problems to be discovered. A second Instrumented Monoski was then assembled and tested at the laboratory of the University of Padua, integrating the improvements that the first model provided.

In particular, the amplifiers were successfully installed inside the load cell and the load cell was calibrated with both a traditional and an innovative approach using Neural Networks. Neural Networks have proven to be an interesting method that can enhance and speed up calibration operations with excellent results. The improved load cell was successfully tested for static and dynamic loads with results comparable to commercial load cells.

Indoor tests were carried out providing an enormous amount of data to analyse.

This interesting work offers the possibility of many future developments: the Instrumented Monoski can soon be used for tests on ski slopes, opening the way for the design of an innovative, cost-effective and high-performance monoski.

13.1 Future developments

Future developments may concern the field of studying stresses and vibrations in order to make the monoski safer and more comfortable.

The calibration of the load cell could be improved by training Neural Networks with multiple coupled loads to train all the range of possible loads. The maximum loads that can be measured by the load cell before it saturates the amplifiers must also be researched.

The linear potentiometer produced excellent results in each test, showing high quality signal, little noise and no sensitivity to vibrations. Another improvement that can be explored to overcome the problems of space and weakness of a linear potentiometer positioned in parallel to the shock absorber, is to use angular potentiometers at the joints of the monoski. Since the kinematic motion is rigid, it is only necessary to know an angle on a joint to solve it. Angular potentiometers are cheap, simple to apply and calibrate, and would completely avoid the problem of opening the monoski to take the chairlift with the potentiometer connected.

Angle potentiometers could also be used to measure the angles of the skier's body segments during the run, instead of gyroscopes, optical systems or IMUs, as it has been done so far, increasing the reliability of the data collected.

The behaviour of the shock absorber varying the settings has not been explored in this thesis, but provides research input for future studies. The same applies to the setting of the COP and suspension kinematics.

In order to make the measuring system applicable to more than one model of monoski, it is possible to think of a different load cell system: using commercial load cells and constructing a different fastening system depending on the model of monoski used. In this way, there would be the reliability of a commercial load cell and, at the same time, the flexibility on which model of monoski to apply it to. This would give the opportunity to study the behaviour of different monoskis and test possible prototypes.

APPENDIX

Load cell amplifiers boards design

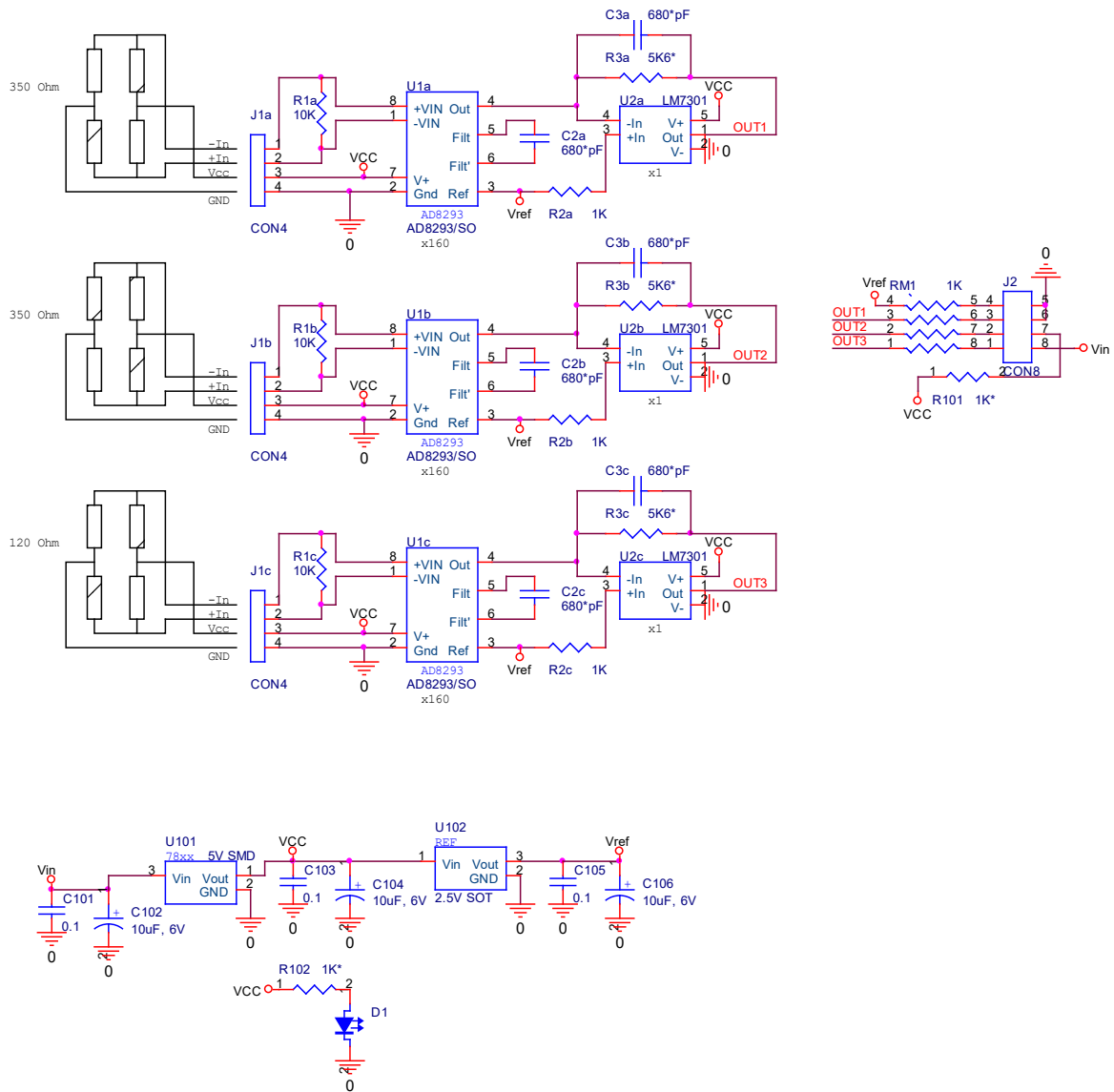


Figure A.1: Principle diagram of a single amplifier board

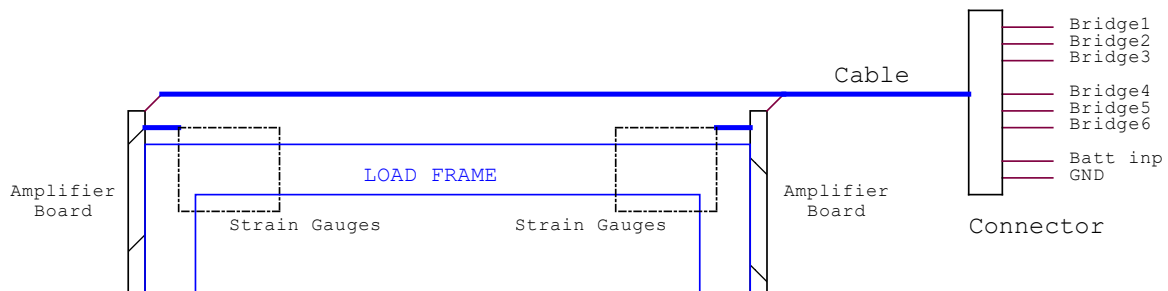


Figure A.2: Amplifiers board mounting

TOP BOT

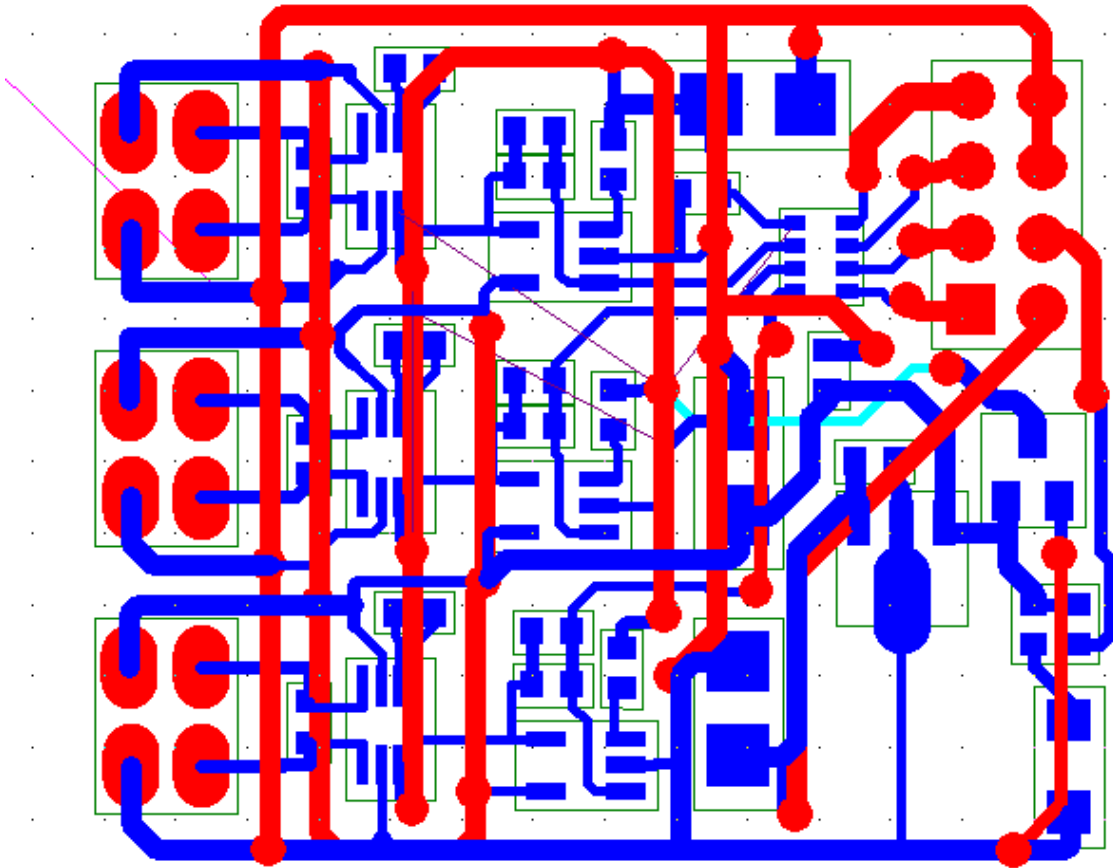


Figure A.3: 'See-through' of two PCB layers

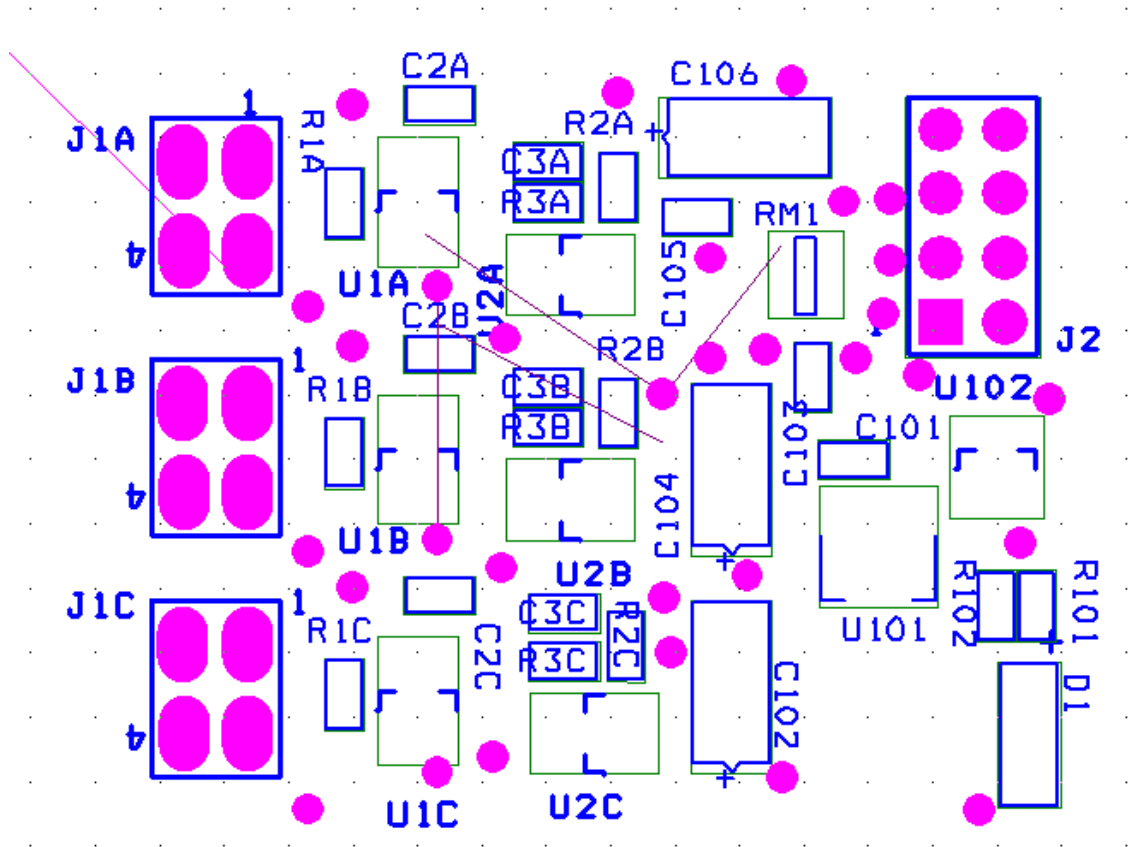


Figure A.4: Component placement

#	Schematic Page	Part Reference	Value	Part N...	Part ...	D...	Source Library	Source Package
1	SCHEMATIC1 : PAGE1	R3	5K6*		Undefined		C:\CADENCE\ORCAD_9.2.3\TOOLS\CAPTURE\LIBRARY\DISCRETE.OLB	R
2	SCHEMATIC1 : PAGE1	C2	680*pF		Undefined		C:\CADENCE\ORCAD_9.2.3\TOOLS\CAPTURE\LIBRARY\IEC\DEVICE.OLB	C
3	SCHEMATIC1 : PAGE1	J1	CON4		Undefined		C:\USERS\AK\DESKTOP\ORCAD WORK\2022\NEW LOADCELL\NEW LOADCELL...	CON4_0
4	SCHEMATIC1 : PAGE1	C3	680*pF		Undefined		C:\CADENCE\ORCAD_9.2.3\TOOLS\CAPTURE\LIBRARY\IEC\DEVICE.OLB	C
5	SCHEMATIC1 : PAGE1	R2	1K		Undefined		C:\CADENCE\ORCAD_9.2.3\TOOLS\CAPTURE\LIBRARY\DISCRETE.OLB	R
6	SCHEMATIC1 : PAGE1	R102	1K*		Undefined		F:\WORK 2003\STUDENTS\RFID WORK\ORCAD-RFID\LIBRARIES\CIS\ANDREL16...	R
7	SCHEMATIC1 : PAGE1	U2	LM7301		Undefined		C:\USERS\AK\DESKTOP\ORCAD WORK\2022\NEW LOADCELL\NEW LOADCELL...	LM7301_0
8	SCHEMATIC1 : PAGE1	J1	CON4		Undefined		C:\USERS\AK\DESKTOP\ORCAD WORK\2022\NEW LOADCELL\NEW LOADCELL...	CON4_0
9	SCHEMATIC1 : PAGE1	C105	0.1		Undefined		C:\CADENCE\PSD_14.2\TOOLS\CAPTURE\LIBRARY\DISCRETE.OLB	CAP NP
10	SCHEMATIC1 : PAGE1	J2	CON8		Undefined		C:\USERS\AK\DESKTOP\ORCAD WORK\2022\NEW LOADCELL\NEW LOADCELL...	CON8_0
11	SCHEMATIC1 : PAGE1	C103	0.1		Undefined		C:\CADENCE\PSD_14.2\TOOLS\CAPTURE\LIBRARY\DISCRETE.OLB	CAP NP
12	SCHEMATIC1 : PAGE1	U1	AD8293/SO		Undefined		F:\WORK\ORCAD-WORK\2018\LOAD_CELL\LOADCELLS_2018.DSN	AD8293/SOT23
13	SCHEMATIC1 : PAGE1	RM1	1K		Undefined		F:\WORK\ORCAD-WORK\2014\ADEVOTECH_2014\CONTROL_BOX.DSN	R-4mat8_0
14	SCHEMATIC1 : PAGE1	U102	2.5V SOT		Undefined		C:\USERS\AK\DESKTOP\ORCAD WORK\2022\NEW LOADCELL\NEW LOADCELL...	CON3_1
15	SCHEMATIC1 : PAGE1	R1	10K		Undefined		C:\CADENCE\ORCAD_9.2.3\TOOLS\CAPTURE\LIBRARY\DISCRETE.OLB	R
16	SCHEMATIC1 : PAGE1	R2	1K		Undefined		C:\CADENCE\ORCAD_9.2.3\TOOLS\CAPTURE\LIBRARY\DISCRETE.OLB	R
17	SCHEMATIC1 : PAGE1	U1	AD8293/SO		Undefined		F:\WORK\ORCAD-WORK\2018\LOAD_CELL\LOADCELLS_2018.DSN	AD8293/SOT23
18	SCHEMATIC1 : PAGE1	C101	0.1		Undefined		C:\CADENCE\PSD_14.2\TOOLS\CAPTURE\LIBRARY\DISCRETE.OLB	CAP NP
19	SCHEMATIC1 : PAGE1	R1	10K		Undefined		C:\CADENCE\ORCAD_9.2.3\TOOLS\CAPTURE\LIBRARY\DISCRETE.OLB	R
20	SCHEMATIC1 : PAGE1	R101	1K*		Undefined		F:\WORK 2003\STUDENTS\RFID WORK\ORCAD-RFID\LIBRARIES\CIS\ANDREL16...	R
21	SCHEMATIC1 : PAGE1	R3	5K6*		Undefined		C:\CADENCE\ORCAD_9.2.3\TOOLS\CAPTURE\LIBRARY\DISCRETE.OLB	R
22	SCHEMATIC1 : PAGE1	U2	LM7301		Undefined		C:\USERS\AK\DESKTOP\ORCAD WORK\2022\NEW LOADCELL\NEW LOADCELL...	LM7301_0
23	SCHEMATIC1 : PAGE1	R3	5K6*		Undefined		C:\CADENCE\ORCAD_9.2.3\TOOLS\CAPTURE\LIBRARY\DISCRETE.OLB	R
24	SCHEMATIC1 : PAGE1	C2	680*pF		Undefined		C:\CADENCE\ORCAD_9.2.3\TOOLS\CAPTURE\LIBRARY\IEC\DEVICE.OLB	C
25	SCHEMATIC1 : PAGE1	J1	CON4		Undefined		C:\USERS\AK\DESKTOP\ORCAD WORK\2022\NEW LOADCELL\NEW LOADCELL...	CON4_0
26	SCHEMATIC1 : PAGE1	C104	10uF, 6V		Undefined		F:\WORK 2003\STUDENTS\RFID WORK\ORCAD-RFID\LIBRARIES\CIS\ANDREL16...	CAPACITOR POL
27	SCHEMATIC1 : PAGE1	D1	GN		Undefined		C:\USERS\AK\DESKTOP\ORCAD WORK\2022\ARDUSHIELD-22\ARDUSHIELD.DSN	DIODE ZENER_2
28	SCHEMATIC1 : PAGE1	U2	LM7301		Undefined		C:\USERS\AK\DESKTOP\ORCAD WORK\2022\NEW LOADCELL\NEW LOADCELL...	LM7301_0
29	SCHEMATIC1 : PAGE1	C3	680*pF		Undefined		C:\CADENCE\ORCAD_9.2.3\TOOLS\CAPTURE\LIBRARY\IEC\DEVICE.OLB	C
30	SCHEMATIC1 : PAGE1	C2	680*pF		Undefined		C:\CADENCE\ORCAD_9.2.3\TOOLS\CAPTURE\LIBRARY\IEC\DEVICE.OLB	C
31	SCHEMATIC1 : PAGE1	C3	680*pF		Undefined		C:\CADENCE\ORCAD_9.2.3\TOOLS\CAPTURE\LIBRARY\IEC\DEVICE.OLB	C
32	SCHEMATIC1 : PAGE1	R2	1K		Undefined		C:\CADENCE\ORCAD_9.2.3\TOOLS\CAPTURE\LIBRARY\DISCRETE.OLB	R
33	SCHEMATIC1 : PAGE1	U1	AD8293/SO		Undefined		F:\WORK\ORCAD-WORK\2018\LOAD_CELL\LOADCELLS_2018.DSN	AD8293/SOT23
34	SCHEMATIC1 : PAGE1	C106	10uF, 6V		Undefined		F:\WORK 2003\STUDENTS\RFID WORK\ORCAD-RFID\LIBRARIES\CIS\ANDREL16...	CAPACITOR POL
35	SCHEMATIC1 : PAGE1	R1	10K		Undefined		C:\CADENCE\ORCAD_9.2.3\TOOLS\CAPTURE\LIBRARY\DISCRETE.OLB	R
36	SCHEMATIC1 : PAGE1	U101	5V SMD		Undefined		C:\USERS\AK\DESKTOP\ORCAD WORK\2022\ARDUSHIELD-22\ARDUSHIELD.DSN	CON3_1
37	SCHEMATIC1 : PAGE1	C102	10uF, 6V		Undefined		F:\WORK 2003\STUDENTS\RFID WORK\ORCAD-RFID\LIBRARIES\CIS\ANDREL16...	CAPACITOR POL

Figure A.5: Bill of components and specifics

Item	Quantity	Reference	Part
15:	1	6	C2c,C2b,C2a,C3c,C3b,C3a 680*pF
16:	2	3	C101,C103,C105 0.1
17:	3	3	C102,C104,C106 10uF, 6V
18:	4	1	D1 GN
19:	5	3	J1c,J1b,J1a CON4
20:	6	1	J2 CON8
21:	7	4	RM1,R2c,R2b,R2a 1K
22:	8	3	R1c,R1b,R1a 10K
23:	9	3	R3c,R3b,R3a 5K6*
24:	10	2	R102,R101 1K*
25:	11	3	U1c,U1b,U1a AD8293/SO
26:	12	3	U2c,U2b,U2a LM7301
27:	13	1	U101 5V SMD
28:	14	1	U102 2.5V SOT

Figure A.6: Bill of components

Technical drawings of the new foot

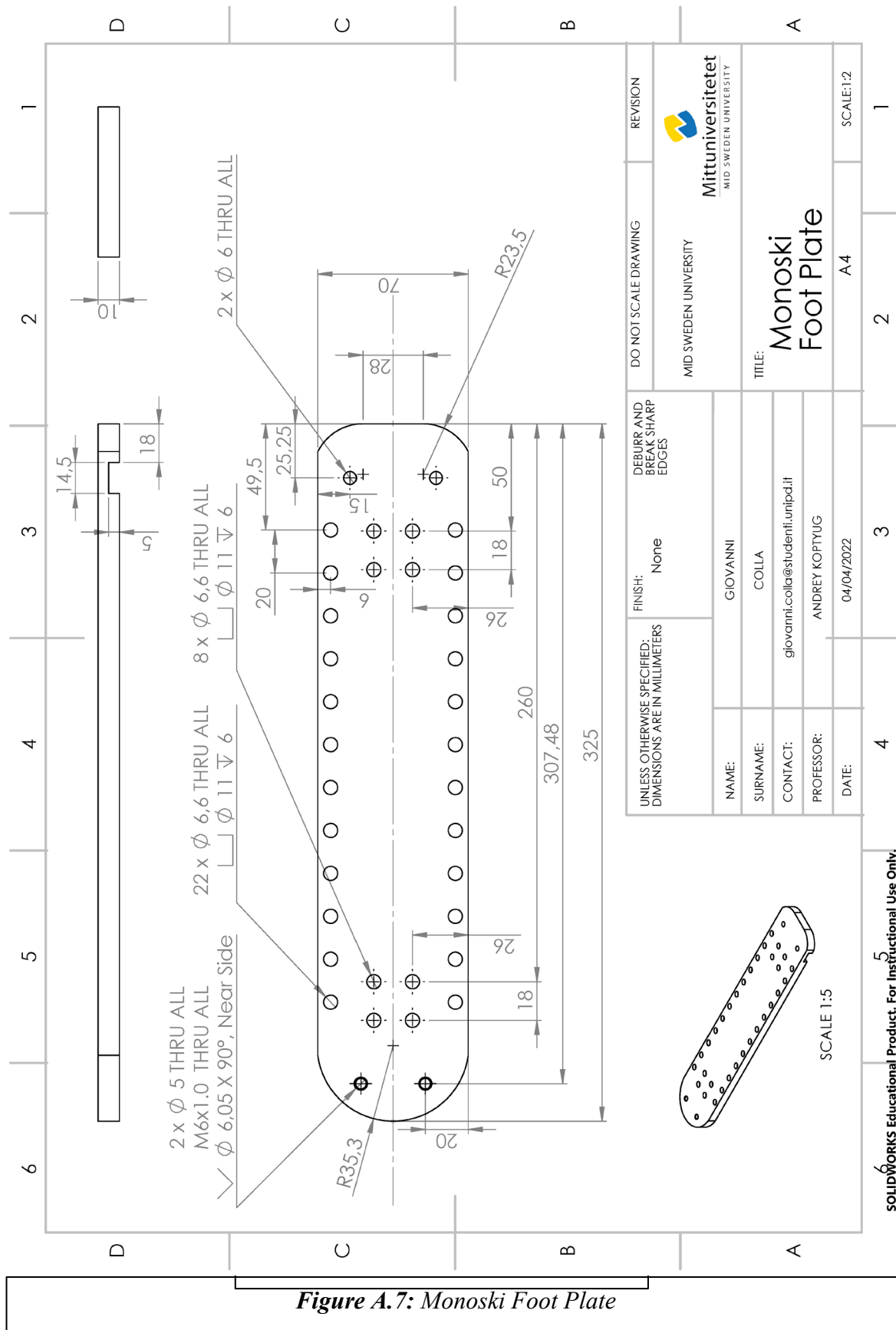


Figure A.7: Monoski Foot Plate

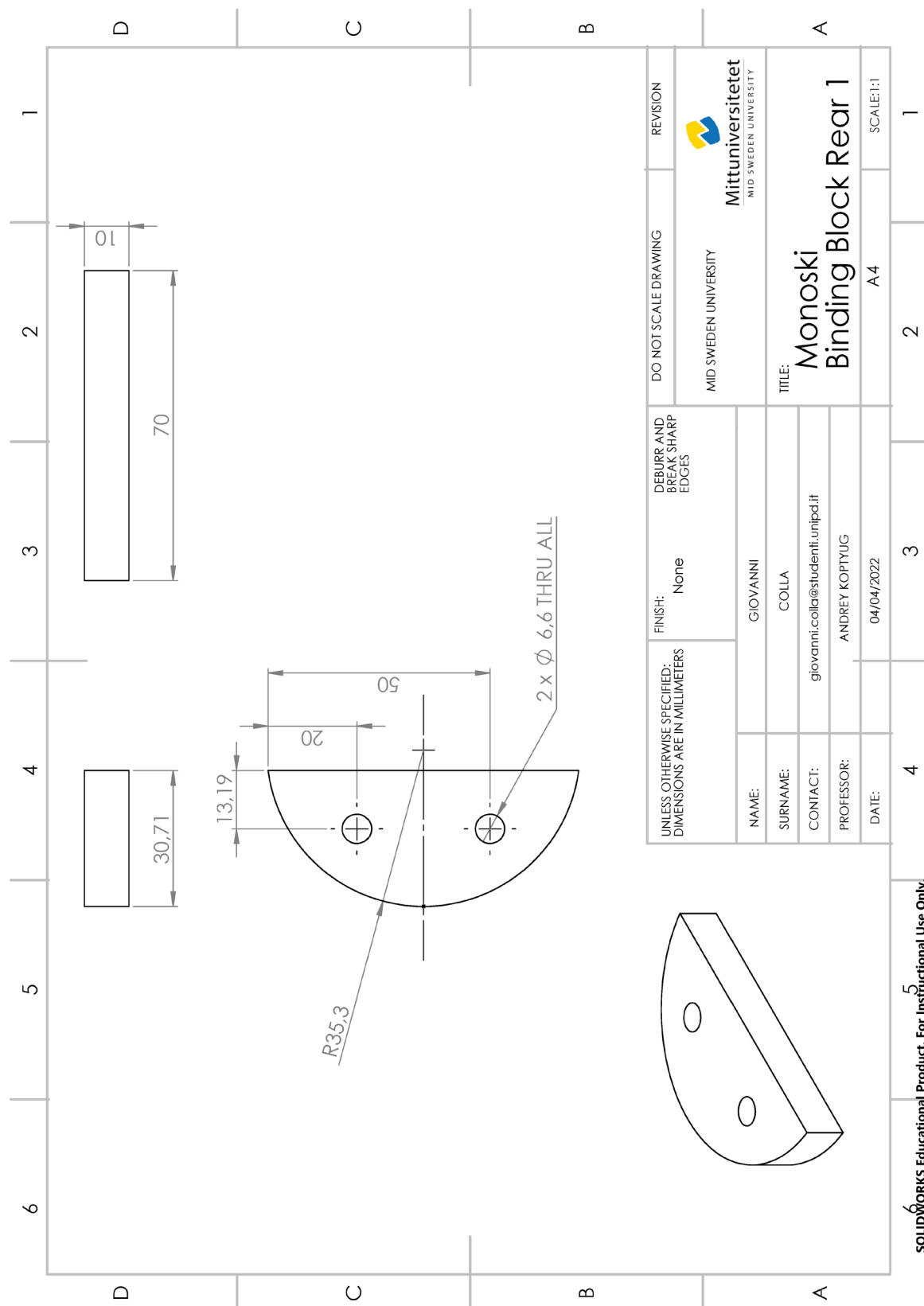


Figure A.8: Monoski Binding Block Rear 1

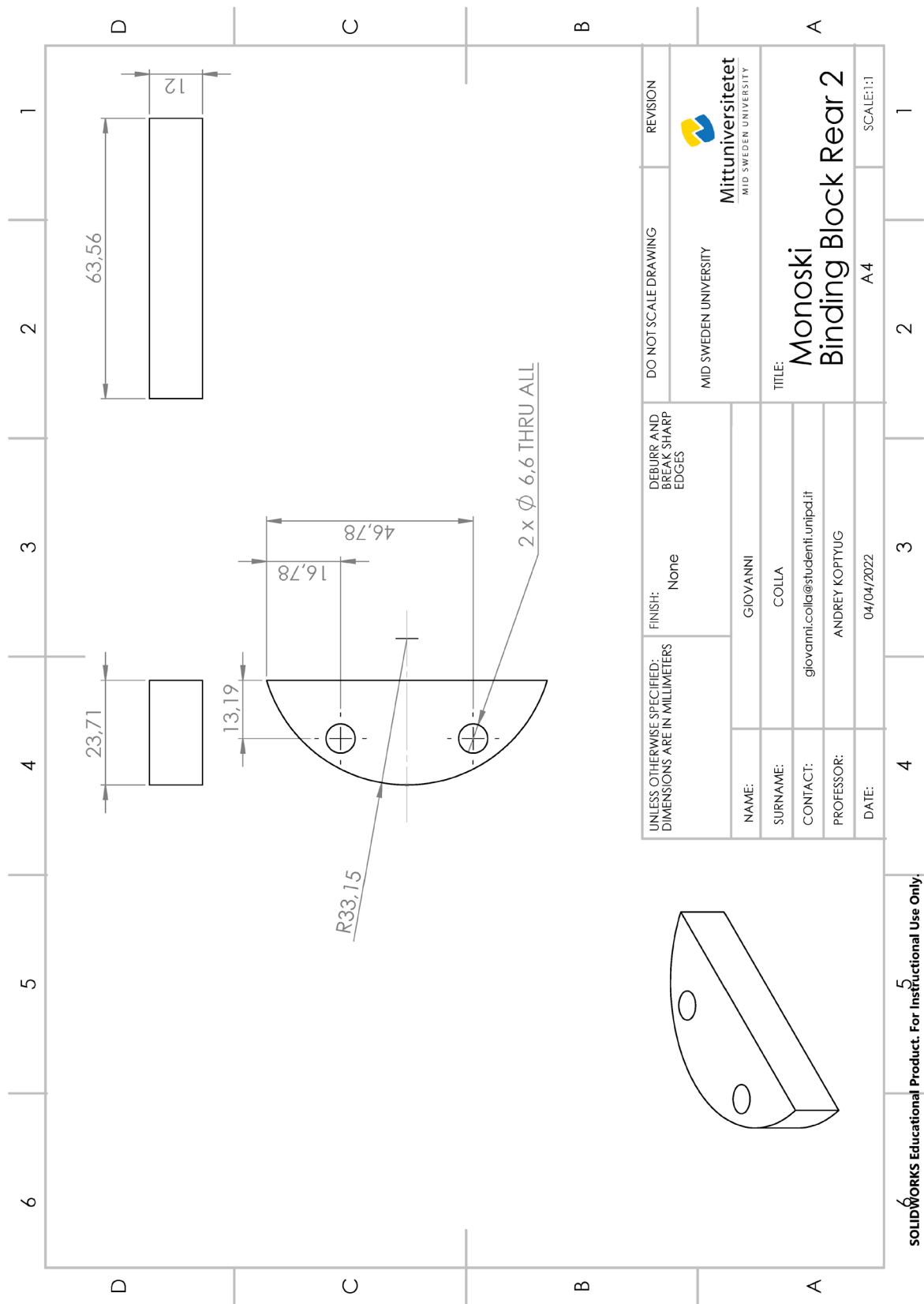


Figure A.9: Monoski Binding Block Rear 2

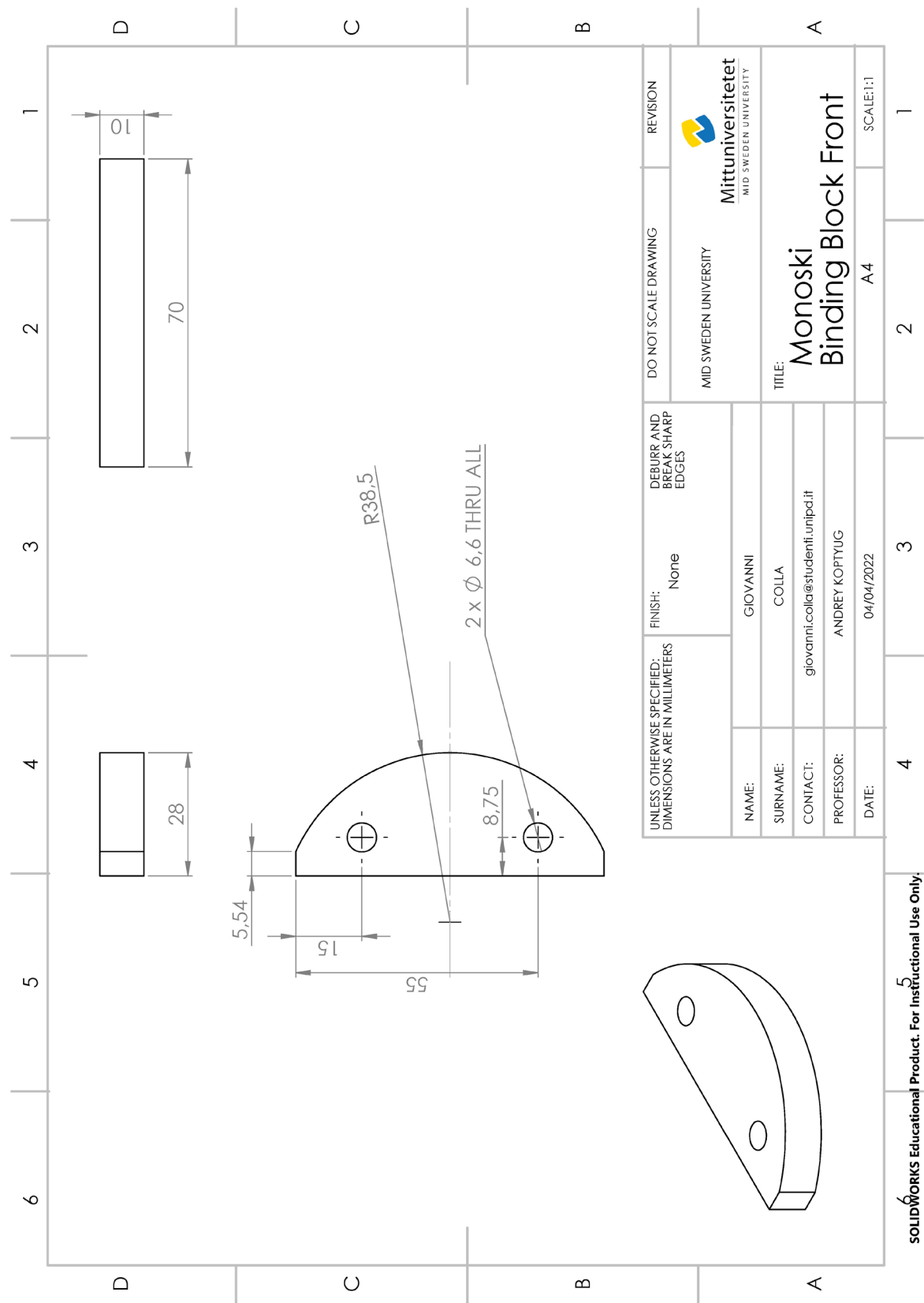


Figure A.10: Monoski Binding Block Front

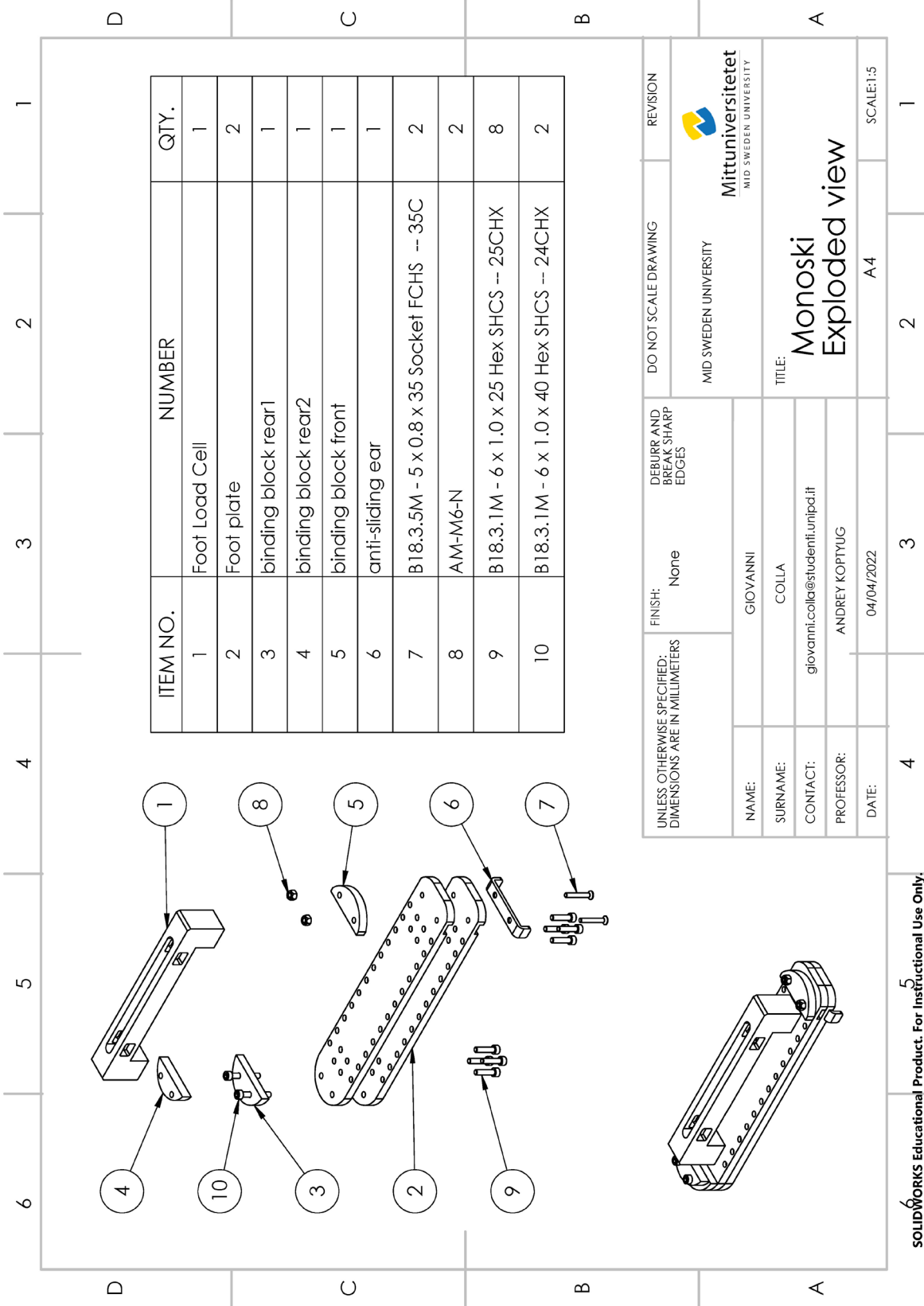


Figure A.12: Monoski Exploded view

Calibration of the load cell

Loads [N]		Ch output averages [V]									
Fy Kistler	Fy Weight	FzFR	FzFL	FyF	2.5V F	5V F	FzRR	FzRL	FyR	2.5V R	5V R
0.3	0	2.624	2.481	1.756	2.473	4.933	2.714	2.310	2.482	2.473	4.916
-18.8	-20	2.627	2.477	1.749	2.473	4.929	2.714	2.310	2.477	2.473	4.911
-28.5	-29	2.629	2.476	1.745	2.473	4.929	2.714	2.309	2.476	2.473	4.911
-49.6	-49	2.632	2.472	1.739	2.473	4.929	2.714	2.309	2.470	2.473	4.911
-67.2	-69	2.634	2.468	1.727	2.473	4.929	2.712	2.310	2.461	2.473	4.911
-96.6	-98	2.638	2.463	1.715	2.473	4.928	2.709	2.312	2.447	2.473	4.911
-115.8	-118	2.641	2.461	1.706	2.473	4.929	2.707	2.313	2.438	2.473	4.911
-144.2	-147	2.644	2.456	1.694	2.473	4.929	2.704	2.315	2.420	2.473	4.911
-162.3	-167	2.646	2.455	1.686	2.473	4.929	2.702	2.317	2.410	2.473	4.911
-171.2	-177	2.647	2.454	1.685	2.473	4.929	2.700	2.318	2.406	2.473	4.911

Figure A.13.: Loads applied and Channel response for Fy calibration

Loads [Nm]		Ch output averages [V]									
Mx Kistler	Mx Weight	FzFR	FzFL	FyF	2.5V F	5V F	FzRR	FzRL	FyR	2.5V R	5V R
0.00	0	2.720	2.574	1.871	3.172	2.052	2.638	2.720	2.574	1.871	3.172
7.09	7	2.612	2.674	1.868	3.023	2.183	2.624	2.612	2.674	1.868	3.023
13.41	14	2.525	2.757	1.883	2.873	2.313	2.604	2.525	2.757	1.883	2.873
19.88	21	2.423	2.854	1.881	2.739	2.432	2.595	2.423	2.854	1.881	2.739
27.01	29	2.306	2.962	1.877	2.590	2.567	2.541	2.306	2.962	1.877	2.590
33.79	36	2.188	3.070	1.876	2.445	2.699	2.540	2.188	3.070	1.876	2.445
40.75	43	2.064	3.177	1.876	2.295	2.836	2.554	2.064	3.177	1.876	2.295
75.21	72	1.425	3.727	1.857	1.529	3.543	2.530	1.425	3.727	1.857	1.529
74.43	72	1.427	3.725	1.859	1.532	3.542	2.531	1.427	3.725	1.859	1.532

Figure A.14: Loads applied and Channel response for Mx calibration

Loads [Nm]		Ch output averages [V]									
My Kistler	My Weight	FzFR	FzFL	FyF	2.5V F	5V F	FzRR	FzRL	FyR	2.5V R	5V R
-1	0	2.735	2.650	1.867	2.548	5.002	3.086	1.994	2.595	2.548	5.008
-24	-29	2.858	2.753	1.875	2.556	5.006	2.987	1.900	2.585	2.556	5.011
-58	-72	2.986	2.874	1.856	2.537	4.987	2.848	1.708	2.596	2.537	4.992
-60	-72	2.976	2.875	1.865	2.546	4.996	2.891	1.710	2.628	2.545	5.001
-84	-100	3.101	2.967	1.854	2.537	4.987	2.755	1.587	2.605	2.536	4.992
-121	-143	3.258	3.110	1.852	2.537	4.987	2.604	1.425	2.612	2.536	4.992
-120	-143	3.249	3.109	1.863	2.546	4.996	2.660	1.431	2.631	2.546	5.001
-186	-215	3.549	3.347	1.859	2.537	4.987	2.358	1.129	2.616	2.536	4.992
-181	-215	3.528	3.346	1.868	2.546	4.996	2.411	1.145	2.628	2.546	5.001
-247	-286	3.842	3.581	1.867	2.545	4.994	2.143	0.842	2.624	2.544	4.999
-246	-286	3.836	3.586	1.870	2.548	4.997	2.148	0.848	2.629	2.547	5.002

Figure A.15: Loads applied and Channel response for My calibration

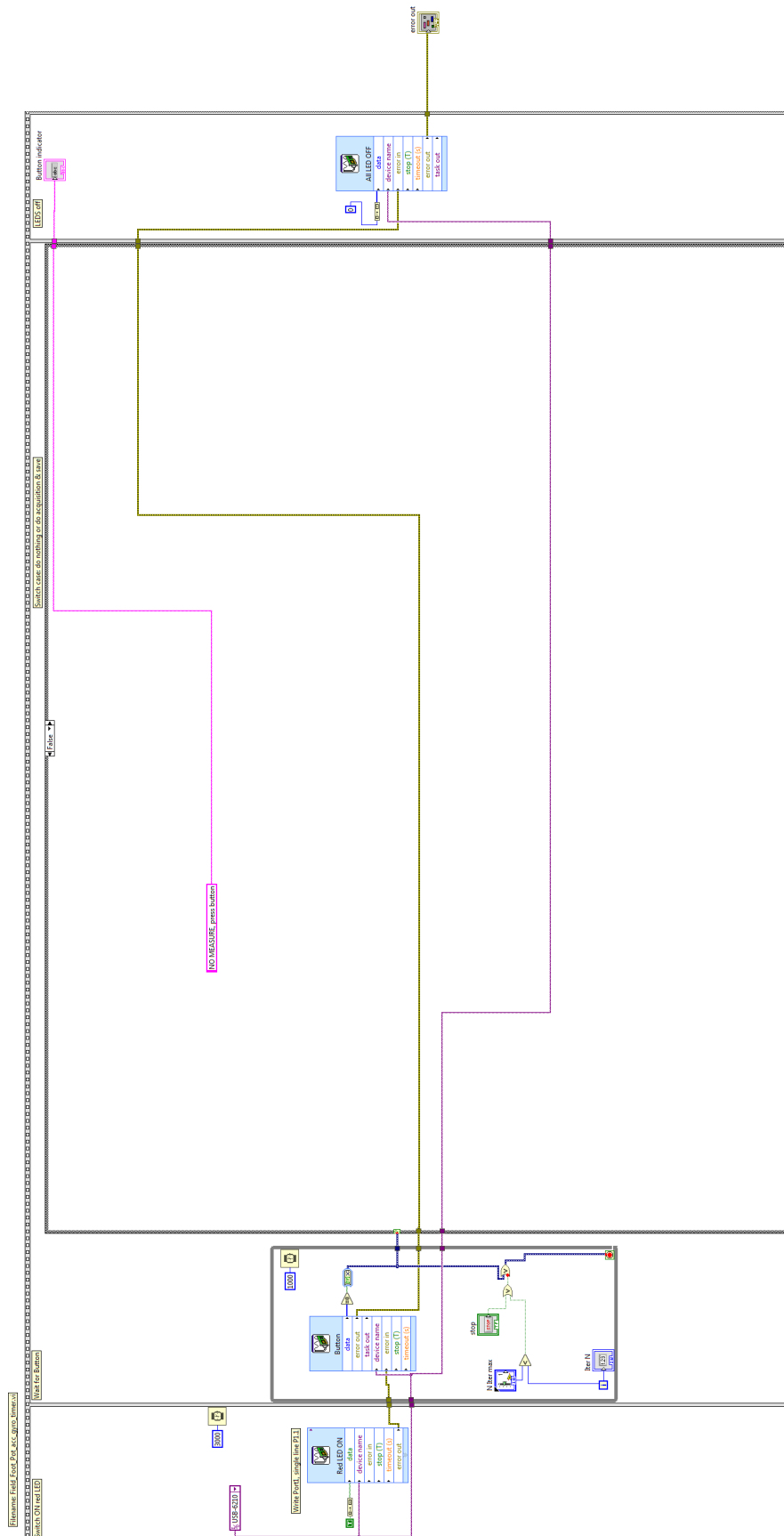


Figure A.17: Program Foot L.C., pot., acc., gyro. IF FALSE

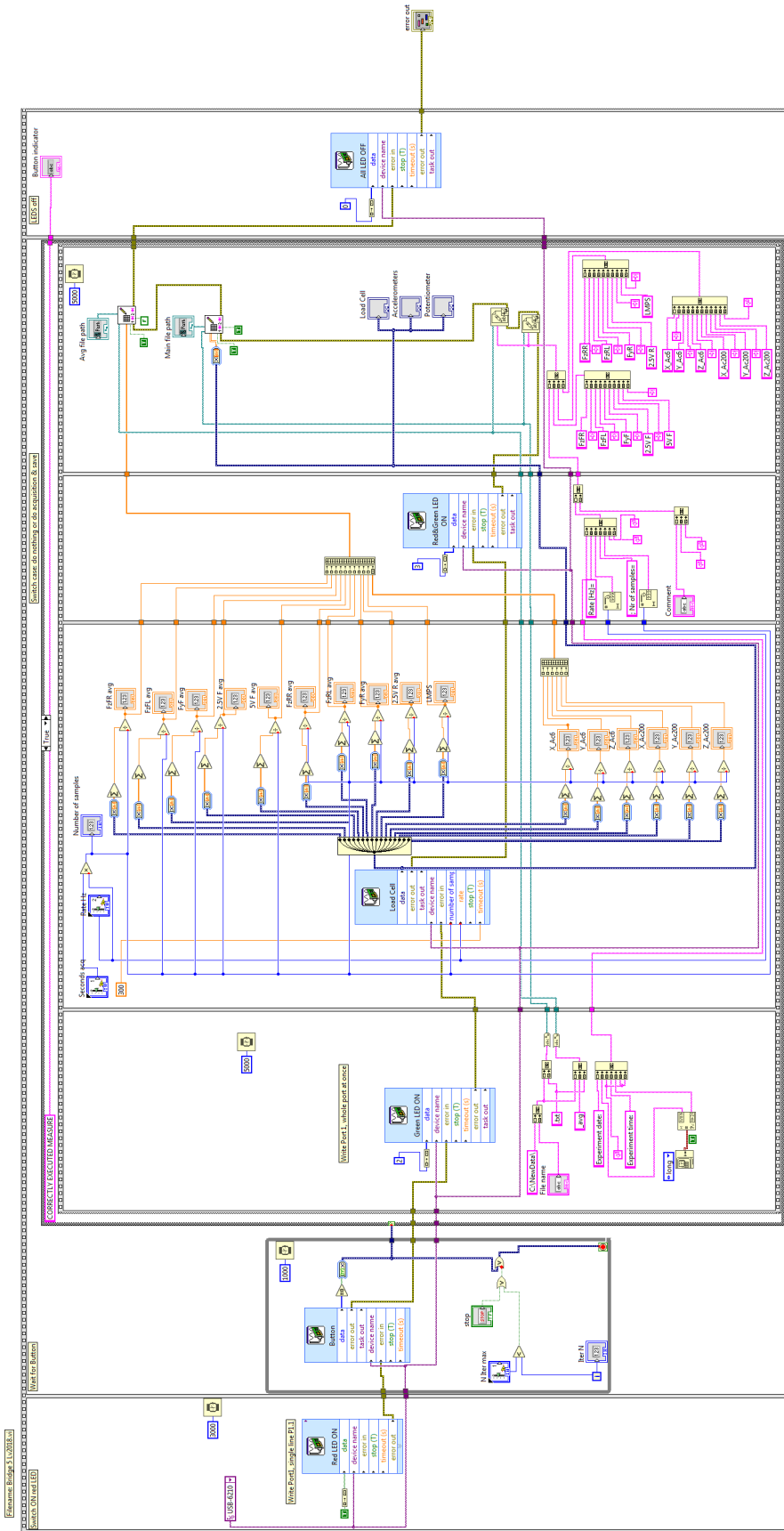


Figure A.18: Program Foot L.C., pot., acc. IF TRUE

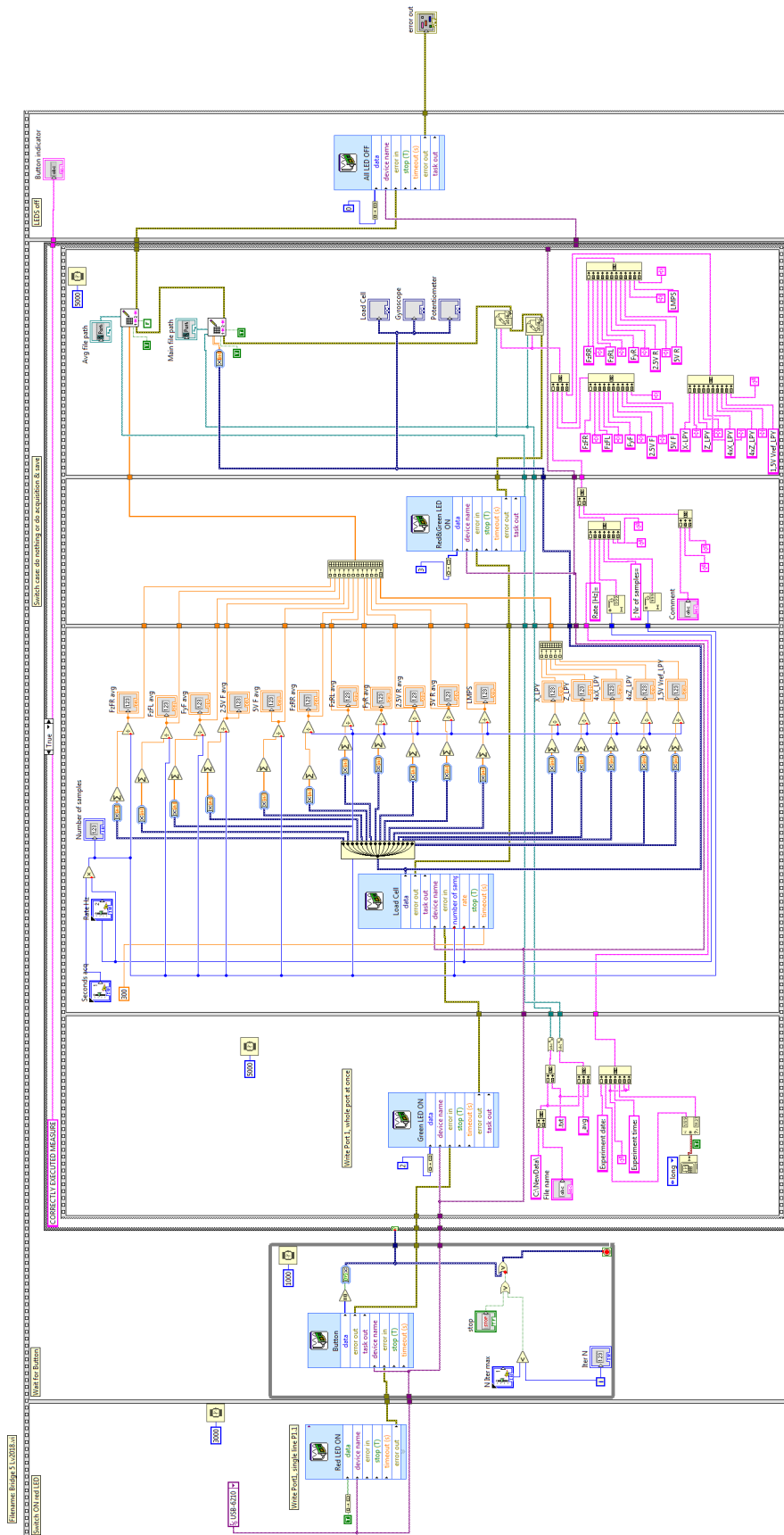
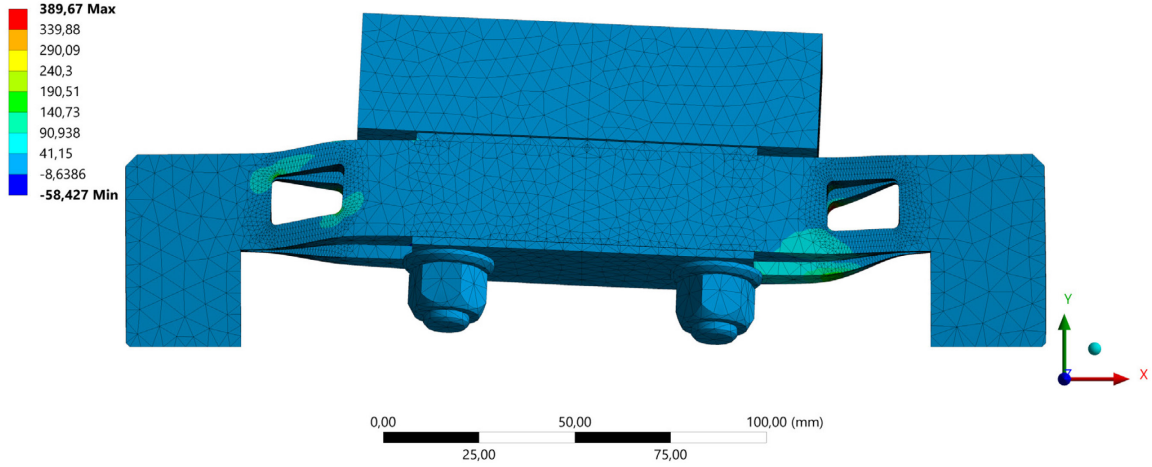


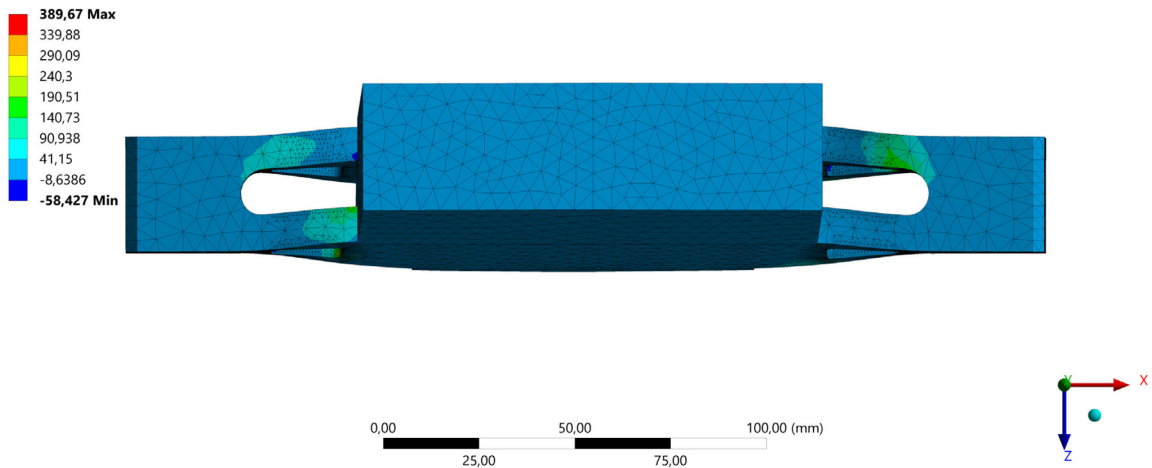
Figure A.19: Program Foot L.C., pot. IF TRUE

FEM analysis of the load cell

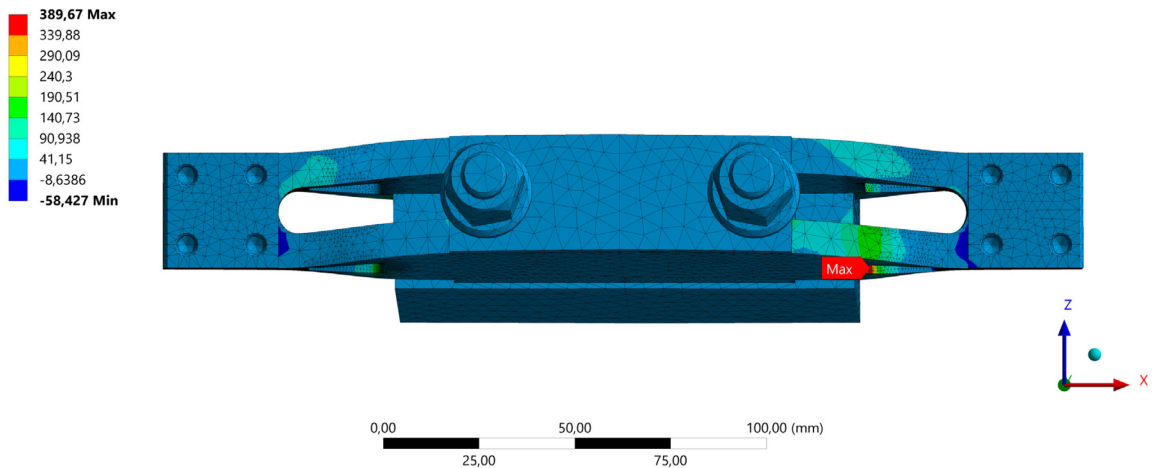
Maximum Principal Stress
Type: Maximum Principal Stress
Combination Name: Combination 1
Unit: MPa
16/10/2022 13:50



Maximum Principal Stress
Type: Maximum Principal Stress
Combination Name: Combination 1
Unit: MPa
16/10/2022 13:51



Maximum Principal Stress
Type: Maximum Principal Stress
Combination Name: Combination 1
Unit: MPa
16/10/2022 13:54



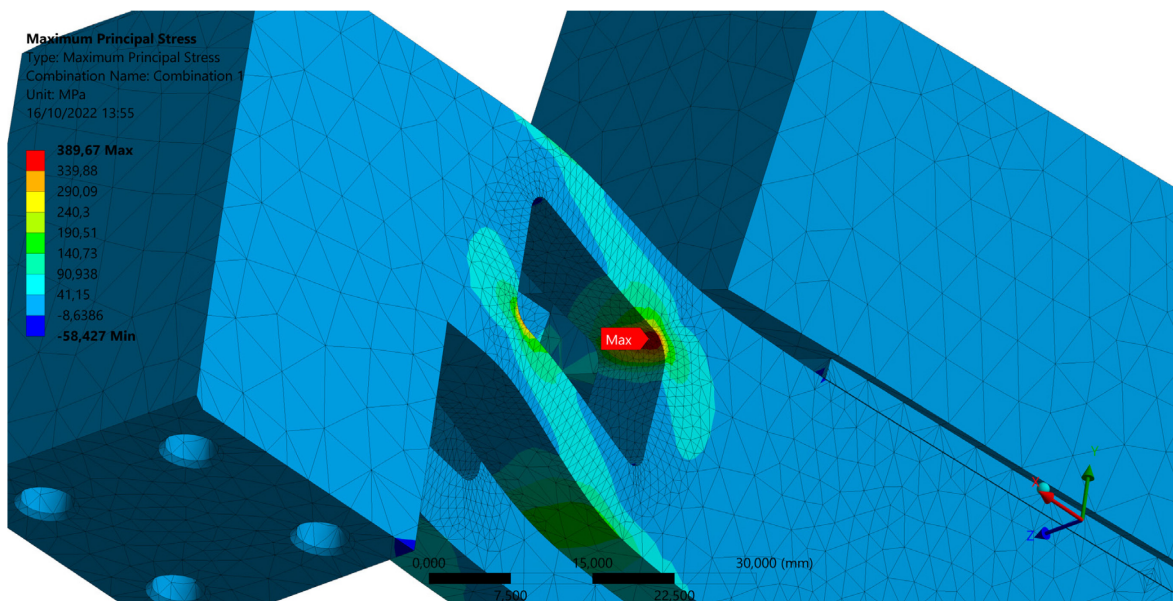
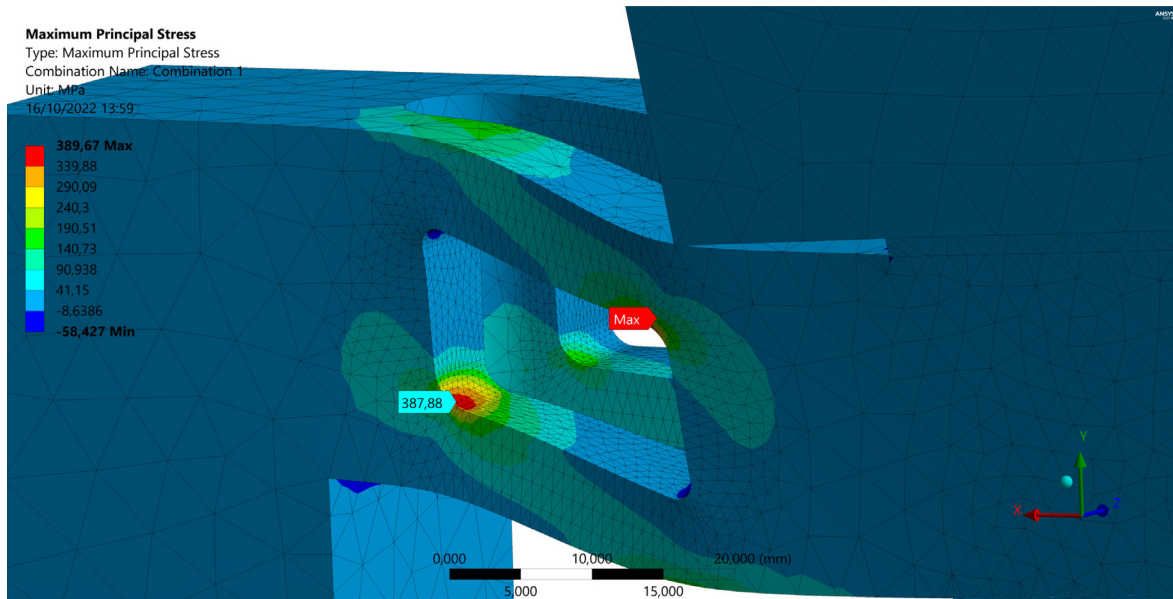


Figure A.20: Maximum principal stress

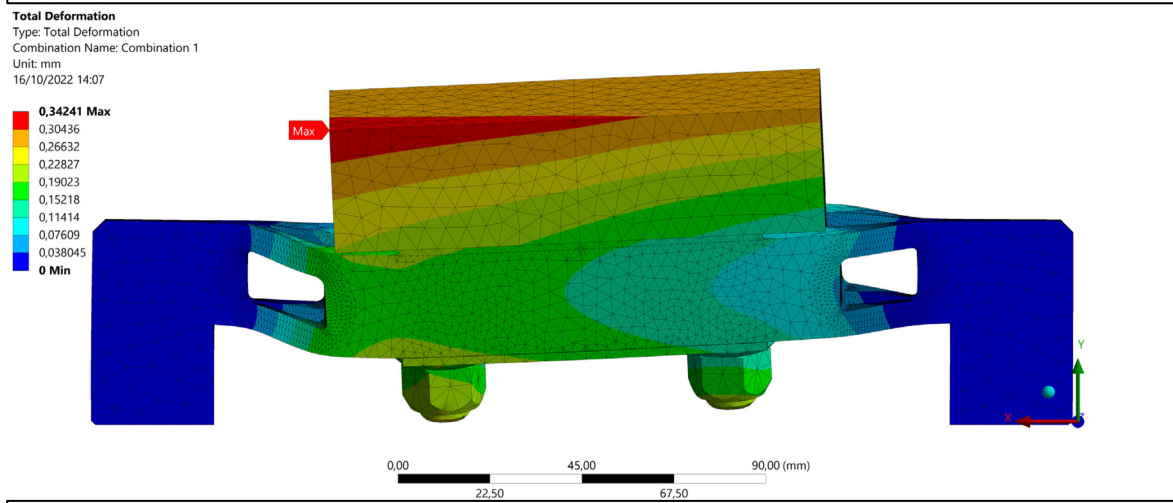


Figure A.21: Deformation

BIBLIOGRAPHY

- [1] Jansson A. Hållfasthetsundersökning på en sitski. 2015.
- [2] Piccinin D. Kinematic and kinetic analysis of a Paralympic skier during slalom. 2016.
- [3] Ferrari M. Design and validation of a dynamometric load cell for the measurement of loads acting on a paralympic monoski. 2016.
- [4] Vanzetto D. Acquisition and analysis of kinematic and kinetic data on a top paralympic skier during giant slalom. 2017.
- [5] Gardin P. Analisi del comportamento strutturale del Sistema complesso sci-attacco scarpone. 2007.
- [6] Petrone N, Vanzetto D, Marcolin G, Bruhin B, Gilgien M. The effect of foot setting on kinematic and kinetic skiing parameters during giant slalom: A single subject study on a Paralympic gold medalist sit skier. *J Sci Med Sport* 2021;24:1049–54. <https://doi.org/10.1016/j.jsams.2020.08.010>.
- [7] Tessier. Tessier Adaptive outdoor sports equipment n.d. <https://www.tessier-adaptive-sports.com/en/home-page-tessier-adaptive-outdoor-sports-equipment/> (accessed September 19, 2022).
- [8] Silseth H, Sletten HS, Grøndahl H, Eikevåg SW, Steinert M. Design of experiment for sports equipment - experimentally mapping the design space for paralympic alpine outriggers. *Proceedings of the Design Society* 2021;1:1073–82. <https://doi.org/10.1017/pds.2021.107>.
- [9] Kistler Group. Instruction Manual Multicomponent Force Plate for Biomechanics Type 9281E.... n.d.
- [10] Kistler Group. Instruction Manual BioWare ® Software Type 2812A.... n.d.
- [11] Yin S, Link YY. Comparison and Analysis of Strain Gauge Balance Calibration Matrix Mathematical Models. 1999.
- [12] Hull ML, Brewer R, Hawkins D. A New Force Plate Design Incorporating Octagonal Strain Rings. vol. 11. 1995.
- [13] Petrone N. Introduction to Strain gauge theory and applications for Loads Measurements 2022.
- [14] Demuth H, Beale M. Neural Network Toolbox For Use with MATLAB User's Guide. 1992.

- [15] MATLAB help n.d. <https://it.mathworks.com/help/matlab> (accessed October 14, 2022).
- [16] ANSYS Inc. ANSYS Workbench Documentation. n.d.
- [17] Mikats S. Development of a 6-component load cell for the application in sports science. 2018.
- [18] Öhlins website n.d. <https://www.ohlins.com/> (accessed October 14, 2022).
- [19] KTC. KTC Datasheet Linear position sensors Pulling Rod Type. n.d.
- [20] Analog Devices. LPY4150AL Datasheet Dual-axis pitch and yaw ± 1500 dps analog gyroscope n.d. <https://www.mouser.co.uk/datasheet/2/389/CD00254147-251801.pdf> (accessed October 14, 2022).
- [21] ST. LIS344ALH Datasheet High performance 3-axis $\pm 2/\pm 6g$ ultracompact linear accelerometer n.d. <https://www.st.com/en/mems-and-sensors/lis344alh.html#> (accessed October 14, 2022).
- [22] Analog Devices. ADXL377 Datasheet 3-Axis ± 200 g Accelerometer n.d. <https://www.analog.com/media/en/technical-documentation/datasheets/ADXL377.pdf> (accessed October 14, 2022).
- [23] NI USB-6210 Specifications n.d. <https://www.ni.com/docs/en-US/bundle/usb-6210-specs/page/specs.html> (accessed October 16, 2022).
- [24] LabVIEW help n.d. <https://www.ni.com/support/> (accessed October 16, 2022).
- [25] Cavacece M, Smarrini F, Valentini PP, Vita L. Kinematic and dynamic analysis of a sit-ski to improve vibrational comfort. *Sports Engineering* 2005;8:13–25. <https://doi.org/10.1007/bf02844128>.
- [26] Petrone N, Panizzolo F, Trabacchin F. Development of a servohydraulic roller test bench for indoor evaluation of the vibrational comfort of bicycle components. 2015.
- [27] Scapinello M. Construction of a test bench for the development of experimental methods for the reproduction of road induced vibrations during indoor cycling. n.d.
- [28] SRI six axis circular load cell extra thin, D65mm F2500N model M3564F n.d. https://www.srisensor.com/188.html?project_root=product.
- [29] Cibir P. Development and testing of a kinetic and kinematic data acquisition system for track measurements of ski touring and alpine ski. 2022.
- [30] Penny & Giles. SLS 130 Linear Displacement Sensor n.d. https://www.cw-industrialgroup.com/getattachment/ee1cbc2e-8583-46d3-ae63-16d7a0fb825e/sls130_technical_data (accessed October 8, 2022).

- [31] Ishige Y, Inaba Y, Hakamada N, Yoshioka S. The Influence of Trunk Impairment Level on the Kinematic Characteristics of Alpine Sit-Skiing: A Case Study of Paralympic Medalists. *J Sports Sci Med* 2022;435–45. <https://doi.org/10.52082/jssm.2022.435>.
- [32] Schmid H. How to use the FFT and Matlab's pwelch function for signal and noise simulations and measurements. 2012.
- [33] Cavacece M, Smarrini F, Valentini PP, Vita L. Kinematic and dynamic analysis of a sit-ski to improve vibrational comfort. *Sports Engineering* 2005;8:13–25. <https://doi.org/10.1007/bf02844128>.